



ARL-CR-0775 • Aug 2015



Advanced Composites for Air and Ground Vehicles: Final Report

prepared by Nicholas Giannaris
Michigan State University
220 Trowbridge Rd.
East Lansing, MI 48824

under contract W911NF-11-2-0017

Approved for public release; distribution is unlimited.

NOTICES

Disclaimers

The findings in this report are not to be construed as an official Department of the Army position unless so designated by other authorized documents.

Citation of manufacturer's or trade names does not constitute an official endorsement or approval of the use thereof.

Destroy this report when it is no longer needed. Do not return it to the originator.



Advanced Composites for Air and Ground Vehicles: Final Report

prepared by Nicholas Giannaris
Michigan State University
220 Trowbridge Rd.
East Lansing, MI 48824

under contract W911NF-11-2-0017

REPORT DOCUMENTATION PAGE				Form Approved OMB No. 0704-0188	
<p>Public reporting burden for this collection of information is estimated to average 1 hour per response, including the time for reviewing instructions, searching existing data sources, gathering and maintaining the data needed, and completing and reviewing the collection information. Send comments regarding this burden estimate or any other aspect of this collection of information, including suggestions for reducing the burden, to Department of Defense, Washington Headquarters Services, Directorate for Information Operations and Reports (0704-0188), 1215 Jefferson Davis Highway, Suite 1204, Arlington, VA 22202-4302. Respondents should be aware that notwithstanding any other provision of law, no person shall be subject to any penalty for failing to comply with a collection of information if it does not display a currently valid OMB control number.</p> <p>PLEASE DO NOT RETURN YOUR FORM TO THE ABOVE ADDRESS.</p>					
1. REPORT DATE (DD-MM-YYYY) August 2015		2. REPORT TYPE Final		3. DATES COVERED (From - To) June 2011–June 2014	
4. TITLE AND SUBTITLE Advanced Composites for Air and Ground Vehicles: Final Report				5a. CONTRACT NUMBER W911NF-11-2-0017	
				5b. GRANT NUMBER	
				5c. PROGRAM ELEMENT NUMBER	
6. EDITOR(S) Nicholas Giannaris				5d. PROJECT NUMBER	
				5e. TASK NUMBER	
				5f. WORK UNIT NUMBER	
7. PERFORMING ORGANIZATION NAME(S) AND ADDRESS(ES) Michigan State University 220 Trowbridge Rd. East Lansing, MI 48824				8. PERFORMING ORGANIZATION REPORT NUMBER	
9. SPONSORING/MONITORING AGENCY NAME(S) AND ADDRESS(ES) US Army Research Laboratory ATTN: RDRL-WMM-A Aberdeen Proving Ground, MD 21005-5069				10. SPONSOR/MONITOR'S ACRONYM(S)	
				11. SPONSOR/MONITOR'S REPORT NUMBER(S) ARL-CR-0775	
12. DISTRIBUTION/AVAILABILITY STATEMENT Approved for public release; distribution is unlimited.					
13. SUPPLEMENTARY NOTES					
14. ABSTRACT <p>The following is a summary performed at the Composite Vehicle Research Center at Michigan State University during the period of performance ending June 20, 2014, including a one-year no-cost extension. The work described herein is cumulative and has been organized mainly into the following research thrust areas: computational modeling; flammability; self-diagnostic composite structures; impact resistance; composite joining; multifunctional composite materials; vehicle survivability and occupant safety; structural integrity of composites; and biomimetics. The research performed in each of these thrust areas is described in this report.</p>					
15. SUBJECT TERMS composites, nanotechnology, material properties, material modeling, nondestructive testing, flammability					
16. SECURITY CLASSIFICATION OF:			17. LIMITATION OF ABSTRACT UU	18. NUMBER OF PAGES 184	19a. NAME OF RESPONSIBLE PERSON William Spurgeon
a. REPORT Unclassified	b. ABSTRACT Unclassified	c. THIS PAGE Unclassified			19b. TELEPHONE NUMBER (Include area code) 410-306-1006

Contents

List of Figures	viii
List of Tables	xiv
1. Thrust Area 1A: Computational Modeling	1
Preface	1
1.1 Multiscale Modeling of Polymer Nanocomposites	1
1.1.1 Summary	1
1.1.2 Introduction	2
1.1.3 Task 1: Develop a Microstructure-Inspired Material Model with Real and Statistically Equivalent Models for Halloysite Nanotube (HNT) Polypropylene Composite	3
1.1.4 Task 2: The 3-D Reconstruction of Exfoliated Graphite Nanoplatelets (xGnP) High-Density Polyethylene (HDPE)	7
1.1.5 Task 3: Develop 3-D RVEs with Cohesive-Element-Based Failure Models to Predict the Stress-Strain Curve for Nanocomposites Under Tensile Loading	11
1.1.6 Summary and Conclusions	23
1.1.7 Outcomes (Journal Papers)	24
1.1.8 References	24
2. Thrust Area 1B: Flammability of Exfoliated Graphite Nanoplatelet (xGnP) Composite Materials	30
2.1 Summary	30
2.2 Introduction	30
2.3 Brief Literature Review	31
2.4 Experimental Methods	32
2.5 Test Plan	33
2.6 Materials	34
2.7 Experimental Setup	34
2.8 Testing and Results	35
2.9 Outcomes	37

2.10	Future Objectives	37
2.11	References	38
3.	Thrust Area 1C: Structural Joining: Similar and Dissimilar Materials	42
3.1	Summary	42
3.2	Topics Addressed/Successfully Implemented	42
3.3	Deliverables and Outcomes	44
3.4	Acknowledgments	48
4.	Thrust Area 2: Self-Diagnostic Composite Structures	49
4.1	Wireless Sensor Networks for Online Monitoring of Heavy-Duty Vehicle Systems	49
4.1.1	Summary	49
4.1.2	Introduction	49
4.1.3	Literature Review	51
4.1.4	Experimental Methods	52
4.1.5	Validation	53
4.1.6	Finite Element Modeling	54
4.1.7	Signal Processing Algorithms for Damage Detection	55
4.1.8	Outcomes	56
4.1.9	References	57
5.	Thrust Area 3A: Structural Integrity of Composites	58
5.1	A Model for Fatigue Life Prediction of Composite Structures	58
5.1.1	Summary	58
5.1.2	Introduction	58
5.1.3	Fatigue Model Overview	59
5.1.4	PFDM and Its Implementation	60
5.1.5	Experimental	60
5.1.6	Evaluation of PFDM	61
5.1.7	Fatigue Testing with S-2 Glass/SC-15 Epoxy Composite	62
5.1.8	References	65
5.1.9	Publications	66
5.2	Multiscale Damage Modeling	68
5.2.1	Summary	68

5.2.2	Introduction	68
5.2.3	Literature Review	68
5.2.4	Approach	69
5.2.5	Results and Discussions	70
5.2.6	Future Work	73
5.2.7	References	74
5.2.8	Publications	76
6.	Thrust 3B: Multifunctional Composite Materials	77
6.1	Summary	77
6.2	Functionalization of GnP	78
6.2.1	Elastomeric Functionalization of GnP	78
6.2.2	Edge Modification of GnP	79
6.2.3	Edge Stitching of GnP	80
6.3	Coating of Carbon Fibers with GnP	80
6.4	Fabrication of GnP “Paper” Films	81
6.5	Interlaminar Toughening of Multilayer Vinyl Ester Composites Using GnP Paper	82
6.5.1	Moderate-Speed Impact Testing	82
6.5.2	High-Speed Blast Testing	83
6.6	Future Directions	84
6.7	Acknowledgments	84
7.	Thrust Area 3C: Vehicle Survivability and Occupant Safety	85
7.1	Scaling Effects in Composites Subjected to Blast Loading	85
7.1.1	Introduction	85
7.1.2	Experimental Methods	85
7.1.3	Materials	86
7.1.4	Experimental Setup	86
7.1.5	Testing and Results	87
7.1.6	Conclusions	87
7.1.7	Outcomes	88
7.2	Developing Triaxial Quasi-3-dimensional (TQ3D) Woven Composites with High-Impact Resistance	89
7.2.1	Introduction	89

7.2.2	Development of Q3D Fabrics	89
7.2.3	Manufacture of TQ3D Fabric	90
7.2.4	Testing Results	90
7.2.5	Outcomes	91
7.3	Developing Projection Moiré Assisted Impact Testing	92
7.3.1	Introduction	92
7.3.2	Experimental Setup and Results	92
7.3.3	Validation and Applications	93
7.3.4	Outcomes	94
8.	Thrust Area 6: Biomimetics	95
8.1	Enhanced Damage Tolerance in Biomimetic Ceramic Composites	95
8.1.1	Summary	95
8.1.2	Introduction	95
8.1.3	Analytical Model	97
8.1.4	Results and Discussion	99
8.1.5	Inferences	102
8.1.6	Outcomes	102
8.1.7	References	103
9.	Thrust Area 7: Design and Manufacturing	105
9.1	Experimental and Numerical Characterization of Flexural Behavior of Vacuum-Assisted Resin Transfer Molding (VARTM)-Infused Composite Sandwich Structures	105
9.1.1	Summary	105
9.1.2	Introduction	105
9.1.3	Experiments	107
9.1.4	Numerical Modeling	110
9.1.5	Results and Discussion	112
9.1.6	Conclusions	120
9.1.7	References	121
9.2	Mechanical Characterization of Glass and Carbon Fiber Composites Fabricated by Resin Infusion	124
9.2.1	Summary	124
9.2.2	Introduction	124
9.2.3	Composite Design and Fabrication	125

9.2.4	Experimental Techniques	127
9.2.5	Results	132
9.2.6	Summary	138
9.2.7	Bibliography	139
9.3	Design and Manufacture of a High-Mobility Multipurpose Wheeled Vehicle (HMMWV) Component	140
9.3.1	Summary	140
9.3.2	Introduction	140
9.3.3	Component Identification	140
9.3.4	Materials and Process	142
9.3.5	Trials	145
9.3.6	Results	146
9.4	Interlaminar Reinforcement of Glass Fiber/Epoxy Composites with Graphene Nanoplatelets	148
9.4.1	Summary	148
9.4.2	Introduction	148
9.4.3	Methods	150
9.4.4	Testing	151
9.4.5	Results and Discussion	153
9.4.6	Conclusion	163
9.4.7	References	164
	Distribution List	167

List of Figures

Fig. 1.1	a) Schematic of serial sectioning, b) slide generated through serial sectioning, and c) HNTs imaged with Auriga SEM	3
Fig. 1.2	a) 2-D SEM images of HNT polypropylene composite and b) 3-D reconstruction of the RVE based on serial sectioning	4
Fig. 1.3	Two-point correlation functions	5
Fig. 1.4	a) The final mesh for real RVE, b) inclusions' mesh in real RVE with average inclusion volume of $0.025 \mu\text{m}^3$, and c) inclusions' mesh in statistical RVE	5
Fig. 1.5	Extracting TPCF of xGnP polymer composite in different directions	8
Fig. 1.6	RVE with preferred orientation and a known distribution of diameters.....	8
Fig. 1.7	Obtaining material parameters using Mcalibration optimization software.....	9
Fig. 1.8	a) Stress-strain response (numerical) and b) stress-strain response (experimental)	10
Fig. 1.9	a) RVE of nanocomposite, b) individual platelet, and c) map of stress in x-x direction	10
Fig. 1.10	Comparison of stress-strain response of UHMWPE and xGnP+UHMWPE	11
Fig. 1.11	3-D representation of the spherical coordinates of a randomly selected point	12
Fig. 1.12	Examples of 3-D models of nanocomposites with different VFs and ARs: a) VF = 1%, AR = 100, b) VF = 1%, AR = 10.....	13
Fig. 1.13	Typical traction-separation law for modeling cohesive failure	13
Fig. 1.14	Comparison of traction-separation response in opening and sliding separation [54]	15
Fig. 1.15	Averaged stress-strain curves for RVEs with random distribution and orientation of GNP. Particle VFs = 0.5%, 1.5%, 2.5%; AR D/t = 40; perfectly bonded GNP.	16
Fig. 1.16	Averaged stress-strain curves for RVEs with random distribution and orientation of GNP. Particle VFs = 1%; AR D/t = 10, 50, 100; perfectly bonded GNP	17
Fig. 1.17	Comparing GNP/HDPE (perfect bonding with different VF and constant AR) and GNP/HDPE (cohesive bonding with different VF and constant AR)	18
Fig. 1.18	Left: GNP/HDPE (perfectly bonded with different VF and constant AR); right: GNP/HDPE (cohesively bonded with different VF and constant AR)	18

Fig. 1.19	Comparing GNP/HDPE (perfectly bonded with different AR and constant VF) and GNP/HDPE (cohesively bonded with different AR and constant VF).....	20
Fig. 1.20	Left: GNP/HDPE (perfectly bonded with different AR and constant VF); right: GNP/HDPE (cohesively bonded with different AR and constant VF).....	20
Fig. 1.21	Study showing the effect of AR (weak bonding)	21
Fig. 1.22	Study showing the effect of VF (weak bonding).....	22
Fig. 1.23	Damage sequence of HDPE/GNP with AR = 100, VF = 1%. Left: weak bonding; Right: strong bonding.	23
Fig. 2.1	Cone calorimeter.....	33
Fig. 2.2	A typical crack pattern that develops after thermal assault	34
Fig. 2.3	Experimental and modeling plan.....	35
Fig. 2.4	Stress field as the material degrades from a controlled burn that initiates at the top surface	36
Fig. 2.5	Modeled crack propagation	36
Fig. 2.6	Process involved in burning of composite materials	38
Fig. 4.1	The schematic of a centralized wireless sensor network consisting of 2 entities: the sensor nodes and the base station. The sensor nodes are mounted on the structure and connected to embedded or surface-bonded transducers. The base station is a remote PC that collects data for processing from the sensor nodes.	51
Fig. 4.2	a) The extension circuit board connected to the Iris mote using the 51-pin connector. The sensor node has a total area less than 25 cm ² . b) The extension circuit board block diagram showing the sensing and actuation modules and the switch that selects which module will be connected to the PZT wafer.	53
Fig. 4.3	Experimental setup for the validation of the sensing circuit. Two PZT wafers with dimensions 8 × 7 mm are bonded to the aluminum plate. Sensor node 1 is connected to PZT1 and sensor node 2 is connected to PZT2. The outputs of the charge amplifier and the envelope detector of sensor node 2 are connected to the oscilloscope.	54
Fig. 4.4	The guided wave signal and its envelope as recorded on the oscilloscope are shown in green and blue, respectively. The sampled envelope data that is transmitted to the base station and their interpolation are also shown. The S ₀ and A ₀ modes incident wave packets are indicated. All the latter wave packets in the signal are due to reflections from the edges of the plate.	54
Fig. 4.5	Lamb wave finite element method model in a single layer carbon fiber-reinforced polymer (CFRP) (left) and 8-layer quasi-isotropic CFRP laminate (right).....	55

Fig. 4.6	Schematic of multilayered composite material and phase velocity dispersion curves.....	55
Fig. 4.7	Imaging of composite plate with impact damage.....	56
Fig. 4.8	Imaging of 450- × 630- × 5-mm composite plate with surface-bonded aluminum stiffener to simulate surface damage	56
Fig. 5.1.1	a) A flowchart for the implementation of the PFDM using an ABAQUS UMAT. b) The empirical equations used in PFDM in determining fatigue life and stiffness/strength degradation.	60
Fig. 5.1.2	Comparisons of PFDM prediction and experiments. a) PFDM vs. DIC: first principal strain (left) and shear strain (right) evolution with fatigue cycles on a $[0_2/90_2]_s$ laminate at $P_{\max} = 25$ kN and $R = 0$. b) Failure patterns of $[0_2/90_2]_s$ (left) and $[45_2/-45_2]_s$ (right) laminates. c) The displacement increases with the number of fatigue cycles, $[0_2/90_2]_s$ at $P_{\max} = 25$ kN and $R = 0$. The prediction-matched experiment up to the onset of delamination. The 2 simulations are shown in red (with modified values of A and B [19]) and blue (with values of A and B [2]).	61
Fig. 5.1.3	S-2 Glass/SC-15 epoxy composite fatigue data. a) Master fatigue curve for uniaxial loading. b) In-plane shear with R-ratio of $R = 0, 0.2$, and 0.4	64
Fig. 5.1.4	Gradual degradation of a) the tensile modulus and b) tensile strength of S-2 Glass/SC-15 epoxy composite measured at $R = 0$	64
Fig. 5.2.1	Diagram of the various length scales associated with a composite structure	68
Fig. 5.2.2	Proposed multiscale workflow for the free-edge analysis of a laminated composite, including the effects of the local microstructure.....	70
Fig. 5.2.3	a) The finite element mesh of the microscale RVE and b) the applied boundary conditions for the free-edge microscale analysis....	70
Fig. 5.2.4	a) Y-stress contour in the $[25/-25/90]_s$ laminate under uniaxial tension (units are in megapascals). b) The strains extracted from the interface and midplane elements.....	71
Fig. 5.2.5	Contours of the max shear stress and the first principal stress at the free edge (X^-) generated in the interface and the midplane micromodels in a $[25/-25/90]_s$ laminate. (Units are in pascals.).....	71
Fig. 5.2.6	a) Normal, b) radial shear, and c) axial shear tractions for midplane and interface elements along the fiber/matrix interface at the region of maximum value. The results are normalized with regard to the matrix strength, σ_t , and the distance to the free edge in the X^- direction. d) Orientation of the cohesive traction directions.	72
Fig. 5.2.7	a) Y-stress contours for the $[0_2/90]_s$ laminate and b) the mesoscale strains extracted from the interface and midplane elements	73

Fig. 6.1	Edge groups that can be attached an xGnP particle.....	78
Fig. 6.2	Impact strength of xGnP vinyl ester composites	79
Fig. 6.3	Edge modification of an xGn particle.....	79
Fig. 6.4	Edge stitching of xGn particles	80
Fig. 6.5	Single-fiber interfacial shear strength for different GnP loadings	81
Fig. 6.6	XGnP papers.....	82
Fig. 6.7	Three types of laminates studied	82
Fig. 6.8	Three composite samples (a, b, and c) after blast test	84
Fig. 7.1.1	Schematic (top) and photo (bottom) of the Laboratory Blast Simulator (LBS).....	86
Fig. 7.1.2	Comparison of a) strain histories, b) displacement histories, and c), a) and b)	87
Fig. 7.2.1	Side view of BQ3D woven composite in a) warp and b) fill directions (left), top view of TQ3D woven composite (center), and TQ3D braiding machine (right)	90
Fig. 7.3.1	Schematic of the overall view (left) and the detailed view (right)	92
Fig. 7.3.2	a) Deformation contours from projection moiré for evenly spaced time step of 0.33 mm and b) profile lines for loading	93
Fig. 7.3.3	a) Comparison between projection moiré (points) and load cell (continuous curve) and b) setup for ballistic impact	93
Fig. 8.1	a) Schematic of staggered architecture of calcium carbonate bricks (shown in green) in biopolymer matrix (shown in yellow); b) expanded view of the 2-dimensional (2-D) unit cell structure (with plane strain infinitesimal deformation) showing the precracked length (L_1) and instantaneous overlap length (L_2) and coordinate systems; c) expanded view of the 2-D unit cell structure (with plane strain infinitesimal deformation) highlighting the elemental blocks and the original overlap length (L_0); d) splitting of parent crack tip for SERR calculations; and e) schematic identifying shear and normal force resultants N_c and Q_c , respectively	98
Fig. 8.2	Variation of interfacial shear stress (at the extremities of the overlap) as a function of varying overlap length and precrack. The figure in the inset shows the expanded view for lower shear levels in the unit cell.	100
Fig. 8.3	SERR ahead of the crack tip with increasing crack in the unit cell.....	101
Fig. 9.1.1	Layup for the VARTM process	107
Fig. 9.1.2	a) 3-point loading ASTM C393 standard configuration, $S = 150$ mm and b) 4-point loading ASTM D7249 long beam standard configuration, $S = 560$ mm, $L = 100$ mm	108
Fig. 9.1.3	Setup of a) 3-point and b) 4-point bending fixture.....	109

Fig. 9.1.4	Cylindrical pivot loading and support bar	110
Fig. 9.1.5	a) 3-point bending experiment for H250, 12.7-mm foam core sandwich panel, and b) sample under load	113
Fig. 9.1.6	a) 3-point bending experiment for H130, 25.4-mm foam core sandwich panel, and b) sample under load	114
Fig. 9.1.7	a) 4-point bending experiment for H250, 12.7-mm foam core sandwich panel, and b) sample under load	115
Fig. 9.1.8	a) 4-point bending experiment for H130, 25.4-mm foam core sandwich panel, and b) sample under load	116
Fig. 9.1.9	Flexural stiffness for H250, 12.7-mm, and H130, 25.4-mm foam sandwich panels	117
Fig. 9.1.10	Flexural analysis of sandwich panel subjected to 4-point bending: a) longitudinal strains (ϵ_{11}) and b) equivalent stresses (megapascals). (Images obtained as output from Digimat/Micross.).....	118
Fig. 9.1.11	Comparison of experimental and simulation-predicted flexural response for sandwich panels subjected to 4-point bending with 12.7- and 25.4-mm core thicknesses.....	119
Fig. 9.1.12	Comparison of flexural failure loads from simulations and experiments.....	120
Fig. 9.2.1	(Left) AGY's S-2 Glass and (right) A&P's Qiso	125
Fig. 9.2.2	Quasi-isotropic layup for S-glass	126
Fig. 9.2.3	VARTM setup	126
Fig. 9.2.4	RTM setup	127
Fig. 9.2.5	Tensile test setup	128
Fig. 9.2.6	Compression test setup	129
Fig. 9.2.7	Iosipescu test setup	130
Fig. 9.2.8	Rail shear test setup	131
Fig. 9.2.9	Flexural test setup.....	132
Fig. 9.2.10	Average ultimate tensile strength comparison.....	133
Fig. 9.2.11	Average elastic modulus comparison.....	133
Fig. 9.2.12	Average laminate compressive strength comparison	134
Fig. 9.2.13	Average laminate compressive modulus comparison	135
Fig. 9.2.14	Average failure shear strength from the Iosipescu and V-Notch rail shear tests methods.....	136
Fig. 9.2.15	Average shear moduli from the Iosipescu and V-Notch rail shear test methods	136
Fig. 9.2.16	Average flexural strength comparison.....	137

Fig. 9.2.17	Average flexural modulus comparison.....	138
Fig. 9.3.1	Tailgate	141
Fig. 9.3.2	Rear bumper assembly.....	141
Fig. 9.3.3	Rear bumper strut	142
Fig. 9.3.4	Fabric and cut preform	143
Fig. 9.3.5	Preform draping.....	143
Fig. 9.3.6	Final layup stage.....	144
Fig. 9.3.7	VARTM setup	144
Fig. 9.3.8	Trial 1 after infusion	145
Fig. 9.3.9	Composite bumper strut prototype	146
Fig. 9.3.10	Highlighted wrinkle in part surface	147
Fig. 9.4.1	Four-point flexural test results for pristine and 0.10, 0.25, and 0.50 wt% GnP samples	153
Fig. 9.4.2	Average maximum flexural strength of pristine and 0.10, 0.25, and 0.50 wt% GnP samples	154
Fig. 9.4.3	Mode-I fracture toughness (G_{Ic}) results of pristine, 0.25 wt%, and 1.0 wt% GnP samples	155
Fig. 9.4.4	SEM image of a pristine mode-I fracture surface. Image a) shows a macrovoid, and images b) and c) are progressively higher magnifications of a void edge, as indicated by the colored boxes.....	156
Fig. 9.4.5	Mode-I fracture surface of a 0.25 wt% GnP sample. Image a) shows a typical channel region, image b) is a closeup of the fibers on the fracture surface, and image c) shows a GnP aggregate lying between fibers, as highlighted by a white box.	156
Fig. 9.4.6	Intertow region of the 0.25 wt% GnP nanocomposite: a) low and b) high magnification.....	157
Fig. 9.4.7	Force-time response of pristine, 0.25 wt%, and 1.0 wt% GnP specimens at 20-, 40-, 60-, and 80-J impact energies, respectively...	158
Fig. 9.4.8	Energy-time response of pristine, 0.25 wt%, and 1.0 wt% GnP specimens at 20-, 40-, 60-, and 80-J impact energies, respectively...	159
Fig. 9.4.9	Force-deflection response of pristine, 0.25 wt%, and 1.0 wt% GnP specimens at 20, 40, 60, and 80 J impact energies, respectively	160
Fig. 9.4.10	Dye-penetration inspection (DPI) images of impacted a) and back b) surfaces	161
Fig. 9.4.11	C-scan images of back surfaces.....	162

List of Tables

Table 1.1 Properties of Halloysite clay nanotube and polypropylene [39] (top) and elastic constants measured using real RVE and statistical RVE (bottom).....	6
Table 1.2 Cohesive zone model parameters for opening and sliding modes [54]	16
Table 1.3 Cohesive parameters for weak bonding.....	21
Table 3.1 Subproject details.....	42
Table 3.2 Technology transfer student information.....	47
Table 4.1 Properties of the Iris mote sensing module, processing module, and RF module.....	53
Table 5.1.1 Fatigue experiments and PFDM predictions of AS4/3501-6 with center hole	62
Table 5.1.2 Mechanical properties of the manufactured S-glass/SC-15 composite	63
Table 5.1.3 Test matrix for PFDM model parameters for a woven composite ...	63
Table 7.1.1 Scaling parameters	86
Table 7.2.1 Central impact induced bending stiffness	90
Table 9.1.1 Foam core properties [25].....	111
Table 9.1.2 Material properties of plain weave S-2 Glass/SC-15 epoxy laminates	111
Table 9.2.1 S-glass and Qiso basic fabric properties	125
Table 9.2.2 Tensile test results.....	134
Table 9.2.3 Compression test results	135
Table 9.2.4 Shear test results	137
Table 9.2.5 Flexural test results	138

1. Thrust Area 1A: Computational Modeling

Farhang Pourboghraat and Azadeh Sheidaei

Preface

Polymer nanocomposites (PNCs) have demonstrated superior electrical, mechanical, physical, and thermal properties and are becoming a major focus for both academic and industrial research and development activities. The goal of this research project was to develop a multiscale material modeling tool that could predict the mechanical properties (stiffness and strength) and failure (delamination) of the polymer nanocomposites under different strain rates. To achieve this goal, the following 3 tasks have been accomplished as milestones for this project.

- Task 1: Develop a microstructure-inspired material model with real and statistically equivalent models for Halloysite nanotube polypropylene composite.
- Task 2: Develop a 3-dimensional (3-D) reconstruction of exfoliated graphite nanoplatelets high-density polyethylene.
- Task 3: Develop 3-D representative volume elements with cohesive element-based failure models to predict the stress-strain curve for nanocomposites under tensile loading.

1.1 Multiscale Modeling of Polymer Nanocomposites

1.1.1 Summary

The focus of this research project was the 3-D reconstruction of Halloysite nanotube and nanoplatelet-reinforced polymer composite. The 3-D reconstruction was performed using 2 different methods. In the first method, several slices of the composite material were obtained using a focused ion beam and scanning electron microscopy (SEM). A representative volume element (RVE) of the real material's micro/nanostructures was then constructed by stacking these morphological images using VCAT software. In the second method, SEM images of the nanocomposite were used to extract statistical 2-point correlation function (TPCF) for reconstruction of an RVE of the nanocomposite. The resulting RVEs obtained from both methods were meshed for finite element (FE) simulation of deformation under tension and shear loadings. The FE results were then used to compute information of interest, such as the stiffness tensor of the nanocomposite and the stress-strain response of the nanocomposite to external loadings. It was

concluded that the statistical method using TPCF [1] alone can produce an approximate microstructure that should be modified using other statistical descriptors, such as the 2-point cluster function and lineal path function, to have better reconstruction of heterogeneous nanocomposites [2].

1.1.2 Introduction

In recent years, (PNCs) have increasingly gained more attention because of their improved mechanical, barrier, thermal, optical, electrical, and biodegradable properties [3–5]. With the addition of less than 5 wt% nanoparticles [4], PNCs offer a wide range of improvements in moduli [6–8], strength, heat resistance [9], and biodegradability [3, 10], as well as a decrease in gas permeability [5,8,11,12] and flammability [5,8,10,13,14].

Although PNCs offer enormous opportunities to design novel material systems, development of an effective numerical modeling approach to predict their properties based on their complex multiphase and multiscale structure is still at an early stage. Molecular dynamics (MD) is becoming a powerful computational tool for the simulation of matter at the molecular scale [15–18]. To estimate macro-level properties of nanocomposites, multiscale homogenization approaches based on continuum mechanics are used. The homogenization techniques can be categorized into statistical methods, such as weak and strong contrast [19,20]; inclusion-based methods, such as self-consistent or Mori-Tanaka [21]; numerical methods, such as finite element analysis (FEA) and asymptotic methods [22]; variational/energy-based methods, such as Hashin-Shtrikman bounds [23]; and empirical/semi-empirical methods, such as Halpin-Tsai and classical upper and lower bounds (Voigt–Reuss) [24]. Finite element modeling (FEM) has been successfully applied to the integrated representative volume elements (RVEs) with a nanometric secondary phase [25–27].

Regardless of the method to reproduce microstructures of the nanocomposite, either with well-aligned RVE [26,27] or randomly distributed RVE with a Monte Carlo scheme [25], the final RVE cannot entirely represent the actual complex and highly heterogeneous nanocomposite structures. Dong et al. [28] developed a framework to incorporate the microstructural images, such as SEM micrographs, into 2-dimensional (2-D) FEM, the so-called object-oriented finite element (OOF) technique. The OOF, however, is limited to elasticity and thermal conductivity calculations in 2-D microstructures [29–32]. Several experimental and theoretical techniques, such as X-ray computed tomography and focused ion beam (FIB)/scanning electron microscopy (FIB/SEM), are being exploited to obtain 3-D microstructure as the input RVE for FEM software [33–35]. Two-point correlation function (TPCF) is the simplest statistical correlation functions that can convey some information about dispersion and distribution of inclusions in

heterogeneous materials. Recently, Deng et al. [36] presented a statistical work based on 2-D realization of the microstructure obtained from SEM images of carbon black particle fillers dispersed in synthetic natural rubber. Their statistical approach is based on TPCF and 2-point cluster function using an annealing technique.

In this study, unlike previous studies, the 3-D reconstruction of the microstructure of polypropylene nanocomposites with 10 wt% (7.2 vf%) HNT fillers was achieved using 1) 3-D morphology-based RVE and 2) an RVE of nanocomposite constructed using statistical TPCFs. FEA was used to deform the RVEs under tension and shear deformations to measure the effective stiffness tensor of the Halloysite nanotube (HNT) polymer composite. The numerically predicted results obtained from both RVEs were compared against the measured experimental data to assess the feasibility of the statistical approach in predicting the various properties of anisotropic nanocomposites.

1.1.3 Task 1: Develop a Microstructure-Inspired Material Model with Real and Statistically Equivalent Models for Halloysite Nanotube (HNT) Polypropylene Composite

1.1.3.1 Serial Sectioning of the Nanocomposite Using FIB-SEM

Simultaneous sectioning and imaging of the nanocomposite (10 wt% HNT+PP) was performed using a dual-column FIB-SEM (Carl Zeiss Auriga CrossBeam). Serial sectioning involved the removal of a known volume of the material by the ion beam followed by an incremental analysis with the electron beam. A schematic of the serial sectioning and the real images recorded during the FIB procedure are presented in Fig. 1.1.

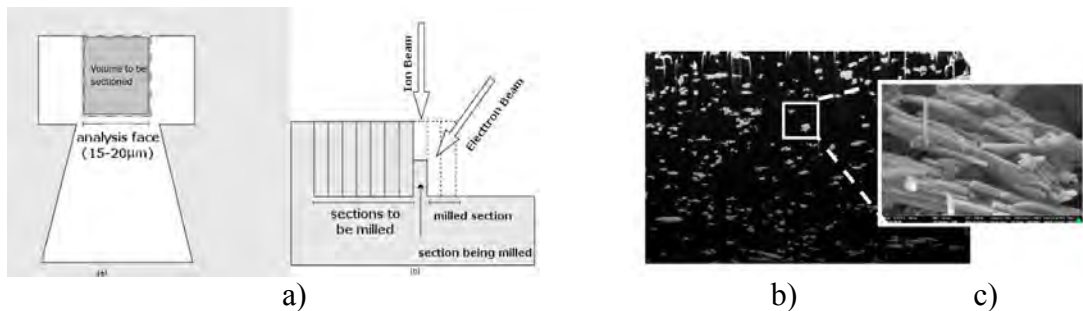


Fig. 1.1 a) Schematic of serial sectioning, b) slide generated through serial sectioning, and c) HNTs imaged with Auriga SEM

The width of each slice was 50 nm; therefore, 50 nm of the nanocomposite was milled away with the ion beam followed by an image capture with the electron beam. Around 60–100 slices were taken per sample—a process that took 2–3 h. A series of 2-D images representing slices or cross sections of the RVE was generated through FIB-SEM cutting. The advantage of using serial sectioning is to obtain a series of slices with the same reference point allowing an automated 3-D reconstruction technique to be applied.

1.1.3.2 3-D Reconstruction Using VCAT Software

The 60 serial sectioning bitmap files obtained through serial sectioning was imported into VCAT software. The 3-D nanocomposite is represented with gray levels between the ranges of colors 0–255 according to the image binarization mode 8-bit HSV (hue, saturation, value) color map. By choosing a color threshold of (0, 0,100), we find that the image part representation gives the best approximation of the dimensions of the cluster of HNTs inside the matrix. A mask property is associated with the matrix that will be a color value between 0 and 255. In this study, each of the 2 phases (matrix and filler) identified in the material was given a unique ID to distinguish between the phases inside the nanocomposite. The resulting 3-D RVE, shown in Fig. 1.2, possesses the most realistic features (size, shape, and distribution) of the actual nanocomposite suitable for calculation of its material properties.

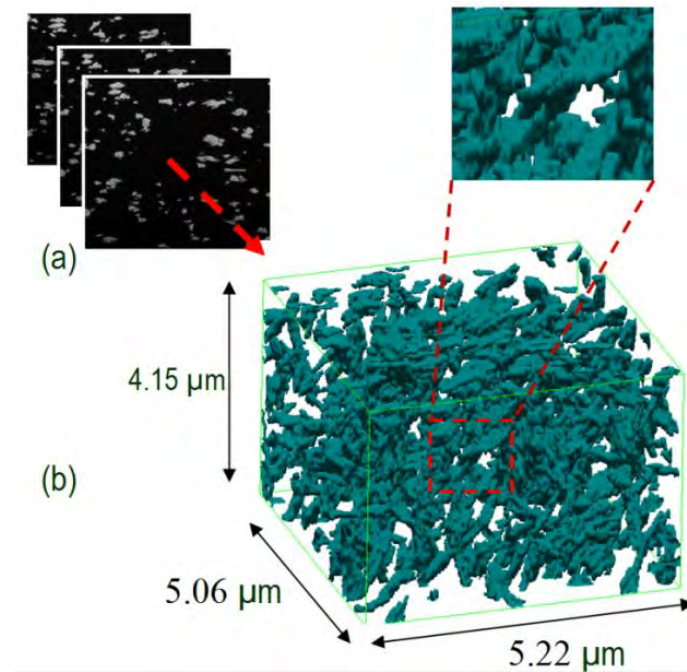


Fig. 1.2 a) 2-D SEM images of HNT polypropylene composite and b) 3-D reconstruction of the RVE based on serial sectioning

1.1.3.3 Finite Element Mesh of the Reconstructed RVEs

The 3-D reconstructed microstructures were exported to the mesh generation software called “vcat2tets” developed by VCAD to create appropriate FE mesh. Inclusions have complex shapes, vary in size and orientations, and their surface curvature varies from one surface element to another. To take into account the influence of these geometric details on the local stress and strain distributions, a very fine mesh has been used to define surfaces of the inclusion and in the regions between closely spaced inclusions. The mesh was then simplified until a target number of tetrahedral elements were achieved. For example, the original FE mesh contained 25,000,000 tetrahedral elements; however, by using the “SimpTets” software developed by VCAD, we reduced the final mesh size to 1,000,000 tetrahedral elements. The 3-D RVE obtained based on statistical methods using the TPCF (Fig. 1.3) was also meshed using vcat2tets software. Figure 1.4 shows the FE mesh for both models after the final simplification.

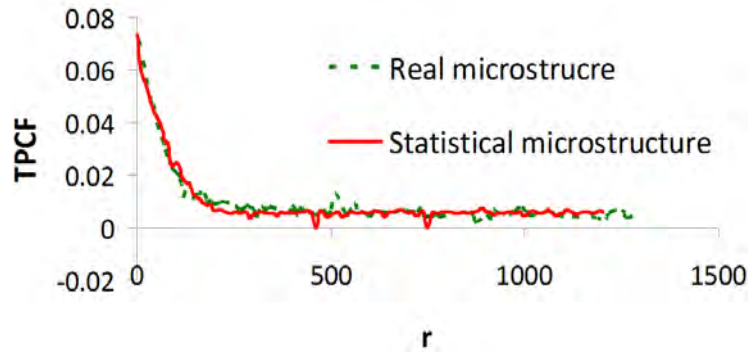


Fig. 1.3 Two-point correlation functions

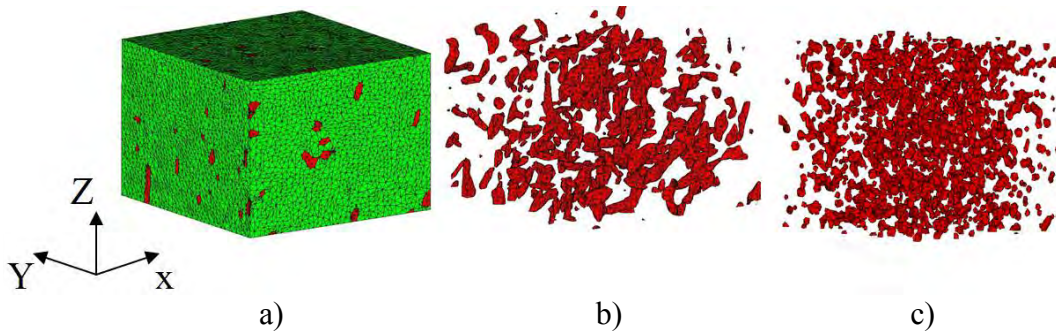


Fig. 1.4 a) The final mesh for real RVE, b) inclusions' mesh in real RVE with average inclusion volume of $0.025 \mu\text{m}^3$, and c) inclusions' mesh in statistical RVE

1.1.3.4 Results and Discussions Based on FEA of RVEs

The FE model illustrated in Figure 1.4 is a rectangular cube representing an RVE with $5.06 \times 5.22 \times 4.15 \mu\text{m}^3$ volume. The created FE mesh was used for numerical simulation and calculation of the mechanical response of the material under various loading conditions. The tensile modulus of the polymer matrix was measured to be 1.3 ± 0.04 GPa. The tensile modulus of HNT was measured numerically and experimentally by many researchers [37,38]. HNT, which has been used in this study, has the inner and outer diameters and length of 20, 85, and 1,000 nm, respectively. Based on the information available in Table 1.1 in Lu et al. [38], we have estimated the tensile modulus of HNT to be 140 GPa.

Table 1.1 Properties of Halloysite clay nanotube and polypropylene [39] (top) and elastic constants measured using real RVE and statistical RVE (bottom)

Halloysite		Density	2.5	g/cc
		Elastic Modulus	140	GPa
		Poisson Ratio	0.4	
Polypropylene		Density	0.9	g/cc
		Elastic Modulus	1.3 ± 0.04	GPa
		Poisson Ratio	0.3	
			Real RVE	Statistical RVE
Elastic Modulus (GPa)	E_{xx}		1.76	1.64
	E_{yy}		1.54	1.64
	E_{zz}		1.93	1.64
Poisson's Ratio	ν_{xy}		0.33	0.33
	ν_{yz}		0.34	0.33
	ν_{zx}		0.33	0.34

In the FEA simulations, it was assumed that both polypropylene matrix and HNT would behave as linear elastic materials with perfect interfacial bonding between the 2 constituents. This idealization of the material behavior was relaxed in later simulations by assuming rate-dependent materials as well as including a third interfacial phase between the matrix and the inclusion. The FE simulations were carried out using ABAQUS commercial software. A total of 6 simulations of the mechanical tests (3 tensile tests and 3 shear tests) were carried out using this RVE. The objective was to find the modulus of elasticity and Poisson's ratios of the RVEs in the X, Y, and Z directions. Using the stress and strain distributions for each test, we calculated the volumetric average value of stresses and strains, and using the generalized Hooke's law, we constructed the compliance tensor (S), as shown in Eq. 1.1. Comparing the constructed compliance tensor for the RVE with the compliance tensor for an isotropic material, as given in Eq. 1.2, we concluded that this HNT composite was an isotropic material. As a result, the elastic modulus in X, Y, and Z directions was found to be $E_{xx} = 1.76$ GPa, $E_{yy} = 1.53$ GPa, and $E_{zz} = 1.93$ GPa, as shown in Table 1.1, which summarizes the computed properties for real and statistical RVEs.

$$\mathbf{S} = \begin{bmatrix} \underline{0.568} & -0.162 & -0.134 & 0.0003 & -0.0025 & -0.002 \\ -0.150 & \underline{0.653} & -0.136 & -0.004 & 0.00757 & 0.0025 \\ -0.141 & -0.15 & \underline{0.516} & 0.006 & -0.0163 & -0.0007 \\ -0.004 & -0.002 & 0.014 & 1.68 & 0.0033 & -0.006 \\ -0.001 & 0.016 & -0.024 & 0.004 & 1.47 & 0.006 \\ -0.007 & 0.002 & -0.0017 & -0.005 & 0.0059 & 1.7 \end{bmatrix} \text{ GPa}^{-1} \quad (1.1)$$

$$\begin{bmatrix} \varepsilon_{11} \\ \varepsilon_{22} \\ \varepsilon_{33} \\ \gamma_{23} \\ \gamma_{31} \\ \gamma_{12} \end{bmatrix} = \frac{1}{E} \begin{bmatrix} 1 & -\nu & -\nu & 0 & 0 & 0 \\ -\nu & 1 & -\nu & 0 & 0 & 0 \\ -\nu & -\nu & 1 & 0 & 0 & 0 \\ 0 & 0 & 0 & 2(1+\nu) & 0 & 0 \\ 0 & 0 & 0 & 0 & 2(1+\nu) & 0 \\ 0 & 0 & 0 & 0 & 0 & 2(1+\nu) \end{bmatrix} \begin{bmatrix} \sigma_{11} \\ \sigma_{22} \\ \sigma_{33} \\ \sigma_{23} \\ \sigma_{31} \\ \sigma_{12} \end{bmatrix} \quad (1.2)$$

The average modulus of elasticity was calculated to be 1.74 and 1.64 GPa for real and statistical RVEs, which are within 5% and 8.8% of the experimental value of 1.8 ± 0.03 GPa. The difference between the estimated value using a numerical approach and the experimental value is related to the interphase region. Unlike micron-sized inclusions, interphase has a large influence on the overall properties of the nanocomposite. The perturbation of the polymer chains near the nanoparticle creates a constrained region around the nanoparticle [40]. This interphase region poses the same length scale as that of the nanoparticle, but its properties are different from the host matrix. It has been shown by many researchers that taking into account the effect of interphase in evaluating the tensile modulus of the nanocomposite will give us higher value for the tensile modulus [41].

1.1.4 Task 2: The 3-D Reconstruction of Exfoliated Graphite Nanoplatelets (xGnP) High-Density Polyethylene (HDPE)

Following the statistical reconstruction technique described in task 1, a 3-D model has been created for the exfoliated graphite nanoplatelet (xGnP)/high-density polyethylene (HDPE) nanocomposite. Figure 1.5 shows that this microstructure is not isotropic, therefore several TPCF curves in different directions are needed. TPCF curves in 0° , 45° , and 90° have been obtained using the SEM image of this nanocomposite.

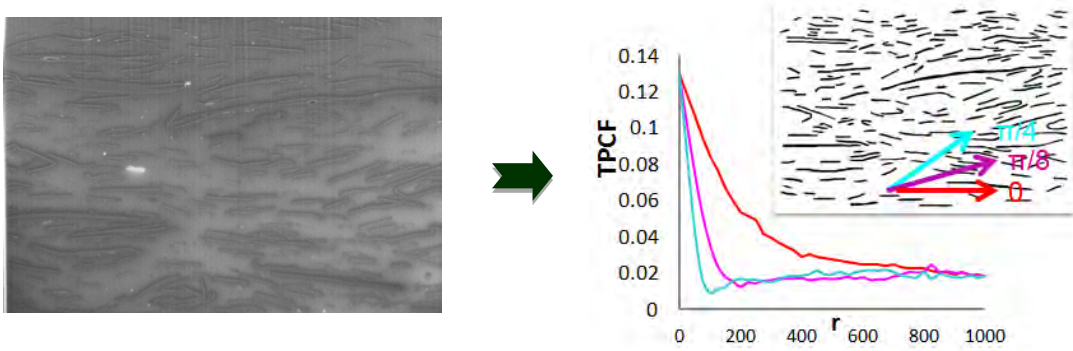


Fig. 1.5 Extracting TPCF of xGnP polymer composite in different directions

Reconstruction has been performed in a couple of steps. First, by controlling the Euler angles of platelets during 3-D reconstruction, we matched TPCF curves of the reconstructed microstructure with the real microstructure. Next, the size distribution of the platelets was incorporated into the simulation using probability distribution function of platelets obtained from SEM images; TPCF curves in different directions have been matched with the ones from SEM images (Fig. 1.6).

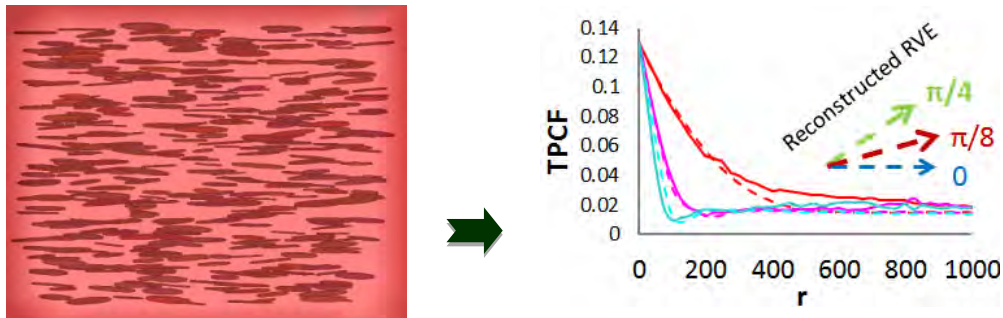


Fig. 1.6 RVE with preferred orientation and a known distribution of diameters

1.1.4.1 xGnP as a Transverse Isotropic Inclusion

Since xGnP is composed of the same material as carbon nanotubes, it shares many of their electrochemical characteristics. The platelet shape, however, offers xGnP edges that are easier to modify chemically for enhanced dispersion in polymers. xGnP is one of the stiffest materials found in nature with the Young's modulus, approximately 1,060 GPa in the plane direction. Graphene sheets are interacting through van der Waals forces; hence, the xGnP modulus perpendicular to the graphene sheets is lower than the other directions. The experimental values for the Young's modulus of xGnP reported in the literature are only for in-plane direction, and there is no value for the other direction. Pyrolytic graphite has a

similar molecular structure as xGnP. Blakslee et al. [42] measured the stiffness of this substance experimentally and provided the stiffness tensor for it. This stiffness tensor has been used as material parameters for xGnP in FE analysis.

$$E(GPa) = \begin{bmatrix} 1060 & 180 & 15 & 0 & 0 & 0 \\ 180 & 1060 & 15 & 0 & 0 & 0 \\ 15 & 15 & 36.5 & 0 & 0 & 0 \\ 0 & 0 & 0 & 430.47 & 0 & 0 \\ 0 & 0 & 0 & 0 & 0.035 & 0 \\ 0 & 0 & 0 & 0 & 0 & 0.035 \end{bmatrix}$$

1.1.4.2 A Viscoplastic Material Model for xGnP Polymer Nanocomposite

In this work, we used a viscoplastic model (hybrid model) for the polymer matrix [43]. This model has been tested for nanocomposites comprising the ultra-high-molecular-weight polyethylene (UHMWPE) and xGnP. The hybrid model is described in detail elsewhere [43].

The viscoplastic model has been calibrated using Mcalibration software in order to obtain material parameters used in the user-defined material model. Figure 1.7 shows experimental data compared with the predicted data at different strain rates. A uniaxial tensile test has been conducted on a dog-bone specimen made of neat polymer at different strain rates. Figure 1.8 shows the results of these simulations compared with experimental results.

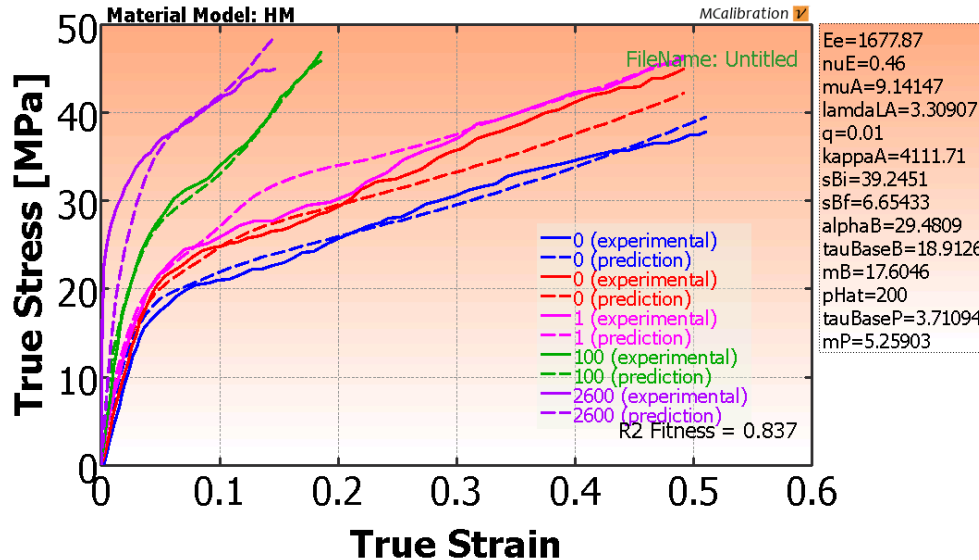


Fig. 1.7 Obtaining material parameters using Mcalibration optimization software

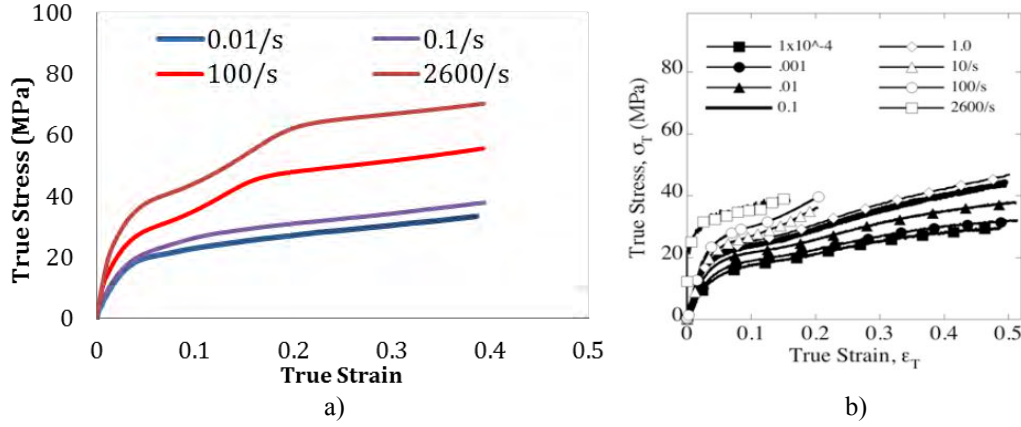


Fig. 1.8 a) Stress-strain response (numerical) and b) stress-strain response (experimental)

The RVE of the nanocomposite comprising xGnP and UHMWPE has been reconstructed for 2 different volume fractions (VFs) (2% and 4%). The viscoplastic model calibrated above has been used for the polymer, and the transverse isotropic elastic model was used for xGnP (Fig. 1.9). Figure 1.10 shows the stress-strain response of a nanocomposite compared to a neat polymer at 1000/s strain rate. The composite becomes stiffer by adding xGnP; however, the nanocomposite still exhibits strain rate dependency.

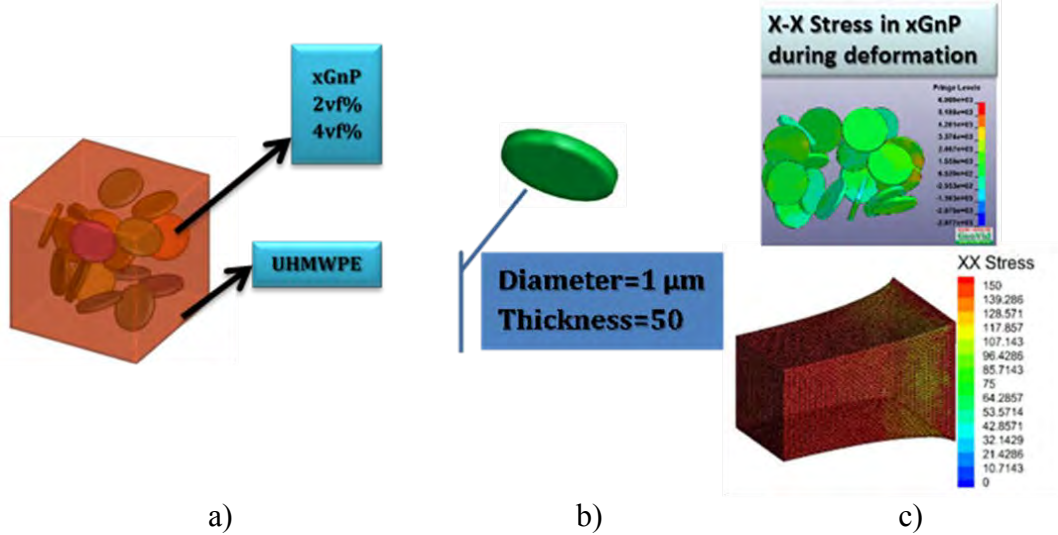


Fig. 1.9 a) RVE of nanocomposite, b) individual platelet, and c) map of stress in x-x direction

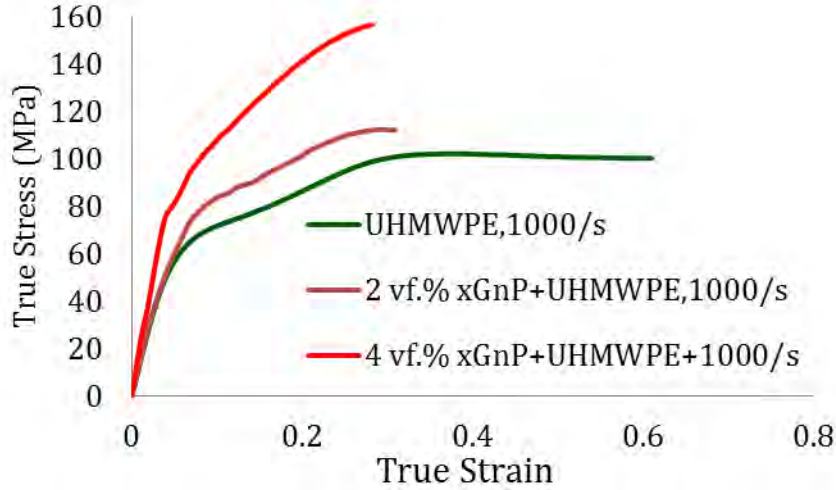


Fig. 1.10 Comparison of stress-strain response of UHMWPE and xGnP+UHMWPE

1.1.5 Task 3: Develop 3-D RVEs with Cohesive-Element-Based Failure Models to Predict the Stress-Strain Curve for Nanocomposites Under Tensile Loading

Conducting an experiment at the nanoscale level in order to understand the micromechanics of nanocomposites is difficult, if not impossible. Therefore, computational and analytical methods must be used to study the mechanics of nanocomposites. A deep understanding of the damage and fracture mechanisms of nanocomposites is crucial for structural design and practical applications. Although damage mechanisms of traditional composites have been widely studied in the literature [44–49], there are few studies [49–52] that report on the damage and fracture mechanisms of nanocomposites.

In this section, a hierarchical multiscale model to study the damage initiation in GNP/HDPE composites will be described. The cohesive zone model (CZM) has been adopted to capture the nanofillers debonding. Choosing the appropriate cohesive parameters is the most important part in the modeling of debonding in nanocomposites. Therefore, the information about interfacial properties of GNP and polymer has been obtained from MD simulations. An RVE composed of GNPs and polymer matrix was created to study the overall stress-strain response of the nanocomposite. The main goal was to perform a systematic computational study on the effects of nanofillers/polymer bonding conditions on the macroscopic response of GNP/polymer composites for different GNP VFs, aspect ratio (AR), and interfacial strength.

1.1.5.1 Representative Volume Element (RVE)

A 3-D RVE consisting of GNP and polymer was created for the nanocomposite. The RVE was generated using an in-house-developed C++ algorithm. Implementation steps used for developing the RVE with the Monte Carlo methodology are defined in the following subsections. Numerical simulations were carried out inside a cubic unit cell of constant side length of 1,000 units (units may be equally interpreted as nanometers). GNPs were modeled as simple discs dispersed inside the RVE. The geometry of each GNP was modeled as 2 parallel circular plates separated by the thickness of the GNP. Each circular plate in the volume of the RVE was identified by a normal vector, a center, and a radius. To achieve a uniformly random scatter of GNPs using the Monte Carlo method, the center of each GNP was selected randomly inside the sample RVE. Then, the associated normal vector was specified by means of random homogeneous functions to produce uniformly distributed random points on the surface of a sphere as following:

$$\begin{cases} \theta = 2\pi v \\ \varphi = \text{Arc cos}(2u - 1) \end{cases} \quad (1.3)$$

In Eq. 1.3, $\theta \in [0, 2\pi]$ and $\varphi \in [0, \pi]$ are spherical coordinates, as shown in Fig. 1.11, and u, v are random variables belonging to $[0, 1]$. The normal vectors thus selected guarantee a uniform random distribution of GNP orientations. For generating each GNP, the procedure of random selection of its center and normal direction was followed successively, and then the next GNP was identically created.

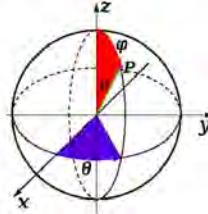


Fig. 1.11 3-D representation of the spherical coordinates of a randomly selected point

The optimum size of the RVE for each VF and AR was determined by increasing the volume of the RVE until the homogenized stress-strain values no longer changed significantly. Figure 1.12 shows RVEs of nanocomposites with different VF and ARs.

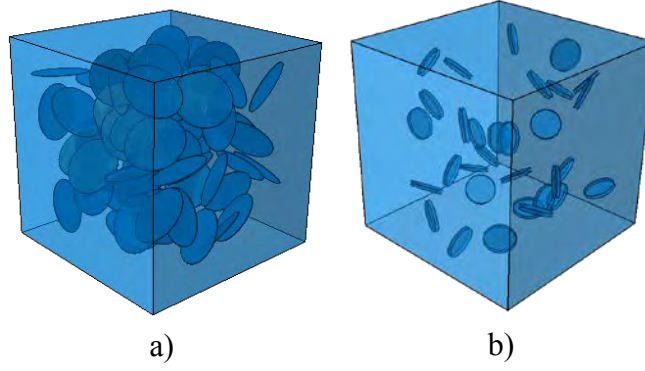


Fig. 1.12 Examples of 3-D models of nanocomposites with different VFs and ARs: a) VF = 1%, AR = 100, b) VF = 1%, AR = 10

1.1.5.2 Cohesive Zone Model (CZM)

The behavior of GNPs and the matrix interface is represented by the CZM defined in terms of bilinear traction/separation law [53]. However, in the GNP/PNCs, the interaction between GNP and polymer is difficult to determine through experimental measurements. Thus, we used the results of the MD simulation by Awasthi et al. [54] on the interfacial interaction between graphene and polyethylene. Figure 1.13 shows a typical traction-separation response with a failure mechanism.

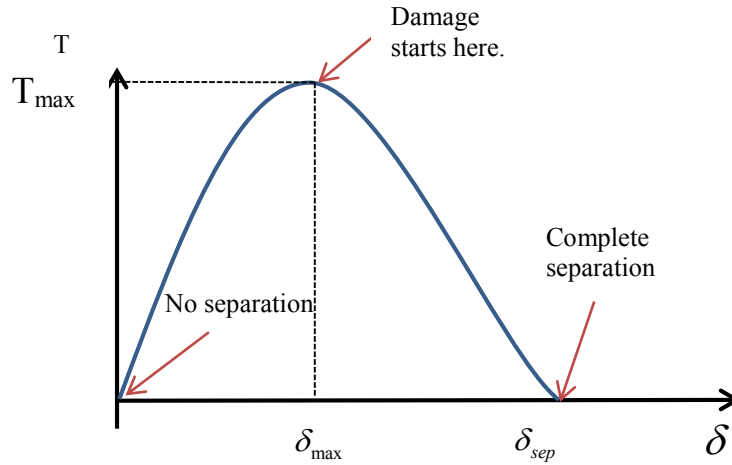


Fig. 1.13 Typical traction-separation law for modeling cohesive failure

The constitutive relation between these traction stresses and separation is given by [55]

$$T = \begin{Bmatrix} t_n \\ t_s \\ t_t \end{Bmatrix} = \begin{pmatrix} k_{nn} & k_{ns} & k_{nt} \\ k_{ns} & k_{ss} & k_{st} \\ k_{nt} & k_{st} & k_{tt} \end{pmatrix} \begin{Bmatrix} \delta_n \\ \delta_s \\ \delta_t \end{Bmatrix} = K \delta \quad (1.4)$$

Here, t_n is the traction stress in the normal direction, t_s , t_t are traction stresses in the first shear and second shear directions, respectively; K is the nominal stiffness matrix, δn is the separation in the normal direction, and δs , δt are separations in the first shear and second shear directions, respectively. After completing the linear elastic traction-separation, damage will be started. Considering cohesive parameters obtained from the MD simulation, the maximum stress criterion was used in this study (see Eq. 1.5). Based on this criterion, damage is assumed to initiate when the maximum contact stress ratio reaches the value of one. This criterion can be represented as

$$MAX \left\{ \frac{\langle t_n \rangle}{t_n^{\max}}, \frac{t_s}{t_s^{\max}}, \frac{t_t}{t_t^{\max}} \right\} = 1. \quad (1.5)$$

A scalar damage variable, D , represents the overall damage at the contact point. It initially has a value of 0 if damage evolution is modeled; D monotonically evolves from 0 to 1 upon further loading after the initiation of damage. The contact stress components are affected by the damage according to

$$t_n = \begin{cases} (1-D)\bar{t}_n, & \bar{t}_n \geq 0 \\ \bar{t}_n & \end{cases}, \quad (1.6)$$

otherwise

$$t_s = (1-D)\bar{t}_s \quad (1.7)$$

and

$$t_t = (1-D)\bar{t}_t, \quad (1.8)$$

where \bar{t}_n , \bar{t}_s , and \bar{t}_t are the contact stress components predicted by the elastic traction-separation behavior for the current separations without damage. The dependence of the fracture energy on the mixed-mode can be defined based on a power law fracture criterion. The power law criterion states that failure under mixed-mode conditions is governed by a power law interaction of the energies required to cause failure in the individual (normal and two shear) modes. It is given by

$$\left\{ \frac{G_n}{G_n^C} \right\}^\alpha + \left\{ \frac{G_s}{G_s^C} \right\}^\alpha + \left\{ \frac{G_t}{G_t^C} \right\}^\alpha = 1. \quad (1.9)$$

With the mixed mode, the fracture energy is equal to $G^C = G_n + G_s + G_t$ when the above condition is satisfied. In the above expression, the quantities G_n , G_s , and G_t refer to the work done by the traction and its conjugate separation in the

normal, the first, and the second shear directions, respectively. The quantities of G_n^C , G_s^C , and G_t^C , which refer to the critical fracture energies required to cause failure in the normal, the first, and the second shear directions, should be specified. In this work we used $\alpha = 1$ [56, 57]. For the linear softening (see Fig. 1.14), an evolution of the damage variable [49], D , reduces to

$$D = \frac{\delta_m^f (\delta_m^{\max} - \delta_m^0)}{\delta_m^{\max} (\delta_m^f - \delta_m^0)}, \quad (1.10)$$

where $\delta_m^f = 2G^C / T_{eff}$ with T_{eff} as the effective traction at damage initiation (defined below). δ_m^{\max} refers to the maximum value of the effective serration attained during the loading history.

$$T_{eff} = \sqrt{T_n^2 + T_s^2 + T_t^2}. \quad (1.11)$$

$$\delta_m = \sqrt{\delta_n^2 + \delta_s^2 + \delta_t^2}. \quad (1.12)$$

In the paper by Awasthi et al. [54], separation studies are conducted for both normal (traction) and sliding (shear) modes, and the cohesive zone parameters, such as peak traction and energy of separation, are evaluated for each mode. Traction-separation curves for normal debonding and sliding modes are shown in Fig. 1.14. This figure shows that the maximum traction for normal mode is higher than the one for sliding mode while the separation point is higher in the shear mode. Cohesive parameters are listed in Table 1.2.

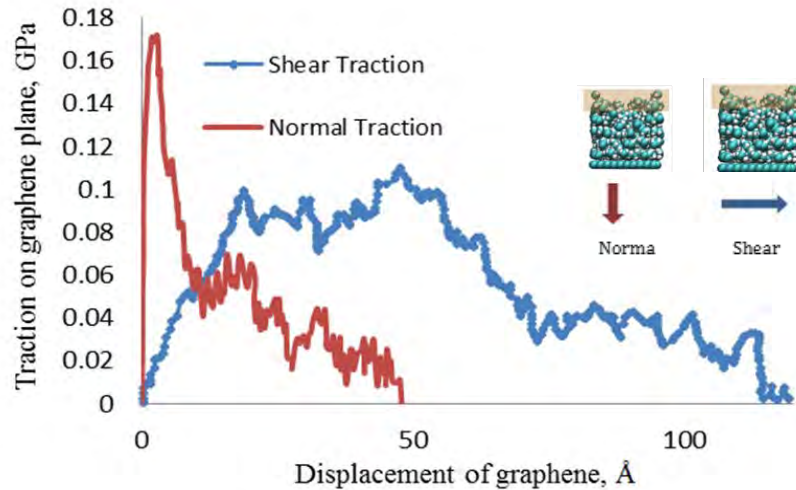


Fig. 1.14 Comparison of traction-separation response in opening and sliding separation [54]

Table 1.2 Cohesive zone model parameters for opening and sliding modes [54]

Fracture Mode	Fracture Energy (MJ/m ²)	Peak Traction (MPa)
Shear mode	331.650	108.276
Normal mode	246.525	170.616

1.1.5.3 The Effect of the GNP's Volume Fraction and Aspect Ratio in Perfectly Bonded Nanocomposites

RVEs of nanocomposites with 3 different VFs (0.5, 1.5, and 2.5) have been created. To study the effect of VF, the AR and the diameter of the inclusions were kept constant for all cases as AR = 40 and Dia. = 10 μm . As is shown in Fig. 1.15, stiffness increases with an increase in the VF. This is in agreement with the rule of mixture [53,58].

For the analysis of the effect of AR, RVEs of nanocomposites with 3 different ARs (10, 50, and 100) have been created. The VF and the diameter of the inclusions were kept constant for all cases as VF = 1% and diameter = 4 μm . The results show that the nanocomposites' stiffness increases as the GNP's AR increases (Fig. 1.16). This is in agreement with the results obtained by Mortazavi et al. [59]. These authors have compared the elastic modulus and thermal conductivity of 2-phase random composites with different inclusion types and ARs using finite elements and Mori-Tanaka methods. They concluded that the elastic modulus and the thermal conductivity of nanocomposites increase by increasing the AR.

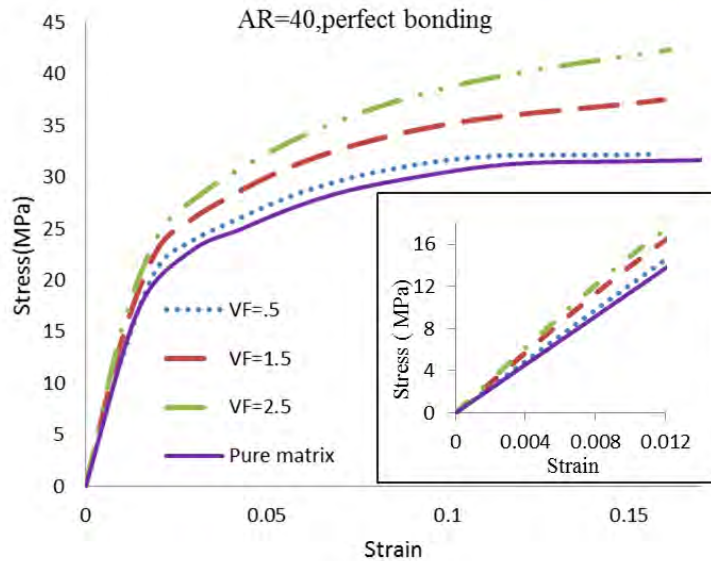


Fig. 1.15 Averaged stress-strain curves for RVEs with random distribution and orientation of GNP. Particle VFs = 0.5%, 1.5%, 2.5%; AR D/t = 40; perfectly bonded GNP.

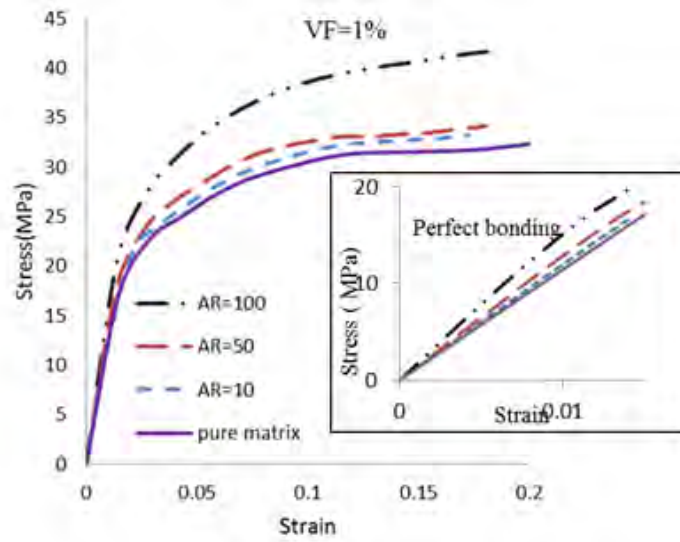


Fig. 1.16 Averaged stress–strain curves for RVEs with random distribution and orientation of GNP. Particle VFs = 1%; AR D/t = 10, 50, 100; perfectly bonded GNP

1.1.5.4 Comparing the Effect of the GNP's Volume Fraction and Aspect Ratio in Perfectly Bonded and Cohesively Bonded Nanocomposites

Here, we compare our predicted results for perfectly bonded and cohesively bonded composites. The CZM parameters are given in Table 1.2 and are based on the results of Awasthi et al. [54] (see Fig. 1.14). Our predicted results for the effects of VF, with a constant AR of 40, are reported in Figs. 1.17 and 1.18.

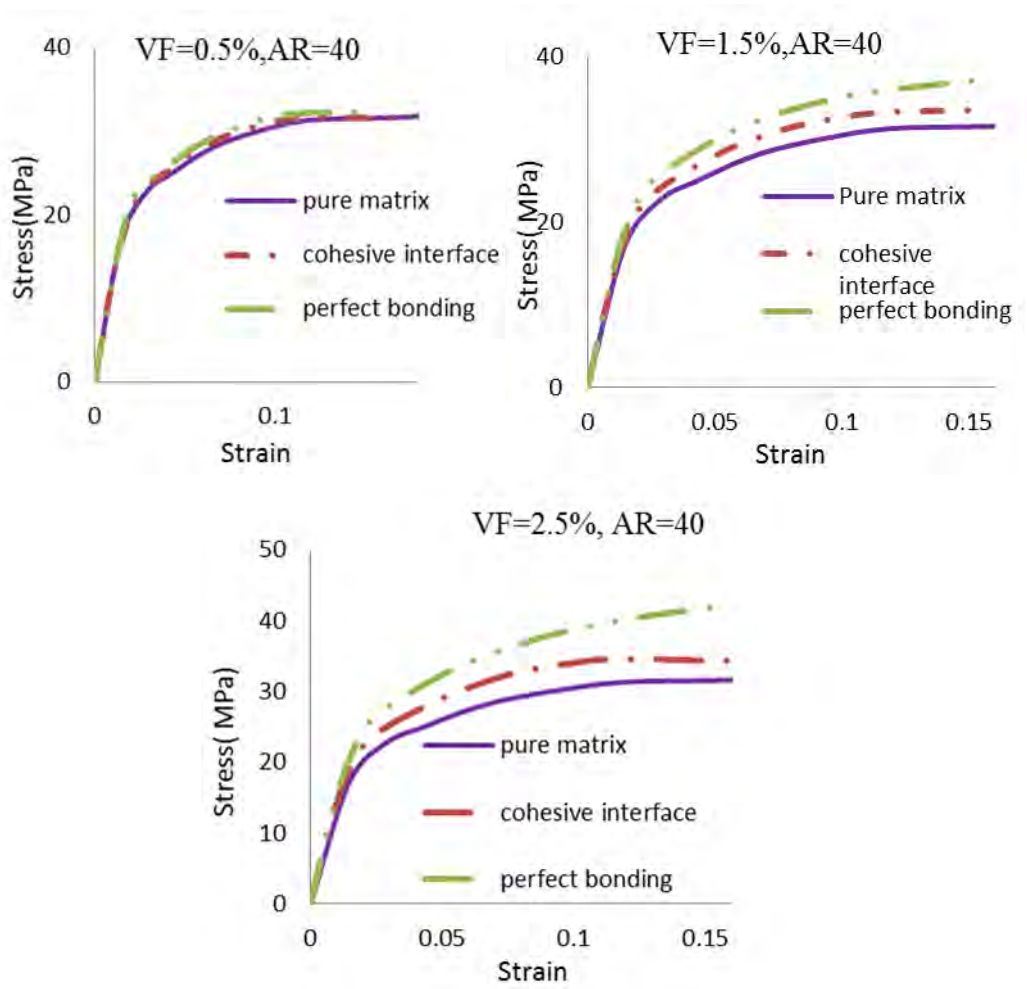


Fig. 1.17 Comparing GNP/HDPE (perfect bonding with different VF and constant AR) and GNP/HDPE (cohesive bonding with different VF and constant AR)

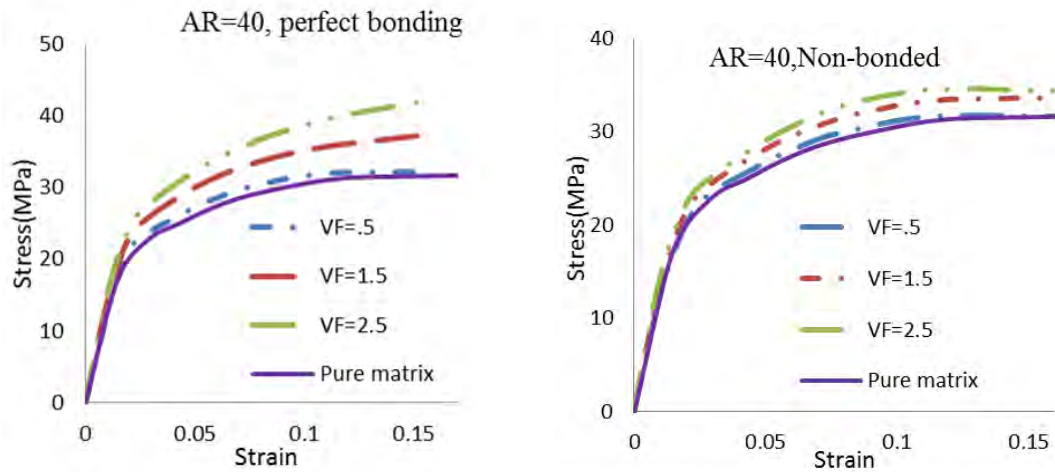


Fig. 1.18 Left: GNP/HDPE (perfectly bonded with different VF and constant AR); right: GNP/HDPE (cohesively bonded with different VF and constant AR)

The 3 graphs comprising Fig. 1.17 show the effect of the VF on the stress-strain responses of the perfectly bonded and cohesively bonded GNP/polymer composites in comparison to a pure polymer matrix. In all cases, when debonding starts to occur, the stress-strain curve for the damaged nanocomposite drops down to lower stress levels and deviates from the perfectly bonded nanocomposite. This is in agreement with the results of the recent micromechanical model presented by Dastgerdi et al. [60]. Figure 1.8 also shows that as VF increases, the difference between cohesively bonded and perfectly bonded responses will increase. This means that in a nanocomposite with a high VF of GNPs, more inclusions will debond compared to those with a low VF.

For the analysis of the effect of AR, we selected the composite of VF = 1% and reported our predicted results in Figs. 1.19 and 1.20 for different ARs (AR = 10, 50, 100). The graphs depicted in Fig. 19 show the effect of the AR on the stress-strain response of the perfectly bonded and cohesively bonded GNP/HDPE nanocomposites as they compare with the response of a pure polymer matrix. In all cases, when the debonding starts to occur, the stress-strain curve for the damaged nanocomposite drops down to lower stress levels and deviates from the perfectly bonded nanocomposites. Figure 1.19 also shows that as AR increases, the difference between bonded and nonbonded responses will increase. This is due to the high surface area in the higher AR, which leads to the larger fracture surface during the debonding. Figure 1.20 shows that by increasing the AR in the cohesive model, the stress-strain response does not increase significantly as compared to the perfect bonding case.

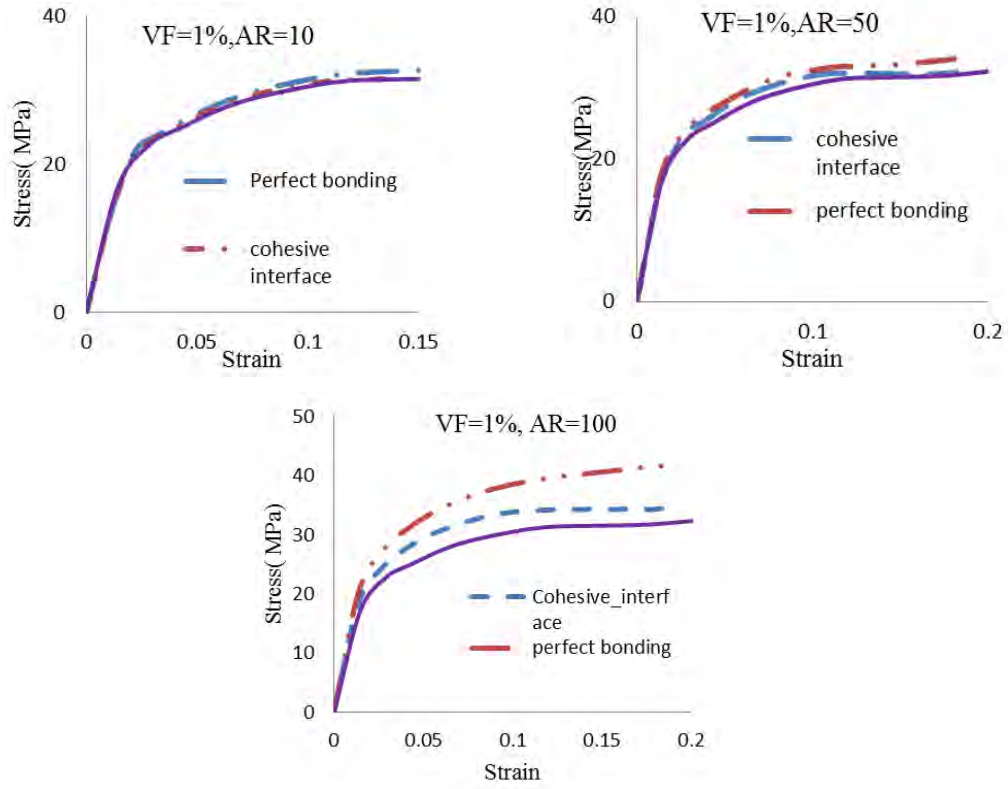


Fig. 1.19 Comparing GNP/HDPE (perfectly bonded with different AR and constant VF) and GNP/HDPE (cohesively bonded with different AR and constant VF)

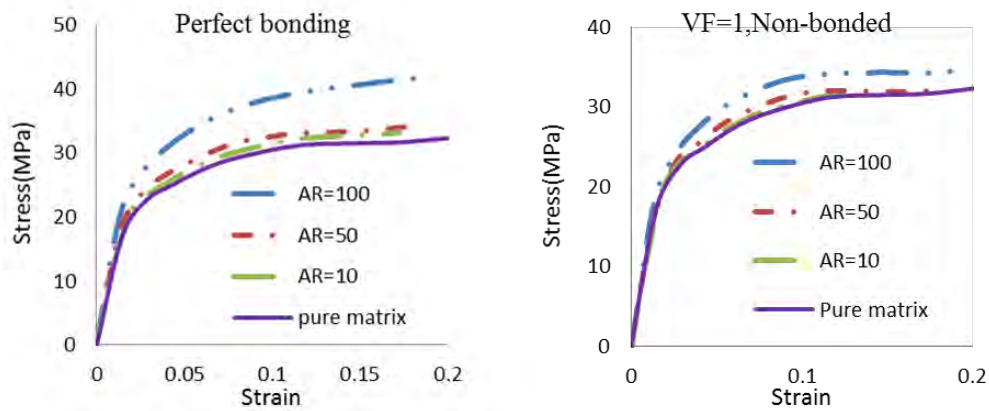


Fig. 1.20 Left: GNP/HDPE (perfectly bonded with different AR and constant VF); right: GNP/HDPE (cohesively bonded with different AR and constant VF)

1.1.5.5 The Effect of the GNP's Aspect Ratio and Volume Fraction in Weakly Bonded Nanocomposites

To analyze the effect of weak bonding, the cohesive zone parameters for weak bonding have been selected (Table 1.3). The effect of the AR on the stress-strain response of the weakly bonded interface is plotted in Fig. 1.21 for a fixed fillers VF of 1% and compared with the response of the pure polymer matrix. This figure indicates that 1) in the first stage of deformation, the stiffness of the nanocomposite increases as the AR of the nanofillers increases, and 2) in the second part of deformation (after yield), the composite will have a lower flow stress compared to the host polymer. This indicates that debonding starts in the nonlinear region (high strains). Figure 1.21 also shows that the increase in the AR of the platelets results in a lower flow stress of the composite. In fact, with a fixed VF, nanocomposites with higher AR inclusions will have more defects compared to those with lower AR inclusions. When nanoplatelets are added to polymers, the nanocomposite is expected to have improved stiffness and toughness, the end result highly depends on the type of bonding generated between the GNP and the host polymer. To improve the interfacial bonding between nanofillers and the host polymer, different types of chemical modifiers have been investigated [61,62].

Table 1.3 Cohesive parameters for weak bonding

Fracture Mode	Fracture Energy (MJ/m ²)	Peak Traction (MPa)
Shear mode	331.650	30
Normal mode	246.525	40

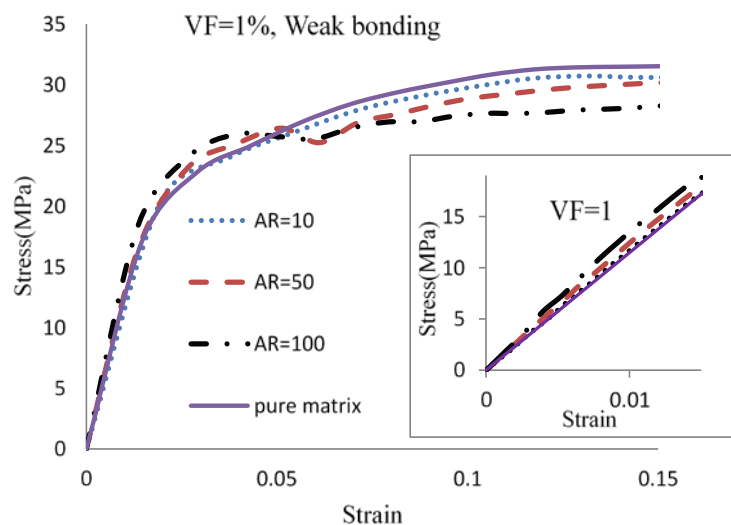


Fig. 1.21 Study showing the effect of AR (weak bonding)

The effect of the VF of the fillers on the overall stress-strain response of the nanocomposite with weak interfacial bonding was shown in Fig. 1.22 for a constant AR of 40. These results show that by increasing the VF of the nanofiller, the nanocomposite will have a lower stress-strain response. This is due to the poor bonding between the filler and the matrix that causes more inclusion debonding for higher filler VFs.

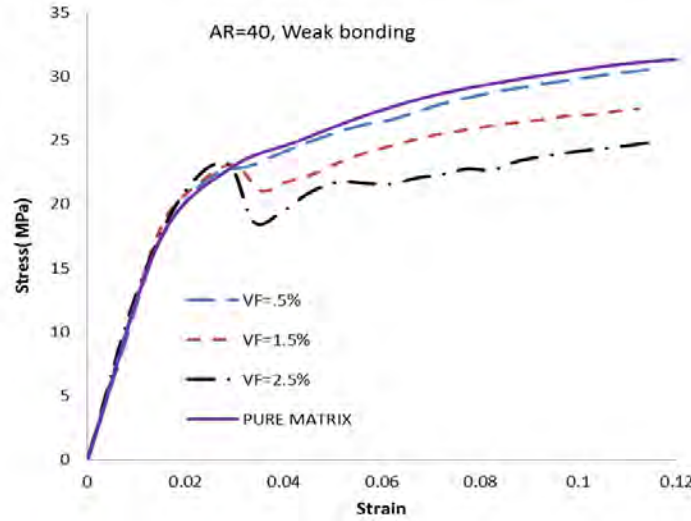


Fig. 1.22 Study showing the effect of VF (weak bonding)

To clearly observe the damage sequence of HDPE/GNP nanocomposites from the numerical predictions' viewpoint, the state of damage at the interface during loading at strains of 6%, 12%, and 24% is shown in Fig. 1.23. As one can observe, the interface damage variable D (called CSDMG) has reached a maximum value of 1.0 for many nodes present in the weakly bonded nanocomposites compared to the strongly bonded nanocomposites.

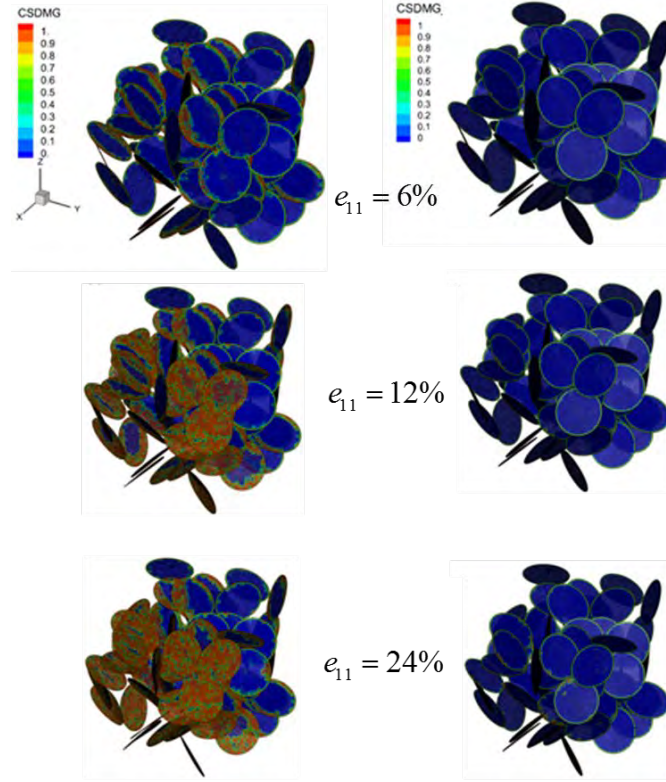


Fig. 1.23 Damage sequence of HDPE/GNP with AR = 100, VF = 1%. Left: weak bonding; Right: strong bonding.

1.1.6 Summary and Conclusions

A hierarchical multiscale model was developed to study the damage initiation in polymer/GNP nanocomposites. The CZM was used to model the polymer/nanofiller debonding. Results from atomic simulations of GNP pullout and debonding tests were used for the CZM. Effects of VF, AR, and fiber-matrix interfacial strength on the overall stress-strain response of the nanocomposite were investigated. Nanocomposites with perfectly bonded fillers were also modeled for comparison with the nanocomposites with cohesive bonding. Results from studying the effect of fillers VF and AR in perfectly bonded composites showed that both stiffness and toughness will increase with increasing VF and AR.

The effect of the GNPs' VF on perfectly bonded and cohesively bonded composites was compared. As expected, the results showed that when the debonding starts to occur, the stress-strain curve for damaged nanocomposites decreases and deviates from those for the perfectly bonded nanocomposites. Results also showed that as VF increases, the difference between cohesively bonded and perfectly bonded responses will increase. This implies that in nanocomposites with a higher VF, more inclusions will debond compared to lower VF.

The effect of AR on the stress-strain response of the perfectly bonded and cohesively bonded GNP/HDPE nanocomposites has been studied. It was also shown that as AR increases, the difference between bonded and cohesively bonded response will increase. The cohesive model has also been tested for weakly bonded composites. The results showed that by having weak bonding between inclusion and polymer, the resulting composite will have a lower stress-strain response after the yield compared to the host polymer and that the increase in the AR of the platelets will lower the flow stress. In fact, with fixed VF, nanocomposites with a higher AR will introduce larger defects in the composite compared to nanocomposites with a lower AR. By adding nanoplatelets into polymers, their stiffness and toughness will be improved provided good bonding exists between the nanofillers and the host polymer. Weak bonding between nanoplatelets and the polymer matrix may result in a composite with low stiffness and toughness. Hence, using different types of chemical modifiers for nanofillers to improve the interfacial bonding is necessary. Our simulation results show that the stiffness still increases with fillers VF in the case of weak bonding, which indicates that debonding becomes noticeably important after the yield point.

1.1.7 Outcomes (Journal Papers)

1. M. Safaei, A. Sheidaei, M. Baniassadi, S. Ahzi, M. Mosavi Mashhadi, F. Pourboghrat, "An interfacial debonding-induced damage model for graphite nanoplatelet polymer nanocomposite," submitted to *Computational Materials Science* (in-review).
2. Tabei, S.A., Sheidaei, A., Baniassadi, M., Pourboghrat, F., Garmestani, H., "Microstructure Reconstruction and Homogenization of Porous Ni-YSZ Composites," *J. of Power Sources*, Volume 235, 1 August 2013, Pages 74–80.
3. Sheidaei, A., Baniassadi, M., Banu, M., Askeland, P., Kuuttila, N, Pourboghrat, F., Drzal, L.T., Garmestani, H., "Mechanical characterization of polymer clay halloysite polymer composite using real microstructure and statistical models," *Composite Science and Technology*, Volume 80, 17 May 2013, Pages 47–54.

1.1.8 References

1. Fullwood, D.T., S.R. Niezgoda, and S.R. Kalidindi, "Microstructure reconstructions from 2-point statistics using phase-recovery algorithms," *Acta Materialia*, 2008. 56(5): p. 942–948.

2. Gommès, C.J., Y. Jiao, and S. Torquato, "Microstructural degeneracy associated with a two-point correlation function and its information content," *Physical Review E*, 2012. 85(5): p. 051140.
3. Chen, B., et al., "A critical appraisal of polymer–clay nanocomposites," *Chem. Soc. Rev.*, 2007. 37(3): p. 568–594.
4. Alexandre, M. and P. Dubois, "Polymer-layered silicate nanocomposites: preparation, properties and uses of a new class of materials," *Materials Science and Engineering: R: Reports*, 2000. 28(1-2): p. 1–63.
5. Sinha Ray, S. and M. Okamoto, "Polymer/layered silicate nanocomposites: a review from preparation to processing," *Progress in polymer science*, 2003. 28(11): p. 1539–1641.
6. Kojima, Y., et al., "Mechanical properties of nylon 6-clay hybrid," *Journal of Materials Research*, 1993. 8(05): p. 1185–1189.
7. Messersmith, P.B. and E.P. Giannelis, "Synthesis and characterization of layered silicate-epoxy nanocomposites," *Chemistry of materials*, 1994. 6(10): p. 1719–1725.
8. Giannelis, E.P., "Polymer layered silicate nanocomposites," *Advanced materials*, 1996. 8(1): p. 29–35.
9. Okada, A. and A. Usuki, "The chemistry of polymer-clay hybrids," *Materials Science and Engineering: C*, 1995. 3(2): p. 109–115.
10. Schmidt, D., D. Shah, and E.P. Giannelis, "New advances in polymer/layered silicate nanocomposites," *Current Opinion in Solid State and Materials Science*, 2002. 6(3): p. 205–212.
11. Yano, K., A. Usuki, and A. Okada, "Synthesis and properties of polyimide-clay hybrid films," *Journal of Polymer Science Part A: Polymer Chemistry*, 1997. 35(11): p. 2289–2294.
12. Bharadwaj, R.K., "Modeling the barrier properties of polymer-layered silicate nanocomposites," *Macromolecules*, 2001. 34(26): p. 9189–9192.
13. Gilman, J.W., "Flammability and thermal stability studies of polymer layered-silicate (clay) nanocomposites," *Applied Clay Science*, 1999. 15(1-2): p. 31–49.
14. Schmidt, G. and M.M. Malwitz, "Properties of polymer-nanoparticle composites," *Current opinion in colloid & interface science*, 2003. 8(1): p. 103–108.

15. Afaghi Khatibi, A. and B. Mortazavi, "A Study on the Nanoindentation Behaviour of Single Crystal Silicon Using Hybrid MD-FE Method," *Advanced Materials Research*, 2008. 32: p. 3.
16. Haile, J.M., *Molecular dynamics simulation : elementary methods*. 1992, New York: Wiley. xvii, 489 p.
17. Komanduri, R., N. Chandrasekaran, and L.M. Raff, "Molecular dynamics (MD) simulation of uniaxial tension of some single-crystal cubic metals at nanolevel," *International Journal of Mechanical Sciences*, 2001. 43(10): p. 2237–2260.
18. Mortazavi, B., Khatibi, A. A., Politis, C., "Molecular Dynamics Investigation of Loading Rate Effects on Mechanical-Failure Behaviour of FCC Metals," *Journal of computational and theoretical nanoscience*, 2009. 6: p. 644–652.
19. Torquato, S., "Effective stiffness tensor of composite media--I. Exact series expansions," *Journal of the Mechanics and Physics of Solids*, 1997. 45(9): p. 1421–1448.
20. Pham, D. and S. Torquato, "Strong-contrast expansions and approximations for the effective conductivity of isotropic multiphase composites," *Journal of applied physics*, 2003. 94(10): p. 6591–6602.
21. Nemat-Nasser, S. and M. Hori, *Micromechanics: overall properties of heterogeneous materials*. Vol. 2. 1999: Elsevier Amsterdam.
22. Dumont, J., et al., "Damage mechanics for 3-D composite," *Composite structures*, 1987. 8(2): p. 119–141.
23. Hori, M. and S. Munasighe, "Generalized Hashin–Shtrikman variational principle for boundary-value problem of linear and non-linear heterogeneous body," *Mechanics of materials*, 1999. 31(7): p. 471–486.
24. Affdl, J. and J. Kardos, "The Halpin-Tsai equations: a review," *Polymer Engineering & Science*, 1976. 16(5): p. 344–352.
25. Sheng, N., et al., "Multiscale micromechanical modeling of polymer/clay nanocomposites and the effective clay particle," *Polymer*, 2004. 45(2): p. 487–506.
26. Zhu, L. and K. Narh, "Numerical simulation of the tensile modulus of nanoclay-filled polymer composites," *Journal of Polymer Science Part B: Polymer Physics*, 2004. 42(12): p. 2391–2406.

27. Fertig III, R.S. and M.R. Garnich, "Influence of constituent properties and microstructural parameters on the tensile modulus of a polymer/clay nanocomposite," *Composites science and technology*, 2004. 64(16): p. 2577–2588.
28. Dong, Y., D. Bhattacharyya, and P.J. Hunter, "Experimental characterisation and object-oriented finite element modelling of polypropylene/organoclay nanocomposites," *Composites science and technology*, 2008. 68(14): p. 2864–2875.
29. Hsueh, C., et al., "Analytical and numerical analyses for two-dimensional stress transfer," *Materials Science and Engineering: A*, 1999. 268(1): p. 1–7.
30. Cannillo, V., C. Leonelli, and A.R. Boccaccini, "Numerical models for thermal residual stresses in Al₂O₃ platelets/borosilicate glass matrix composites," *Materials Science and Engineering A*, 2002. 323(1-2): p. 246–250.
31. Cannillo, V., et al., "Numerical modelling of the fracture behaviour of a glass matrix composite reinforced with alumina platelets," *Composites Part A: Applied Science and Manufacturing*, 2003. 34(1): p. 43-51.
32. Wang, Z., et al., "Effects of pores and interfaces on effective properties of plasma sprayed zirconia coatings," *Acta materialia*, 2003. 51(18): p. 5319–5334.
33. Ray, S.S., "A new possibility for microstructural investigation of clay-based polymer nanocomposite by focused ion beam tomography," *Polymer*, 2010. 51(17): p. 3966–3970.
34. Velichko, A., C. Holzapfel, and F. Mücklich, "3-D characterization of graphite morphologies in cast iron," *Advanced Engineering Materials*, 2007. 9(1-2): p. 39–45.
35. Faessel, M., et al., "3-D Modelling of random cellulosic fibrous networks based on X-ray tomography and image analysis," *Composites science and technology*, 2005. 65(13): p. 1931–1940.
36. Deng, H., et al., "Utilizing Real and Statistically Reconstructed Microstructures for the Viscoelastic Modeling of Polymer Nanocomposites," *Composites Science and Technology*, 2012.
37. Guimarães, L., et al., "Structural, electronic, and mechanical properties of single-walled halloysite nanotube models," *The Journal of Physical Chemistry C*, 2010. 114(26): p. 11358–11363.

38. Lu, D., et al., "Direct Measurements of the Young's Modulus of a Single Halloysite Nanotube Using a Transmission Electron Microscope with a Bending Stage," *Journal of Nanoscience and Nanotechnology*, 2011. 11(9): p. 7789–7793.
39. Wang, A., et al., "Synthesis of mesoporous carbon nanosheets using tubular halloysite and furfuryl alcohol by a template-like method," *Microporous and Mesoporous Materials*, 2008. 108(1-3): p. 318–324.
40. Kojima, Y., et al., "Mechanical properties of nylon 6-clay hybrid," *Journal of Materials Research(USA)*, 1993. 8(5): p. 1185–1189.
41. Mesbah, A., et al., "Experimental characterization and modeling stiffness of polymer/clay nanocomposites within a hierarchical multiscale framework," *Journal of Applied Polymer Science*, 2009. 114(5): p. 3274–3291.
42. Blakslee, O., et al., "Elastic Constants of Compression-Annealed Pyrolytic Graphite," *Journal of Applied Physics*, 1970. 41(8): p. 3373–3382.
43. Bergström, J., C. Rimnac, and S. Kurtz, "Prediction of multiaxial mechanical behavior for conventional and highly crosslinked UHMWPE using a hybrid constitutive model," *Biomaterials*, 2003. 24(8): p. 1365–1380.
44. Kushch, V., et al., "Numerical simulation of progressive debonding in fiber reinforced composite under transverse loading," *International Journal of Engineering Science*, 2011. 49(1): p. 17–29.
45. Zhang, B., et al., "A virtual experimental approach to estimate composite mechanical properties: Modeling with an explicit finite element method," *Computational Materials Science*, 2010. 49(3): p. 645–651.
46. Kushch, V., S. Shmegeera, and L. Mishnaevsky Jr, "Explicit modeling the progressive interface damage in fibrous composite: Analytical vs. numerical approach," *Composites Science and Technology*, 2011. 71(7): p. 989–997.
47. Orifici, A., I. Herszberg, and R. Thomson, "Review of methodologies for composite material modelling incorporating failure," *Composite structures*, 2008. 86(1): p. 194–210.
48. McCartney, L., "Mechanics of matrix cracking in brittle-matrix fibre-reinforced composites," *Proceedings of the Royal Society of London. A. Mathematical and Physical Sciences*, 1987. 409(1837): p. 329–350.
49. Bheemreddy, V., et al., "Modeling of fiber pull-out in continuous fiber reinforced ceramic composites using finite element method and artificial neural networks," *Computational Materials Science*, 2013. 79: p. 663–673.

50. Zerda, A.S. and A.J. Lesser, "Intercalated clay nanocomposites: morphology, mechanics, and fracture behavior," *Journal of Polymer Science Part B: Polymer Physics*, 2001. 39(11): p. 1137–1146.
51. Wang, K., et al., "Epoxy nanocomposites with highly exfoliated clay: mechanical properties and fracture mechanisms," *Macromolecules*, 2005. 38(3): p. 788–800.
52. Yoshimura, A. and T. Okabe, "Damage Growth Analysis in Particle-Reinforced Composite Using Cohesive Element," *Advanced Composite Materials*, 2011. 20(6): p. 569–583.
53. Alger, M.S., "Polymer science dictionary," 1997: Springer.
54. Awasthi, A.P., D.C. Lagoudas, and D.C. Hammerand, "Modeling of graphene–polymer interfacial mechanical behavior using molecular dynamics," *Modelling and Simulation in Materials Science and Engineering*, 2009. 17(1): p. 015002.
55. Version, A., 6.11 Documentation. Dassault Syst emes Simulia Corp., Providence, RI, USA, 2011.
56. Dai, G. and L. Mishnaevsky Jr, "Damage evolution in nanoclay-reinforced polymers: A three-dimensional computational study," *Composites Science and Technology*, 2013. 74: p. 67–77.
57. Reeder, J.R., *3-D mixed-mode delamination fracture criteria—an experimentalist's perspective*, 2006.
58. Askeland, D.R., P.P. Fulay, and W.J. Wright, *The Science and Engineering of Materials: Si Edition*. 2011: CengageBrain. com.
59. Mortazavi, B., et al., "Modeling of two-phase random composite materials by finite element, Mori–Tanaka and strong contrast methods," *Composites Part B: Engineering*, 2013. 45(1): p. 1117–1125.
60. Nafar Dastgerdi, J., G. Marquis, and M. Salimi, "Micromechanical modeling of nanocomposites considering debonding of reinforcements," *Composites Science and Technology*, 2014.
61. Miyagawa, H. and L.T. Drzal, "The effect of chemical modification on the fracture toughness of montmorillonite clay/epoxy nanocomposites," *Journal of adhesion science and technology*, 2004. 18(13): p. 1571-1588.
62. Azeez, A.A., et al., "Epoxy clay nanocomposites–processing, properties and applications: A review," *Composites Part B: Engineering*, 2013. 45(1): p. 308–320.

2. Thrust Area 1B: Flammability of Exfoliated Graphite Nanoplatelet (xGnP) Composite Materials

Thomas J Pence and Indrek S Wichman

2.1 Summary

This project provided modeling and measurement of the breakdown of composite vehicle materials when subjected to flame and general thermal assault. The materials considered are load-carrying structural materials. The stress associated with load carrying then has an effect on the material degradation process, typically causing a certain acceleration in the breakdown. This research is both crucial and timely because previous models of material degradation in hostile environments do not take into account the interaction between the solid mechanics and the thermal/combustion processes. Previous models are one sided, focusing on one or the other without consideration of the important interaction effects. In contrast, our focus on this interaction permits us to simulate the material degradation and hence quantify its effect with respect to the service life and survivability of a composite vehicle in thermal environments brought on by flaming combustion. A particular striking aspect of our study concerns how the pattern of material breakdown is highly sensitive to the thermal conduction pathways in the material. This has a marked effect on crack formation during combustion and degradation. Our experimental work similarly reveals a range of crack formation patterns.

2.2 Introduction

This thrust area provides a quantitative ability to assess the flammability of composite materials. The key project focuses upon flammability of materials incorporating exfoliated graphite nanoplatelets (xGnPs). Currently, the flammability of xGnP composites is not well understood in any quantitative sense, and the complex microstructural character of composite materials incorporating xGnP mitigates against the use of simple combustion theories for describing its flammability. The research therefore combines the latest concepts from both combustion modeling and solid mechanics to provide a new conceptual understanding of how combustion damages the composite material and how this breakdown can accelerate the combustion process.

In general, there is a strong need for an accurate description of the process by which such materials release combustible volatile gases to the atmosphere in

combustion that is either deliberate (energy conversion) or accidental/hazardous (fire). Composite materials are currently being manufactured with a complex internal physical structure to offer numerous benefits ranging from structural uses in buildings and aircraft or spacecraft to uses in combat vehicles. A requirement for these materials is that they also perform well under extreme thermal assault. However, assessing composite material performance in this area has received little attention compared to performance studies with respect to structural integrity, manufacturability, light-weighting, and repairability. This research remedies this deficiency by addressing this pressing need.

The overall research program involves a combination of nonintrusive experimental diagnostics, advanced theory, and detailed numerical computations to investigate the solid mechanical and thermochemical processes occurring when composite materials burn. It provides a means for understanding the key mechanisms at the continuum and subcontinuum level that deform the combustion-supporting surfaces and rear-surface regions. Some of these key mechanisms include crack formation; the development of deformed, peeled layers of surface; and the influence of internal thermal stresses on the generation and transport of volatile vapors to the flame for combustion. Experimental studies employing state-of-the-art facilities so as to permit tightly controlled burning processes provide key material parameter measurements. Complementary experiments provide a detailed assessment of the accuracy and, hence, predictive capability, of the engineering analysis.

2.3 Brief Literature Review

The morphological changes produced when a material degrades in a broad surface layer can generate the following: 1) intense, sustained surface combustion that is difficult to extinguish [1]; 2) complex, unpredictable surface burn patterns [2]; 3) changes in flammability limits, including unquenched burning in low oxidizer environments [3]; 4) generation of noxious pollutants [4]; 5) weakened structural behavior, i.e., reduced structural support [5]; and 6) diminished resistance to impact or blast [6].

Numerous studies have examined the breakdown of heated surfaces. Such surfaces supply gas-phase fuel for combustion by degrading in a complex manner. Only recently have they been examined using nonintrusive diagnostics [7,8]. Reviews of propellant modeling are available [9]. Some models have depicted the propellant as packed mixed size and type spheres embedded in a thermoplastic matrix [10]. In fire safety research, some investigations have emphasized models/correlations that characterize material degradation [11–13]. Studies have

been published on modeling solid burning [14]; estimating mass loss rates of polymeric materials in fire [15–17]; and modeling specific physical events for aircraft fires [18,19]. Aspects of these studies consider 1) evolved combustible products [20–23]; 2) the addition of fire retardants to mitigate or suppress combustion [22,24]; 3) the incorporation of decomposition models in surface burning codes [25,26]; and 4) the rate of ignition of combustible materials [27]. Most of the aforementioned studies focus on materials that do not bubble, form char, produce microexplosions, or undergo complex time-dependent decomposition [25,28]. Many studies use “ideal thermoplastic materials” [28–30], such as poly(methyl methacrylate), to study thermoplastics or pure research-grade cellulose to study charring materials [31,32].

For complex materials, the surface is actually a layer of finite thickness. This layer often forms cracks and voids that are distributed in a complex. The nature of the degraded surface layer structure exhibits enormous variation between materials. The surface morphology alters combustion by 1) forming fissures that allow exposure of internal material to external heating; 2) allowing volatiles to escape from inside the material into the gas to support combustion; and 3) forming cracks and voids that weaken the material, making it susceptible to physical breakdown into smaller fragments that are more readily consumed by the flame. Additional review commentary of surface degradation and combustion can be found in refs. 29, 30, and 33–36.

2.4 Experimental Methods

Measurements have been made of the evolving surface morphology in a suite of composite samples involving xGnP during pyrolysis and combustion. The MSU cone calorimeter (Fig. 2.1) has been employed to evaluate product gas distribution and produce a “chemical signature” of the decomposition process by subjecting the sample to a specified incoming radiant flux. This facility has been extensively used to test commercial materials (ASTM E1354 [37], NFPA 271 [38], ISO 5660 [39]) for evolution of dioxide, carbon dioxide, carbon monoxide, and various nitrous oxide (NO_x) species. Using radiant energy to heat the samples, we have characterized how changes in surface morphology influence volatile release and burning rate in a suite of xGnP samples. Because surface morphology is an important indicator of the influence of material physical structure (i.e., its proclivity for forming voids, cracks, and fissures), we have been able to assess how in-depth chemicals (volatiles) flow into the gas to enhance combustion as the material degrades.



Fig. 2.1 Cone calorimeter

2.5 Test Plan

A computational modeling capability has been developed to correlate with the experimental characterization work. This model allows continuous refinement by making use of existing mathematical techniques and available software. To accomplish this, we have replaced certain simplified assumptions that current models use in either the gas or solid phase. Gas combustion models that treat the flame realistically often make highly simplified assumptions for how reactants are supplied by the degrading solid. Conversely, models that describe material breakdown make highly simplified assumptions for how heat is supplied to the degrading solid interior, how the stresses develop and relieve themselves, and how these mechanical factors yield substructural changes that can modify pyrolysis.

Numerical fire models that focus only on the gas and flame are highly developed in their ability to simulate fluid mechanical transport, heat transfer, and chemical reaction to support combustion. The couplings between these processes are understood and permit the application of well-understood analysis techniques at length scales ranging from atomistic to continuum. We have used the National Institute of Standards and Technology Fire Dynamics Simulator to address the phenomenological gas-phase modeling part of this project.

Modeling the solid part has required more attention. Describing material degradation and its consequent effect on mechanical performance is *not* well developed for combustion problems involving thermal assault. The standard paradigm is instantaneous conversion from solid to gas at a rate determined by local temperature. This does not take into account the necessary features of fissure formation and crack development, as we have observed in our experiments. The

project therefore has focused on providing such a capability. This has enabled us to create new computational procedures that successfully predict how material degradation during combustion is dependent upon the structural and thermal properties of the composite material.

2.6 Materials

A wide variety of samples have been analyzed using the cone calorimeter. Figure 2.2 shows a typical crack pattern that developed after thermal assault. Different combinations of xGnP materials have been subjected to controlled combustion in the cone calorimeter. In addition, the materials have been simulated for crack pattern development during degradation using our developed computational routines. Of particular relevance is the effect of thermal conduction upon the cracking pattern. Different material designs as obtained by manipulating the concentration and placement of xGnP lead to different thermal conduction properties of the composite. These, in turn, can give very different patterns of crack development for the same far-field combustion profile.



Fig. 2.2 A typical crack pattern that develops after thermal assault

2.7 Experimental Setup

The integration of experiment with theory, computation, and analysis allows output from the experiments to provide input to the analysis. It also enables rational design of experiments to provide validation for the computational methods. Figure 2.3 summarizes how this has been accomplished. In addition to making use of commercial combustion simulation software and certain FEA procedures for failure analysis, MSU-developed computational mechanics methods enable us to incorporate our fundamentally new models for material degradation into our engineering simulations. The necessary numerical

procedures have been implemented on a variety of computational platforms. For relatively simple simulations, our codes run well on standard laptop machines. However, for a full accounting of a material degradation from flame ignition through charring combustion, we have found it necessary to use the super computer available to us through the MSU Institute for Cyber-Enabled Research (<http://icer.msu.edu/hpcc>). In particular, one of the graduate students involved in this project attended a workshop at Iowa State University in the summer of 2013 to learn the appropriate coding methods to convert our computational software for use on the MSU high-performance super computer. At present we are able to routinely run on a variety of platforms.

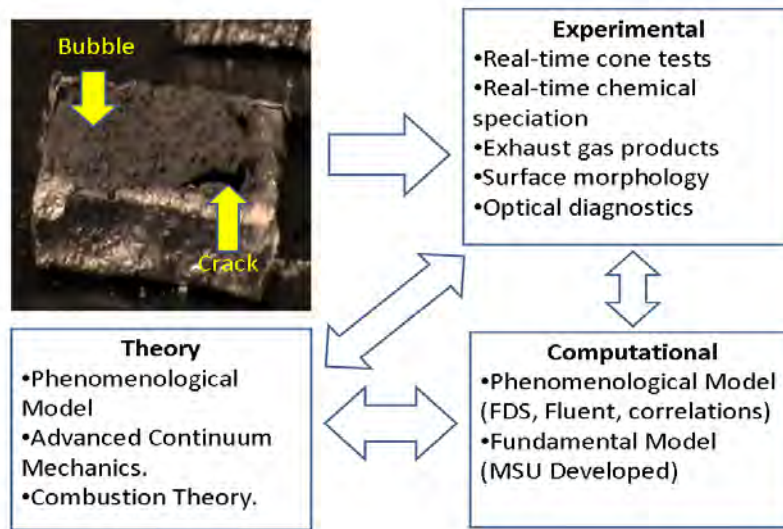


Fig. 2.3 Experimental and modeling plan

2.8 Testing and Results

The experiments indicate that cracks propagate to produce material regions that frustrate conduction but enhance convection by providing internal access for the surrounding hot gases. Consequently, conduction and convection in the solid are modified. As combustion proceeds, material fragments break away, and this exposes a fresh (internal) surface for burning. This has been extensively measured in our calorimeter experiments.

Figure 2.4 shows the stress field as the material degrades because of a controlled burn that initiates at the top surface. This figure can be regarded as a “snapshot” of a particular instance in the combustion process. The darkest locations are due to the presence of deep penetrating cracks that have formed. The finite element method used here tracks crack nucleation and growth in response to stresses that develop as the material loses mass during subsurface pyrolysis. The resulting

chemical reactions are heat mediated, and the degree of mass loss is correlated with the evolution of the various volatile species in the reaction. In this simulation, the cracks advance by a failure criterion based on the maximum principal stress, although other failure conditions are also being modeled. The computational implementation in this simulation is accomplished by a cell removal algorithm.

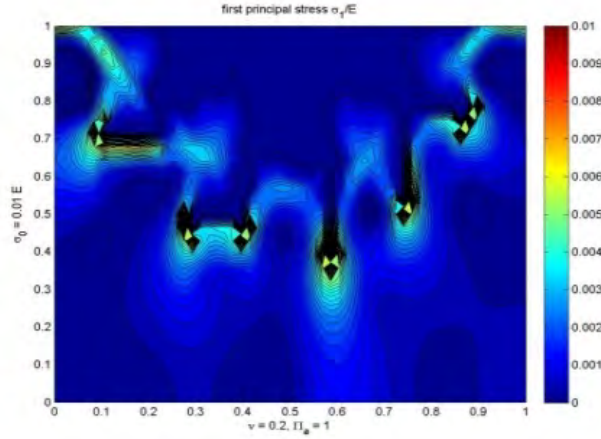


Fig. 2.4 Stress field as the material degrades from a controlled burn that initiates at the top surface

Figure 2.5 depicts the development of a particular crack pattern that evolves with time. This is only one of many different crack patterns that can develop for the same combustion conditions. Changes in the crack pattern are sensitive to the thermal conduction properties, the material stiffness, the pyrolysis conditions, and the crack advance criteria as embodied in a failure condition. All of these can be altered by the choice of base material in conjunction with the composite reinforcing and the use of any particulate additions. The analysis methods that have been developed in the course of this project would enable a design engineer to evaluate the effect of alternative design choices.

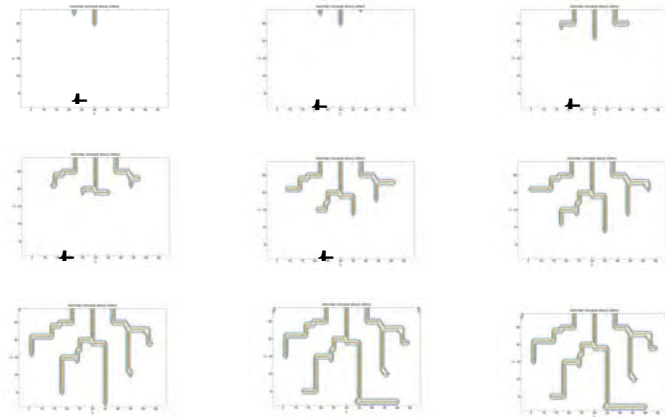


Fig. 2.5 Modeled crack propagation

2.9 Outcomes

The cross-thrust nature of this project makes this research fundamentally new. As such, only now are the first papers being readied for publication. However, the research results have been communicated directly to Army Research Office personnel at the Composite Vehicle Research Center review meetings. In addition, Pence and Wichman worked directly with US Army Tank-Automotive and Armaments Command personnel on-site in a full-day briefing seminar and research workshop that took place September 3, 2013, in Warren, Michigan. Of particular interest was the frame-by-frame analysis of material degradation for a variety of possible material choices. The implications for the improved design of composite systems were then the major topic of the round table-style discussion.

2.10 Future Objectives

This project has demonstrated the feasibility of incorporating flammability analysis within the broader structural analysis and standard life-cycle evaluation algorithms that provide the usual engineering tools for composite vehicle development. The methods that we have developed are fundamentally new. Specifically, these methods have required us to consider the combustion-solid interaction in a coordinated way that acknowledges how the various physical processes interact on a variety of time and length scales, as depicted in Fig. 2.6.

This project has resulted in the development of new capabilities that will enable engineers to construct safer, cheaper, and more reliable vehicles. This is especially true with respect to military vehicles that operate in harsh environments and that, in a combat setting, are routinely subject to combined blast and thermal assault. We are eager to move this project from the current successful proof-of-concept stage (which is inherently research based) to the stage where it combines research and development so as to provide improved military vehicle capability.

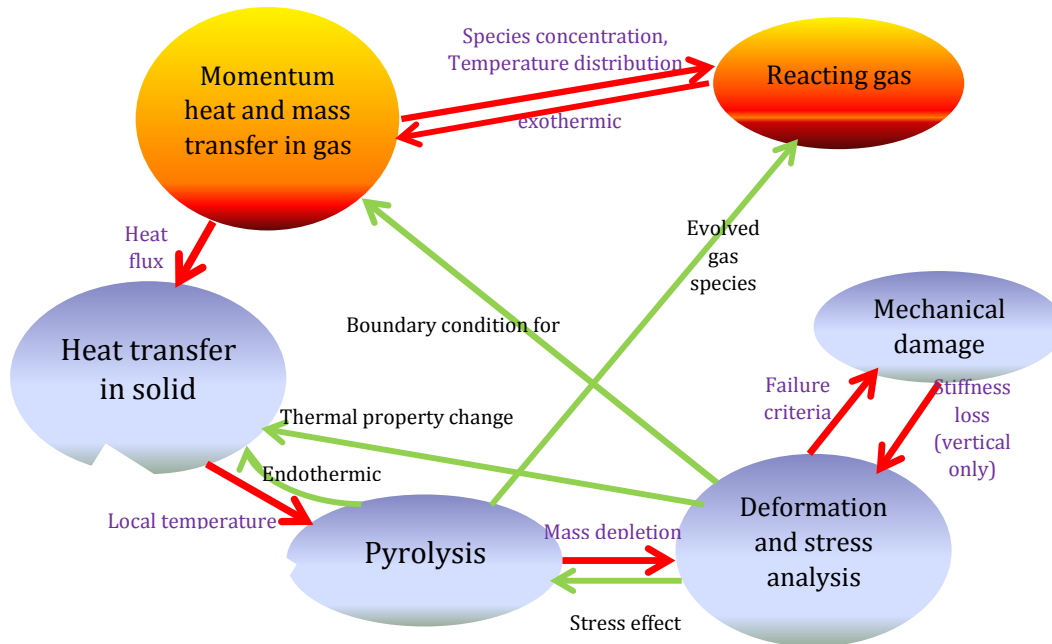


Fig. 2.6 Process involved in burning of composite materials

2.11 References

1. Anthony P Hamins, G. Gmurczyk, William L Grosshandler, R. G. Rehwoldt, I Vazquez, Thomas George Cleary, Cary Presser, K Seshadri, "Flame Suppression Effectiveness," *NIST SP 861* (1994). See also: A. P. Hamins, "Vehicle Fire Research Needs," *NIST Internal Report # NISTIR7406*, March (2007).
2. S. L. Olson, F. J. Miller, and I. S. Wichman, "A New Species of Fire: Characterizing Fingering Flamelets Using Biological Population Measures," *Combustion Theory and Modeling* 10, 323-347 (2006).
3. S. L. Olson, F. J. Miller, S. Jahangirian, S. and I. S. Wichman, "Flame Spread over Thin Fuels in Actual and Simulated Microgravity Conditions," *Combustion and Flame*, Vol. 156, pp. 1214-1226. (2009).
4. M. Elomaa, L. Sarvaranta, E. Mikkola, R. Kallonen, A. Zitting, C. A. P. Zevenhoven and M. Hupa, "Combustion of Polymeric Materials," *Critical Reviews in Analytical Chemistry*, Vol. 27:3, pp. 137-197. (1997). See also C. E. Baukal, *Industrial Combustion Pollution and Control*, Marcel-Dekker, NY (2004).
5. R. Fike, "Strategies for Enhancing the Fire Resistance of Steel Structures Through Composite Construction," Ph. D. Thesis, Department of CivilEngineering, Michigan State University (2010).

6. Li, Q. Li, D. Liu B. Raja and D. Templeton, "Designing Composite Vehicles Against Blast Attack". SAE World Congress, Detroit, MI April 16-19 Paper 2007-01-0137. (2007).
7. T. Parr, and D. Hanson Parr, "Optical Diagnostics of Solid Propellant Flame Structures," in Solid Propellant Chemistry, Combustion and Motor Interior Ballistics. *Progress in Astronautics and Aeronautics*, AIAA 185, Eds V. Yang, T. B. Brill, W. Z. Ren. (2000).
8. F. Canty, N. Seryn and D. Gramer, "Solid Fuel Pyrolysis Phenomena and Regression Rate, Part 2: Measurement Techniques, *AIAA* 218, Eds. Chiaverini and K. K. Kuo, pp. 167-205 (2007).
9. M. Chiaverini, "Review of Solid Fuel Regression Rate Behavior in Classical and Nonclassical Hybrid Rocket Motors," *Progress in Astronautics and Aeronautics*, *AIAA* 218, Eds. *Surface Layer Morphology in Flaming Combustion* 2, M. Chiaverini and K. K. Kuo, pp. 31-125 (2007). See also G. Lengelle, "Solid Fuel Pyrolysis Phenomena and Regression Rate, *Part 1: Mechanisms*, *ibid*, pp. 127-165(2007).
10. Y. Damion, T. L. Jackson, V. Topalain, J. Freund and J. Buskmaster, "Effect of Propellant Morphology on Acoustics in a Planes Rocket Motor," *Theoretical and Computational Fluid Mechanics*, Vol. 23, pp. 63-77 (2009). Buckmaster or other U. Ill. propellant research item.
11. C. Lautenberger, "A Generalized Pyrolysis Model for Combustible Solids". Ph. D. Dissertation, Department of Mechanical Engineering, University of California at Berkeley, Berkeley, CA (2007).
12. C. Lautenberger and A. C. Fernandez-Pello, "Generalized Pyrolysis Model for Combustible Solids". *Fire Safety Journal*, Vol. 44, pp. 819-839 (2009).
13. N. Dempsey and M. Janssens, "SFPE Engineering Guide for Estimating Material Pyrolysis Properties for Fire Modeling". *WPI/SWRI/SFPE Report 10012011*. October (2011).
14. G. T. Linteris, L. Gewuerz, K. McGrattan and G. Forney, "Modeling Solid Sample Burning." Manuscript submitted. (2012).
15. F. Kempel, B. Schartel, G. T. Linteris, S. I. Stoliarov, R. E. Lyon, R. N. Walters and A. Hofmann-Bollinghaus, "Prediction of the Mass Loss Rate of Polymer Materials: Impact of Residue Formation." *Combustion and Flame*, Vol. 159, pp. 2974-2984 (2012).

16. G. T. Linteris, M. Zammarano, B. Wilthan, L. Hanssen, "Absorption and Reflection of Infrared Radiation by Polymers in Fire-Like Environments," *Fire and Materials*, Vol. 36, pp. 537 -553 (2012). DOI:10.1002/fam1113.
17. G. T. Linteris, "Numerical Simulations of Polymer Pyrolysis Rate: Effect of Property Variations." *Fire and Materials*, DOI: 10.1002/fam.1066 (2010).
18. S. I. Stoliarov and R. E. Lyon, "Thermo-Kinetic Model of Burning," *Report No. DOT/FAA/AR-TN08/17*(2008).
19. S. I. Stoliarov, S. Crowley, R. E. Lyon, G. T. Linteris." "Prediction of the Burning Rates of Non-Charring Polymers." *Combustion and Flame*, Vol. 156, pp. 1068-1083. (2009).
20. A. A. Stec, P. Fardell, P. Blomqvist, L. Bustamante-Valencia, L. Saragoza, E. Guillaume, "Quantification of Fire Gases by FTIR: Experimental Characterization of Calibration Systems." *Fire Safety Journal*, Vol. 46, pp. 225-233 (2011).
21. J. Luche, T. Rogaume, F. Richard, E. Guillaume, "Characterization of Thermal Properties and Analysis of Combustion Behavior of PMMA in a Cone Calorimeter." *Fire Safety Journal*, Vol. 46, pp. 451-461 (2011).
22. L. Bustamante, T. Rogaume, E. Guillaume, G. Rein, J. L. Torero, "Analysis of Principal Gas Products of Polyether Polyurethane Foam at Different Irradiance Levels." *Fire Safety Journal*, Vol. 44, pp. 933-940 (2009).
23. R. Ghosh, I. S. Wichman, C. Cramer, C. and R. Loloee, "Time Resolved Measurements of Pyrolysis and Combustion Products of PMMA," *Fire and Materials DOI: 10.1002/fam.129*(2012).
24. I. S. Wichman, "Material Flammability, Combustion, Toxicity and Fire Hazard in Transportation," *Progress in Energy and Combustion Science*, Vol. 29, pp. 247-299. (2003).
25. K. McGrattan, "Burning Rate." Chapter 14 of updated explanation of *NIST Fire Dynamics Simulator* (FDS), pp. 359-384. (2012).
26. K. B. McGrattan, S. Hostikka and J. E. Floyd, "Fire Dynamics Simulator User's Guide." *NIST Special Publication 1019*. National Institute of Standards and Technology (NIST), Gaithersburg, MD, October. (2007). For the FDS see <http://fire.nist.gov/fds/>.
27. V. Babrauskas, *Ignition Handbook*, Fire Science Publishers, Issaquah, WA. Co-published by the Society of Fire Protection Engineers (SFPE) (2011).

28. Y. Long, “A Numerical Study of Flame Spread Over Thin Cellulosic Fuels in Microgravity,” Ph.D. thesis, Department of Mechanical Engineering, Michigan State University, East Lansing, MI. (2007).
29. I. S. Wichman, “Theory of Opposed-Flow Flame Spread,” *Progress in Energy and Combustion Surface Layer Morphology in Flaming Combustion Science*, Vol. 18, pp. 553-593. (1992).
30. Y. Long and I. S. Wichman, “Theoretical and Numerical Analysis of a Spreading Opposed-Flow Diffusion Flame,” *Proceedings of the Royal Society A*, Vol. 65, pp. 3209–3238 (2009). Also: doi:10.1098/rspa.2009.0152.
31. C. Di Blasi, "Modeling and Simulation of Combustion Processes of Charring and Non-Charring Solid Fuels," *Progress in Energy and Combustion Science*, Vol. 19, pp. 71-104. (1993).
32. C. Di Blasi, "The State of the Art of Transport Models for Charring Solids." *Polymer International*. Vol. 49, pp. 1133-1146. (2000).
33. B. Moghtaderi, "The State of the Art in Pyrolysis Modeling of Lignocellulosic Solid Fuels." *Fire and Materials*, Vol. 30, pp. 1-30 (2006).
34. G. Zheng, I. S. Wichman, and A. Benard, "Opposed Flow Flame Spread Over Polymeric Materials: Influence of Phase Change," *Combustion and Flame*, Vol. 124, pp. 387 -408. (2001).
35. G. Zheng, I. S. Wichman, and A. Benard, "Opposed Flow Ignition and Flame Spread for Melting Polymers with Navier-Stokes Gas Flow," *Combustion Theory and Modeling*, Vol. 6, pp. 317 -337. (2002).
36. G. Zheng, I. S. Wichman, and A. Benard, "Energy Balance Analysis of Ignition Over a Melting Polymer Subjected to a High Radiation Heat Flux in a Channel Cross Flow," *Fire Safety Journal*, Vol. 38, pp. 229-256. (2003).
37. ASTM E1354-14e1, Standard Test Method for Heat and Visible Smoke Release Rates for Materials and Products Using an Oxygen Consumption Calorimeter, ASTM International, West Conshohocken, PA, 2014.
38. NFPA 271. Standard Method of Test for Heat and Visible Smoke Release Rates for Materials and Products Using an Oxygen Consumption Calorimeter. National Fire Protection Association. Quincy, MA; 2009.
39. ISO 5660. Reaction-to-fire tests - Heat release, smoke production and mass loss rate - Part 1: Heat release rate (cone calorimeter method) and smoke production rate (dynamic measurement). International Organization for Standardization. Geneva, Switzerland; 2015.

3. Thrust Area 1C: Structural Joining: Similar and Dissimilar Materials

Mahmood Haq, Lawrence T Drzal, Alfred Loos, Gary Cloud, Lalita Udpa, Eann Patterson, and Nicholas Giannaris

3.1 Summary

The overall work can be classified into 3 fronts: 1) robust multimaterial joining (in plane, out of plane, torsional, and large-scale implementations), 2) enhancing/tailoring damage resistance in polymer systems and resulting structural components (dissimilar materials joints, all-composite battery tray, etc.), and 3) development of design tools and database(s)—simulations using integrated experimental validation and robust measurement (nondestructive evaluations and health monitoring).

Table 3.1 provides a list of ongoing subprojects that are not expanded upon in this report.

Table 3.1 Subproject details

Subprojects / Title(s)	Time Period
Enhancing Damage Resistance of Structural Composites Using Novel Hybrid xGnP/CTBN Platelets: A Computational Materials Approach (Sponsor: US Army Research Laboratory)	06/2010–05/2011
Damage and Fatigue Enhancements of Novel GnP/CTBN Composites: From the Lab to Large-Scale Structural Applications (Sponsor: US Army Research Laboratory)	06/2011–05/2012
Hybrid Bonding of Dissimilar Materials (Sponsor: US Army Tank Automotive Research, Development and Engineering Center [Fundamental/ Non-Classified Research])	10/1/2012– Current
Multi-Material Joining: Adhesively Bonded Pi-/T-joints (Sponsor: US Army Tank Automotive Research, Development and Engineering Center [Fundamental/ Non-Classified Research])	10/1/2012– Current

3.2 Topics Addressed/Successfully Implemented

For brevity, the details of each subproject listed in Table 3.1 are not elaborated in this report. Instead, a bulleted list of the topics that were successfully implemented and delivered is provided below. Also, the outcomes of the project in terms of publications and training of personnel are briefly provided. Please contact the PI/POC for additional details on any of the specific topics discussed herein.

- Determination of effect of surface preparation in bonded multimaterial joints.

- Out-of-autoclave, cost-effective manufacturing of structural joints and quality control.
- Damage-induced (manufacturing flaws and impact induced) behavior of joints and other structural components.
- Enhancement of fracture toughness and impact resistance of joints using novel hybrid graphene/CTBN (rubber) particles. Other micro-/nano-modifications include nanoclay and glass micro-spheres.
- Fatigue behavior of multimaterial joints and novel tailorable materials: experimental evaluation of the effect of nano- and micro-modifications on resulting structural components.
- Notched behavior of structural composites and resulting joints: experimental and numerical evaluation.
- Tailored fiber placement and its efficiency in rapid manufacturing, light-weighting, and development of robust joints and other structural composites.
- Environmental testing: 1) structural behavior at extreme temperatures (32 °F and 120 °F) and 2) moisture absorption (soak test + periodic testing).
- Novel hybrid fastening system (patented technology developed by Dr Gary Cloud) that produces dissimilar joints with numerous possibilities including “zero-slip” behavior, reduced/delayed delaminations under load, and enhanced load-carrying capacities relative to conventional mechanical fastening techniques.
- Effect of curing-induced shrinkage of resins and its effect on strengths of adhesive joints and other structural components.
- Nondestructive evaluation and health monitoring of multimaterial joints and structures.
- Large-scale light-weighting structural applications: 1) composite I-beams for bridging applications and their flexural behavior and 2) prototypes of bumper attachments using Pi/T-joints and simulations regarding the feasibility of this work.

3.3 Deliverables and Outcomes

Provided below is a list of outcomes in the form of book chapters, publications, conference presentations, and proposals. This list is preliminary and may be missing some publications.

Book Chapters:

- [1] Chapter 22: Haq M., Khomenko A., Udpa L., Udpa S. (2014). “Fiber Bragg-Grating Sensor Array for Health Monitoring of Bonded Composite Lap-Joints.” *Experimental Mechanics of Composite, Hybrid, and Multifunctional Materials, Volume 6, pp. 189-195. Springer, New York, USA.*
- [2] Chapter (TBA): Khomenko A, Koricho EG, Haq M (2014). “Monitoring the effect of micro-/ nano – fillers on curing-induced shrinkage in epoxy resins” *Fillers and Reinforcements for Advanced Nanocomposites, Wood Head Publisher, the part of Elsevier.* Under Final Review.
- [3] Chapter (TBA): Koricho EG, Khomenko A, Haq M (2014). “Influence of Micro-fillers on Impact Response of Glass Fiber Reinforced Plastic (GFRP) Composite” *Fillers and Reinforcements for Advanced Nanocomposites, Wood Head Publisher, the part of Elsevier.* Under Final Review

Journals (Published + Submitted):

- [4] Karpenko O., Haq M., Khomenko A., Udpa L., Udpa S. (2014). “Lamb wave based monitoring of delamination growth in mode I and mode II fracture tests.” *Fracture and Fatigue, 7:33-43.*
- [5] Umer R, Waggy EM, Haq M, Loos AC. (2012) “Experimental and Numerical Characterization of Flexural Behavior of VARTM-Infused Composite Sandwich Structures,” *Journal of Reinforced Plastics and Composites, 31: 67-76.*
- [6] Koricho EG, Khomenko A, Fristedt T, Haq M (2014), “Innovative Tailored Fiber-Placement Technique for Enhanced Damage Resistance in Notched Composite Laminate,” Manuscript submitted to *Journal of Composite Structures*, Under Review.
- [7] Koricho EG., Khomenko A, Haq M., “Impact Behavior of Glass Micro-bubbles Reinforced Thermoplastic Adhesive Joints,” Manuscript submitted to *Journal of Composite Structures*, Under Review.

Journals (Manuscripts under Internal Review, to be submitted):

- [8] Haq M., Koricho E.G. and Khomenko A. “Experimental, FEA and Analytical Studies of Multi-Materials Joining for Automotive Applications”. *To be submitted (December 2014) to Journal of Adhesion Science and Technology.*
- [9] Haq M., Khomenko A., Udpa L., Udpa S., “Fiber Bragg-Grating Array for Health Monitoring of Bonded Composite Lap-joints”. *To be submitted (December 2014) to Composite Structures.*

- [10] Haq M., Cloud G. "Novel Hybrid Fastening System" *To be submitted (December, 2014) to Composite Structures.*
- [11] Haq M, Patterson EA, Drzal LT. "Pull-out Behavior of Adhesively Bonded Composite Pi-joints: Numerical Modeling of Damage and Validation with Experiments," *Journal of Reinforced Plastics and Composites.* Communicated Aug. 2014.
- [12] Haq M., Patterson E.A., Drzal L.T. "Impact Behavior of Adhesively Bonded Structural Composite T-joints," *To be submitted (December, 2014) to Composite Structures.*
- [13] Haq M., Drzal L.T., Patterson E.A. "Health Monitoring of Composite Pi/T-joints using FBG Sensors," *To be submitted (December, 2014) to Journal of Reinforced Plastics and Composites*

Conference Publications:

- [14] Dib G, Karpenko O, Koricho E, Khomenko A, Haq M, Udpa L, Udpa SS, "Feasibility of PZT Ceramics for Impact Damage Detection in Composite Structures." *41st Annual Review of Progress in Quantitative Nondestructive Evaluation (QNDE 2014), Boise, ID, USA. July 20-25, 2014.*
- [15] Karpenko O, Dib G, Koricho E, Khomenko A, Haq M, Udpa L, Udpa SS. "Structural Health Monitoring of Adhesively Bonded Lap-Joints During Fatigue Testing" *41st Annual Review of Progress in Quantitative Nondestructive Evaluation (QNDE 2014), Boise, ID, USA. July 20-25, 2014.*
- [16] Haq M., Khomenko A., Cloud G. "Novel Hybrid Fastening System with Nano-additive Reinforced Adhesive Inserts," *SEM 2014 Annual Conference & Exposition on Experimental and Applied Mechanics, Greenville, SC USA June 2-5, 2014.*
- [17] Koricho E.G., Khomenko A., Haq M, "Fatigue Behavior of Glass-Bubbles Modified Adhesively Bonded Composite Joints For Automotive Applications," *SEM 2014 Annual Conference & Exposition on Experimental and Applied Mechanics, Greenville, SC USA June 2-5, 2014.*
- [18] Khomenko A., Koricho E.G., Haq M., "Measurement of Curing-induced Shrinkage in Nano-modified Resins and its Effect on Tensile strengths," *SEM 2014 Annual Conference & Exposition on Experimental and Applied Mechanics, Greenville, SC USA June 2-5, 2014..*
- [19] Koricho E.G., Khomenko A., Haq M., "Innovative Tailored Fiber-Placement Technique for Enhanced Damage Resistance in Notched Composite Laminate," *1st Int. Conference on Mechanics of Composites (MECHCOMP2014), Long Island, NY State, USA, 8-12 June 2014.*
- [20] Koricho E.G., Khomenko A., Haq M., "Impact Behavior of Glass Micro-bubbles Reinforced Thermoplastic Adhesive Joints," *1st Int. Conference on Mechanics of Composites (MECHCOMP2014), Long Island, NY State, USA 8-12 June 2014.*

- [21] Ripberger J., Khomenko A., Haq M., Gianaris N., Cloud G., "A Tailorable Fastening System for Dissimilar Material Joining." *13th Annual Society of Plastic Engineers (SPE) and Automotive Composites Conference & Exhibition (ACCE)*, Novi, MI, USA, Sept. 2013.
- [22] Haq M., Drzal L.T., Cloud G., "Metal-Composite Bonded Pi- joints." *SEM 2013 Annual Conference & Exposition on Experimental and Applied Mechanics*, Chicago, IL, USA, June 3-5, 2013.
- [23] Haq M., Cloud, G., "Flexible Hybrid Fastening System." *SEM 2013 Annual Conference & Exposition on Experimental and Applied Mechanics*, Chicago, IL, USA, June 3-5, 2013.
- [24] Haq M., Khomenko A., Udpa L., Udpa S., "Fiber Bragg-Grating Array for Health Monitoring of Bonded Composite Lap-joints." *SEM 2013 Annual Conference & Exposition on Experimental and Applied Mechanics*, Chicago, IL, USA, June 3-5, 2013.
- [25] Karpenko O., Haq M., Udpa L., Udpa S., "Lamb Wave Based Monitoring of Delamination Growth in Mode I and Mode II Fracture Tests." *SEM 2013 Annual Conference & Exposition on Experimental and Applied Mechanics*, Chicago, IL, USA, June 3-5, 2013.
- [26] Haq M., Umer R., Loos A.C., Drzal L.T., "Manufacturing and Impact Behavior of Sandwich Composites with embedded Graphene Platelets." *The 19th International Conference on Composite Materials*, Montreal, Canada. July 28-August 2013.
- [27] Haq M., Karpenko O., Khomenko A., Udpa L., Udpa S., Gianaris N., "Guided Wave Inspection of Bonded Dissimilar Material Joints." *ISEM2013-International Symposium on Applied Electromagnetics and Mechanics*, Quebec, Canada, July 31-August 2, 2013.

Conference Publications (Accepted for Presentation in 2014):

- [28] Koricho E.G., Khomenko A., Haq M., "Fatigue Behavior of Bonded Pi/T-joints," *2014 ASC 29 / US-Japan 16 / ASTM D30 Conference*, San Diego, CA, USA, 8-10 Sept. 2014. (Accepted)
- [29] Khomenko A., Koricho E.G., Haq M., "Fiber Bragg-Grating Sensors for SHM and FEM of In-Service Bonded Multi material Pi-joints" *2014 ASC 29 / US-Japan 16 / ASTM D30 Conference*, San Diego, CA, USA, 8-10 Sept. 2014. (Accepted).
- [30] Khomenko A, Koricho EG, Cloud G, Haq M. "Torque-Load Monitoring in Bolted Joints using Innovative 'MoniTorque' Bolts," *The Composites and Advanced Materials Expo (CAMX)*, Orlando, FL, October 13-16, 2014.
- [31] Koricho EG, Khomenko A, Haq M, Fristedt T, Belingardi G, Martoran B., "Development of Composite Control Arm for Automotive Applications using Tailored Fiber Placement (TFP)," *The Composites and Advanced Materials Expo (CAMX)*, Orlando, FL, October 13-16, 2014.

- [32] Koricho EG, Khomenko A, Belingardi G, Martoran B, Drzal LT, Haq M. "Influence of Hybrid (Micro- and Nano-) Fillers on Impact Response of GFRP composite," The Composites and Advanced Materials Expo (CAMX), Orlando, FL, October 13-16, 2014.

Proposals and White Papers:

- [P1] Haq M., Cloud G., "Flexible Hybrid Fastening System for Multi-Material Joining," *Submitted to TARDEC on Jan. 14, 2013. Result- Not funded, but few elements of the proposal were implemented in Multi-Material Pi-joint work.*
- [P2] Haq M., Cloud G., "Flexible Hybrid Fastening System for Dissimilar Material Joining," *Submitted to DoE on April, 2013. Result- Concept Paper was accepted, final proposal was not funded, but a few elements of the proposal were implemented in Multi-Material Pi-joint work.*
- [P3] Haq M., Drzal L.T., Udpa L., Loos A.C., Gianaris N., "Active, Tailorable Adhesives for Dissimilar Material Bonding, Repair and Reassembly," Submitted to U.S. Department of Energy (DoE), Awarded \$600k, October 1, 2013 to December 2016. NOTE: This proposal is intellectually entirely different than the multi-material joining projects funded by TARDEC/ARL. Nevertheless, the findings/ limitations from the TARDEC funded MMJ projects were used to develop innovative solutions as proposed to DoE.

Technology Transfer (Trained Workforce): Undergraduate students mentored and trained in manufacturing and experimental testing of composites and multimaterial joining. All undergraduates trained thus far are US citizens or permanent residents. The students' status and current employment information is found in Table 3.2.

Table 3.2 Technology transfer student information

Student	Status	Employment/Internship
Alexander Bonnen	Sophomore, honor student, currently working on MMJ projects	Williams International and Stryker Inc.,
Benjamin Bosworth	Graduated Dec. 2013	Pratt & Miller (full-time)
Christopher Churay	Sophomore, left group in May, 2013	MSU Formula 1 SAE team
Stephanie Fierens	Sophomore, honor student, currently working on MMJ projects	Not Available
Morgan Hoxsie	Junior, worked in summer 2013	Not Available
Caroline Williams	Senior, worked in summer 2013	Not Available
Jack Potterack	Senior, worked in summer 2013	Not Available
Jacob Ripberger	Sophomore, worked in summer 2013	Not Available
Mark Dawson	Graduated May 2013	ALCOA (full-time)
Saurabh Sinha	Junior, left group in Aug. 2013	Toyota
Erik Stitt	Graduated Mar. 2014.	Schlumberger (full-time)
Gerges Dib	PhD, Graduated July 2014	Pacific Northwest National Laboratory (full-time)

3.4 Acknowledgments

The PI (Dr Mahmood Haq) would like to acknowledge the sponsors for their support. The PI would like to thank the co-PIs, postdocs, students, and other collaborators for their tremendous support and teamwork to achieve the desired deliverables. The experimental facilities of the Composite Vehicle Research Center (CVRC) and Michigan State University are duly acknowledged. The support of CVRC staff in preparation of text fixtures is acknowledged. Most importantly, the feedback from the program managers from all sponsors, including but not limited to Dr Doug Templeton, Dr Bill Spurgeon, Dr Roger Crane, Dr Maureen Foley, Dr Richard Gerth, Mr Vlad Gendlin, Mr Dani Shaffren, Mr Demetrios Tzelepis, and Ms Lynne Krogsrud are highly appreciated. Their continuous feedback and interest has provided direction and increased the productivity of the funded research.

4. Thrust Area 2: Self-Diagnostic Composite Structures

Lalita Udpa, Mahmood Haq, Gerges Dib, and Oleksii Karpenko

4.1 Wireless Sensor Networks for Online Monitoring of Heavy-Duty Vehicle Systems

4.1.1 Summary

The use of wireless sensor networks for structural health monitoring has the potential to significantly increase safety and reduce manufacturing and maintenance costs. Wireless sensor networks use low-footprint “smart” active sensor nodes that are permanently mounted on the structure. The sensor nodes should be self-powered and have the means to detect changes in the structure indicating impending hazards and to communicate wirelessly with other sensor nodes or base stations when anomalies are detected. They should also have processing power to be able to decide if a detected event indicates a hazard before transmission. This report presents the sensor node hardware and software implementation for passive and active sensing of elastic guided waves. A distributed control algorithm is presented for controlling a wireless sensor network from a base station. A proof-of-concept implementation of the sensor nodes for damage detection in a plate is demonstrated.

4.1.2 Introduction

Structural health monitoring (SHM) serves to improve safety and reduce maintenance costs by providing real-time information about the structure’s integrity and warning about impending hazards. The integration of SHM systems within industrial structures can change current safety and inspection practices, eliminating the need for regularly scheduled inspections and migrating toward condition-based inspections. An SHM system uses a network of sensors that are permanently surface mounted or embedded in the structure.

The ultrasonic guided wave method using built-in thin piezoelectric films has emerged as a promising option for locating and characterizing damage in SHM. Guided waves are elastic stress waves that are guided within the confines of a structure’s surface when one dimension of the structure is smaller than the propagating wavelength. A guided wave travels along the surface of the structure with nonpropagating perturbations (standing wave) along the thickness. The propagating wave energy diffuses only in 2 dimensions, reducing attenuation and

allowing the wave to propagate for a longer distance. This allows the monitoring of a large structural area using a sparse network of fixed sensors, which makes it attractive in SHM applications.

A main challenge in implementing an SHM system using guided waves is to transfer data from the lead-zirconate-titanate (PZT) sensor network to a base station. Connecting the sensors directly through cables and wires has a high installation and material cost. Wireless sensor networks (WSNs) offer a promising solution for continuous SHM. WSNs are inherently highly scalable and configurable and do not require high installation and maintenance cost. A sensing device is connected to the PZT sensor to acquire and digitize the measured waveforms. Because of the lack of physical wiring, those devices need to be self-powered. This limits the amount of power available to them, requiring the use of low-power electronics, which limits the computational performance. This poses a challenge for actuating high-power guided wave signals and also data acquisition of high-frequency signals, which requires sampling rates higher than those supported by current low-power wireless sensing devices.

The simplest architecture of a WSN for SHM is the centralized architecture, as shown in Fig. 4.1. There are 2 different entities in this architecture: the sensor nodes and the base station. The sensor nodes are smart low-power devices equipped with signal conditioning and data acquisition devices, microcontroller, digital memory, power supply, and a radio. Multiple sensor nodes are deployed on the structure and connected to the PZTs, forming a wireless sensor network. Because of power scarcity, the computational speed, wireless transmission power, and data acquisition speed are limited. The presence of a microcontroller enables us to control the sensor node, thus making WSNs highly configurable and automated. This is achieved by programming the microcontroller using software. One base station communicates and controls the network of sensor nodes mounted on the structure. The base station has a gateway that is responsible for transferring data from the WSN to a PC and vice versa. The PC has a user interface where an administrator could control and configure the network or individual sensor nodes. It also has visualization and prognostic tools, indicating the presence of potential hazards in the structure.

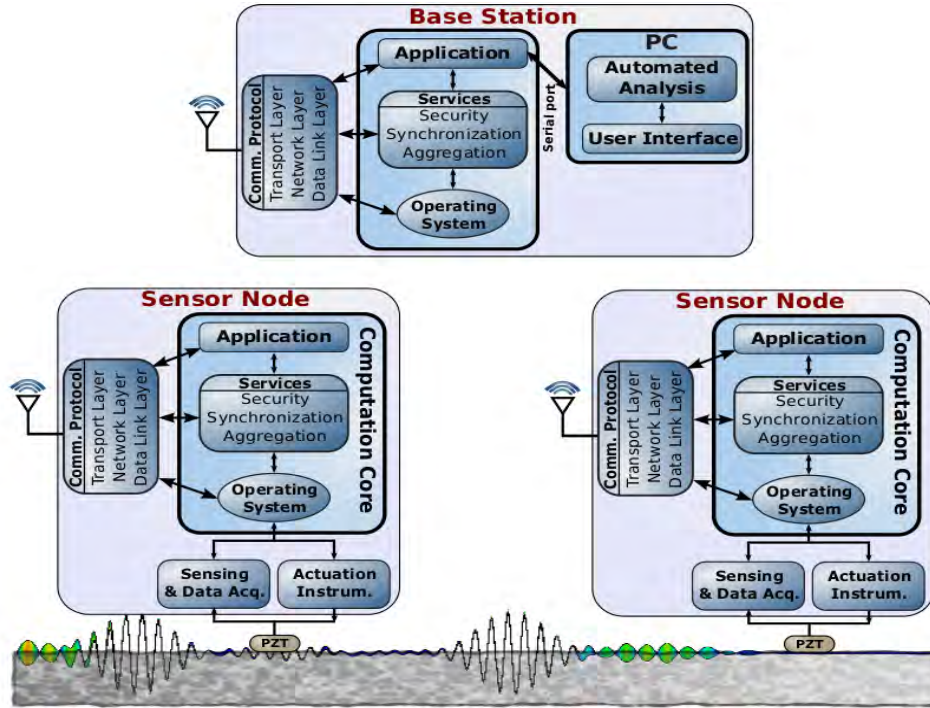


Fig. 4.1 The schematic of a centralized wireless sensor network consisting of 2 entities: the sensor nodes and the base station. The sensor nodes are mounted on the structure and connected to embedded or surface-bonded transducers. The base station is a remote PC that collects data for processing from the sensor nodes.

4.1.3 Literature Review

The use of guided waves as the inspection method is attractive for SHM applications since such waves can be excited at one point and they can propagate long distances with little attenuation [1]. This allows the inspection of large areas in a structure using minimal sensing points. PZT piezoelectric wafers are used as transducers for the excitation and sensing of guided waves in the structure. Those PZT wafers are most commonly used in SHM because of their low cost, low weight, small size, and the practicality of surface bonding or embedding them in a structure [2].

There is not much research conducted in the integration of in-situ wireless technology for continuous monitoring using guided waves. Many sensor nodes for wireless SHM systems have been developed since the late 1990s. A summary review of sensor nodes developed for SHM until the year 2005 can be found in refs. 3 and 4. Most of the described sensor nodes do not include an actuation interface and are used for measuring the frequency response of structures under vibration using accelerometers, requiring the acquisition of signals with bandwidth of just a few hundred hertz. This project aims to develop a sensor node for SHM using a guided wave ultrasonic technique with an ability to actuate the

transducer and to acquire signals with a bandwidth up to 1 MHz. Those issues impose a challenge in wireless sensor networks because of the limited power sources, which are usually in the form of small batteries. Consequently, this limits the resources available for data acquisition, processing, and communication.

4.1.4 Experimental Methods

A prototype for data actuation and guided wave actuation using a wireless module was built and verified. As shown in Fig. 4.1, the sensor node hardware includes the following modules: 1) a data acquisition module, which should be designed to acquire data depending on the selected transducer; 2) a microcontroller that coordinates the behavior of all the components of the sensor node, stores acquired measurements, and carries simple computations locally; and 3) the RF interface for wireless communication.

For actuation, it is desirable to use a narrowband excitation signal, which will minimize the effect of dispersion. The excitation signal that is most commonly used is the Hanning window tone burst signal. When a narrowband excitation signal is used, the sensed signal has a similar bandwidth, and the wave reflections from defects are determined by the peaks of the sensed signal envelope. The sensor node used in this work is the Iris wireless module (also called Iris mote), available from Memsic Corporation (www.memsic.com). The Iris mote hardware components and properties are summarized in Table 4.1. It operates on 2 AA batteries, and it is designed using hardware components with very low power consumption for maximizing the batteries' lifetime. For data acquisition, the Iris mote has a 10-bit analog-to-digital converter, and the sampling frequency is limited to 273 ksps, which is not sufficient for sampling ultrasonic guided wave signals having a bandwidth up to 500 kHz. Moreover, the Iris mote does not have an actuation interface that is needed for guided wave excitation. However, it has a 51-pin connector that makes peripheral interfaces of the microcontroller available for connection to external boards that could extend its functionality. This connector was used to implement an extension circuit board for signal conditioning that would allow the acquisition of narrowband ultrasonic signals with a central frequency up to 1 MHz from the piezoelectric transducer. The extension circuit board also provides an actuation interface that could convert a digital square signal into an analog tone burst narrowband signal for exciting the transducer. The extension circuit board is designed using off-the-shelf circuit components and operational amplifiers.

Table 4.1 Properties of the Iris mote sensing module, processing module, and RF module

Component	Properties
Sensing module	Resolution: 10 bits
<i>Analog to digital convertor</i>	Sampling frequency: 273 ksps
Processing module	7.37-MHz processing clock
<i>ATmega1281 μcontroller</i>	Digital I/O interface pins
	Storage: 8-kB RAM
	Flash memory: 512 kB
Wireless communication module	IEEE 802.14.5 compliant
<i>RF230 Zigbee radio</i>	Bit rate: 250 kbps
	Range: 50 m (indoor), 300 m (outdoor)

The extension circuit board connected to the Iris mote and the block diagram of its circuit components are shown in Fig. 4.2. The extension circuit board is provided its own power source using 4 AAA batteries.

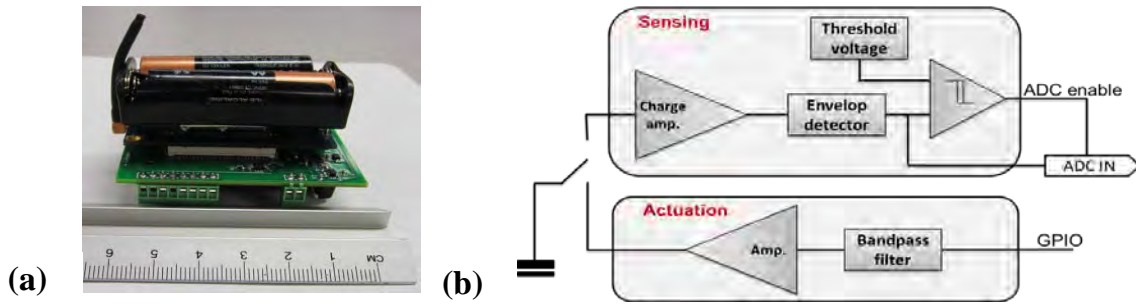


Fig. 4.2 a) The extension circuit board connected to the Iris mote using the 51-pin connector. The sensor node has a total area less than 25 cm². b) The extension circuit board block diagram showing the sensing and actuation modules and the switch that selects which module will be connected to the PZT wafer.

4.1.5 Validation

The experimental setup shown in Fig. 4.3 was used to test the performance of the sensor nodes for active guided wave inspection. Two PZT wafers are bonded to an aluminum plate using epoxy, and each PZT wafer is connected to a sensor node. Sensor node 1 is used for actuation, and sensor node 2 is used for sensing. The outputs of the charge amplifier and the envelope detector of sensor node 2 are connected to the oscilloscope. The resulting sensed signal and its envelope recorded on the oscilloscope and the envelope data samples received at the base station are shown in Fig. 4.4. The envelope signals have been scaled to compensate for the sensing gain and the attenuation of the low-pass filter in the envelope detector. The charge amplifier output is time shifted to compensate for the group delay of the low-pass filter. The envelope detector has good sensitivity to the data variation and detects all the peaks of the wave packets. The interpolated digital signal samples transmitted wirelessly to the base station closely match the analog envelope signal from the oscilloscope.

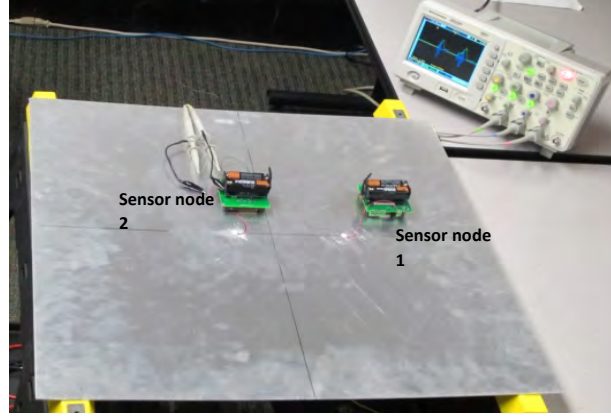


Fig. 4.3 Experimental setup for the validation of the sensing circuit. Two PZT wafers with dimensions 8×7 mm are bonded to the aluminum plate. Sensor node 1 is connected to PZT1 and sensor node 2 is connected to PZT2. The outputs of the charge amplifier and the envelope detector of sensor node 2 are connected to the oscilloscope.

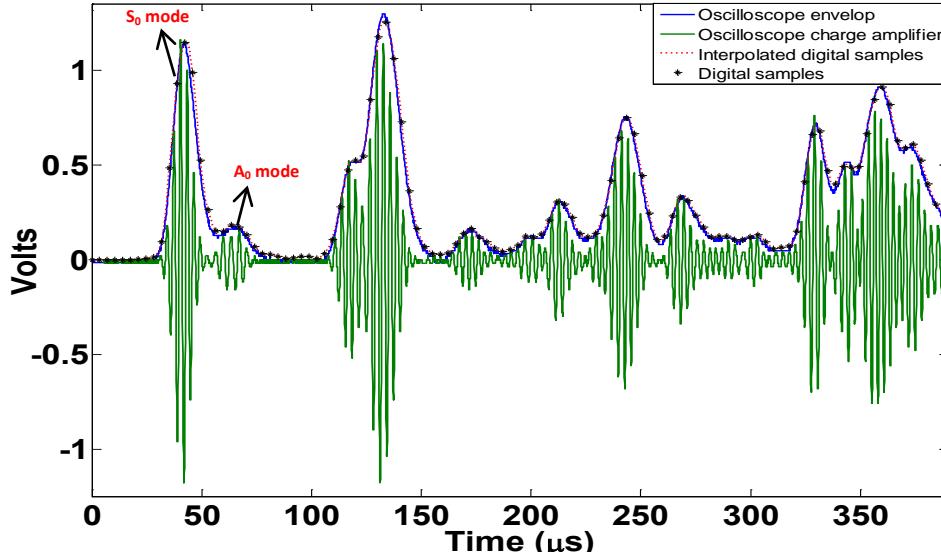


Fig. 4.4 The guided wave signal and its envelope as recorded on the oscilloscope are shown in green and blue, respectively. The sampled envelope data that is transmitted to the base station and their interpolation are also shown. The S_0 and A_0 modes incident wave packets are indicated. All the latter wave packets in the signal are due to reflections from the edges of the plate.

4.1.6 Finite Element Modeling

The finite element modeling software package Explicit/Abaqus is used to obtain the numerical data. In each simulation a 5-cycle Hanning window tone burst at 100 kHz frequency actuation signal is applied to one transducer using the perfectly bonded piezoelectric actuator assumption. The results in Fig. 4.5 show the wave propagation in a single-layered and multilayered (8) composite plate.

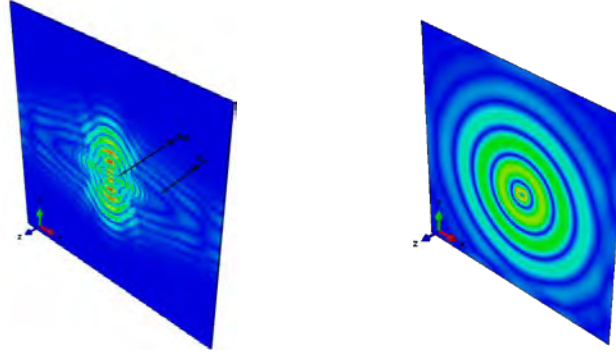


Fig. 4.5 Lamb wave finite element method model in a single layer carbon fiber–reinforced polymer (CFRP) (left) and 8-layer quasi-isotropic CFRP laminate (right)

4.1.7 Signal Processing Algorithms for Damage Detection

Experimental measurements from PZT sensors mounted on aluminum and composite plates were processed successfully using signal processing algorithms. As a first step, the dispersion curves for 8-layer, 5-mm-thick woven composite plates using Lamb wave equation for anisotropic media and a transfer matrix method were obtained. A schematic of the test sample and the corresponding dispersion curves are presented in Fig. 4.6. An efficient 2-stage algorithm for near-real-time decomposition of Lamb waves into constitutive modes, which includes time-frequency analysis and matching pursuit, was then applied.

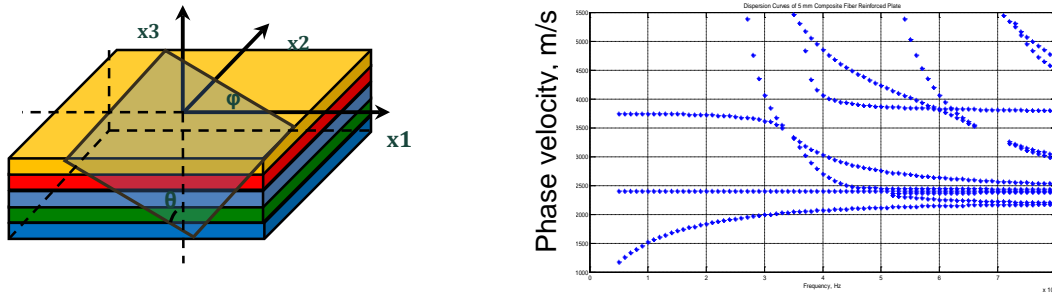


Fig. 4.6 Schematic of multilayered composite material and phase velocity dispersion curves

Low variation of the group velocity at the inspection frequency (200 kHz) makes it possible to apply the standard diagnostic imaging algorithm to damage detection in woven composite materials. Diagnostic imaging was performed using the Lamb wave data from healthy and damaged samples. A-0 mode at 80 kHz was considered. The ellipses, which define the most possible damage location, were computed for sensor pairs that detected the presence of damage. The results of imaging impact damage on a composite plate and a surface-bonded stiffener are presented in Figs. 4.7 and 4.8.

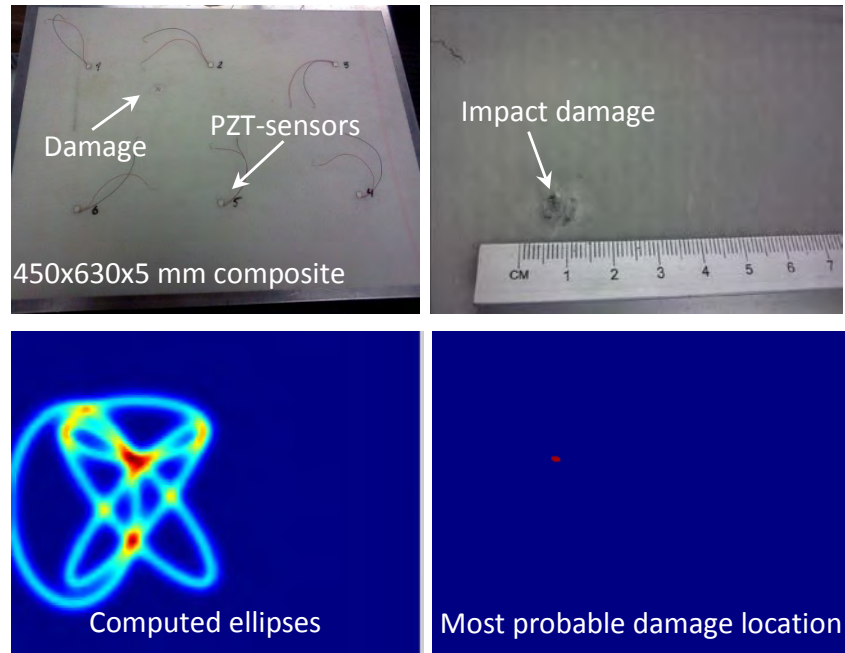


Fig. 4.7 Imaging of composite plate with impact damage

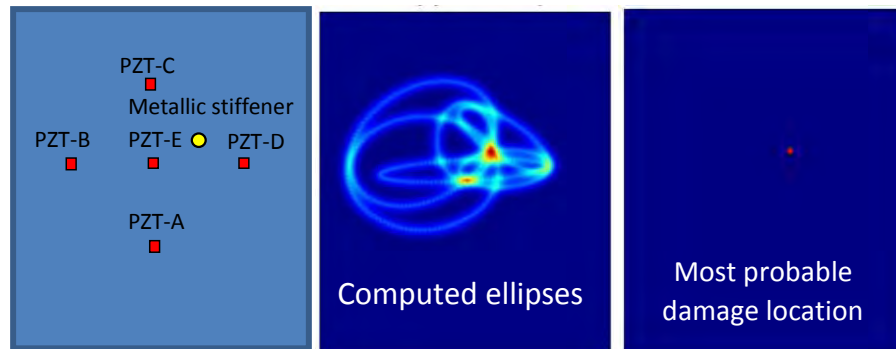


Fig. 4.8 Imaging of 450- x 630- x 5-mm composite plate with surface-bonded aluminum stiffener to simulate surface damage

4.1.8 Outcomes

The results of the research were disseminated in the following publications:

G. Dib, R. Latral, L. Udpa, G. Yang, "A wireless sensor node for structural health monitoring using guided wave inspection," *Materials Evaluation* (Fellowship paper), vol. 71, 2013.

G. Dib, R. Latteral, L. Udpa, "Wireless sensor networks for continuous health monitoring using ultrasonic inspection methods", ASNT Fall Conference, Orlando, FL, 2012.

4.1.9 References

- [1] Alleyne, D.N. and Cawley, P. (1992) “Optimization of Lamb wave inspection techniques”, *NDT&E*, pp. 11–22.
- [2] Sirohi, J. and Chopra, I. (2000) “Fundamental Understanding of Piezoelectric Strain Sensors”, *Journal of Intelligent Material Systems and Structures*, vol. 11.
- [3] Akyildiz, I.F., Su, W., Sankarasubramaniam, Y. and Cayirci, E. (2002) “Wireless sensor networks: a survey”, *Computer Networks*, pp. 393–422.
- [4] Lynch, J. and Loh, K.J. (2006) “A Summary Review of Wireless Sensors and Sensor Networks for Structural Health Monitoring”, *The Shock and Vibration Digest*, vol. 38, no. 2, pp. 91–1.

5. Thrust Area 3A: Structural Integrity of Composites

5.1 A Model for Fatigue Life Prediction of Composite Structures

Xinran Xiao, Andrew Conway, and Arun Krishnan

5.1.1 Summary

This chapter presents the effort on the development of a 3-dimensional finite element-based progressive fatigue damage module capable of lifetime prediction in fiber-reinforced composite materials. A progressive fatigue damage model (PFDM) [1,2] was selected for evaluation. The PFDM was implemented in ABAQUS through a user-defined material model. The model predictions were compared with fatigue experiments of AS4-3506-1 composite laminates with a central hole. The effort on generating PFDM parameters for an S-2 Glass/SC-15 epoxy composite is reported.

5.1.2 Introduction

The overall objective of this thrust area is to develop the capability for the evaluation and prediction of fatigue life and durability for 3-dimensional (3-D) composite components. The work started with a literature review. Much to our surprise, despite the availability of a great amount of fatigue test data and a fundamental understanding of fatigue damage mechanisms of composite materials, a general design tool that translates the knowledge and data generated with lab-scale coupons to structural applications did not exist. Three integrated composite fatigue prediction tools were reported in open literature—namely, the progressive fatigue damage model (PFDM) [1,2], MRLife [3], and MAE [4] models. However, none of the models has been evaluated by a second group besides the work of the original developers.

Among the 3 models, the PFDM is most closely aligned with the finite element analysis (FEA) widely used in structural design. The PFDM incorporates a set of empirical stiffness and strength degradation rules and master fatigue curves established from testing unidirectional composite into FEA. It allows the stress analysis of composite structures with arbitrary lay-up configurations and loading sequences with a gradually degraded property. The parameters for PFDM are available for the AS4-3506-1 composite [2]. The PFDM was selected for investigation.

To evaluate the PFDM, the model was implemented as a user material model in ABAQUS. Fatigue experiments were carried out with AS4-3506-1 composite plates with a central hole. The strain field evolution during fatigue experiment was recorded with digital image correlation (DIC) measurement. Our results showed that the PFDM was capable of predicting the strain redistribution due to fatigue damage in the 2 types of AS4-3506-1 laminates examined. This led to the suggestion to work on materials relevant to the sponsors. In response to this need, we worked on generating PFDM parameters for a plain weave S-glass/CS-15 epoxy composite. The total number of fatigue tests required is 240. So far, about 45% of the tests have been completed.

5.1.3 Fatigue Model Overview

Fatigue life prediction for composite structures lags far behind as compared to that for metallic or other structures. Metal fatigue is characterized by crack initiation and propagation. Fatigue life prediction often concerns the propagation of one major crack [5,6]. With fracture mechanics-based methodologies, one can predict the remaining life of components with cracks with high confidence.

In comparison, fatigue damage mechanisms in composites are far more complicated. Composite materials are inhomogeneous at the micro and meso levels. The inhomogeneity and anisotropy mean that multiple damage modes, such as matrix cracking, fiber/matrix debonding, fiber fracture, fiber buckling, and delamination, may occur at different scales. These damage modes may grow at different rates and interact in a variety of ways under the influence of the local stress field. The fatigue damage process starts early in the life of a composite structure and is characterized by a reduction in the stiffness at damage zones. This leads to a continual redistribution of stress within the structure over time.

A large body of literature on fatigue damage mechanisms in composites has been generated since the 1960s. Comprehensive reviews on various aspect of composite fatigue are available in the literature. A detailed mechanism-based review on composite fatigue has been provided by Hahn [7]. The state-of-the-art of damage analysis for the prediction of structural integrity and durability of composite materials can be found in refs. 8–10. The effect of variable amplitude of loading on fatigue of composites has been investigated by Post et al. [11].

Despite the wide range of fatigue models, the generality of the approaches remains very limited. There is a gap between the complex distribution of stresses found within the load-bearing structures of civil and military vehicles and available fatigue models, which are often developed for a single material system under a specific loading, such as uniaxial tension/compression.

In the past decade, several research groups have attempted to incorporate fatigue models within the framework of a structural finite element simulation. Among the available integrated composite fatigue prediction tools [1–4], the PFDM developed by Shokrieh and Lessard [1,2] has proven to be the most general in terms of allowing variable lay-up configurations, loading conditions, and geometries to be modeled. However, the available model parameter is restricted to a given unidirectional material system, and delamination was modeled implicitly (i.e., there was no separation between the plies in the finite element model).

5.1.4 PFDM and Its Implementation

Based on a modeling strategy originally developed by Adam et al. [16], the PFDM couples normalized models of fatigue life, residual stiffness, and residual strength [2,17] with standard FEA. Figure 5.1.1 provides a summary of the equations in the model and a flowchart for its implementation in ABAQUS user-defined material model (UMAT).

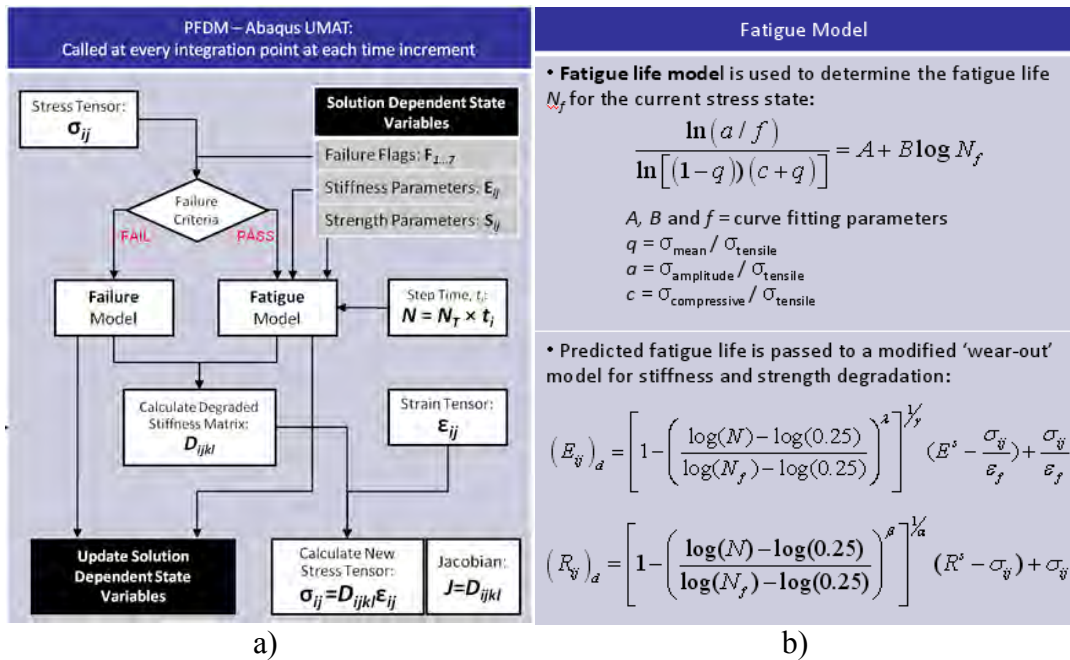


Fig. 5.1.1 a) A flowchart for the implementation of the PFDM using an ABAQUS UMAT. b) The empirical equations used in PFDM in determining fatigue life and stiffness/strength degradation.

5.1.5 Experimental

The PFDM parameters are available for AS4/3501-6 [2] and, therefore, the evaluation was carried out with AS4/3501-6. The AS4/3501-6 carbon/epoxy laminates were manufactured from prepreg using the standard autoclave cure

cycle at the University of Utah. Specimens were cut from the plates using a water-cooled, diamond-tipped circular saw. A 10-mm-diameter central circular hole was machined using a carbide drill bit.

Fatigue tests were conducted in the tension-tension regime with an R-ratio of 0 at 10 Hz. Three types of laminates were tested: $[0_2/90_2]_s$, $[45_2/-45_2]_s$, and $[0/90/0/90]_s$. DIC measurements were taken at prescribed fatigue cycle increments. Istra4D software by Dantec Dynamics was used for DIC analyses.

5.1.6 Evaluation of PFDM

The evolutions of the strain fields predicted by simulations are compared side by side with DIC measurements in Fig. 5.1.2a for $[0_2/90_2]_s$ at $P_{\max} = 25$ kN and $R = 0$. In these figures, the left half of the contours shows the results from the PFDM, while the right half presents the DIC results from the fatigue experiments. The predicted full-field strains agreed very well with the DIC measurements. In Fig. 5.1.2a, a black dotted vertical line near the root of the hole can be seen in the DIC measurement, which was caused by the loss of painted speckle pattern due to longitudinal splits at the specimen surface. Because of the loss of speckle pattern, a full-field DIC image was no longer available beyond $N = 9000$. Good correlations between the finite element prediction and DIC measurement were also observed in other load cases. Figure 5.1.2b compares the failure pattern between predictions and experiments. The agreement is reasonably good.

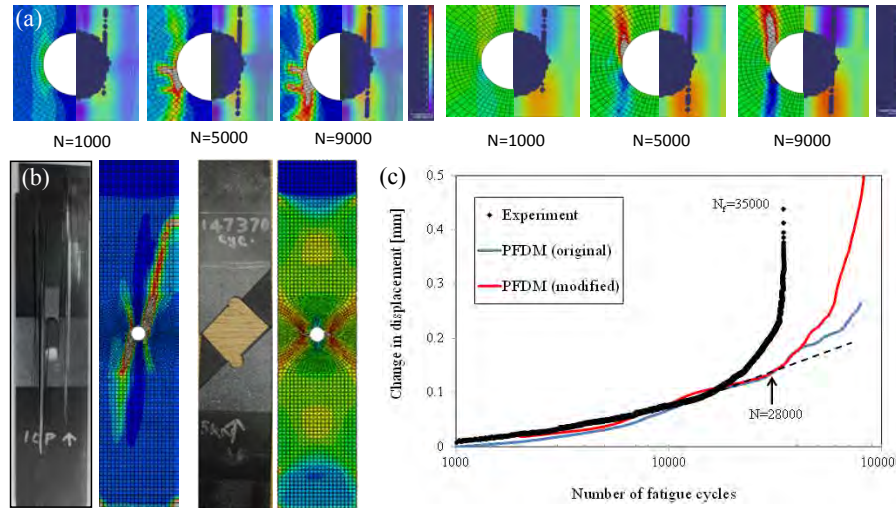


Fig. 5.1.2 Comparisons of PFDM prediction and experiments. a) PFDM vs. DIC: first principal strain (left) and shear strain (right) evolution with fatigue cycles on a $[0_2/90_2]_s$ laminate at $P_{\max} = 25$ kN and $R = 0$. b) Failure patterns of $[0_2/90_2]_s$ (left) and $[45_2/-45_2]_s$ (right) laminates. c) The displacement increases with the number of fatigue cycles, $[0_2/90_2]_s$ at $P_{\max} = 25$ kN and $R = 0$. The prediction-matched experiment up to the onset of delamination. The 2 simulations are shown in red (with modified values of A and B [19]) and blue (with values of A and B [2]).

Table 5.1.1 compares the number of cycles to failure by PFDM prediction and fatigue experiments for 3 types of laminates. The predicted fatigue life in general is longer than the experimental value. As shown in Fig. 5.1.2c, PFDM predicted the change in specimen compliance closely up to $N = 20,000$. The rapid increase in compliance in experiment was due to delamination. The overprediction in simulation is likely due to the lack of explicit modeling of delamination in the current model.

Table 5.1.1 Fatigue experiments and PFDM predictions of AS4/3501-6 with center hole

Laminate	R ratio	P_{max} (kN)	N_f experiment	N_f prediction
$[0_2/90_2]_s$	0	15	>200000	>200000
$[0_2/90_2]_s$	0	25	35000	80000
$[45_2/-45_2]_s$	0	5	147500	>200000
$[45_2/-45_2]_s$	0	6.5	1479	43000
$[0/90/0/90]_s$	0	28	>275000	134000

In summary, the PFDM is capable of predicting the strain redistribution and the change in global stiffness in a laminated composite structure being subjected to fatigue load up to the point when damage progresses into delamination (i.e., into the fourth stage of the 5-stage fatigue damage development process established by Reifsnider and his co-workers [18]). Although the PFDM approach requires an extensive material characterization program, once the model parameters are established, the PFDM can be a great asset in evaluating various design options against fatigue failure.

The PDFM has 2 major limitations: 1) Based entirely on data generated with a unidirectional laminate, the PFDM lacks the ability to model delamination in general laminates. Using the rapid increase in structural compliance as an indication of failure can improve the accuracy of fatigue failure prediction. To have a complete model for composite fatigue, it is necessary to include delamination. 2) The PFDM lacks of a proper algorithm to account for the effect of fatigue damage accumulation on cycle life under variable amplitude loading conditions (i.e., a cumulative damage rule). To this end, a novel degraded strength-based model for cumulative damage has been proposed [19].

5.1.7 Fatigue Testing with S-2 Glass/SC-15 Epoxy Composite


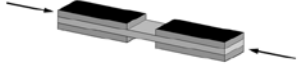
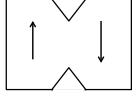
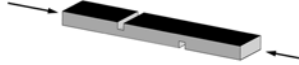
Plain weave S-glass/SC-15 epoxy composite panels of $24 \times 12 \times 0.2$ inches were manufactured at the Composite Vehicle Research Center lab through a vacuum-assisted resin transfer molding process. Table 5.1.2 presents the quasi-static properties of the manufactured composite. These properties are comparable with literature data.

Table 5.1.2 Mechanical properties of the manufactured S-glass/SC-15 composite

Test	Modulus (GPa)	Strength (MPa)	Test Method
Tensile	24.3 ± 1.1	477.9 ± 19.3	ASTM D3039
Compression	...	280.1 ± 27.8	ASTM D3410 modified
In-plane shear	2.24	59.0 ± 3.0	ASTM D7078

Assume the woven composite being in-plane isotropic, a total of 240 fatigue experiments are needed to establish the empirical relationships in the PFDM, as detailed in Table 5.1.3.

Table 5.1.3 Test matrix for PFDM model parameters for a woven composite

Loading	Specimen	Testing standard	Residual stiffness/strength	S-N curve
Tension		ASTM D3039/D3479	30	30
Compression		ASTM D3410 Modified	30	30
In-plane shear		ASTM D7078	30	30
Out-of-plane shear		ASTM D3846 modified	30	30
total			120	120

Note: Green cells = completed fatigue tests required for PFDM for S-glass/CS-15 epoxy composite.

The data under uniaxial loading have been generated at 4 different R-ratios: $R = 0.4, 0, -1$, and 10 . At each R-ratio at least 3 stress amplitude values were chosen. A minimum of 3 specimens were tested in fatigue at each value of stress amplitude. Figure 5.1.3a presents the master fatigue curves with $R = 0.7, 0.4, 0, -1$, and 10 . The results clearly indicate that the master curve under uniaxial loading needs to be separated into 2 curves: one for tensile-tension region and the other for tension-compression and compression-compression [21]. Figure 5.1.3b presents in-plane shear fatigue SN curves that have been measured with $R = 0, 0.2$, and 0.4 .

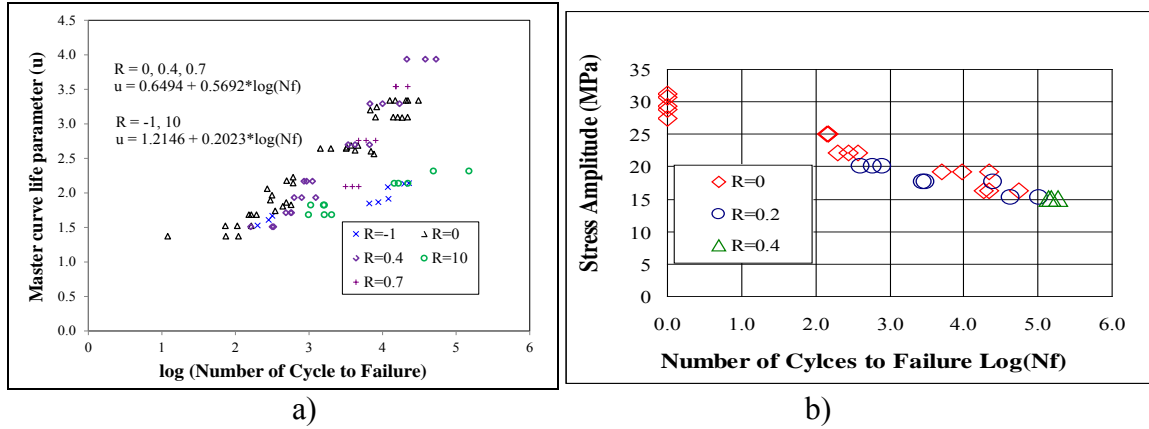


Fig. 5.1.3 S-2 Glass/SC-15 epoxy composite fatigue data. a) Master fatigue curve for uniaxial loading. b) In-plane shear with R-ratio of R = 0, 0.2, and 0.4.

The gradual degradation under tensile fatigue with R = 0 has been measured with specimens fatigued till 10%, 20%, 40%, and 60% of the fatigue life with a stress amplitude at 60%, 70%, or 80%. The results are presented in Fig. 5.1.4a and b for the tensile module and strength, respectively. Additional experiments are needed to extend the data for 80% of the fatigue life. The gradual degradation experiment under in-plane shear loading was just about to start when the funding for this project ended in August 2013.

In summary, about 45% of the fatigue tests required for PFDM for S-glass/CS-15 epoxy composite have been completed (shown in Table 5.1.3 in the cell shaded in green). Most of the fatigue tests were carried out by 4 undergrad students: Thomas Stevenson (2012–13), Eric Rightor (2012–13), Gabrielle Colby (2013), and Garrett Dunn (2013).

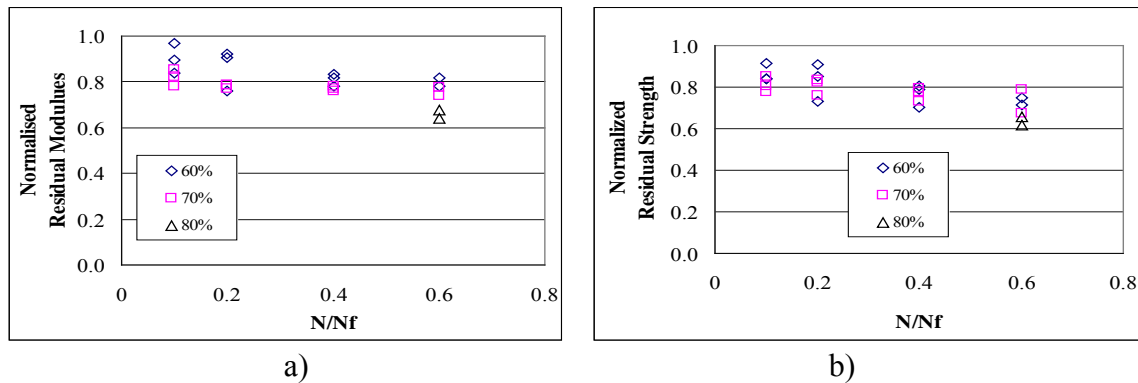


Fig. 5.1.4 Gradual degradation of a) the tensile modulus and b) tensile strength of S-2 Glass/SC-15 epoxy composite measured at R = 0

5.1.8 References

- [1] Shokrieh, M.M. and L.B. Lessard, “Progressive Fatigue Damage Modeling of Composite Materials, Part I: Modeling,” *Journal of Composite Materials*, 2000, 34(13), p. 1056–1080.
- [2] Shokrieh, M.M. and L.B. Lessard, “Progressive Fatigue Damage Modeling of Composite Materials, Part II: Material Characterization and Model Verification,” *Journal of Composite Materials*, 2000, 34(13), p. 1081–1116.
- [3] Lesko, J.J. and S.W. Case, “Multifunctional Composites for Next Navy Seaframes,” *Overall Project Final Report*, 2009.
- [4] Sihn, S. and J.W. Park, “MAE: An Integrated Design Tool for Failure and Life Prediction of Composites,” *Journal of Composite Materials*, 2008, 42(18), p. 1967–1988.
- [5] RW. Hertzberg, *Deformation and Fracture Mechanics of Engineering Materials*, 4th edition, John Wiley & Sons, Inc, New York, 1996.
- [6] R.J. Sanford, *Principles of Fracture Mechanics*, Prentice Hall, Upper Saddle River, NJ, 2003.
- [7] Hahn T., *Fatigue of Composites, Delaware Composites Design Encyclopedia, Vol.1*, Eds C Zweben, T. Hahn, TW Chou, Technomic Publishing Co. Inc, Lancaster, PA, 1989.
- [8] Talreja R, “Damage analysis for structural integrity and durability of composite materials,” *Fatigue & Fracture of Engineering Materials and Structures*, 29 (7), 481–506, 2006.
- [9] Reifsnider KL, Case SW, *Damage Tolerance and Durability of Materials Systems*, Wiley-Interscience, New York, 2002.
- [10] Reifsnider KL, *Damage and Damage Mechanics, in Fatigue of Composite Materials*, ed. Reifsnider KL, Elsevier, New York, 1991.
- [11] Post NL, S.W. Case, J.J. Lesko, “Modeling the variable amplitude fatigue of composite materials: A review and evaluation of the state of the art for spectrum loading,” *International Journal of Fatigue*, 30 (2008) 2064–2086.
- [12] Conway AR, Xiao X, “Finite Element Based Fatigue Modeling of Fiber Reinforced Composite Materials: A State-of-the-art Review,” *MSU Final Report for TACOM Cooperative Agreement Number W56HZV-07-2-0001*, 19 May 2010.

- [13] Allen, D.H., *Damage Evolution in Laminates*, in *Damage Mechanics of Composite Materials*, R. Talreja, Editor. 1994, Elsevier, New York.
- [14] Talreja, R., *Damage Mechanics of Composite Materials*. 1994, New York, Elsevier.
- [15] Tserpes, K.I., et al., “Fatigue Damage Accumulation and Residual Strength Assessment of CFRP Laminates,” *Composite Structures*, 2004, 63(2), p. 219–230.
- [16] Adam T, Fernando G., Dickson R.F., Reiter H., Harris B., *Fatigue Life Prediction for Hybrid Composites*. *International Journal of Fatigue*, 1989, 11(4), p. 233–237.
- [17] Conway A., Xiao X., “Progressive Fatigue Damage Modeling in CFRP Laminates using an ABAQUS UMAT Approach,” 26th ASC/Second joint ASC-CACSMA conference on composites, September 26–28, 2011.
- [18] Reifsnider, K.L., *Damage and Damage Mechanics*, in *Fatigue of Composite Materials*, Elsevier, New York, 1991.
- [19] Christopher Cater, Xinran Xiao, Arun Krishnan,” Cumulative Fatigue Damage Prediction of Composite Structures,” *Proceeding of ICCM19*, Montreal, July, 2013
- [20] Shokrieh, M.M. “Progressive Fatigue Damage Modeling of Composite Materials,” Thesis, 1996.
- [21] Xinran Xiao, Arun Krishnan, Thomas Stevenson, “Master Fatigue Curve For A Plain Weave Glass/Epoxy Composite,” *DURACOSYS 2012*, Brussels, Belgium, September 2012.

5.1.9 Publications

- [1] A. R. Conway, X. Xiao, “Implementing a Finite Element Module for Fatigue Damage Modeling in Fiber Reinforced Composite Materials,” *American Society for Composites 25th Technical Conference*, September 20–22, 2010.
- [2] Conway A., Xiao X., “Progressive Fatigue Damage Modeling in CFRP Laminates using an ABAQUS UMAT Approach,” 26th ASC/Second joint ASC-CACSMA conference on composites, September 26–28, 2011.
- [3] Krishnan A., Conway A., Xiao X., “Validation of a Progressive Fatigue Damage Modeling for composite laminates using Digital Imaging Correlation,” *Proceedings of the American Society for Composites 27th Technical Conference*, Fort Worth, Dallas, September 2012.

- [4] Xinran Xiao, Arun Krishnan, Thomas Stevenson, "Master Fatigue Curve for A Plain Weave Glass/Epoxy Composite," *DURACOSYS 2012*, Brussels, Belgium, September 2012.
- [5] Christopher Cater, Xinran Xiao, Arun Krishnan, "Cumulative Fatigue Damage Prediction of Composite Structures," *Proceeding of ICCM19*, Montreal, July, 2013.

5.2 Multiscale Damage Modeling

Christopher Cater and Xinran Xiao

5.2.1 Summary

This paper presents the development of a multiscale method for composite damage modeling, particularly at the free edge. The free-edge effect has been studied extensively at the mesoscale. In this work, it was explored at the scale of fiber and matrix with a top-down one-way coupling multiscale approach.

5.2.2 Introduction

Fiber-reinforced polymer (FRP) composites are hierarchical in nature, containing a variety of length scales that factor into the overall properties of the composite [1]. The various length scales associated with FRP composites can be classified as shown in Fig. 5.2.1.



Fig. 5.2.1 Diagram of the various length scales associated with a composite structure

The microscale constituents, and their relative volume fractions, could be adjusted along with a chosen reinforcement architecture (laminated, woven, braided) to obtain a composite best fit for the intended application. A consequence of the hierarchical nature of FRP, however, is an increased complexity, particularly in modeling the damage and failure due to a variety of mechanisms evolving at several length scales [2,3]. A multiscale approach is required to address the problem.

The objective of this work is to investigate the effect of microstructural parameters on the initiation of material failure at the free edge. Such parameters include the effect of microstructure (fiber/matrix properties, fiber volume fraction) on the potential sources of failure initiation (fiber/matrix separation, matrix cracking, etc.).

5.2.3 Literature Review

The free-edge stresses have long been studied in available literature. These span from approximate closed-form solutions [4–6] to 2-dimensional (2-D) generalized plane strain analysis using finite elements [7,8] and to advanced higher-order generalized laminate theories to capture the interlaminar stresses in a 2-D domain space [9–17]. A more comprehensive review can be found by Mittelstedt and

Becker [18]. Recent work has focused on developing 3-dimensional (3-D) models of the laminate free-edge problem utilizing submodeling techniques [19] or new finite element approaches [20]. While the previous research has been successful in characterizing the nature of the free-edge stresses with respect to changes in lamina orientation, geometry, and loading conditions, these analyses have been restricted to the mesoscale domain.

Multiscale investigations on free-edge stresses have started to appear in literature. Dustin and Pipes [21] compared the stress singularity associated with lamina interfaces at the free edge (mesoscale) to that associated with fiber termination at the free edge (microscale). Fiber/matrix interface cracking was also found to be an initiating damage mechanism of interply cracking in [+15/-15]_s laminates [22]. Other works include numerical simulations of free-edge stresses in single-fiber finite element models under simplified transverse tensile loading and uniform temperature change [23]. Multifiber models have also been investigated near a free edge by using domain decomposition [24], a superposition method [25], and dehomogenization methods [26–28]. These recent works have highlighted the stresses at the microscale (fiber/matrix) near the free edge and the criticality of defects; yet, they are still unable to address the following research questions: 1) What are the microscale stresses at various locations in the lamina and how do they influence damage initiation/evolution? 2) What is the coupled relation between mesoscale parameters (lamina thickness/orientation) and microscale properties (matrix properties, fiber volume fraction, fiber/matrix interface) in relation to initial laminate failure?

5.2.4 Approach

This work revisits the problem of free-edge effects in composite laminates using a combined multiscale modeling and computational micromechanics approach. A schematic of the proposed approach is illustrated in Fig. 5.2.2 for a laminate under uniaxial tension. At the macroscale, the material is assumed to be orthotropic and homogeneous at lamina level, and will experience a uniform displacement in the loading direction. This extensional displacement is prescribed to the mesoscale in the z-direction. At the mesoscale, a submodel is used to capture the free-edge stresses within the laminate. Each lamina is modeled as homogeneous and orthotropic with multiple layers of elements through its thickness. Using a semi-concurrent multiscale scheme, the mesoscale is linked to a microscale through the use of a representative volume element (RVE), which captures the local heterogeneity of the fiber/matrix constituents. Periodicity will be employed at

both the mesoscale and microscale models in the loading (z) direction (to allow for the analysis of off-axis laminates), and a free edge will explicitly be captured at the right, or x-, boundary.

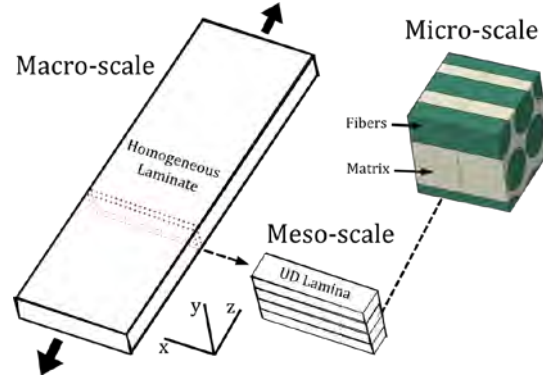


Fig. 5.2.2 Proposed multiscale workflow for the free-edge analysis of a laminated composite, including the effects of the local microstructure

The boundary conditions for the free-edge analysis at the microscale are given in Fig. 5.2.3 [29]. The mesoscale strains at regions of interest are used to provide the necessary displacement boundary conditions for the free-edge microscale analysis.

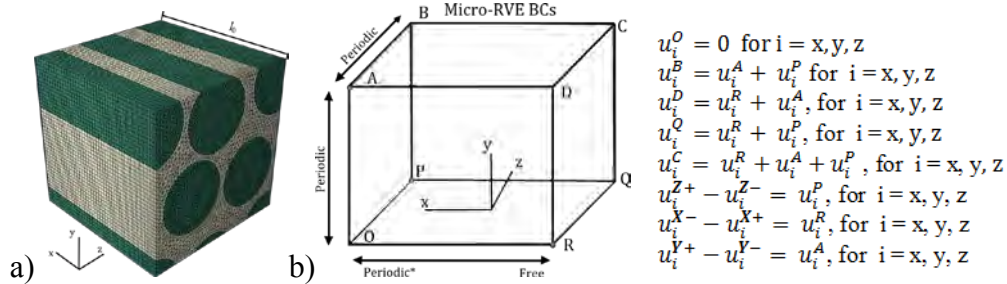


Fig. 5.2.3 a) The finite element mesh of the microscale RVE and b) the applied boundary conditions for the free-edge microscale analysis

5.2.5 Results and Discussions

The 2 composite laminates investigated were $[25/-25/90]_s$, and $[0_2/90]_s$. For each laminate, 2 specific regions of interest were investigated: 1) the interlaminar interface between the $-25/90$ or $0/90$ plies (interface micromodel) and 2) the midplane of the laminate (midplane micromodel).

5.2.5.1 $[25/-25/90]_s$ Laminate

The through-thickness, or (σ_y) , stress component from the mesoscale model is shown in Fig. 5.2.4. Figure 5.2.4a shows a region near the free edge, where the 2 elements used for extracting boundary conditions for the midplane and interface

micromodels are indicated. The strain components at the mesoscale integration points are presented in Fig. 5.2.4b, where the logarithmic strain presented in the 1-2-3 coordinate system is analogous to the x-y-z. The most notable difference between the 2 locations is the presence of large interlaminar shear strains, particularly in the 2-3 (y-z) plane at the interface, caused by the mismatch in extensional-shear coupling between the -25° and 90° plies.

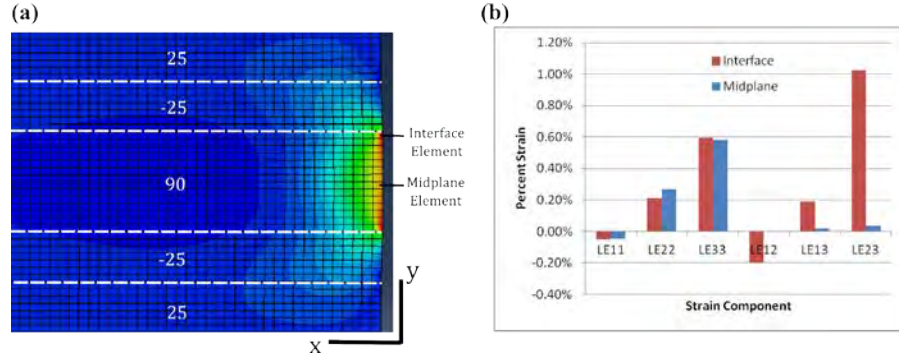


Fig. 5.2.4 a) Y-stress contour in the [25/-25/90]_s laminate under uniaxial tension (units are in megapascals). b) The strains extracted from the interface and midplane elements.

Figure 5.2.5 shows the matrix Tresca and first principal stress contours at the free edge (X^-) obtained with the micromodels. The predicted max shear stress at the interface was 33% higher than that found at the midplane. Additionally, the locations of highest max shear stress varied. The midplane micromodel had max shear stresses between fibers in the macro-loading (z) direction. The interface micromodel, on the other hand, showed high max shear stresses in locations both between proximal fibers as well as at an angle from the z-axis. The difference in high shear stress regions in the 2 micromodels was likely due to the increased shear strain (mesoscale) closer to the interlaminar interface.

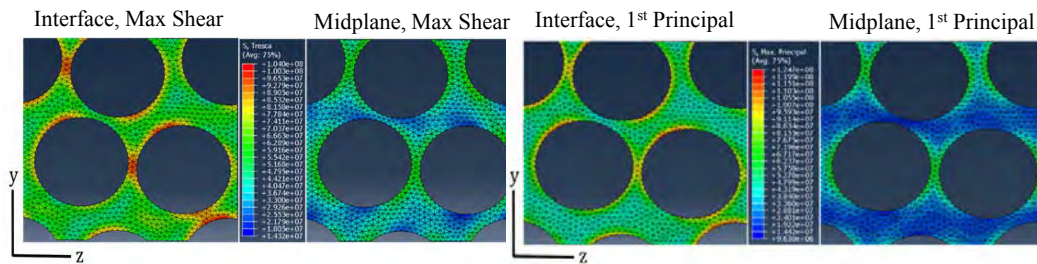


Fig. 5.2.5 Contours of the max shear stress and the first principal stress at the free edge (X^-) generated in the interface and the midplane micromodels in a [25/-25/90]_s laminate. (Units are in pascals.)

The first principal stress was 35% higher at the interface as compared to the midplane. For both locations, the regions of highest first principal stress at the free edge coincided with those containing the highest Tresca stresses, near the

fiber/matrix boundary. The direction of the first principal stress in these regions was normal to the fibers, indicating a potential source of opening (fiber/matrix debonding) failure.

The cohesive stress between the fiber and matrix was extracted from the micromodels. Figure 5.2.6 (a–c) plots the normal (τ_N), radial shear (τ_R), and axial shear (τ_A) stresses along the fiber length at the location that had the highest stress normalized to the matrix tensile strength (σ_t). As shown, a 20% higher maximum normal stress between the fiber/matrix is found at the interface as opposed to the midplane. The radial stress exhibited a singularity as the free edge was reached. The regions of highest radial shear stress between the fiber and matrix for both models were collocated with the max Tresca stress in the matrix. The max axial shear stress, Fig. 5.2.6c, was the only fiber/matrix stress component to be higher at the midplane than the interface. The axial shear component, however, vanishes to zero on the traction free edge, limiting its importance in fiber/matrix debonding at the free edge. Based on the results from the normal and shear stresses between the fiber and matrix, fiber/matrix debonding at free edge is likely to occur as a mixed-mode fracture caused by the local fiber/matrix material mismatch rather than driven solely by the macroscopic loading.

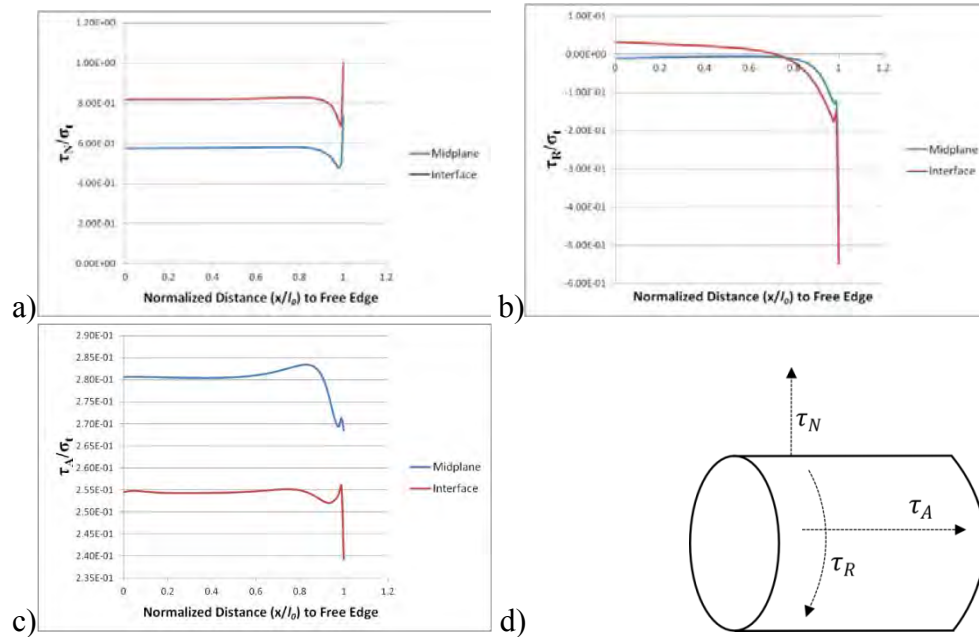


Fig. 5.2.6 a) Normal, b) radial shear, and c) axial shear tractions for midplane and interface elements along the fiber/matrix interface at the region of maximum value. The results are normalized with regard to the matrix strength, σ , and the distance to the free edge in the X-direction. d) Orientation of the cohesive traction directions.

5.2.5.2 $[0_2/90]_s$ Laminate

Figure 5.2.7a presents an excerpt of the free-edge stress contours for the normal, or y-stress, component. The mesoscale strains extracted from the interface and midplane elements are shown in Fig. 5.2.7b. Unlike the $[25/-25/90]_s$ laminate, the $[0_2/90]_s$ shows minimal shearing (zero for the y-z and x-z shear directions) and an 8% increase in the y-strain (shown as LE2).

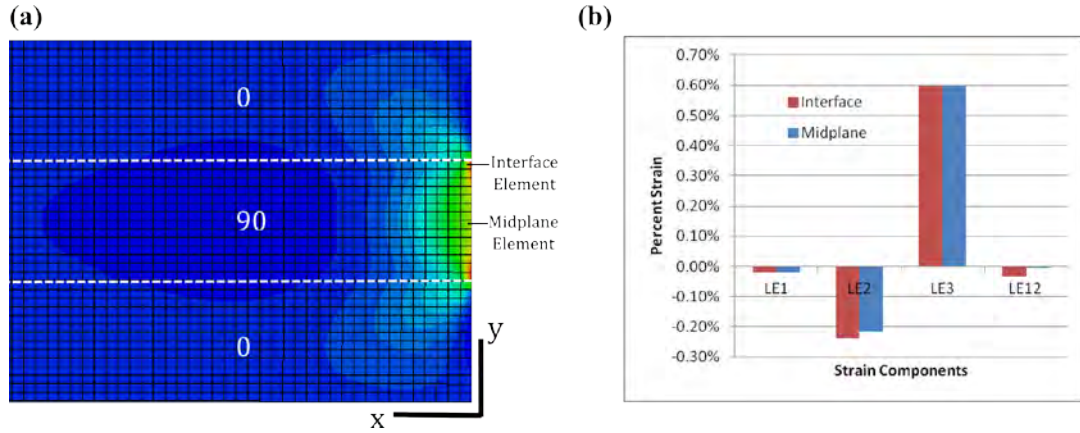


Fig. 5.2.7 a) Y-stress contours for the $[0_2/90]_s$ laminate and b) the mesoscale strains extracted from the interface and midplane elements

The microscale Tresca stress contours for the interface and midplane micromodels in the $[0_2/90]_s$ laminate match both qualitatively and quantitatively to those of the midplane results for the $[25/-25/90]_s$ laminate. Thus, these matrix shear stresses are a function of the material inhomogeneity, local fiber/matrix free-edge effects, and the macroscopic displacement (in the z direction) alone and not lamina-level shear stresses. In all cases, the matrix shear stress in the cross-ply laminate was less than those of the interface element micromodel for the $[25/-25/90]_s$.

The maximum principal stresses at the microscale in the $[0_2/90]_s$ laminate was about 14.7% higher than that in $[25/-25/90]_s$ laminate for their respective midplane regions (the angle ply laminate had higher values at the interface). The highest stress was found to align with the macroscopic loading (z-direction) between adjacent fibers and coincided location of highest high-fiber/matrix interfacial stresses.

5.2.6 Future Work

The proposed multiscale approach allows the investigation of the microstructure at the free edge in composite laminates. This approach will improve the understanding of the coupling between mesoscale characteristics, such as laminate

thickness and orientation, and the microscale characteristics, such as fiber and matrix properties, fiber volume fraction, and packing patterns, as well as address the complexities of material nonlinearity and residual stresses.

5.2.7 References

- [1] Degrieck J, Van Paepegem “W. Fatigue damage modeling of fibre-reinforced composite materials: Review,” *Appl Mech Rev* 2001;54:279.
- [2] Pineda EJ, Waas AM, Bednarczyk BA, Collier CS, Yarrington PW. “A Multiscale Progressive Damage and Failure Modeling Approach for Laminated Fiber Reinforced Composites,” *Adv Math Model Exp Methods Mater Struct* 2010:43–56.
- [3] Talreja R. “Damage analysis for structural integrity and durability of composite materials,” *Fatigue Fract Eng Mater Struct* 2006;29:481–506.
- [4] Pagano NJ, Pipes RB. "Some observations on the interlaminar strength of composite laminates," *Int J Mech Sci* 1973;15:679–92.
- [5] Pipes RB, Goodsell J, Ritchey A, Dustin J, Gosse J. "Interlaminar stresses in composite laminates: Thermoelastic deformation," *Compos Sci Technol* 2010;70:1605–11.
- [6] Goodsell J, Pagano NJ, Kravchenko O, Pipes RB. "Interlaminar stresses in composite laminates subjected to anticlastic bending deformation," *J Appl Mech Trans ASME* 2013;80.
- [7] Wang ASD, Crossman FW. "Some New Results on Edge Effect in Symmetric Composite Laminates," *J Compos Mater* 1977;11:92–106.
- [8] Raju IS, Crews Jr JH. "Interlaminar Stress Singularities at a Straight Free Edge in Composite Laminates," *DTIC Document*; 1980.
- [9] Robbins, JR. DH, Reddy JN. "Variable Kinematic Modelling of Laminated Composite Plates,"pdf. *Int J Numer Methods Eng* 1996;39:2238–317.
- [10] Nguyen V-T, Caron J-F. "A new finite element for free edge effect analysis in laminated composites," *Comput Struct* 2006;84:1538–46.
- [11] Nguyen V-T, Caron J-F. "Finite element analysis of free-edge stresses in composite laminates under mechanical an thermal loading," *Compos Sci Technol* 2009;69:40–9.

- [12] Lo SH, Zhen W, Cheung YK, Wanji C. "An enhanced global–local higher-order theory for the free edge effect in laminates," *Compos Struct* 2007;81:499–510.
- [13] Carreira RP, Caron J-F, Diaz Diaz A. "Model of multilayered materials for interface stresses estimation and validation by finite element calculations," *Mech Mater* 2002;34:217–30.
- [14] Diaz A, Caron J-F, Pedro Carreira R. "Software application for evaluating interfacial stresses in inelastic symmetrical laminates with free edges," *Compos Struct* 2002;58:195–208.
- [15] Tahani M, Nosier A. "Free edge stress analysis of general cross-ply composite laminates under extension and thermal loading," *Compos Struct* 2003;60:91–103.
- [16] Nosier A, Bahrami A. "Free-edge stresses in antisymmetric angle-ply laminates in extension and torsion," *Int J Solids Struct* 2006;43:6800–16.
- [17] Nosier A, Maleki M. "Free-edge stresses in general composite laminates," *Int J Mech Sci* 2008;50:1435–47.
- [18] Mittelstedt C, Becker W. "Free-edge effects in composite laminates," *Appl Mech Rev* 2007;60:217–45.
- [19] Romera JM, Cantera MA, Adarraga I, Mujika F. "Application of the submodeling technique to the analysis of the edge effects of composite laminates," *J Reinf Plast Compos* 2013;32:1099–111.
- [20] Esquej R, Castejon L, Lizaranzu M, Carrera M, Miravete A, Miralbes R. "A new finite element approach applied to the free edge effect on composite materials," *Compos Struct* 2013;98:121–9.
- [22] Lecomte-Grosbras P, Paluch B, Brieu M. "Characterization of free edge effects: Influence of mechanical properties, microstructure and structure effects," *J Compos Mater* 2013;47:2823–34.
- [21] Dustin JS, Byron Pipes R. "Free-edge singularities meet the microstructure: Important considerations," *Compos Sci Technol* 2012;72:933–7.
- [23] Andrews EW, Garnich MR. "Stresses around fiber ends at free and embedded ply edges," *Compos Sci Technol* 2008;68:3352–7.
- [24] Raghavan P, Moorthy S, Ghosh S, Pagano NJ. "Revisiting the composite laminate problem with an adaptive multi-level computational model," *Compos Sci Technol* 2001;61:1017–40.

- [25] Fish J, Wagiman A. "Multiscale finite element method for a locally nonperiodic heterogeneous medium," *Comput Mech* 1993;12:164–80.
- [26] Yan CK. *On homogenization and de-homogenization of composite materials*. Drexel University, 2003.
- [27] Chung S. *Effects of interlaminar stress gradients on free edge delamination in composite laminates*. Drexel University, 2003.
- [28] Dustin JS, Pipes RB. *Multi-Scale Modeling of Free-Edge Micro-Cracks with XFEM*, American Institute of Aeronautics and Astronautics; 2014.
- [29] Christopher Cater, Xinran Xiao, "Multiscale Investigation of Free Edge Effects in Laminated Composites," *Proceedings of the American Society for Composites 29th Technical Conference*, San Diego, CA, September, 2014.

5.2.8 Publications

- [1] Christopher Cater, Xinran Xiao, "Multiscale Investigation of Free Edge Effects in Laminated Composites," *Proceedings of the American Society for Composites 29th Technical Conference*, San Diego, CA, September, 2014.
- [2] Christopher Cater, Xinran Xiao, "Energy based multiscale modeling with non-periodic boundary conditions," *Proceedings of the American Society for Composites 28th Technical Conference*, College Station, PA, September, 2013.
- [3] Christopher Cater, Xinran Xiao, "Boundary conditions for the multiscale analysis of composites featuring local RVE damage," *Proceedings of the American Society for Composites 27th Technical Conference*, Arlington, TX, October 2012.

6. Thrust 3B: Multifunctional Composite Materials

Lawrence T Drzal

6.1 Summary

While investigating multifunctional composites, we have conducted research toward utilizing easy-to-manufacture, low-cost carbon nanoparticles to modify the material behavior of composites of interest to the US Army and Marines.

The objectives of this work are as follows:

- To demonstrate the ability to improve/control composite fracture and impact toughness by incorporating distributed and layered nanoparticles with functionalized elastomeric coatings.
- To define the multifunctionality gained by incorporating exfoliated graphite nanoparticles (xGnPs) into fiber-reinforced polymer (FRP).
- To transfer knowledge to other thrust areas to stimulate cross-disciplinary advances and to disseminate results externally.

In order to achieve the objectives of this project, 4 parallel material research efforts were undertaken.

- First, we have focused on the functionalization of the surface of the xGnP particles to allow them to be dispersed in various vinyl ester and epoxy resins. By manipulating the surface treatments and coatings, we can increase the toughness, strength, and blast resistance of these same resin systems.
- Second, additional properties can be enhanced by incorporating GnP and controlling its orientation and concentration. These properties include electrical conductivity, thermal conductivity, and barrier properties that can be enhanced by adding only a few percent of these particles to polymers.
- Third, the application of the GnP to the surface of conventional carbon-reinforcing fibers with a suitable fugitive sizing has been shown to improve the adhesion, transverse properties, and interfacial shear strength.
- Fourth, insertion of GnP to the interlaminar region of the composite as a thin film (paper) can be used to control and direct energy absorption under

blast and impact conditions, reducing the amount of structural damage to the composite.

These findings are detailed in the following subsections.

6.2 Functionalization of GnP

Graphene nanoplatelet particles (GnPs) are produced by a top-down approach using an intercalation and exfoliation approach. The resulting GnP consists of a few layers (~7–15) of graphene with a small concentration (~2%–3%) of oxygen groups located at the GnP edges (Fig. 6.1). The basal surfaces of GnP are hydrophobic, low-energy surfaces with no evidence of disruption of the graphene lattice. The edge groups are not optimized for interaction with the various thermoset resin chemistries of interest to the Army and Marines and require functionalization for achieving the best mechanical properties.

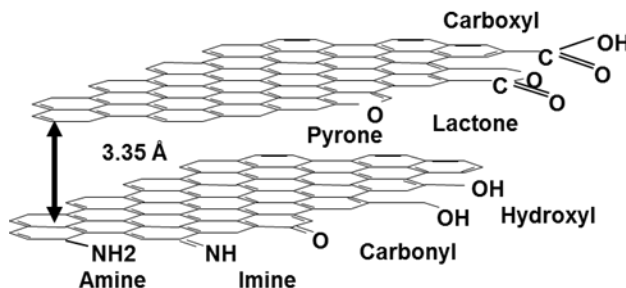


Fig. 6.1 Edge groups that can be attached an xGnP particle

6.2.1 Elastomeric Functionalization of GnP

We attached carboxy-terminated poly butadiene co-acrylonitrile (CTBN) rubber to the edges of GnP using Hypro CTBNX 1300-13 rubber (Hycar, USA) at concentrations ranging from 0.5 to 10 wt%. Composite specimens with various amounts of CTBN-functionalized GnP were mixed into a vinyl ester matrix (Derakane 411-350 cured with methyl ethyl ketone peroxide using a cobalt octoate catalyst). With the addition of pristine GnP, the flexural modulus increased as much as 45%, and the modulus still was 36% higher with 5 wt% CTBN–GnP. The flexural strength decreased over the base vinyl ester but only by 31%. More importantly, the un-notched Izod impact strength of 3% xGnP-g-Epoxy-Amine-GMA reinforced the 510A-40 vinyl ester nanocomposites increased about 230%, compared to neat vinyl ester and 3% xGnP reinforced vinyl ester nanocomposite (Fig. 6.2). The result strongly depended on the CTBN coating concentration and the CTBN-coated xGnP loading. Optimum results were achieved with 3% xGnP with 10 wt% CTBN. The notched Izod impact tests did

show the beneficial effect of elastomeric coating of the GnP nanoparticles. The coating of CTBN onto GnP particles was successfully scaled up to produce large batches (~75 g).

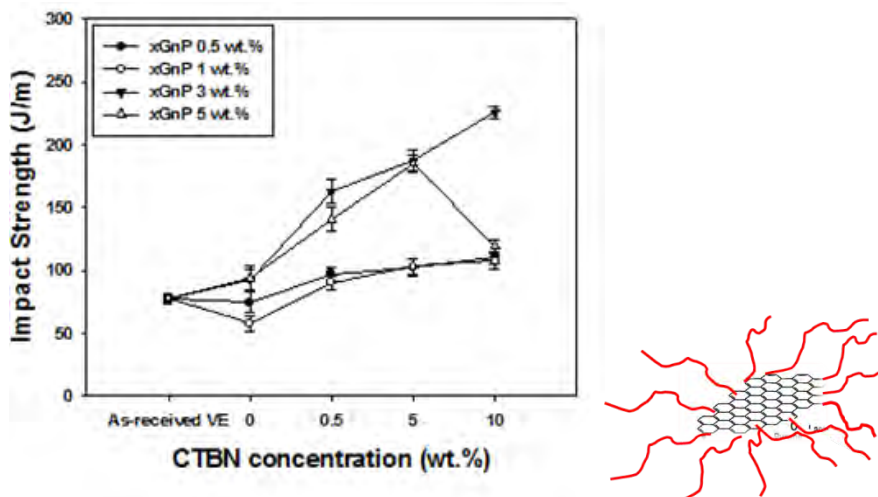


Fig. 6.2 Impact strength of xGnP vinyl ester composites

6.2.2 Edge Modification of GnP

Functionalization of xGnP basal plane as well as the edges via the covalent interaction of sugar azide with C=C of xGnP was investigated to increase the number of sites. Covalent functionalization of graphene nanoparticles (GnPs) was conducted, employing 2,3,4-Tri-O-acetyl- β -D-xylopyranosyl azide followed by fabrication of an epoxy/functionalized graphene nanocomposite (Fig. 6.3). Successful functionalization of GnP was confirmed via thermogravimetric analysis and X-ray photoelectron spectroscopy. Raman spectroscopy indicated that the functionalization was on the edge of graphene sheets, as the basal plane was not perturbed as a result of the functionalization. An epoxy/functionalized GnP composite system produced an increase in the flexural modulus (~18%) and glass transition temperature (~10 °C) compared to an unfunctionalized GnP-based epoxy composite.

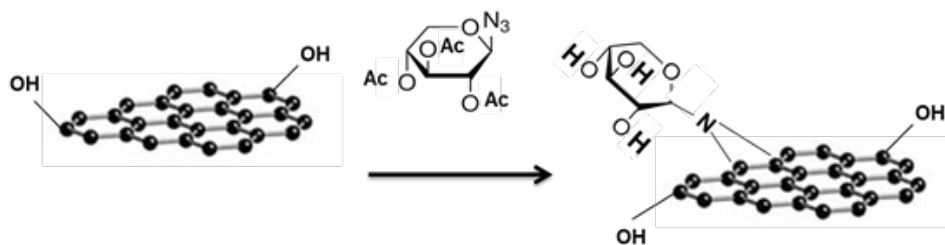


Fig. 6.3 Edge modification of an xGnP particle

6.2.3 Edge Stitching of GnP

GnP is subject to shear separation of the graphene sheets under mechanical loading. In order to achieve better properties, it would be quite beneficial to tie the adjacent graphene layers together so they do not shear apart layer by layer in a process called “edge stitching” (Fig. 6.4). The edge-stitched GnP can reinforce the epoxy matrix in a superior fashion compared to unmodified xGnP. Functionalization of GnP edges was investigated via the covalent interaction of diamine with the COOH group of GnP at the edges. Conversion of COOH group at the edges to COCl groups improves the reactivity; subsequent covalent functionalization of the COCl groups at the edges can be accomplished with diamine. An edge-stitched functionalized xGnP stack acts as a robust reinforcing filler as slippage between layers will be minimized. Epoxy composites made with 1% edge-stitched GnP produced a 58% increase in fracture energy as exhibited by the increase in strain-to-failure and increased area under the tensile stress-strain curve.

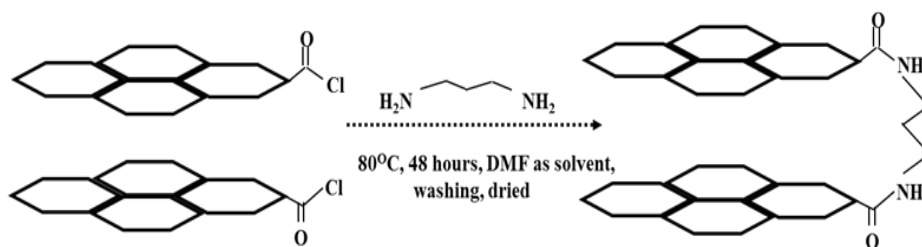


Fig. 6.4 Edge stitching of xGn particles

6.3 Coating of Carbon Fibers with GnP

The use of nanoparticles offered a very effective way to modify fiber-reinforced composites without altering the fiber-matrix composition. A problem occurs when a resin modified with nanoparticles is infused into the fiber preform. Filtering of nanoparticles takes place at the periphery of the composites as a result of the high tortuosity produced by the fibers and their small interfiber spacing. To be effective, the nanoparticles should be located in between the reinforcing fibers and near, but not on, the fiber surface. In a process developed at Michigan State University, a fugitive sizing can be used to coat the carbon fibers with the appropriate amount of nanoparticles prior to composite fabrication. A sizing has been formulated using a slightly cross-linked epoxy as the sizing vehicle in which GnP is suspended and applied to the fibers. The sizing is designed so that it swells and dissolves after impregnation and before vitrification, allowing the GnP to be confined to the fiber-matrix interphase. The single-fiber interfacial shear strength

test was used to evaluate the effectiveness of the GnP particles. It was found that 3 wt% of GnP in a 4 wt% sizing increased the carbon fiber-epoxy interfacial shear strength by 55% (Fig. 6.5).

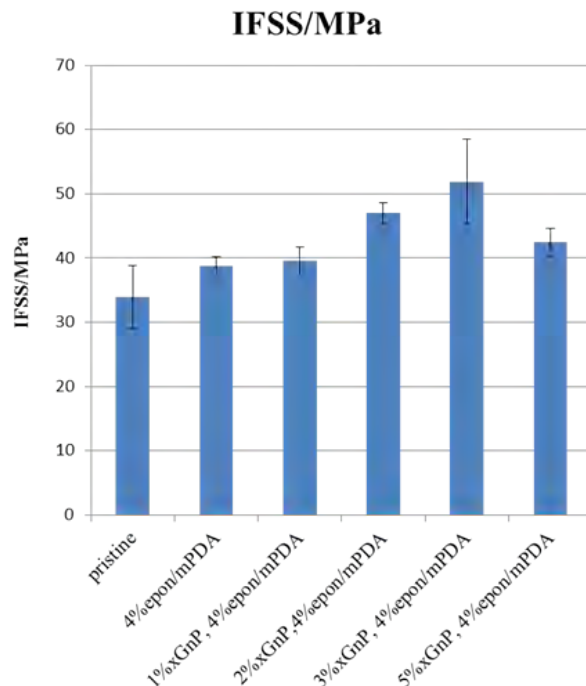


Fig. 6.5 Single-fiber interfacial shear strength for different GnP loadings

6.4 Fabrication of GnP “Paper” Films

Besides the coating of individual GnP particles onto the fiber surface, a goal was to produce a GnP film that could be easily applied between composite lamina. This would allow control of the interlaminar strength under static and impact conditions. A simple process was developed for producing GnP “paper” in thicknesses from 3 to 30 μm , with various xGnP sizes 1, 15, and 50 μm and coupled with and without a reactive elastomeric interlayer. The procedure consists of dissolving polyethyleneimine (PEI) in water followed by the addition of the requisite amount of GnP. A ratio of GnP:PEI:water of 1:0.5:1000 was found to give the best results. The PEI is a cationic polyelectrolyte that binds to the GnP and also is attracted to the water, creating a robust suspension. The suspension is slowly filtered on a micron-sized filter and then dried and pressed followed by a 300 $^{\circ}\text{C}$ heat treatment to decompose the PEI. The resulting “paper”, Fig. 6.6, is self-supporting with a high degree of GnP alignment in the plane. Samples as large as 30 \times 30 cm have been fabricated. The resulting GnP “paper” has an electrical conductivity of 6×10^5 S/cm (0.1 ohm/sq), which is about 1.5 orders of

magnitude less than copper—a density of approximately 1.6, which is approximately 15% that of copper, and a thermal conductivity of approximately 200 W/mK (in-plane) and 5 W/mK (through thickness), making it also a lightweight substitute for copper.

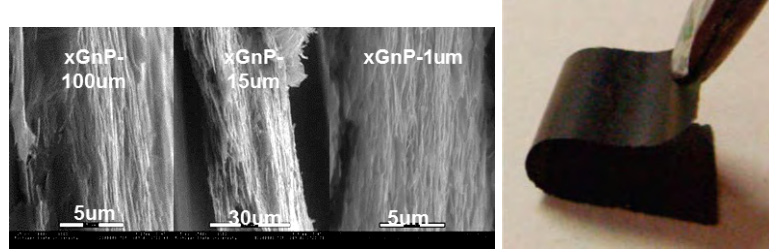


Fig. 6.6 XGnP papers

6.5 Interlaminar Toughening of Multilayer Vinyl Ester Composites Using GnP Paper

6.5.1 Moderate-Speed Impact Testing

Multilayer composite laminates using Shield Strand balanced weave fabric (Owens Corning S glass, 0.025 inch thick) and vinyl ester matrix (DER 411-350) from Ashland Specialty Chemical with 2-butanone peroxide (Luperox) and cobalt octoate accelerator were fabricated in 5- to 10-layer samples, 15 × 15 cm (Fig. 6.7). Low-speed impact testing was conducted at a speed of 12 m/s using a 50-mm tup.

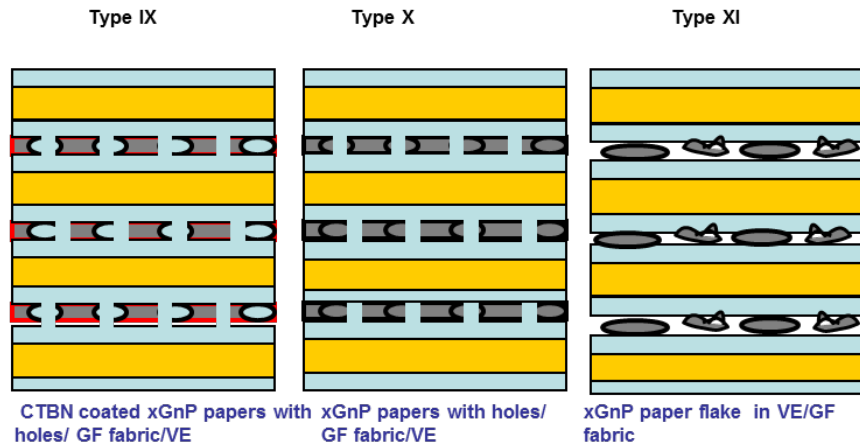


Fig. 6.7 Three types of laminates studied

Pristine or CTBN-coated GnP-5 μm, 25 μm, and hybrid 5/25 μm (40/60 wt%) papers were successfully made in a larger size (12 × 12 inches). Compressing the wet CTBN-modified xGnP paper at approximately 415 psi is necessary to produce an intact paper. The thickness of the CTBN-coated GnP paper can be controlled

from 50 to 400 μm by adjusting the GnP loading or suspension amount, but thinner papers will require alternative methods. GnP paper in thicknesses from 100 to 150 μm was inserted between layers of the laminate. Six-millimeter-diameter holes were inserted in the xGnP paper to allow resin flow to take place between lamina. The vinyl ester matrix concentration was important for mechanical properties, while the GnP concentration was more important for electrical properties. The composite with the greater fraction of holes showed higher flexural strength and modulus compared to other investigated composites. Among the CTBN coated xGnP paper reinforced multilayered composites Laminate construction type 11 gave the best combination of properties. The smaller CTBN coated GnP is the most effective. Laminate construction type 10 (80% porous ~ 24 micron GnP paper) showed the best impact energy without loss of mechanical properties.

In order to enhance the impact resistance between the GnP and vinyl ester, a greater degree of interaction between the xGnP and the resin is required through a larger number of functional groups and/or “strengthening” the xGnP. Incorporation of a Nylon 6 toughening polymer, which is compatible with the vinyl ester, shows better impact energy.

6.5.2 High-Speed Blast Testing

The “best” composite laminate was evaluated for blast damage resistance in collaboration with Professor Liu. The blast wave attained a speed of approximately 1000 m/s, and the sample size was $125 \times 125 \times 3.2$ mm thick. The samples tested were the a) glass fabric /vinyl ester composite, type-4 laminate construction; b) CTBN-coated GnP-15, type-11 laminate construction; and c) 40- μm GnP paper with 10% holes of 6-mm diameter in type-14 laminate construction (Fig. 6.8). The unmodified composite a) showed evidence of severe delamination, fiber and matrix cracking, and front surface damage due to the interaction of the high-temperature blast front with the front surface to the composite laminate. The incorporation of CTBN-modified GnP particles between lamina b) reduced damage and out-of-plane deformation under blast loading compared to the standard composition a). However, the incorporation of GnP “holey” paper between lamina c) reduced damage and out-of-plane deformation under blast loading. The holes produced controlled delamination perpendicular to the propagating blast front truncating through-the-thickness damage. The high thermal conductivity of the GnP paper in this composite appears to improve the damage reduction from interacting with the hot gasses at the blast front.

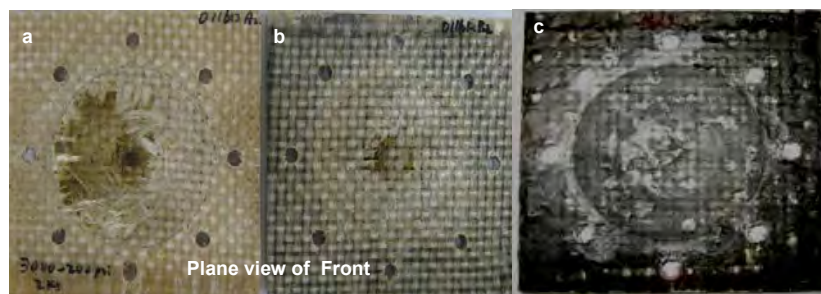


Fig. 6.8 Three composite samples (a, b, and c) after blast test

6.6 Future Directions

The insertion of GnP thin films fabricated with at least a 10% concentration of 6-mm holes can significantly reduce blast damage to a composite through controlled lateral delamination and high lateral heat conduction. Since numerous combinations and permutations of hole size, placement, and concentration exist for each laminate construction, a combined experimental and modelling program would identify the optimum material combinations to make blast-resistant composites for Army military vehicles.

6.7 Acknowledgments

The graphene nanoplatelets used in this research was supplied by XG Sciences, an exclusive licensee of the MSU process for producing GnP. XG Sciences has a production facility operating at 80 tons per year capacity and sells GnP at a bulk price of approximately \$15/lb depending on quantity and grade.

7. Thrust Area 3C: Vehicle Survivability and Occupant Safety

Dahsin Liu, Guojing Li, and Dan Schleh

7.1 Scaling Effects in Composites Subjected to Blast Loading

7.1.1 Introduction

The motivation behind this study is to identify the feasibility of predicting the behavior of prototype composite structures in the real-world operations based on the results obtained from laboratory coupon tests. If a relation or even a correlation exists between the prototype and the coupon counterparts, it can significantly ease the effort in composite structure design. However, issues concerning size scaling and loading complexity between coupon specimens and prototype structures must be carefully addressed. This study focuses on characterizing the scaling effect, if there is any, on the behavior of composites under high-pressure loading. No geometrical parameter in microscopic scale is considered. Only simple geometry, such as a plate, is of interest in the investigation.

7.1.2 Experimental Methods

Based on Buckingham's theory, a linear scaling was required for specimen dimensions. Having considered the availability of composite material and the capability of testing facility, we determined a dimensional scaling ratio of 3:5:10 for the investigation. Since the composite plates were made of plain-weave glass fabrics and an epoxy matrix, their thicknesses should be scaled similarly to that of the dimensional scaling ratio of 3:5:10. Accordingly, composite plates consisting of 3, 5, and 10 layers of fabrics were determined for the scaling investigation. The in-plane dimensions of the specimens were also chosen to be 75, 125, and 250 mm, following the scaling ratio of 3:5:10.

The specimen dimensions and thicknesses are summarized in Table 7.1.1. The true scaling ratio for the thicknesses from manufactured composites is not exactly the same as that based on the layer number. Besides, there was no scaling in the fiber microstructure, including fiber diameter, tow size, and cell size, since all composite materials were made of identical glass fabrics.

Table 7.1.1 Scaling parameters

Scaling Factor	(3)	(5)	(10)
Specimen Diameter (mm)	75	125	250
Specimen Thickness (layer number / mm)	3 / 2.01	5 / 3.12	10 / 6.07
Scaling Factor	(3)	(4.66)	(9.06)
Blast Tube Diameter (mm)	3.75	6.25	12.5
Blast Duration (ms)	6.3	11.7	23.3
Scaling Factor	(3)	(5.57)	(11.10)

7.1.3 Materials

A glass woven fabric and an epoxy matrix were chosen for this study because of their flexibility in making composite materials with various thicknesses and dimensions for scaling study. The glass fabric was of orthogonal plain weave, and the widths of both warp and fill tows were 9.5 mm (0.375 inches). There was no microscopic scaling because of the use of the fabric, i.e., the tow size for various specimen sizes was constant. In manufacturing composite specimens, an epoxy matrix was chosen for vacuum-assisted resin transfer molding processing based on its low viscosity and adequate properties.

7.1.4 Experimental Setup

For simulating blast loading, a facility named the Laboratory Blast Simulator (LBS) was designed, constructed, and used. As shown in Fig. 7.1.1, the LBS is based on a piston-assisted shock tube because of its capability to produce pressure waves with a high pressure of 210 MPa, a high temperature around 1,000 °C, and a high speed about 5 Mach. To achieve a blunt wave front, i.e., a shock wave, as those that occurred in real blasts, a second diaphragm was installed right before the blast tube to convert the 80-mm-diameter pressure waves generated in the shock tube into smaller pressure waves, such as 3.75-, 6.25-, and 12.5-mm-diameter ones used for the scaling studies.

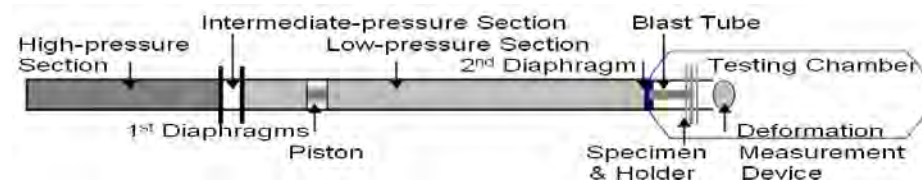


Fig. 7.1.1 Schematic (top) and photo (bottom) of the Laboratory Blast Simulator (LBS)

7.1.5 Testing and Results

Figure 7.1.2a shows the strain histories (based on the electrical resistance strain rosette attached close to the center of the 10-layer specimens), while Fig. 7.1.2b shows the deformation histories, based on projection moiré (see Fig. 7.1.2c), at the center of 10-layer specimens. The deformation results seem to be more consistent among different tests than the strain results. This may be because the strain gage is of a point technique and the associated results can be strongly affected by the local fiber structure, while the projection moiré is of a global technique and the associated results are less sensitive to the local material fluctuation. Both results seem to also reveal strong vibration and wave propagation during the high-pressure loading.

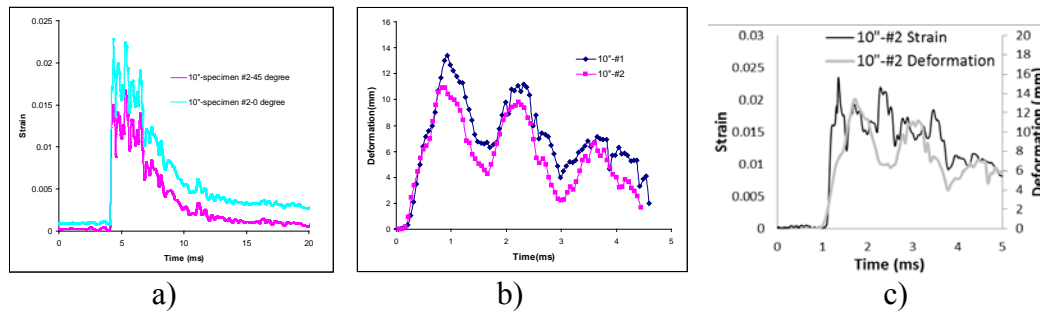


Fig. 7.1.2 Comparison of a) strain histories, b) displacement histories, and c) a) and b)

Fig. 7.1.2 presents strain and deformation histories on the same diagram for comparison for a 10-layer specimen. Artificial justifications were made for qualitative comparison. It is interesting to see a similar trend between the strain history and the deformation history for the 10-layer specimen. The results seems to also indicate the strong effect of the wave front. A shock wave front in the 10-layer specimen (250 mm in diameter) produces a steep strain increase while a gradually increased pressure wave front yields a mild strain increase in the beginning of strain history. The strain rates for all 3 cases can also be found from the strain histories. They are 230/s, 210/s, and 180/s for 3-, 5-, and 10-layer specimens, respectively. They are of medium strain ranges—even the pressure wave is as high as 105 MPa.

7.1.6 Conclusions

The high-pressure testing presented in this study is a unique technique for characterizing the stiffness of composite materials—so-called pressurizing stiffness. Three scaling cases in a ratio of 3:5:10 have been investigated. The strain rates of the cases studied were around 200/s. Considering experimental variations, we find that the experimental results show clear similarity among the

deformation histories of the 3 cases after they are scaled by the respective dimensional ratios, implying that there is no significant effect due to scaling among the 3 sizes studied. The stiffness scaling ratio of the 3 scaling cases is 3.00:5.14:9.22, similar to that of dimensional scaling ratio, further confirming the similarity among the 3 scaling cases.

7.1.7 Outcomes

1. Laboratory Blast Simulator (LBS) shown in Fig. 7.1.1 was developed.
2. Liu, Guojing and Liu, D., “Scaling Effect in Composite Plates Subjected to High-Pressure Waves,” *Proceedings of the American Society for Composites, Twenty-Sixth Technical Conference*, Montreal, Quebec, Canada, September 26-28, 2011.

7.2 Developing Triaxial Quasi-3-dimensional (TQ3D) Woven Composites with High-Impact Resistance

Dahsin Liu, Corey Anderson, and Kirit Rosario

7.2.1 Introduction

Owing to their high stiffness, high strength, high energy absorption, and low density, fiber-reinforced polymer-matrix composites have been considered to be excellent lightweight materials with high impact resistance. With flat fibers, laminated composites have excellent in-plane properties for structures subjected to membrane stresses. However, they are prone to out-of-plane loading, which can cause severe delamination. To improve delamination resistance, 2-dimensional (2-D) orthogonal woven fabrics have been used because the identical property between adjacent layers gives low delamination cause. Three-dimensional (3-D) braided composites should also have high delamination resistance owing to the fibers along the thickness. However, their in-plane properties may be compromised by these fibers.

7.2.2 Development of Q3D Fabrics

In designing a composite with coordinated high in-plane strength and high impact-induced delamination resistance, we have developed a quasi-3-dimensional (Q3D) woven composite because of its high degree of fiber straightness and minimum undulation (interlocking) between adjacent layers. A Q3D woven composite is not a 3-D composite since it does not have fiber yarns specifically oriented in the thickness direction. A Q3D woven composite, however, is a kind of 3-D composite because all the adjacent yarns interlocked with one another layer-by-layer to form a 3-D network. Fig. 7.2.1 (left) shows a through-thickness view of an interlocking network of a biaxial Q3D (BQ3D) woven composite. The degree of interlocking is minimal because each yarn only interlocks with the adjacent ones above and below it, hence retaining high in-plane properties due to a low degree of undulation. Because the interlocks are huddles to delamination propagation, they provide efficient delamination resistance to the Q3D composites.



Fig. 7.2.1 Side view of BQ3D woven composite in a) warp and b) fill directions (left), top view of TQ3D woven composite (center), and TQ3D braiding machine (right)

7.2.3 Manufacture of TQ3D Fabric

A triaxial Q3D (TQ3D) woven composite has 3 yarns with 60° between any 2 yarns. Fig. 7.2.1 (center) shows the top view of the TQ3D woven fabric. It looks like a 2-D triaxial woven composite. However, all the adjacent yarns in the thickness direction are interlocked with one another layer-by-layer through the thickness similar to the biaxial Q3D counterpart; hence, there is no interfacial layer with a pure matrix as those in laminated composites. A braiding machine, shown in Fig. 7.2.1 (right), has proved the manufacturability of the TQ3D fabric.

7.2.4 Testing Results

TQ3D woven composite has been proved to be superior to its laminated and 2-D woven counterparts. When a transverse force acts on it, the force can be efficiently distributed to all yarns in the plane and through the thickness via the tight interlocking system of the TQ3D weave, hence reducing potential local damage. Central impact results, given in Table 7.2.1, show that TQ3D composite $[0/60/-60]_4$ has 12.5% and 20% higher stiffness than its 2-D woven $[0/60/-60]_4$ and laminated $[0/60/-60]_4$ counterparts, respectively. The outstanding Q3D woven composites should be excellent candidate materials for high-performance combat vehicles exposed to constant dynamic impacts.

Table 7.2.1 Central impact induced bending stiffness

	Laminated	2-D Woven	Q3D
Average Bending Stiffness (kN/mm)	0.456	0.485	0.546

7.2.5 Outcomes

1. The Braiding Machine for Preparing TQ3D Fabrics, Fig. 7.2.1b.
2. Liu, Dahsin, C.D. Anderson, K. Rosario and C.-F. Yen, “Development of Quasi-three-dimensional Woven Composites for Higher Impact Resistance,” *SAMPE* 2012, Baltimore, MD, May 21-24, 2012.

7.3 Developing Projection Moiré Assisted Impact Testing

PIs: Dahsin Liu, Brandon Gulker, Ryan Lureau, and Dan Schleh

7.3.1 Introduction

Measuring dynamic contact forces, such as those due to ballistic impact and crash load, is critically important to the investigation of the material and structure involved. Until an instrumented projectile capable of measuring direct contact force due to high-velocity impact is available (it is recently developed by the author), an indirect measurement method may be sought. This study uses an optical method, so-called projection moiré or fringe projection, to measure the out-of-plane deformation of the nonimpacted surface of a structure component under low-velocity impact to recover the contact force history on the contact surface.

7.3.2 Experimental Setup and Results

As a method for measuring full-field out-of-plane displacement, projection moiré provides high measuring quality with a simple experimental setup, as shown in Fig. 7.3.1. Based on an image-processing program developed by Heredia and Patterson, this study presents the implementation of projection moiré in instrumented low-velocity impact testing. The moiré fringe patterns are shown in Fig. 7.3.2a, and the out-of-plane displacement profiles are shown in Fig. 7.3.2b.

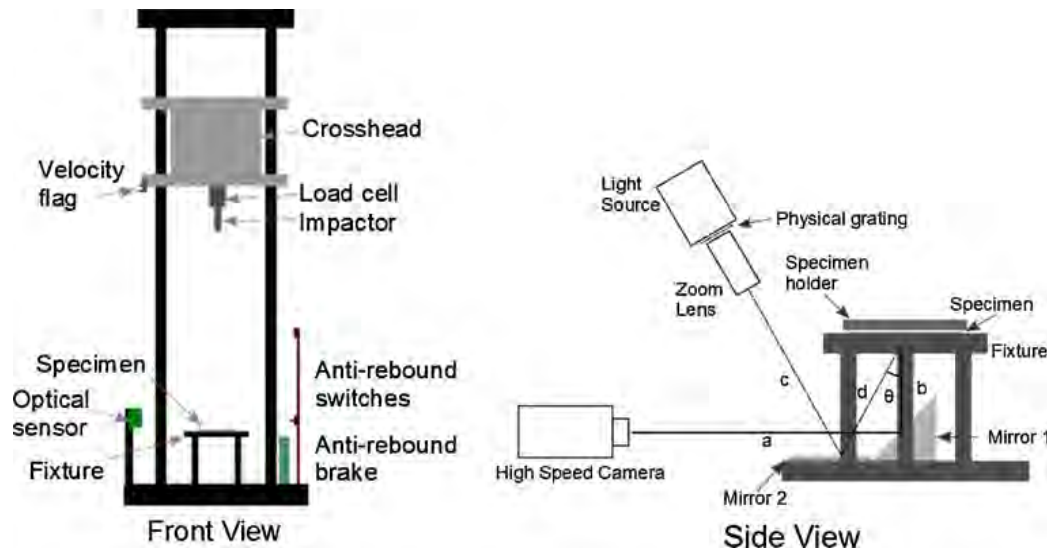


Fig. 7.3.1 Schematic of the overall view (left) and the detailed view (right)

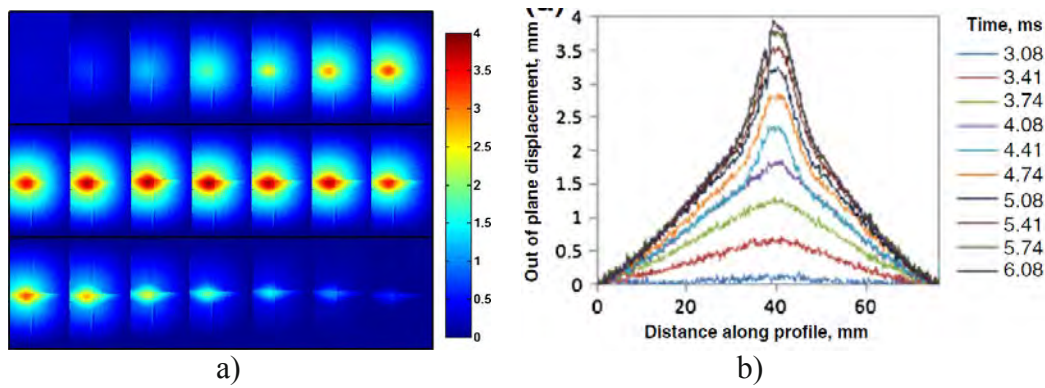


Fig. 7.3.2 a) Deformation contours from projection moiré for evenly spaced time step of 0.33 ms and b) profile lines for loading

7.3.3 Validation and Applications

Fig. 7.3.3a shows that the results from projection moiré agree reasonably well with those obtained directly from the load cell. In an attempt to better document the composite response to impact loading, the possibility of correlating the external out-of-plane displacement measurement with the internal delamination is also investigated. It is found that the recovered out-of-plane displacement is able to show the propagation of the internal delamination (the bumps in the central portion of the curves in Fig. 7.3.2b) of the composites under impact loading. Besides low-velocity impact, the projection moiré technique can also be extended for applications involving ballistic impact. Figure 7.3.3b shows a setup for such application.

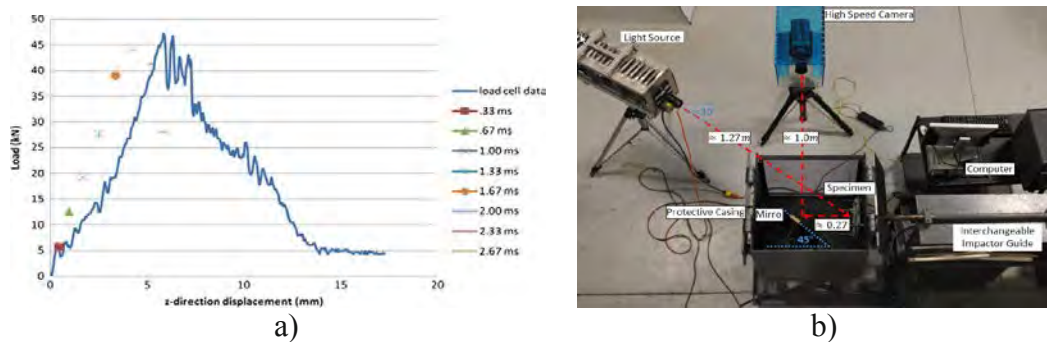


Fig. 7.3.3 a) Comparison between projection moiré (points) and load cell (continuous curve) and b) setup for ballistic impact

7.3.4 Outcomes

1. The Projection Moiré Assisted Ballistic Impact Testing System, Fig. 7.3.3b.
2. Schleh, D. and Liu, D., “Fringe Projection in Horizontal Impact,” *ICCES* 2013, Bellevue, Washington, May 20-27, 2013.
3. Gulker, B.G., Lureau, R. and Liu, D., “Investigation of Impact Response of Composites with Projection Moiré Enhancement,” *Experimental Mechanics*, 54(1), 35-43, 2014.

8. Thrust Area 6: Biomimetics

Srinivasan Arjun Tekalur

8.1 Enhanced Damage Tolerance in Biomimetic Ceramic Composites

8.1.1 Summary

The main objective of this thrust area was to use nature as an inspiration to design a new class of impact-resistant materials. There exists a great demand to generate lightweight, durable, and energy-efficient structural materials. In order to attain this goal, researchers have been studying design guidelines that exist in natural composites in order to implement the same in the development of synthetic composites. Of the innumerable structural biological composites found in nature, the nacreous layer in seashells has received significant attention owing to its unique architecture and exceptional mechanical properties. From the perspective of structural application, it is imperative to understand the suitability/applicability of these types of composites, should they be subjected to a variety of loading rates. In our investigations, we have attempted to address why bioinspired nacre-mimetic composites are well suited for impact loading conditions. We have also tried to understand the mechanics of these types of composites when subjected to impact loading and unearth the parametric attributes that are responsible for superior resistance. Additionally, interpretation is provided to understand what it takes for the nacreous layer to promote significant fracture resistance and weight reduction. Excerpts from our investigations provide beneficial guidelines in designing tough bioinspired composites at any length scale.

8.1.2 Introduction

Over the past decade, research has been aimed at producing composites that are both lightweight and durable via extracting design principles from structural biological composites (e.g., nacre). The inner shining layer in seashells is referred to as the nacreous layer and exhibits a staggered architecture in the form of an overlapping arrangement of mineral tablets in a soft polymeric matrix (Jackson et al. 1988; Sarikaya et al. 1990). What makes nacre an ideal model for biomimetic inspiration are 2 promising aspects: light weight and superior toughness (Barthelat and Espinosa 2007; Jackson et al. 1988; Kessler et al. 1996; Kamat et al. 2000; Sarikaya et al. 1990). Light weight is accomplished via embedding a polymeric matrix in a network of ceramic/mineral bricks, whereas toughness has been attributed to existence of a multitude of toughening mechanisms—namely, tablet

pull-out (Jackson et al. 1988), crack deflection through the biopolymer (Menig et al. 2000), platelet interlocks (Katti et al. 2005), presence of nanoasperities (Evans et al. 2000; Wang et al. 2001), diffusive tablet sliding (Barthelat et al. 2007) arising from tablet waviness, aragonite bridge reinforcements at interface (Song et al. 2003), relocking of tablets (Meyers et al. 2008) due to persistent contact of broken aragonite bridges, and synchronized deformation twinning of the nanoscale particles in ceramic bricks (Huang et al. 2011). All of the aforementioned factors contribute to both interfacial strengthening and fracture resistance in varying degrees of resistance. However, there is a lack in establishing the nexus between characteristic overlap length and optimized joint performance; and, thus, in order to address this aspect, we chose the nacreous layer in seashells as our model material for the purpose of investigation and in presenting the corresponding design guideline.

Existing literature studies associate global toughness of nacre on the basis of numerous mechanisms, including crack deflection by the biopolymer. In our investigation we have approached the problem from a local perspective by considering a unit cell. Multifarious factors are associated with toughening in nacre. In our current article, we hypothesize that crack deflection by the polymeric matrix is the most dominant mechanism associated with nacre. We have found that the toughness contribution associated with crack deflection is raised significantly via the choice of optimal overlap length in the unit cell. This, in turn, reduces the strain energy release rate ahead of the crack tip (locally) to the lowest possible extent apart from promoting tortuosity in subsequent unit cells. Using fracture mechanics concepts, we observed that the choice of characteristic overlap length is based upon minimization of strain energy release rate (SERR) ahead of crack tip. To illustrate this, we have developed an analytical model to calculate crack-tip fracture toughness. Note that in our current investigation, we are not trying to predict the global fracture toughness of nacre/nacre-mimetic composites. Additionally, the micromechanics associated with crack deflection and jump from one unit cell to another resulting in a highly tortuous crack path is also explained in the current article. From the context of biomimetics, valuable insights can be drawn with respect to microstructure-property relationship. Excerpts drawn from the current investigation would provide beneficial guidelines in the choice of characteristic/optimal overlap lengths, under quasi-static loading, while designing adhesively bonded structures.

8.1.3 Analytical Model

We develop our analytical model by taking into consideration a unit cell with plane strain infinitesimal deformations, as shown in Figs. 8.1b and c. The following assumptions are associated with the analytical model:

- 1-dimensional analysis based on “shear-lag” theory (Volkersen 1938).
- Participating members exhibit linear elastic behavior (ceramic bricks, biopolymer).
- Normal stress distribution in the ceramic bricks (no bending).
- Shear stress distribution in the biopolymer.
- Since the biopolymer is very thin compared to the brick thickness, the stress distribution is considered constant throughout the joint thickness (Luo and Tong 2004).
- There is no rotation of the transverse normal about the y-axis, which is directed into the plane of the paper.

The unit cell has been discretized into 4 elemental blocks (labeled 1 to 4). The total width of the mineral tablets is $2b$, and the thickness of the biopolymer is given by η . Local rectangular Cartesian coordinate systems for elemental blocks 1–4 have been defined as shown in Fig. 8.1b. It has also been assumed that there is no rotation of the transverse normal about the y-axis.

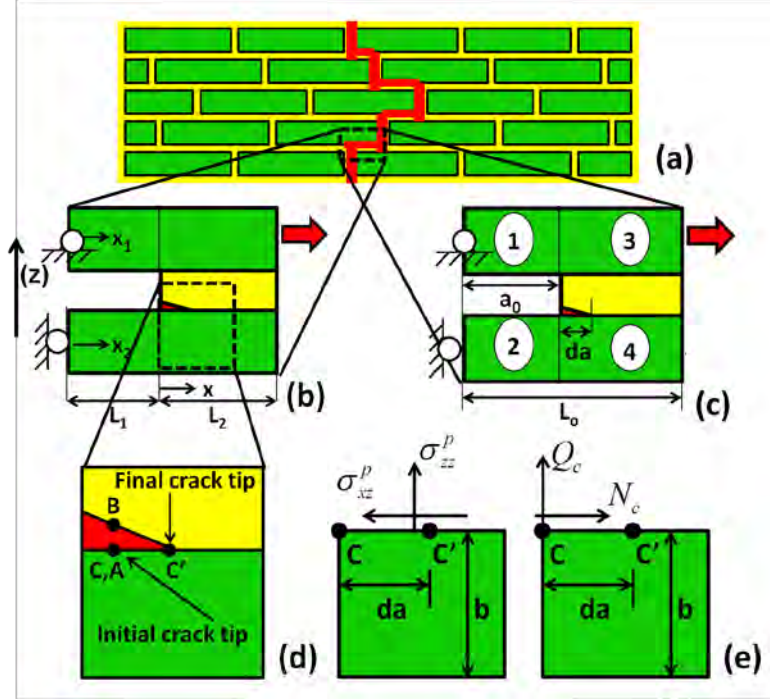


Fig. 8.1 a) Schematic of staggered architecture of calcium carbonate bricks (shown in green) in biopolymer matrix (shown in yellow); b) expanded view of the 2-dimensional (2-D) unit cell structure (with plane strain infinitesimal deformation) showing the precracked length (L_1) and instantaneous overlap length (L_2) and coordinate systems; c) expanded view of the 2-D unit cell structure (with plane strain infinitesimal deformation) highlighting the elemental blocks and the original overlap length (L_0); d) splitting of parent crack tip for SERR calculations; and e) schematic identifying shear and normal force resultants N_c and Q_c , respectively

8.1.3.1 Computation of Strain Energy Release Rate

Considering plane strain conditions, we assume a virtual crack tip displacement by an amount da . The parent crack tip at point C splits into points A and B, and translates to point C'. From Dugdale's cohesive strip model, SERR ahead of a crack-tip due to incremental increase in crack length is equivalent to work (or, rather, energy) required to close that infinitesimal increment and is thus computed as follows (Chadegani 2008):

$$G = \frac{W}{da} = \frac{1}{2da} \left[N_c (u_x^B - u_x^A) + Q_c (u_z^B - u_z^A) \right], \quad (8.1)$$

where W represents the work required to close the virtual crack. As shown in Figs. 8.1d and e, shear and normal force resultants, N_c and Q_c , respectively, can be computed as follows:

$$N_c = - \int_{x=0}^{da} \sigma_{xz}^p dx. \quad (8.2)$$

$$Q_c = \int_{x=0}^{da} \sigma_{zz}^p dx. \quad (8.3)$$

σ_{xz}^p and σ_{zz}^p are obtained from the solution of the problem prior to virtual crack-tip extension. u_x^A , u_z^A , u_x^B , and u_z^B are found out by solving the problem by substitution of overlap length $L_2 = L_o - a_0$ by $L_2 = L_o - a_0 - da$ and by using the following relations:

$$u_x^A = u_x^2 \Big|_{x_2=a_0-da}. \quad (8.4)$$

$$u_z^A = u_z^2 \Big|_{x_2=a_0-da}. \quad (8.5)$$

$$u_x^B = u_x^1 \Big|_{x_1=a_0-da}. \quad (8.6)$$

$$u_z^B = u_z^1 \Big|_{x_1=a_0-da}. \quad (8.7)$$

In order to investigate the effect of the SERR component that contributes to crack propagation, Eq. 8.8 can alternatively be written as

$$G_{II} = \frac{1}{2da} \left[N_c \left(u_x^B - u_x^A \right) \right]. \quad (8.8)$$

$$G_I = \frac{1}{2da} \left[Q_c \left(u_z^B - u_z^A \right) \right]. \quad (8.9)$$

$$MMP = \tan^{-1} \left(\frac{G_{II}}{G_I} \right). \quad (8.10)$$

8.1.4 Results and Discussion

To test the validity of the analytical model, the variation of shear stress at the mineral biopolymer interface is plotted for varying overlap lengths and pre-crack in the unit cell, as shown in Fig. 8.2. The properties of the mineral component in the nacreous layer (Barthelat et al. 2006) are $E1 = 144$ GPa, $E2 = 76$ GPa, $E3 = 82$ GPa, $G12 = 47.2$ GPa, $G13 = 25.6$ GPa, $G23 = 41.3$ GPa, $\nu12 = 0.44$, $\nu13 = -0.06$, $\nu23 = 0.18$, $2b = 0.5$ μm . The properties of the biopolymer layer in nacre (Xu et al. 2011) are $E_p = 10.57$ GPa, $G_a = 1.4$ GPa, $\nu_a = 0.45$, $\eta = 20$ nm. The observed overlap length in the nacreous layer is reported to be 1.67 μm (Espinosa et al. 2011).

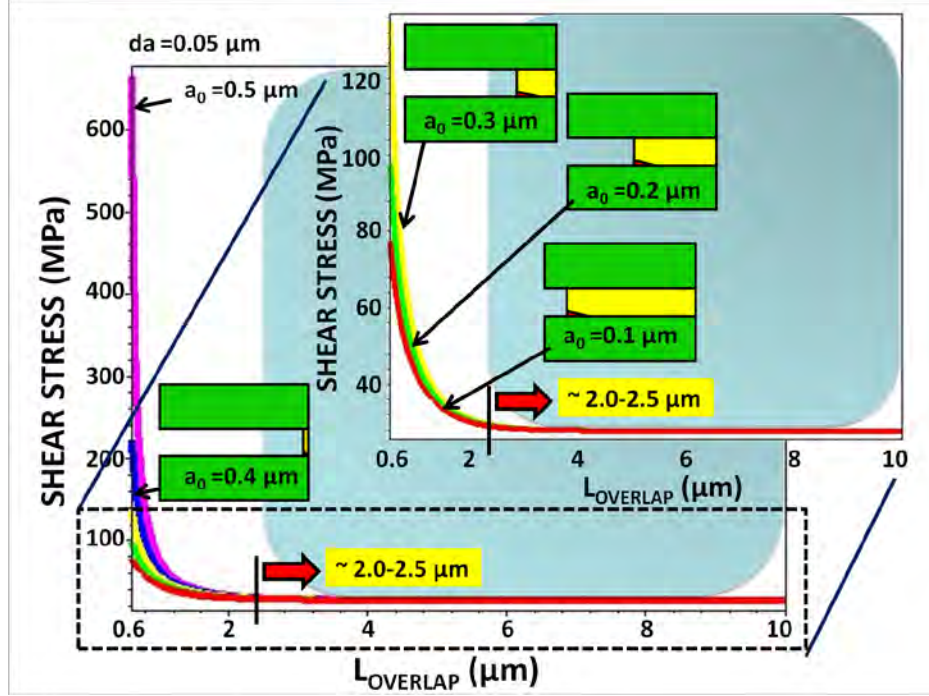


Fig. 8.2 Variation of interfacial shear stress (at the extremities of the overlap) as a function of varying overlap length and precrack. The figure in the inset shows the expanded view for lower shear levels in the unit cell.

When an external load is applied, interfacial shear stress attains a maximum value at the extremities of its overlap. As it can be seen from Fig. 8.2, the maximum interfacial shear stress (at the ends of the joint) attains a minimum value for overlap length exceeding 2–2.5 μm and reaches the shear strength of the biopolymer $\equiv 37 \text{ MPa}$ (Jackson et al. 1988). This observation is in direct agreement with those obtained by Dutta et al. (2013) in their estimation of characteristic overlap length in nacre under dynamic rates of loading, respectively. The highlighted light-blue region on the right-hand side of 2–2.5 μm might be considered the safe zone, as it contributes to a minimization of shear stress at the interface and optimizes inter-mineral load transfer via shear deformation of the intermediate biopolymer.

However, we hypothesize that under quasi-static rates of loading, an interplay exists between crack-tip fracture toughness and overlap length that not only leads to a state of minimization of SERR ahead of the crack tip but also influences crack tortuosity in the nacreous layer. Figure 8.3 shows the variation in SERR ahead of the parent crack tip with increasing crack length for reported overlap length in the nacreous layer. Fracture toughness of the organic matrix varies between 30 and 160 mJ/m^2 (Song et al. 2003), whereas intrinsic fracture toughness of the organic interface has an upper limit varying between 400 and

1,000 mJ/m^2 . This value is comparable to the mineral toughness in the nacreous layer. This wide variation can be associated with the viscoelastic nature of the biopolymer, the presence of nanoasperities, mineral bridges, or a combination of all the modes. Once the strain energy release rate ahead of the crack tip reaches its critical value, the crack will start to grow. As the crack size increases, the void within the unit cell also increases; therefore, the x-axis in Fig. 8.3 corresponds to (increasing) crack volume in the unit cell.

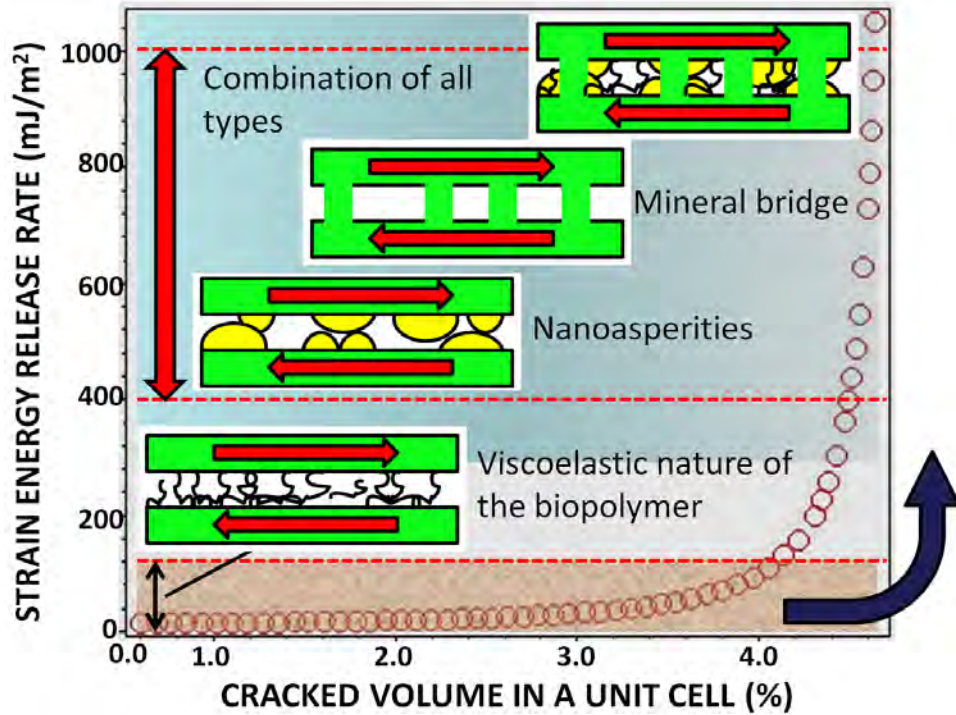


Fig. 8.3 SERR ahead of the crack tip with increasing crack in the unit cell

As mentioned previously, given the nature of biological composites, there are multiple critical toughness values reported that arise from one or a combination of multiple parameters (for instance, toughness associated with the viscoelastic nature of the biopolymer, nanoasperities, mineral bridges or a combination of a few or all of those). Figure 8.3 attempts to address how these barriers are passed over once the crack progresses and the strain energy release rate ahead of the crack tip starts increasing with progressive crack growth. de Gennes and Okumura (2000) and Okumura and de Gennes (2001) presented an analytical solution for a layered system based on the laminar architecture of the seashells. They also included the effects of a weaker stress concentration ahead of the crack tip in these materials in comparison to traditional isotropic elastic materials under quasi-

static loading conditions. However, the role played by the existence of characteristic overlap length on weakening the SERR associated with crack-tip advance in the nacre/nacre-mimetic materials has not been investigated yet.

8.1.5 Inferences

In our current investigation, an analytical model has been developed to explain the reason for the highly tortuous crack path in the nacreous layer in seashells. It has also been observed that characteristic overlap length exists in the nacreous layer, which contributes to the minimization of the strain energy release rate ahead of the crack tip and thereby allays fracture and raises fracture resistance against crack growth. Using the analytical model, we have investigated the crack growth conditions in detail, which explains the reason associated with crack jump/deflection at multiple interfaces. Excerpts drawn from the current study would provide beneficial guidelines in designing lightweight and tough adhesively bonded structures. In addition to what is shown above, our thrust area research has shown experimentally that these biomimetic composites are indeed superior in terms of mechanical properties and fracture resistance while compared with neat ceramic materials. Additionally, they offer weight savings of up to 45% when compared with using neat ceramic alone.

8.1.6 Outcomes

- 1) Abhishek Dutta, Srinivasan Arjun Tekalur, “Crack tortuosity in the nacreous layer – Topological dependence and biomimetic design guideline,” *International Journal of Solids and Structures*, v 51, January 2014, p325–335
- 2) Abhishek Dutta and Srinivasan Arjun Tekalur, “Synthetic staggered architecture composites”, *Materials and Design*, v46, April 2013, p 802–808
- 3) Abhishek Dutta, Srinivasan Arjun Tekalur and Milan Miklavcic, “Optimal overlap length in staggered architecture composites under dynamic loading conditions”, *Journal of Mechanics and Physics of Solids*, v61, n1, January 2013, p145-160
- 4) Abhishek Dutta, Simona Fermani, Srinivasan Arjun Tekalur, Abigail Vanderberg and Giuseppe Falini, “Calcium phosphate scaffold from biogenic calcium carbonate by fast ambient condition reactions”, *Journal of Crystal Growth*, v336, n 1, December 2011, p50–55

8.1.7 References

- Barthelat, F., Li, C.-M., Comi, C., Espinosa, H.D. 2006. “Mechanical properties of nacre constituents and their impact on mechanical performance,” *J. Mater. Res.* 21(8), 1977–1986.
- Barthelat, F., Espinosa, H.D., 2007. “An Experimental Investigation of Deformation and Fracture of Nacre-Mother of Pearl,” *Exp. Mech.* 47, 311–324.
- Barthelat, F., Tang, H., Zavattieri, P., Li, C.M., Espinosa, H., 2007. “On the Mechanics of Mother-of-Pearl: A Key Feature in the Material Hierarchical Structure,” *J. Mech. Phys. Solids* 55, 306–337.
- Chadegani, A., 2008. “Strain energy release rate of adhesive-bonded composite joints with a prescribed interlaminar crack,” M.S. Thesis-Wichita State University (<http://hdl.handle.net/10057/2023>).
- de Gennes, P.G., Okumura, K., 2000. “On the toughness of biocomposites,” *C. R. Acad. Sci. Paris, t.1, Ser. IV*, 257–261.
- Dutta, A., Tekalur, S.A., Miklavcic, M., 2013. “Optimal length scales in staggered architecture composites under dynamic loading conditions,” *J. Mech. Phys. Solids* 61(1), 145–160.
- Espinosa, H.D., Juster, A.L., Latourte, F.J., Loh, O.Y., Gregoire, D., Zavattieri, P.D., 2011. “Tablet-Level Origin of Toughening in Abalone Shells and Translation to Synthetic Composite Materials,” *Nature Comm.* 2, 173.
- Evans, A., Suo, Z., Wang, R., Aksay, I., He, M., Hutchinson, J., 2001. “Model for the Robust Mechanical Behavior of Nacre,” *J. Mater. Res.* 16, 2475–2484.
- Huang, Z., Li, H., Pan, Z., Wei, Q., Chao, Y.J., Li, X., 2011. “Uncovering high-strain rate protection mechanism in nacre,” *Sci. Rep.* 1, 148; DOI:10.1038/srep00148.
- Jackson, A.P., Vincent, J.F.V., Turner, R.M., 1988. *The mechanical design of nacre*. P. R. Soc. London B. 234, 415–440.
- Kamat, S., Su, X., Ballarini, R., Heuer, A.H., 2000. “Structural basis for the fracture toughness of the shell of the conch *Strombus gigas*,” *Nature*, 405, 1036–1040.
- Katti, K.S., Katti, D.R., Pradhan, S.M., Bhosle, A., 2005. “Platelet interlocks are the key to toughness and strength in nacre,” *J. Mater. Res.* 20, 1097–1110.

- Kessler, H., Ballarini, R., Mullen, R.L., Kuhn, L.T., Heuer, A.H., 1996. "A biomimetic example of brittle toughening: (I) steady state multiple cracking," *Comp Mater Sci.* 5, 157–166.
- Luo, Q., Tong, L., 2004. "Linear and higher order displacement theories for adhesively bonded lap joints," *Int. J. Solids Struct.* 41(22–23), 6351–6381.
- Menig, R., Meyers, M.H., Meyers, M.A., Vecchio, K.S., 2000. "Quasi-static and dynamic mechanical response of *Haliotis rufescens* (abalone) shells," *Acta Mater.* 48, 2383–2398.
- Meyers, M., Lin, A., Chen, P., Muyco, J., 2008. "Mechanical Strength of Abalone Nacre: Role of the Soft Organic Layer," *J. Mech. Behav. Biomed. Mater.* 1, 76–85.
- Sarikaya, M., Gunnison, K.E., Yasrebi, M., Aksay, J.A., 1990. "Mechanical property-microstructural relationships in abalone shell," *Mater. Res. Soc.* 174, 109–116.
- Song, F., Soh, A., Bai, Y., 2003. "Structural and mechanical properties of the organic matrix layers of nacre," *Biomaterials* 24, 3623–3631.
- Volkersen, O., 1938. *Die Nietkraftverteilung in zugbeanspruchten Nietverbindungen mit konstanten Laschenquerschnitten*, *Luftfahrtforsch* 15, 41.
- Wang, R., Suo, Z., Evans, A., Yao, N., Aksay, I., 2001. "Deformation mechanisms in nacre," *J. Mater. Res.* 16, 2485–2493.

9. Thrust Area 7: Design and Manufacturing

9.1 Experimental and Numerical Characterization of Flexural Behavior of Vacuum-Assisted Resin Transfer Molding (VARTM)-Infused Composite Sandwich Structures

R Umer, EM Waggy, M Haq, and AC Loos

9.1.1 Summary

Experimental and numerical characterization of sandwich materials is required to fully exploit the benefits offered by these materials and to efficiently design them. In this work, the flexural behavior of resin-infused composite sandwich structures was investigated. Panels with 2 different polyvinylchloride foam densities and thicknesses were studied. The S-2 Glass fabric face sheets were resin infused and bonded to the core in a single-step process using epoxy resin. Sandwich beams machined from the panels were subjected to 3- and 4-point bending tests. Finite element-based simulations predicting the flexural response of the sandwich panels were performed and compared with experiments. Excellent agreement in finite element-predicted failure loads and experiments were observed.

9.1.2 Introduction

Composite sandwich structures have been used extensively for aerospace, marine, and ground vehicle applications because of their high specific strength and stiffness, high shock resistance, and resistance to corrosion. Polymeric foams derived from materials such as polyvinylchloride (PVC), polyurethane, polyethylene terephthalate, expanded polystyrene slabs, etc., are gaining attention as the core material for sandwich structures for a variety of applications [1–3]. A wide range of characterization and resulting properties of sandwich structures are possible, depending on the materials used, their configurations, and testing schemes. An experimentally validated, simulations-based approach can eliminate the costly trial and error experiments and can be used as a design tool for such complex materials and structures [4]. Such an approach is being implemented in this work with respect to the flexural behavior of sandwich structures.

Although extensive research has been devoted to the flexural behavior of composite laminates, the flexural behavior of sandwich structures is limited [5–8]. In this context, considerable work describing the static flexural behavior of sandwich beams has been reported [9–11]. It is commonly agreed that the failure of a sandwich structure can occur through several damage mechanisms [12–17],

such as 1) skin compressive/tensile failure, 2) core shear failure, 3) delamination, i.e., skin–core debonding, 4) local skin wrinkling, and 5) core indentation. One of the main issues limiting the accurate modeling of the sandwich structures is the intrinsic anisotropy and the non-homogeneity of the sandwich structures [18]. This issue can be overcome with detailed experimental characterization and accurate modeling. Additionally, it is reported that the presently available data on mechanical properties necessary to allow a correct and reliable design of complex sandwich structures is not sufficient [18]. One way to address this issue is to develop and implement experimentally validated simulations. A limited number of critical experiments are performed, and computational simulations that accurately and realistically model the behavior of the components are created. These simulations are validated by the experiments and then can be used as a design tool to extrapolate the experimental matrix. The use of this approach is attempted in this work, and the developed simulations are compared with actual experimental response.

Considerable work on theoretical and numerical analysis of sandwich panels exists and is well documented [18]. Also, the failure modes of sandwich beams under static [8,19,20] and cyclic loads [21] have been investigated. The numerical models that study the progressive collapse of the sandwich structures have also been reported [19–24]. The data reported in the literature show a large variation depending on the type of materials used, material and experimental configurations, parameters sought, and applications. Nevertheless, it is commonly agreed [18–24] that the accuracy of the simulations depends on the realistic modeling and accurate properties of the constituents. Hence, the simulations performed in this work use experimentally characterized material properties and are compared with experimental flexural response of the various experimental tests.

In this work, sandwich panels created with foams having 2 different densities and thicknesses were studied. Additionally, the thickness of face sheets (skins) was varied depending on the core thicknesses and the test setup as per ASTM C-393 requirements. Finite element–based simulations using experimentally characterized material properties were used to study the flexural behavior of the vacuum-assisted resin transfer molding (VARTM)-infused composite sandwich panels. The details on materials, VARTM infusion, sample preparation, testing schemes, simulations, and results are provided in the following sections. Overall, experimentally validated simulations can be used to predict the performance of novel sandwich panels beyond the existing experimental data and hence can be used as an efficient design tool.

9.1.3 Experiments

9.1.3.1 Materials

The reinforcement used for the face sheets was Owens Corning ShieldStrandS, S-2 Glass plain weave fabric with an areal weight of 818 g/m². The core material consisted of DIAB Divinycell [25] nonporous H130 and H250 PVC foams with thicknesses 25.4 and 12.7 mm, respectively. The distribution medium was AIRTECH Advanced Materials Group Resinflow 60 low-density/high-density polyethylene blend fabric. The resin used was 2-part toughened epoxy—namely, SC-15 obtained from Applied Poleramic.

9.1.3.2 Resin Infusion

The sandwich panels were fabricated using VARTM. A steel mold (609.6 × 914.4 mm) with point injection and point vent was used to fabricate 304.8- × 609.6-mm sandwich panels. A schematic of the VARTM layup is shown in Fig. 9.1.1. The number of layers of glass fabric in each face sheet depends on the thickness of the foam core. For 25.4-mm-thick foam panels, 4 plies of glass fabric were used on both of the face sheets, but for the 12.7-mm-thick foam, only 2 plies on each side were used, according to design criteria specified in ASTM C-393 [26]. Two layers of resin distribution medium were used over the top face sheet, and only one layer of distribution was used under the bottom face sheet. This was done to equalize the resin infiltration times for the top and bottom face sheets, resulting in uniform flow and reproducible manufacturing of the panels. After the materials were placed, the mold was sealed using a vacuum bag and sealant tape. The mold was then infused under vacuum with a pressure of 1 atm. The resin-infused sandwich panel was cured in a convection oven at 60 °C for 2 h and postcured at 94 °C for 4 h.

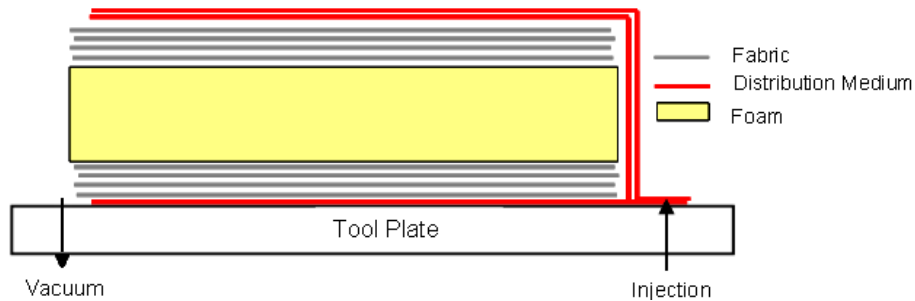


Fig. 9.1.1 Layup for the VARTM process

9.1.3.3 Experimental Test Setup and Procedure

The 3-point flexural test specimens were prepared in accordance with ASTM C-393 standards [26]. The 3-point flexural test uses a 150-mm support span with the center loading. The specimen length and width was 200 and 75 mm, respectively. The 4-point flexural test specimens were prepared in accordance with ASTM D-7249 standards [27]. The 4-point flexural test specimens have a 560-mm support span length, with a loading span length of 100 mm. The specimen length and width were 610 and 75 mm, respectively. Both 3- and 4-point flexural tests were conducted on panels containing both H130 (25.4-mm thickness) and H250 (12.7-mm thickness) foams. A schematic of 3- and 4-point flexural tests is illustrated in Fig. 9.1.2.

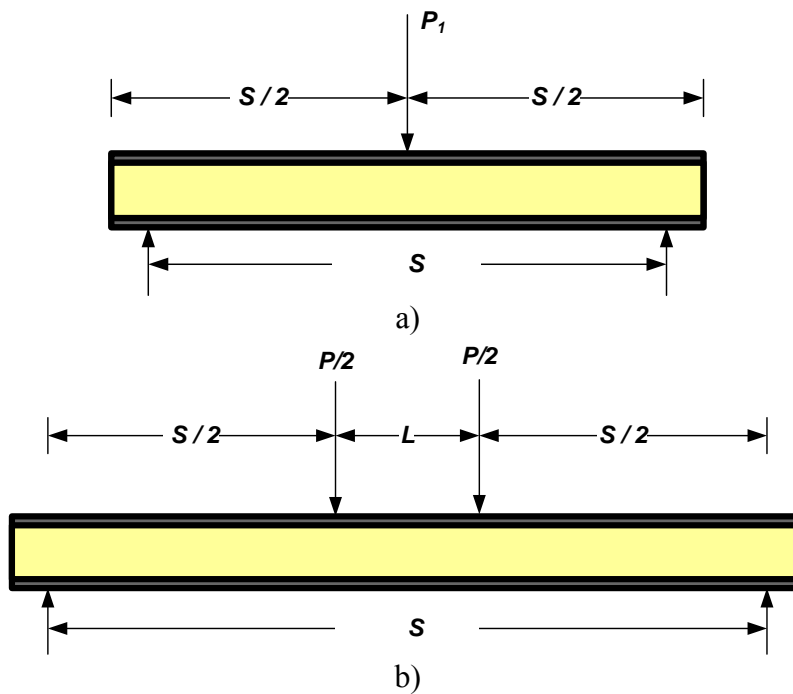


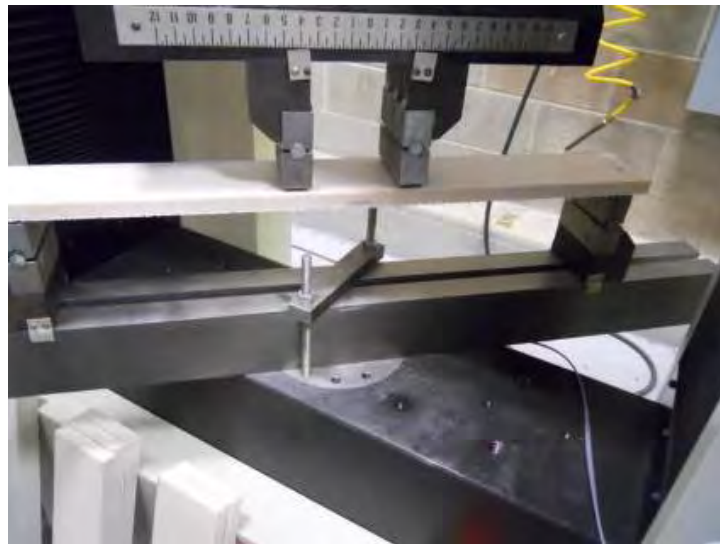
Fig. 9.1.2 a) 3-point loading ASTM C393 standard configuration, $S = 150$ mm and b) 4-point loading ASTM D7249 long beam standard configuration, $S = 560$ mm, $L = 100$ mm

The flexural testing was performed on an MTS Insight 100 material testing workstation. Figure 9.1.3 shows the experimental setup for both 3- and 4-point tests. All the supports and loading bars used cylindrical pivots, as shown in Fig. 9.1.4. The test setup consisted of a base comprising a steel beam with a T-slot that allowed movement of support blocks to vary the span. The support block holds 12.7-mm-diameter steel bars (cylindrical pivot) that allow free rotation of the specimen at the loading and support points. Rubber pressure pads were used on the flat steel loading block to prevent any local failures at the face sheets. The

rubber pads having a Shore-A durometer of 55 and thickness of 3 mm were glued to the loading block to prevent slipping. The loading and support bars were 75 mm long, equaling the width of the test specimens. A laser extensometer was used to measure the midspan deflection of beams.



a)



b)

Fig. 9.1.3 Setup of a) 3-point and b) 4-point bending fixture



Fig. 9.1.4 Cylindrical pivot loading and support bar

The test specimens were carefully placed on the support bars to ensure that the loading was symmetric and that the sample was level. The test was performed at a loading rate of 6 mm/min, and data were recorded at a sampling rate of 2.5 Hz. An average preload force of (100 N) was applied initially to ensure that the loading bar was also level and symmetric with the test specimen. The specimens were tested until failure. The flexural stiffness was then calculated as per procedure described in ASTM standard D 7250 [28].

9.1.4 Numerical Modeling

Numerical simulations were performed to evaluate the flexural behavior of sandwich panels tested in this study. In this work, numerical simulations were conducted using Micross [29], a finite element–based multiscale analysis tool for the modeling of bending and in-plane shear tests of sandwich panels. Micross is a part of the commercially available finite element package Digimat [30]. The software creates 3-dimensional models of the sandwich panels with inputs of material properties and dimensions of the facing and the core. The number of layers and orientations of the laminae in the skins were also provided as an input. Also, the loading and boundary conditions, including the width of the loading pads, were provided as input for both 3- and 4-point loading configurations. The facing sheets were modeled as a linear elastic orthotropic material. The tensile properties of the facing sheets were experimentally characterized, and the fracture

properties were obtained from literature [31], corresponding to the materials similar to the ones used in this work. The properties of the core were also modeled as linear elastic material and were obtained from the manufacturer [25]. Tables 9.1.1 and 9.1.2 provide the summary of material properties used in the simulations.

Table 9.1.1 Foam core properties [25]

Foam	Density (kgm⁻³)	Tensile Modulus (MPa)	Tensile Strength (MPa)	Shear Modulus (MPa)	Shear Strength (MPa)	Compressive Modulus (MPa)	Compressive Strength (MPa)
H130	130	175	4.8	50	2.2	170	3.0
H250	250	320	9.2	104	4.5	300	6.2

Table 9.1.2 Material properties of plain weave S-2 Glass/SC-15 epoxy laminates

Young's Modulus (Ex^a, Ey^a, Ez) (GPa)	24.85, 24.85, 11.04
Shear Modulus (Gxy, Gyz, Gxz) GPa	2.67, 1.97, 1.97
Poisson's Ratio (xy, yz, xz)	0.11, 0.18, 0.18
Axial Tensile Strength^a (MPa)	490
Axial Compressive Strength (MPa)	238
Transverse Tensile Strength (MPa)	58
Transverse Compressive Strength (MPa)	58
Shear Strength (MPa)	62

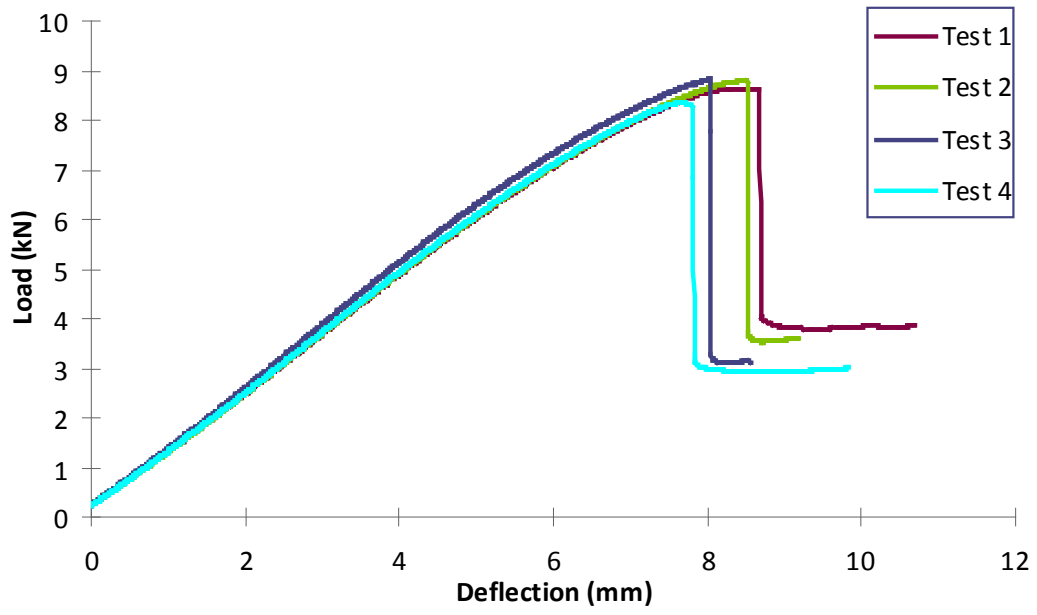
^a Experimentally measured, remaining data obtained from Deka et al. [31]

Microcross automatically generates the finite element mesh for the assembled sandwich panel corresponding to the loading and the boundary conditions. The mesh consists of hexahedral elements for the core and shell elements for the facing sheets. The core and facing elements share the same nodes at the interface. The interaction at the interface is simply tied and does not include sliding conditions or cohesive zones. The models had approximately 3,200 elements with an average element size of 5 mm. Also, the failure theories to predict skin failure based on maximum allowable stresses and global failure theories based on Tsai-Wu, Tsai-Hill, and Azzai-Tsai-Hill theories are built in the software to predict the failure loads, stress/strain states, and the locations of failure. In this work, the flexural response corresponding to the experimental tests were simulated. Hence, four cases were simulated: a) 3-point bending with 12.7-mm H250 foam, b) 3-point bending with 25.4-mm H130 foam, c) 4-point bending with 12.7-mm H250 foam, and d) 4-point bending with 25.4-mm H130 foam. The peak loads at failure and the flexural response were compared with experiments.

9.1.5 Results and Discussion

9.1.5.1 3-Point Bending Tests

Six specimens were tested in 3-point bending for each type of core. The only acceptable modes of failure were compressive facing failure due to bending on the top or tensile facing failure due to bending on the bottom. The applied load versus deflection data sets for successful tests corresponding to the panels with H250 foam cores are plotted in Fig. 9.1.5 along with a photograph of a representative failed specimen. The load-deflection response shows a linear behavior before failure. Figure 9.1.6 shows the load-deflection responses for successful tests and a photograph of a representative failed specimen corresponding to panels with the H130 foam core. As expected, the H130 response was found to be different compared to the H250 foam core panel. The curve was linear until an average applied load of 6 kN and then tends to become nonlinear because of core crushing, as shown in Fig. 9.1.6. This is mainly attributed to low density of H130.



a)



b)

Fig. 9.1.5 a) 3-point bending experiment for H250, 12.7-mm foam core sandwich panel, and b) sample under load

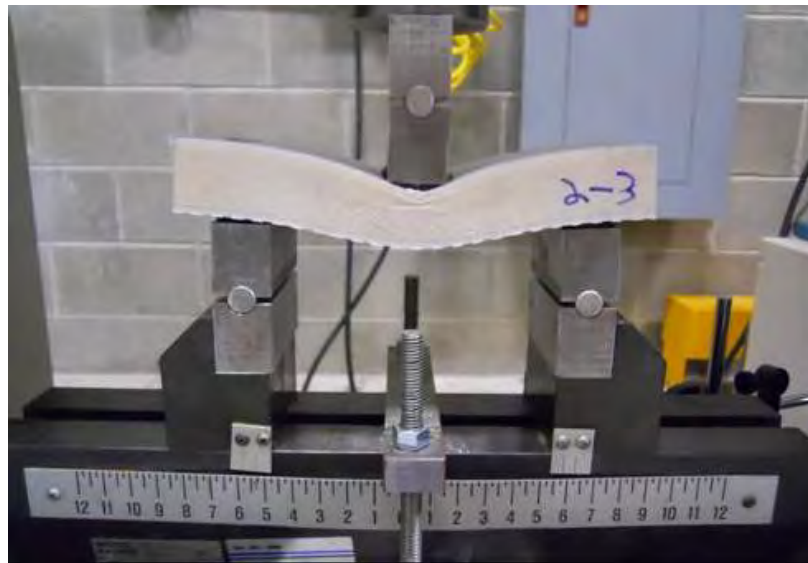
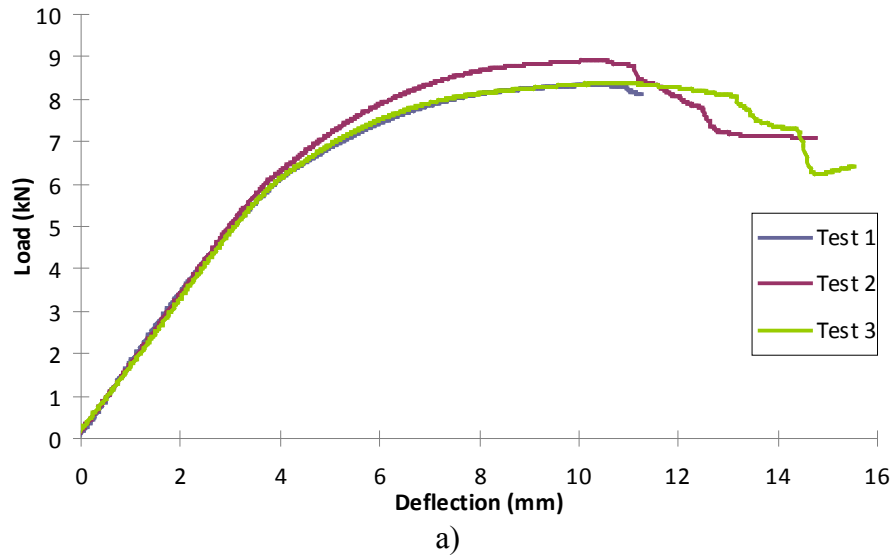


Fig. 9.1.6 a) 3-point bending experiment for H130, 25.4-mm foam core sandwich panel, and b) sample under load

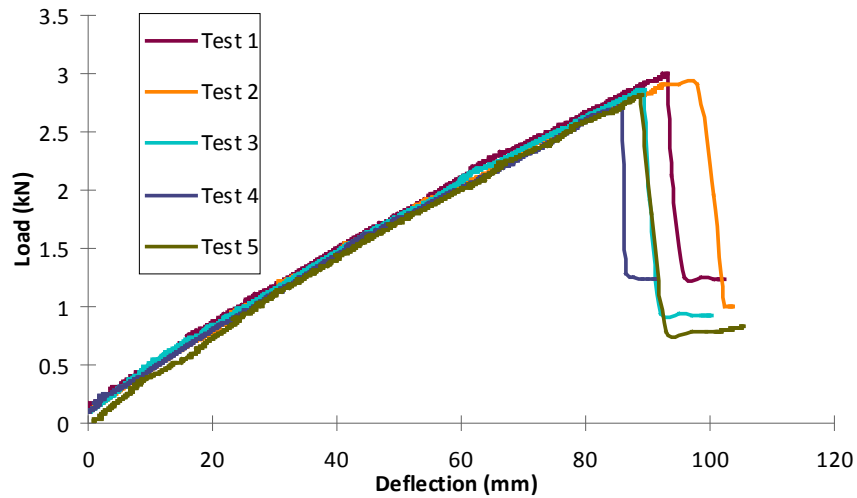
9.1.5.2 4-Point Bending Tests

The 4-point flexural response for sandwich panels with the H250 foam core is presented in Fig. 9.1.7 along with a photograph of a representative failed specimen. The tests were found to be repeatable, and the average peak loads were found to be around 3 kN prior to failure for all specimens. All failures occurred in the top face sheet. The flexural responses for panels with H130 foam core are presented in Fig. 9.1.8 along with a photograph of a representative failed specimen. The recorded data were used to calculate the flexural stiffness (D) as per ASTM D-7250 recommendations using Eq. 9.1.1. A single 4-point loading

configuration and another 3-point loading configuration are required to obtain the flexural stiffness (D):

$$D = \frac{3P_1S_1^3(141 - 121S_2^2 / S_1^2)}{1936\Delta_1(11 - 9P_1S_1\Delta_2 / P_2S_2\Delta_1)}, \quad (9.1.1)$$

where P represents the applied load, S_1 is the support span in the 4-point loading configuration, S_2 is the support span in the 3-point loading configuration, and Δ_1 and Δ_2 are deflections under 3- and 4-point loading configurations, respectively, corresponding to the applied load. The flexural stiffness of the H250, 12.7-mm-thick foam core specimens was found to be 7.54 N-m² with a standard deviation of ± 0.823 N-m². The flexural stiffness of the H130, 25.4-mm-thick foam core specimens was found to be 46.5 N-m² with a standard deviation of ± 4.41 N-m². The results are also illustrated in Fig. 9.1.9.

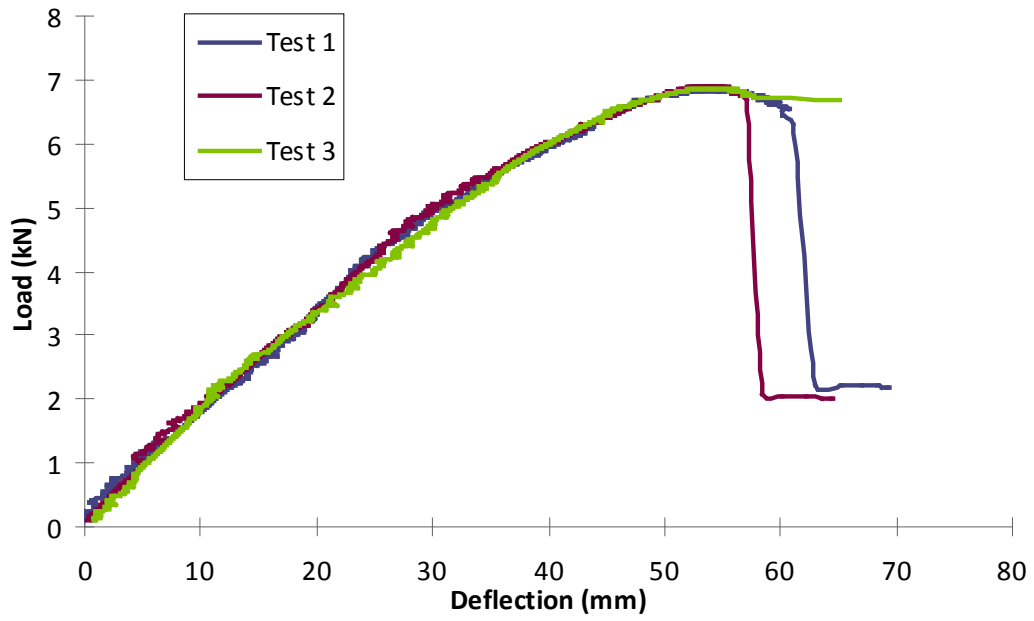


a)



b)

Fig. 9.1.7 a) 4-point bending experiment for H250, 12.7-mm foam core sandwich panel, and b) sample under load



a)



b)

Fig. 9.1.8 a) 4-point bending experiment for H130, 25.4-mm foam core sandwich panel, and b) sample under load

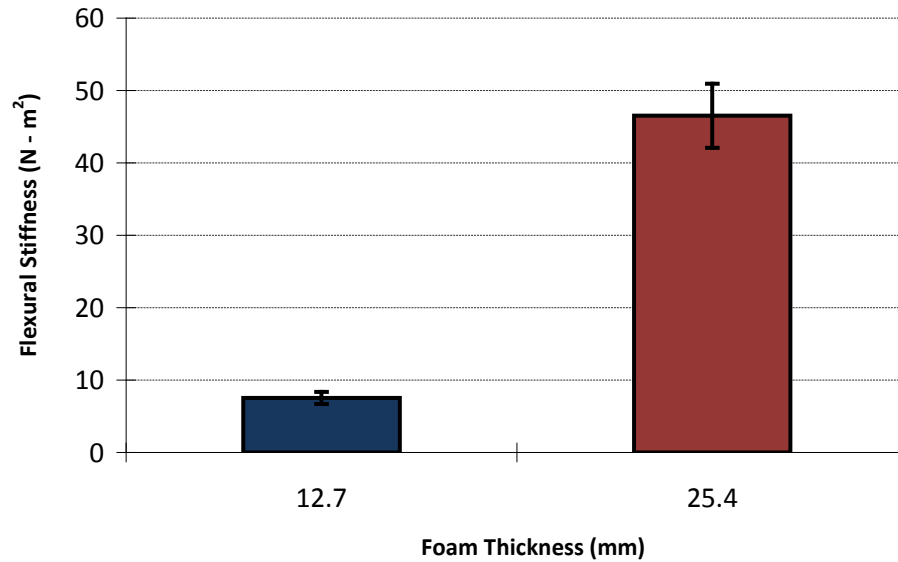


Fig. 9.1.9 Flexural stiffness for H250, 12.7-mm, and H130, 25.4-mm foam sandwich panels

9.1.5.3 Simulation Results

The flexural behavior of sandwich panels corresponding to various experimental tests was simulated. For brevity, the comparison and discussion of predicted flexural response from the simulations and experiments are reported only for the 4-point bending cases. A similar analogy applies for the 3-point cases. Nevertheless, for the sake of completion, the peak flexural loads from all 4 cases are reported. The software used to perform the numerical simulations (Micross) allows 3 mesh refinement levels: coarse (~1000 elements), standard (~3000 elements), and fine (~9000 elements). An initial mesh-refinement study revealed that the results from standard and fine meshes agreed well both in terms of capturing the failure mode and the load-carrying capacity. All of the following simulations followed standard mesh refinement and were found to agree well with experiments.

Figure 9.1.10 provides the longitudinal strains and equivalent stresses for the 4-point bending case with 12.7-mm H250 foam. The loading and boundary conditions are also shown in Fig. 9.1.10. Similar images for longitudinal strains/stresses were obtained for the other cases but are not shown here for brevity. Figure 9.1.11 compares the predicted flexural response with experiments for the sandwich beams subjected to 4-point bending. An excellent agreement between experiments and simulations was observed throughout the complete flexural response for sandwich panels with H250, 12.7-mm foam thickness. This agreement was not observed for the case of H130, 25.4-mm foam beams, wherein good agreement was found only in the linear regime. At applied loads near the

ultimate, the simulation predictions deviate from the experimental response. This was expected, as the simulations were performed with linear elastic properties for both the core and the facing sheets, thereby resulting in a linear response. In reality, at loads near the ultimate, complex mechanisms such as local shear deformations in the foam and micro-cracking contribute to softening and increase in the total displacements. Similar results have been reported by Feldhusen et al. [32], thereby supporting the results in this study. Also, the core used in the 25.4-mm H130 beams is less dense than the 12.7-mm H250 foam, causing higher nonlinear deformations in the core. Nevertheless, the simulation-predicted failure type (face sheet) and peak loads agreed well with the experiments.

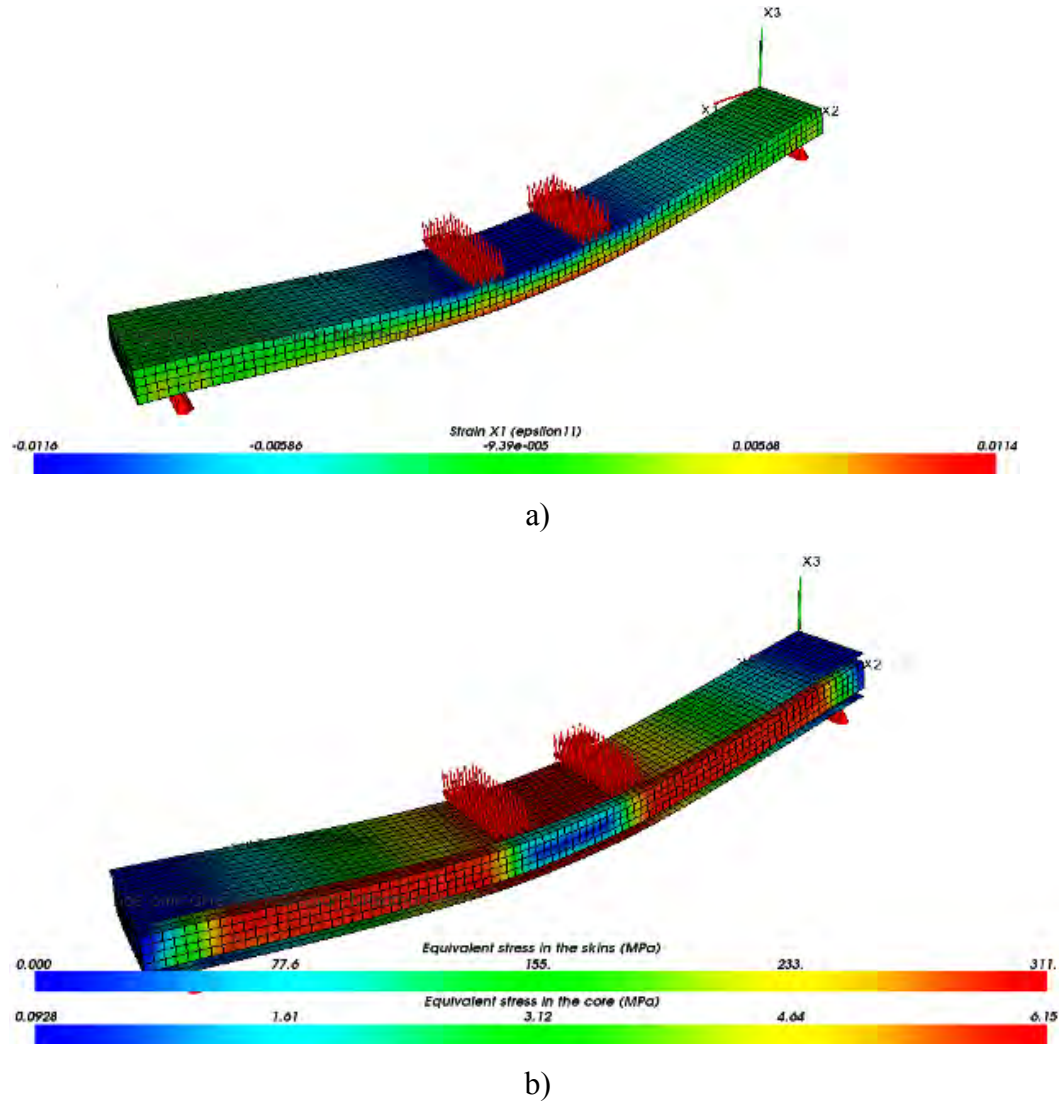


Fig. 9.1.10 Flexural analysis of sandwich panel subjected to 4-point bending: a) longitudinal strains (ϵ_{11}) and b) equivalent stresses (megapascals). (Images obtained as output from Digimat/Micross.)

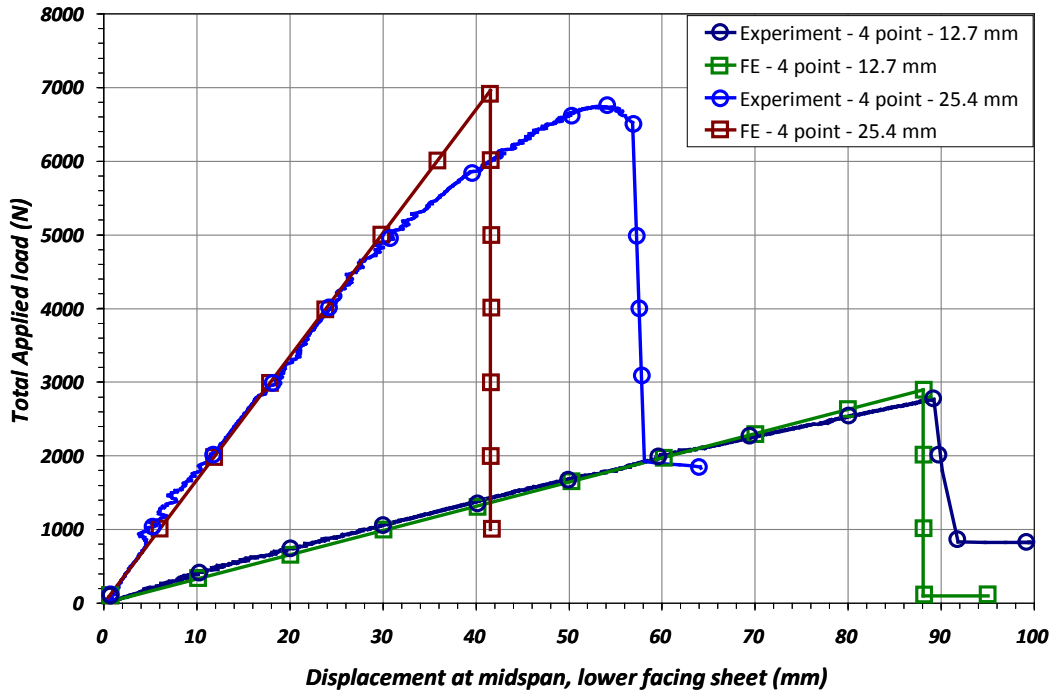


Fig. 9.1.11 Comparison of experimental and simulation-predicted flexural response for sandwich panels subjected to 4-point bending with 12.7- and 25.4-mm core thicknesses

Figure 9.1.12 compares the experimental and predicted ultimate failure loads for the various sandwich beams studied in this work. The simulations-predicted failure loads agreed well with experiments. Also, the numerical predictions were slightly higher than experimental results for all cases, except for the case of sandwich beams with a 25.4-mm core subjected to 3-point bending. In this case, the failure was caused by excessive deformation of the core. Experimental observations revealed that the deformation in the core induced local buckling of the face sheet followed by compressive failure of the face sheet. These complex interactions, including nonlinear deformations of the core, are currently not simulated. Models that address these issues will eliminate the discrepancy observed and further increase the accuracy of the simulations.

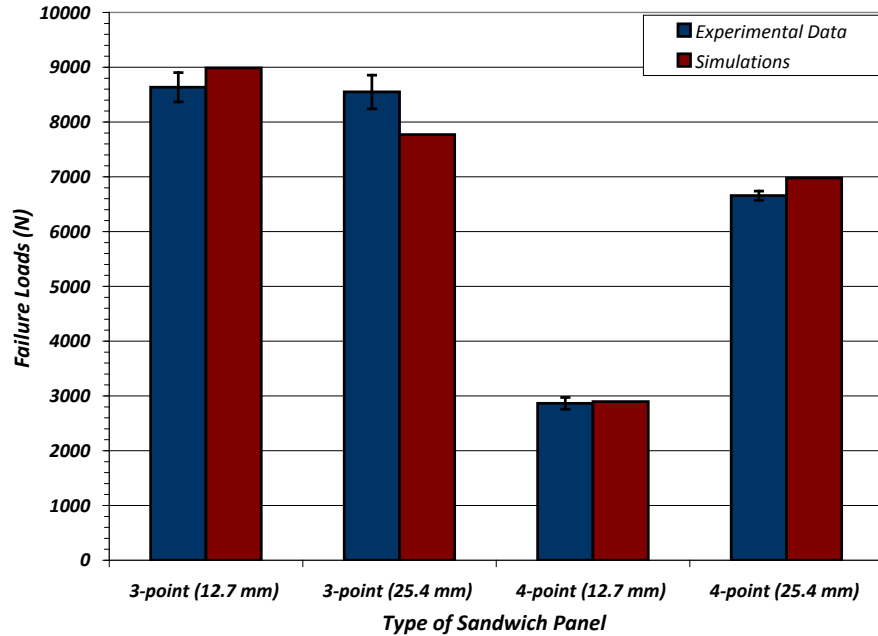


Fig. 9.1.12 Comparison of flexural failure loads from simulations and experiments

Overall, the simulation predictions agreed well with experiments in both the failure loads and mode of failure. These experimentally validated simulations can be used to further extrapolate the results beyond existing experiments. Also, the experimentally validated simulations can be used as a design tool and can eliminate the costly trial-and-error approach of developing efficient structural sandwich panels.

9.1.6 Conclusions

An integrated experimental and numerical program was carried out to evaluate the flexural properties of foam core composite sandwich panels, resin-infused by a single-step VARTM process. The flexural behavior for sandwich panels with 2 different core thicknesses and foam densities was studied using 3- and 4-point bending tests. Finite element models simulating the tests were performed using accurate material properties for the cores and facing sheets. Results revealed excellent agreement between simulations and experiments in predicting failure loads. A wide range of characterization is possible, depending on the constituents, material layout/configuration, and testing schemes. Hence, experimentally validated simulations that successfully predict both the failure mode and the capacity, such as the ones developed in this work, can be used as a robust design tool to predict the properties of sandwich beams beyond the experimental matrix and to develop efficient, novel structural sandwich composites. A similar approach can be extended to other structural materials and components.

9.1.7 References

- [1] Kabir, M.E., Saha, M.C. and Jeelani, S. (2006). "Tensile and fracture behavior of polymer foams." *Materials Science and Engineering A*, 429: 225–235.
- [2] Sharma, S. (2010). "Process development issues of glass-carbon hybrid-reinforced polymer composite wind turbine blades." *Journal of Composite Materials*, 44(4):437–456.
- [3] Williams, C., Juska, T., Duer, C. and Caiazzo, A. (2004). "Progress in materials for marine composite structures." In: *Proc. International SAMPE Technical Conference* (SAMPE Long Beach, CA). p.1845–1853.
- [4] Gates, T.S., Odegard, G.M., Frankland, S.J.V. and Clancy, T.C. (2005) "Computational materials: Multiscale modeling and simulation of nanostructured materials." *Composites Science and Technology*, 65:2416–2434.
- [5] Kabir, M.E., Saha, M.C. and Jeelani, S. (2006). "Tensile and fracture behavior of polymer foams." *Materials Science and Engineering A*, 429:225–235.
- [6] Vaikhanski, L. and Nutt, S.R. (2003). "Fiber-reinforced composite foam from expandable PVC microspheres." *Composites: Part A*, 34:1245–53.
- [7] Mouritz, A.P. and Thomson, R.S. (1999). "Compression, flexure and shear properties of a sandwich composite containing defects." *Composite Structures*, 44:263–78.
- [8] Borsellino, C., Calabrese, L. and Valenza, A. (2004). "Experimental and numerical evaluation of sandwich composite structures." *Composites Science and Technology*, 64:1709–1715.
- [9] Burman, M. and Zenkert, D. (1997). "Fatigue of foam core sandwich beams - 2: effect of initial damage." *International Journal of Fatigue*, 19(7):563–578.
- [10] Corigliano, A., Rizzi, E. and Papa, E. (2000). "Experimental characterization and numerical simulations of a syntactic-foam/glass-fibre composite sandwich." *Composites Science and Technology*, 60:2169–2180.
- [11] Fam, A. and Sharaf, T. (2010). "Flexural performance of sandwich panels comprising polyurethane core and GFRP skins and ribs of various configurations." *Composite Structures*, 92:2927–2935.

- [12] Kanny, K., Mahfuz, H., Carlsson, L.A., Thomas, T. and Jeelani, S. (2002). "Dynamic mechanical analyses and flexural fatigue of PVC foams." *Composite Structures*, 58:175–183.
- [13] Marasavina, L., Sadowski, T., Kneć, M. and Negru, R. (2010). "Non-linear behaviour of foams under static and impact three point bending." *International Journal of Non-Linear Mechanics*, 45(10):969–975.
- [14] Majumdera, P., Srinivasagupta, D., Mahfuza, H., Joseph, B., Thomas, M.M. and Christensen, S. (2003). "Effect of processing conditions and material properties on the debond fracture toughness of foam-core sandwich composites: experimental optimization." *Composites: Part A*, 34:1097–1104.
- [15] Yen, K.S., Ratnam, M.M. and Akil, H.M. (2010). "Measurement of flexural modulus of polymeric foam with improved accuracy using moiré method." *Polymer Testing*, 29:358–368.
- [16] Russo, A., and Zuccarello, B. (2007). "Experimental and numerical evaluation of the mechanical behaviour of GFRP sandwich panels." *Composite Structures*, 81:575–586.
- [16] Shahdin A, Mezeix L, Bouvet C, Morlier J, Gourinat Y. (2009). "Fabrication and mechanical testing of glass fiber entangled sandwich beams: A comparison with honeycomb and foam sandwich beams." *Composite Structures*, 90:404–412.
- [18] Gibson, L.J., Ashby, M.F. (1988). *Cellular Solids Structure and Properties*. Pergamon Press.
- [19] Steeves, C.A. and Fleck, N.A. (2004). "Collapse mechanisms of sandwich beams with composite faces and a foam core, loaded in three-point bending. Part II: experimental investigation and numerical modelling." *International Journal of Mechanical Sciences*, 46:585–608.
- [20] Tagarielli, V.L., Fleck, N.A. and Deshpande, V.S. (2004). "Collapse of clamped and simply supported composite sandwich beams in three-point bending." *Composites: Part B*, 35:523–534.
- [21] El Mahi, A., Farooq, M.K., Sahraoui, S. and Bezazi, A. (2004). "Modelling the flexural behaviour of sandwich composite materials under cyclic fatigue." *Materials and Design*, 25:199–208.

- [22] Sarzynski, M.D. and Ochoa, O.O. (2005). "Carbon Foam Core Composite Sandwich Beams: Flexure Response." *Journal of Composite Materials*, 39(12):1067–1080.
- [23] Bezazi, A., El Mahi, A., Berthelot, J.M., Bezzazi, B. (2009). "Experimental Analysis of Behavior and Damage of Sandwich Composite Materials in Three Point Bending. Part2. Fatigue Test Results and Damage Mechanisms." *Strength of Materials*, 41(3):257–267
- [24] Kulkarni, N., Mahfuz, H. and Jeelani, S. (2004). "Fatigue Failure Mechanism and Crack Growth in Foam Core Sandwich Composites under Flexural Loading." *Journal of Reinforced Plastics and Composites*, 23(1):83-94.
- [25] DIAB®, "Divinycell H Technical Data," 2010.
- [26] ASTM C-393. (2006). *Standard Test Method for Core Shear Properties of Sandwich Constructions by Beam Flexure*, ASTM International.
- [27] ASTM D-7249. (2006). *Standard Test Method for Facing Properties of Sandwich Constructions by Long Beam Flexure*, ASTM International.
- [28] ASTM D-7250. (2006). *Standard Practice for Determining Sandwich Beam Flexural and Shear Stiffness*, ASTM International.
- [29] Micross® Version 1.1.2. (2010). e-Xstream engineering SA, Belgium.
- [30] Digimat® Version 4.0.2. (2010). e-Xstream engineering SA, Belgium.
- [31] Deka, L.J., Bartus, S.D. and Vaidya, U.K. (2007). "Numerical Modeling of Simultaneous and Sequential Multi-Site Impact Response of S-2 Glass/Epoxy Composite Laminates." In: *Proceedings of Composites and Polycon. American Composites Manufacturers Association*, Tampa, Florida USA, October 17–19.
- [32] Feldhusen, J., Torsakul, S., Brezing, A.N. and Krishnamoorthy, S.K. (2008). "An Approach to Numerical Modeling and Simulation of Cellular Foam Sandwich Structures in Commercial FE-Softwares." In: *Proceedings of the IEEE International Conference on Industrial Engineering and Engineering Management, IEEM*, p. 836–84

9.2 Mechanical Characterization of Glass and Carbon Fiber Composites Fabricated by Resin Infusion

Alfred Loos and Stephen Sommerlot

9.2.1 Summary

For use as a benchmark to compare later with novel alterations of composite materials, woven glass and carbon fiber composites fabricated by resin infusion methods were constructed and tested for basic mechanical properties. These are the first steps toward the ultimate goal of producing lightweight composite materials for protective panels in vehicles that have a high resistance to impact. The selected materials used were AGY's plain weave S-2 Glass, A&P Technology's Qiso-brand braided triaxial fabric, and Applied Poleramic SC-15 epoxy resin. Resin transfer molding (RTM) and vacuum-assisted resin transfer molding (VARTM) are presented as means for fabrication, while basic mechanical properties are explored through tensile, shear, flexural, and compressive testing. The S-Glass test specimens were fabricated by both VARTM and RTM, while the carbon fiber Qiso was created using VARTM only, producing 3 comparable specimen types. Results generally showed that the Qiso produced the highest strength characteristics followed by the RTM-produced S-Glass, and finally the VARTM S-Glass. The corresponding moduli—elastic, compressive, flexural, and shear—followed similar trends, with the Qiso generally having the greatest strength characteristics, followed by RTM then VARTM S-Glass.

9.2.2 Introduction

Protective paneling in vehicles must be produced from high-quality, high-strength materials. Composite materials, paired with their lightweight behavior, fill this role well. Using a woven glass fabric, S-Glass produced by AGY, and a triaxial-braided carbon fiber fabric, Qiso, produced by A&P Technology, Michigan State University's Composite Vehicle Research Center produced composite materials. These fabrics, when infused with Applied Poleramic's SC-15 epoxy resin through either resin transfer molding (RTM) or vacuum-assisted resin transfer molding (VARTM), were machined into test specimens so that basic mechanical properties could be explored. These properties, once combined with later penetration and blast testing, will form a benchmark to compare novel alterations of similar composite materials. Those novel alterations will be used to enhance desired properties of the composites so that the ultimate goal of producing materials for protective panels in

vehicles can be optimized and validated. Data produced from such basic mechanical testing of tensile, shear, flexural, and compression paired with other literature can also serve as a basic reference for the materials' properties.

9.2.3 Composite Design and Fabrication

9.2.3.1 Materials

As stated earlier, AGY's S-Glass and A&P Technology's Qiso were used as reinforcements in the composites fabricated. These fabrics can be seen in Fig. 9.2.1. S-Glass is a plain weave glass fiber material, while Qiso is a triaxial-braided carbon fiber fabric. Table 9.2.1 shows a direct comparison of the S-Glass and Qiso's basic properties.

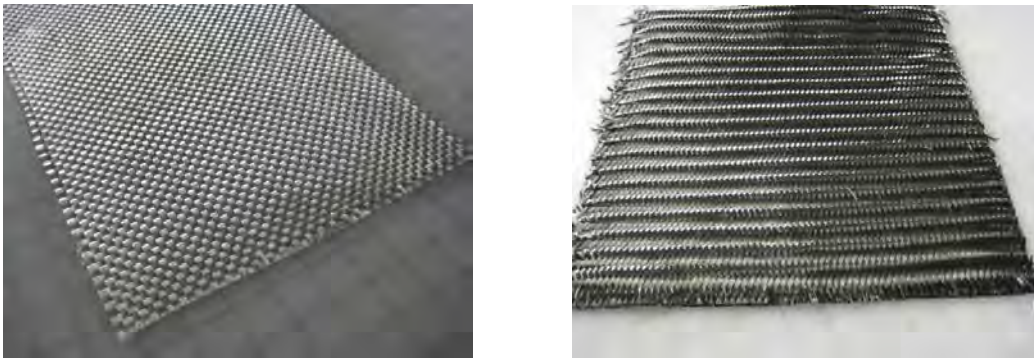


Fig. 9.2.1 (Left) AGY's S-2 Glass and (right) A&P's Qiso

Table 9.2.1 S-glass and Qiso basic fabric properties

	S-Glass	Qiso
Material	Glass fiber	Carbon fiber
Fiber orientation	Plain weave	0, $\pm 60^\circ$
Thickness (inches)	0.03	0.021
Areal weight (g/m ²)	815	531

The matrix to pair with these reinforcements was chosen to be Applied Poleramic's SC-15 epoxy resin. This is a 2-phase epoxy cycloaphatic amine with a viscosity at ambient temperature of 350 centipoise.

9.2.3.2 Preform Layup

Before resin infusion could begin, the reinforcement's material was cut to size and oriented in a specific layup. Composites were fabricated in panels that were either 12 \times 12 inches or 12 \times 24 inches. The S-2 Glass, because of its plain weave fiber orientation, was stacked in a quasi-isotropic 9-layer layup. This layup is illustrated in Fig. 9.2.2. The Qiso's triaxial-braided 0, $\pm 60^\circ$ fiber orientation offers

equal material weight in all directions, which provides an initial quasi-isotropic characteristic. A 4- or 6-ply-thick layup was then used, where the 0° fibers were stacked in line. A 4-layer-thick Qiso panel was used for tensile testing because of the material's high strength, while a 6-ply layup was used for the remaining tests.

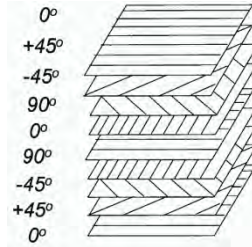


Fig. 9.2.2 Quasi-isotropic layup for S-glass

9.2.3.3 Fabrication

In the VARTM process, either an S-2 Glass or Qiso preform was sealed on a plate, sandwiched by peel plies, and covered by an infusion medium underneath a vacuum bag. Pulling down to full vacuum, we introduced resin at an inlet at one end of the preform and pulled through to the exit at the opposite end. This method creates a quick, fairly compressed full resin infusion. Continued under vacuum, the plate holding the composite was placed in a curing oven for a 6-h cure cycle. This cycle complies with the manufacturer's recommended curing process, which includes 2 h of oven time at 60°C and then 4 h at 94°C . Figure 9.2.3 shows a VARTM setup where the preform, covered in infusion medium (red material) and peel plies (blue material), is sealed under vacuum as resin advances through the fibers. Tacky tape (yellow) surrounds the setup as a means for the vacuum bag to seal.

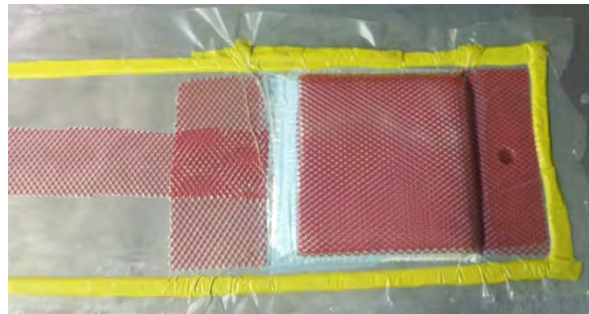


Fig. 9.2.3 VARTM setup

The RTM process, which was only used with the S-Glass, is a compressive molding procedure. The quasi-isotropic S-2 Glass preforms were placed in a specially designed mold where resin could be introduced and then the mold could be compressed until a full cure was achieved. To accomplish this, a TMP 140-Ton

vacuum hot press was employed to clamp the mold and then heat it with the same 6-h cure cycle used in the VARTM process, as SC-15 resin was continued to be used as the matrix. With the mold under minimal pressure, resin was introduced to the preform through an inlet at the top center of the mold via air pressure from a pressure pot. Once full infusion was achieved, as resin exits from the 2 outlet holes on the mold's sides, the TMP press was used to clamp with sufficient force to fully close the mold, and the curing cycle could begin. This process compacts the S-2 Glass fibers greatly, and that difference, compared to VARTM, is evident in test results. Figure 9.2.4 displays an RTM setup.

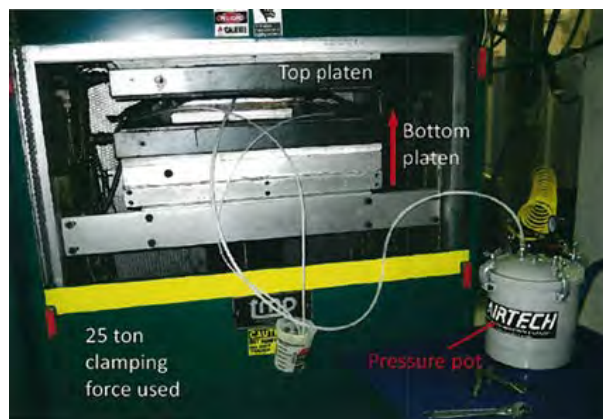


Fig. 9.2.4 RTM setup

9.2.4 Experimental Techniques

9.2.4.1 Tensile Testing

Tensile testing was conducted in accordance with ASTM D3039 procedures. VARTM S-Glass specimens were tested straight-sided with no tabs, while the Qiso and RTM S-Glass specimens, because of their higher-strength characteristics, required end tabs to create successful gage length failures. Initial untabbed trials resulted in slipping or failure under the grips. The tabs for the Qiso coupons were created from 6-ply Qiso composite pieces in accordance with ASTM tab recommendations (roughly 2 inches in length) and adhered with Loctite Super Glue Gel Control. The Qiso test coupons were machined from a 4-layer Qiso VARTM panel to ensure that the testing frames could provide sufficient load for specimen failure. The tabs for the RTM S-2 Glass samples were composed of a thinner fiberglass material. Tests were run at a speed of 5 mm/min until failure, so both the tensile strength and elastic modulus could be attained. All coupons had their 0° fibers running along the length of each specimen. Strain for all tests was calculated with the aid of EIR's model LE-05

laser extensometer with a laser gage length of 50 mm. The results and comparisons of these tests are found in the Results section. The setup of this test can be seen in Fig. 9.2.5.

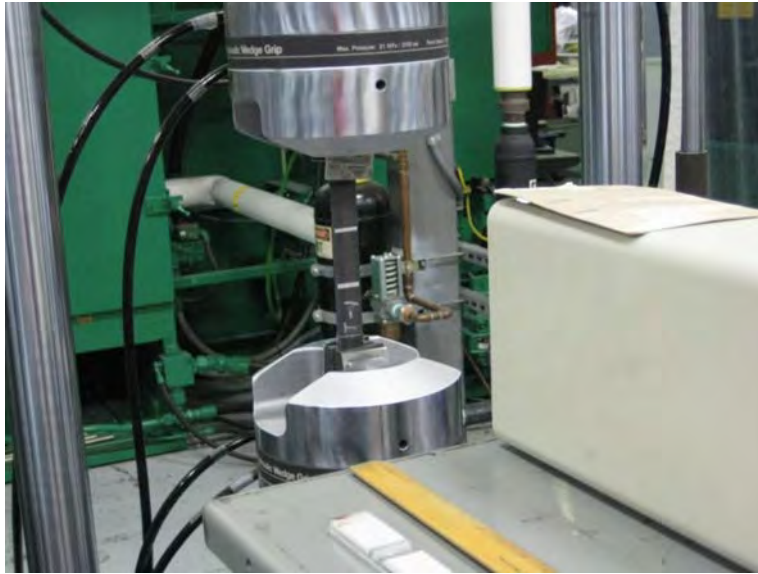


Fig. 9.2.5 Tensile test setup

9.2.4.2 Compressive Testing

The 3 material types were tested for compressive properties using ASTM 6641 and a Combined Loading Compression (CLC) test fixture from Wyoming Test Fixtures. The fixture was loaded into a 100-kN screw-driven MTS Insight between 2 compression platens. This setup can be seen in Fig. 9.2.6. All samples were straight sided and untabbed. All coupons were machined to be 12 mm wide by 140 mm long, allowing for a 13-mm (~0.5 inch) gage length. The specimens were cut so that the 0° fibers were positioned vertically with the coupon lengths. Tests were conducted with a crosshead speed of 0.05 inches/min and until failure occurred. Strain calculations were made from data acquired by the LE-05 laser extensometer with a laser gage length of 70 mm. Laminate compressive strength and modulus were calculated from these data. The compressive modulus was measured over a range of axial strain of 1,000 to 3,000 microstrain. All coupons produced acceptable gage length failures, and their results are found in the Results section.



Fig. 9.2.6 Compression test setup

9.2.4.3 Shear Testing

Two major tests were used to define shear properties for the composite materials tested. The V-Notched Beam Method or Iosipescu Shear Method (ASTM D5379) was used for both the VARTM- and RTM-produced S-2 Glass, while the Qiso material was tested with the V-Notch Rail Shear Method (ASTM D7078). Both tests used fixtures produced by Wyoming Test Fixtures. In initial Iosipescu tests, Qiso samples would experience crushing at the loading points before gage length failure occurred, so a different test (V-Notch Rail Shear) was needed that could handle the high-strength specimens. The Iosipescu coupons were 20 mm thick by 76 mm long with 90° notches at the center allowing for a 12-mm gage length. The coupons were cut so that the 0° fibers were in line with the length of the specimen. The Iosipescu specimens were tested at 0.05 inches/min with a 100-kN MTS Insight until failure occurred. To acquire strain data, strain gages were adhered in line with the gage length of each coupon. Strain at $\pm 45^\circ$ orientations were measured on the rosettes so that shear strain could be calculated by adding the absolute value of strain in both orientations. The RTM S-Glass specimens were tested with 120-ohm strain gages, but because of exhausted supplies, 350-ohm gages were ordered to finish with the VARTM S-2 Glass samples. The ultimate shear strength and the shear modulus of elasticity were calculated for. The shear modulus was observed over a $4,000 \pm 200$ microstrain range with the lower strain point inside the 1,500 to 2,500 microstrain range. As for the Qiso samples, a larger coupon was used: 56 mm wide by 76 mm long. Similar to the Iosipescu coupons, each V-Notch Rail specimen had 90° notches cut at the center

of the specimen so that a 31-mm gage length through the center of the sample was achieved. We adhered 350-ohm strain gages to these specimens so $\pm 45^\circ$ strain orientations could be measured to later calculate for shear strain. The shear modulus (chord modulus) was calculated using the same stipulations as the Iosipescu tests. The coupons were loaded into the Rail Shear fixture with the gripping bolts torqued to the recommended 40 ft-lb using a torque wrench. A 100-kN screw-driven MTS Insight was employed, while specimens were tested with a crosshead speed of 2 mm/min until gage length failure occurred. The setups for Iosipescu and Rail Shear tests can be seen in Figs. 9.2.7 and 9.2.8, respectively.

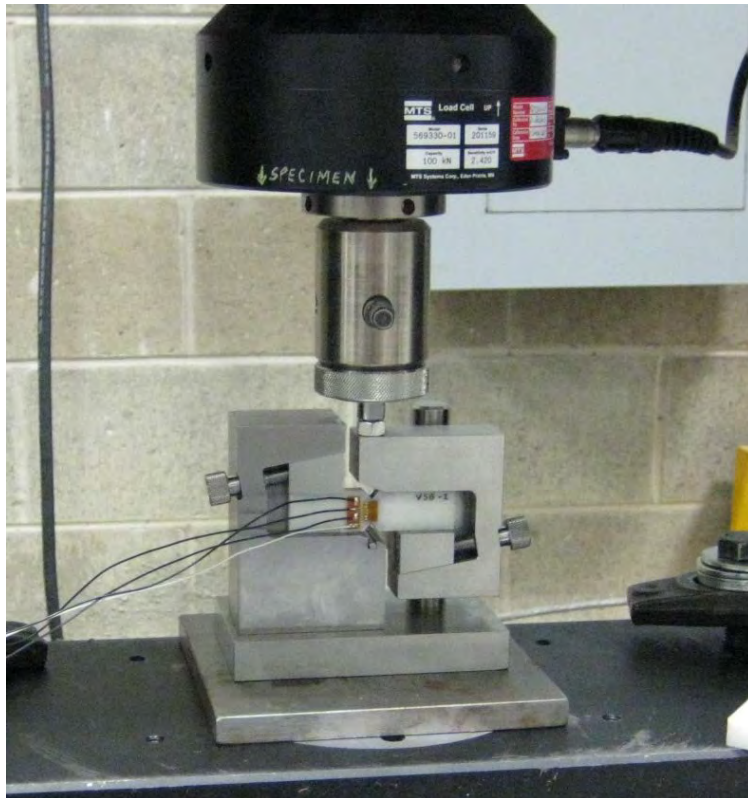


Fig. 9.2.7 Iosipescu test setup



Fig. 9.2.8 Rail shear test setup

9.2.4.4 Flexural Testing

Flexural tests were conducted in adherence to ASTM 6272 procedures for 4-point bending. Both RTM and VARTM S-2 Glass samples were tested using a load span of one-third of the support span distance. The Qiso coupons were tested with a load span of half the support span and with a higher span-to-depth ratio, 40:1, in order to decrease shear deflections so that the apparent modulus would not be reduced. The LE-05 laser extensometer was used to measure strain as coupons were tested to failure to observe both the flexural strength and the flexural modulus. Flexural modulus was defined as the slope of the elastic portion of the materials' stress-strain curves. Specimens were tested at crosshead speeds calculated from the ASTM depending on the load span to support span ratio and the span-to-depth ratio. The Qiso, for instance, was tested at 8 mm/min, faster than the S-2 Glass coupons because of its higher span-to-depth ratio. Figure 9.2.9 displays the flexural test setup.

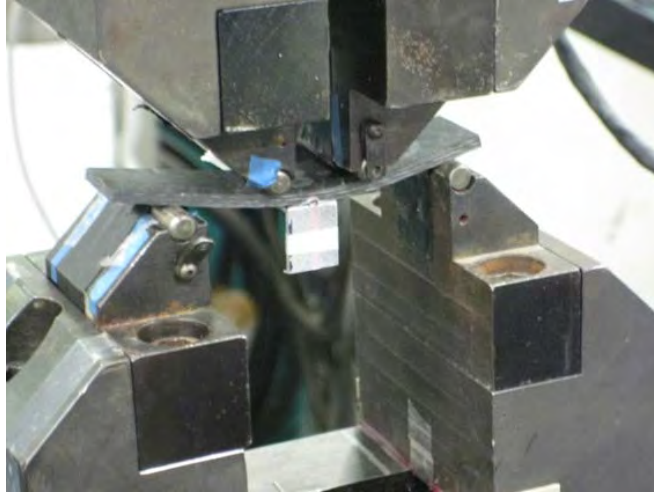


Fig. 9.2.9 Flexural test setup

9.2.5 Results

All experiments were completed with at least 5 specimens tested, in adherence to general ASTM procedure. If significant deviation from the average existed or inconsistency during a specific test occurred, a data set could be deemed unrepresentative of its corresponding test group. The results from all tests, ultimate strengths and moduli, were averaged and presented graphically. The tensile test results for ultimate tensile strength and elastic moduli can be seen in Figs. 9.2.10 and 9.2.11, respectively. Note that all error bars represent 1 standard deviation of the data above and below the average. Numerical representation of the data then follows in Table 9.2.2.

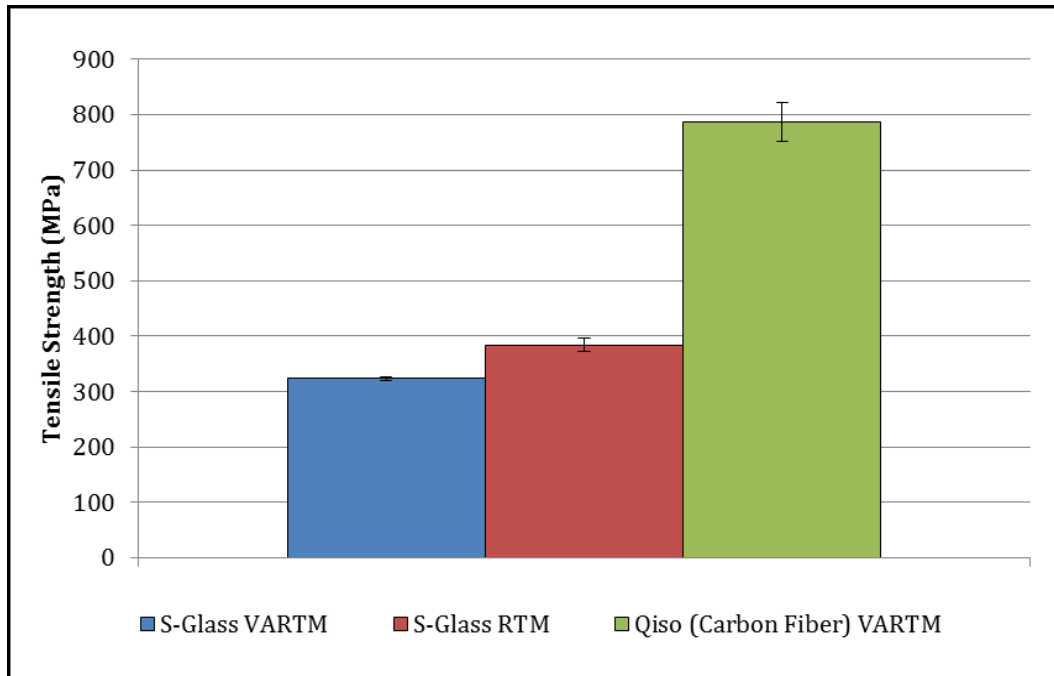


Fig. 9.2.10 Average ultimate tensile strength comparison

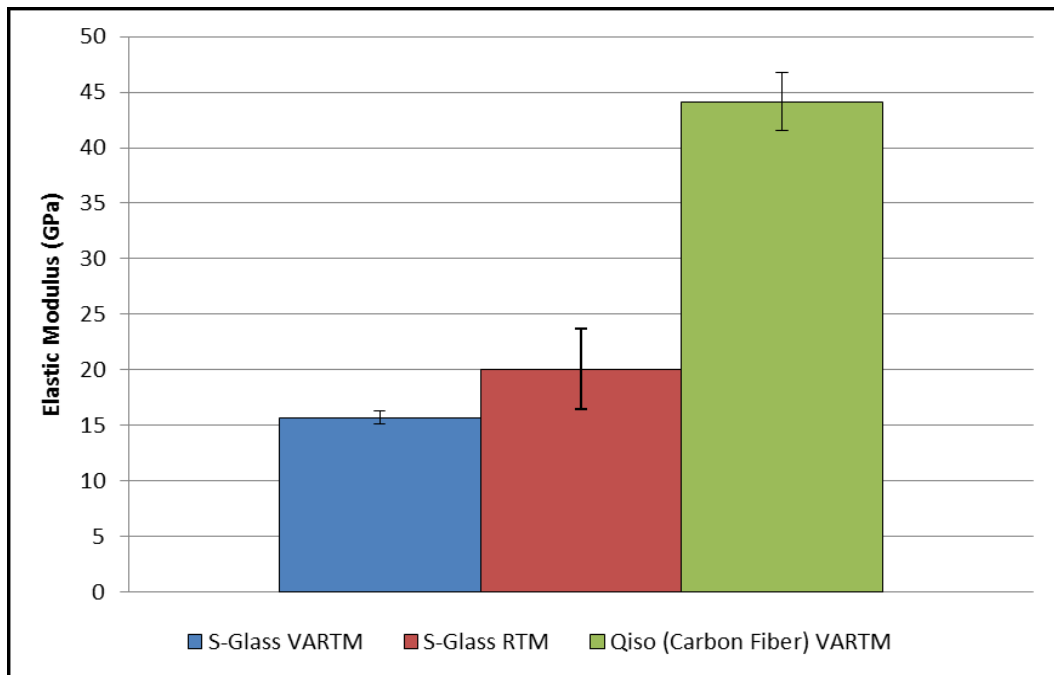


Fig. 9.2.11 Average elastic modulus comparison

Table 9.2.2 Tensile test results

Material	Qiso		RTM S-2 Glass		VARTM S-2 Glass	
	Tension		Tension		Tension	
Property	Modulus (GPa)	Strength (MPa)	Modulus (GPa)	Strength (MPa)	Modulus (GPa)	Strength (MPa)
Average	44.14	786.17	20.06	383.65	15.69	323.89
STD	2.64	34.93	3.61	11.98	0.6	3.29
CV (%)	5.98	4.44	17.98	3.12	3.85	1.02

Results from compressive testing now follow in Figs. 9.2.12 and 9.2.13, where the average laminate compressive strengths and laminate compressive moduli are displayed. Table 9.2.3 shows the numerical averages and other statistics of these results.

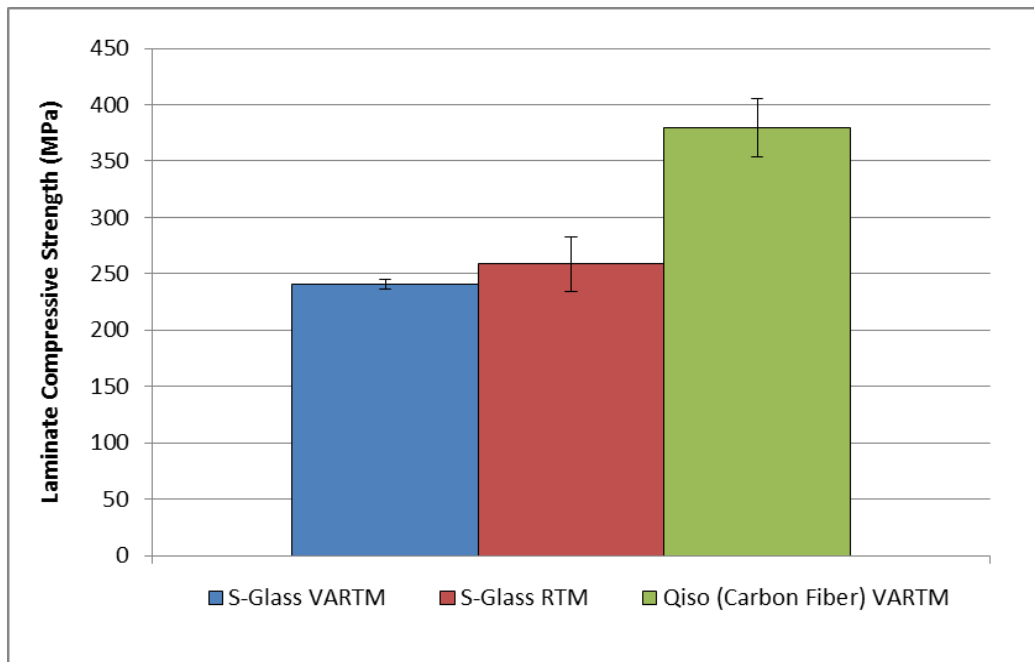


Fig. 9.2.12 Average laminate compressive strength comparison

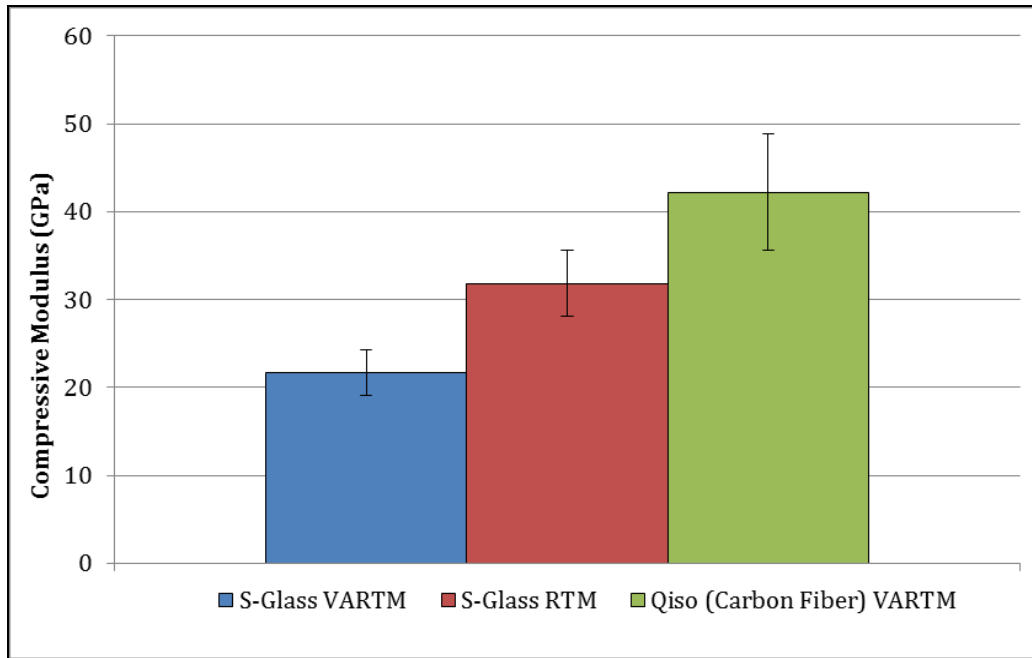


Fig. 9.2.13 Average laminate compressive modulus comparison

Table 9.2.3 Compression test results

Material	Qiso		RTM S-2 Glass		VARTM S-2 Glass	
	Compression		Compression		Compression	
Property	Modulus (GPa)	Strength (MPa)	Modulus (GPa)	Strength (MPa)	Modulus (GPa)	Strength (MPa)
Average	42.23	379.09	31.83	258.60	21.66	240.78
STD	6.68	25.92	3.75	23.99	2.57	4.31
CV (%)	15.81	6.84	11.78	9.28	11.87	1.79

The Iosipescu and V-Notch Rail Shear strength test results are shown in Fig. 9.2.14. Note that these results include the RTM and VARTM S-Glass samples from Iosipescu tests and Qiso data from the V-Notch Rail Shear Test Method. Following in Fig. 9.2.15, the shear chord moduli for each material can be found while the method employed for testing is also noted. Table 9.2.4 displays the numerical data represented in the figures.

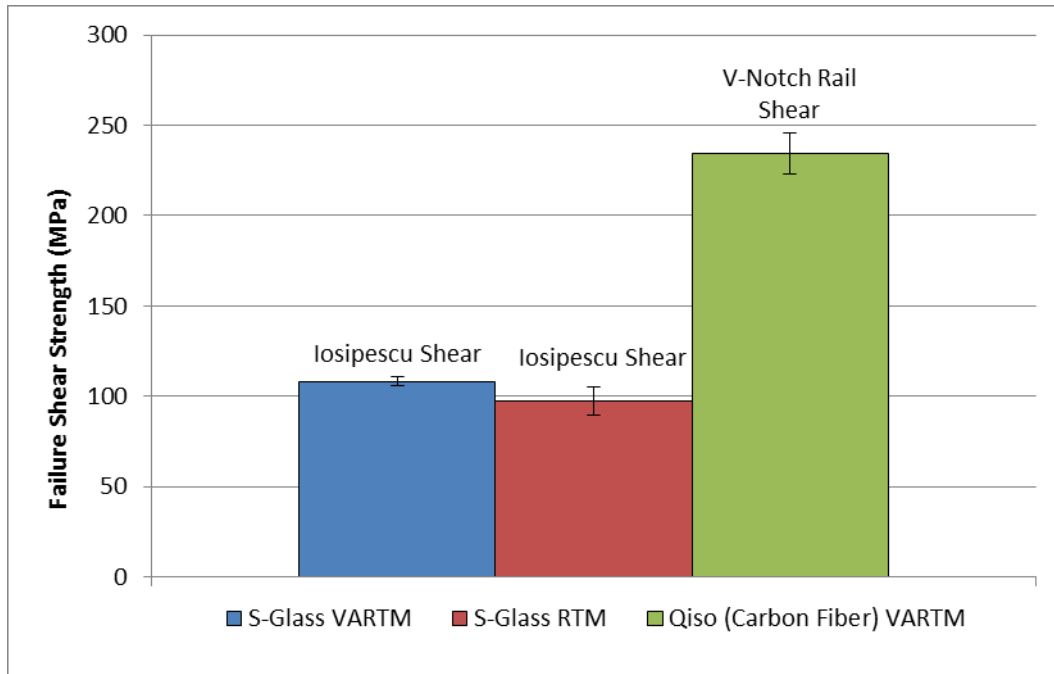


Fig. 9.2.14 Average failure shear strength from the Iosipescu and V-Notch rail shear tests methods

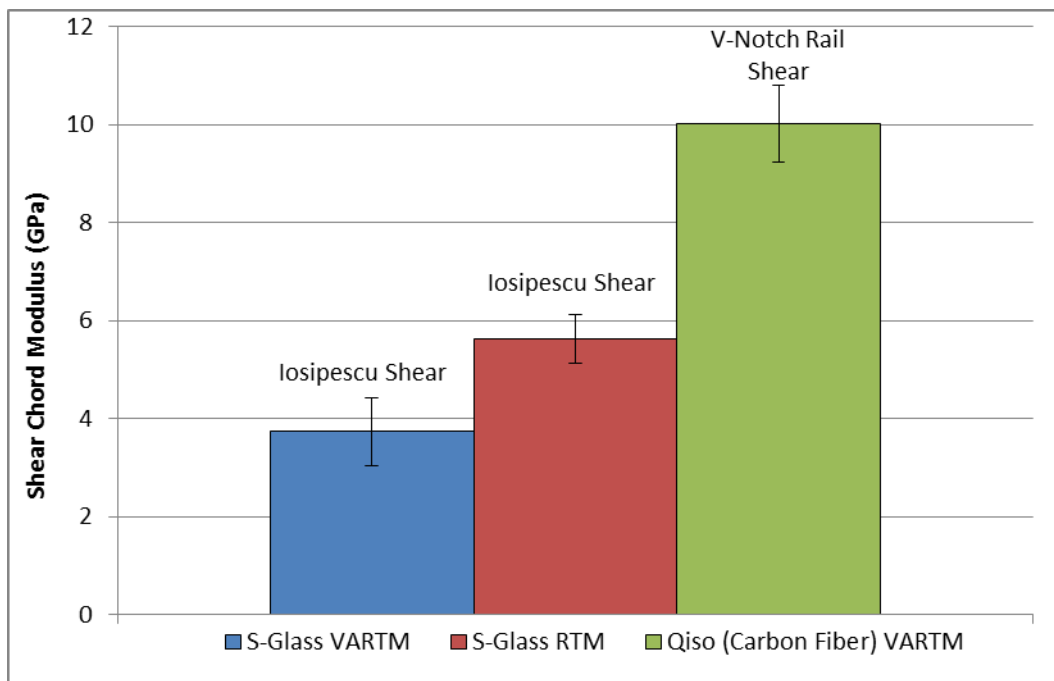


Fig. 9.2.15 Average shear moduli from the Iosipescu and V-Notch rail shear test methods

Table 9.2.4 Shear test results

Material	Qiso		RTM S-2 Glass		VARTM S-2 Glass	
	Shear		Shear		Shear	
Property	Modulus (GPa)	Strength (MPa)	Modulus (GPa)	Strength (MPa)	Modulus (GPa)	Strength (MPa)
Average	10.02	234.61	5.62	97.43	3.74	108.19
STD	0.79	11.29	0.5	7.92	0.69	2.55
CV (%)	7.86	4.81	8.97	8.13	18.36	2.36

The final set of results is from the flexural testing. Figures 9.2.16 and 9.2.17 display the average flexural strength and flexural modulus of elasticity from each material type tested. Table 9.2.5 displays the numerical data represented in the figures.

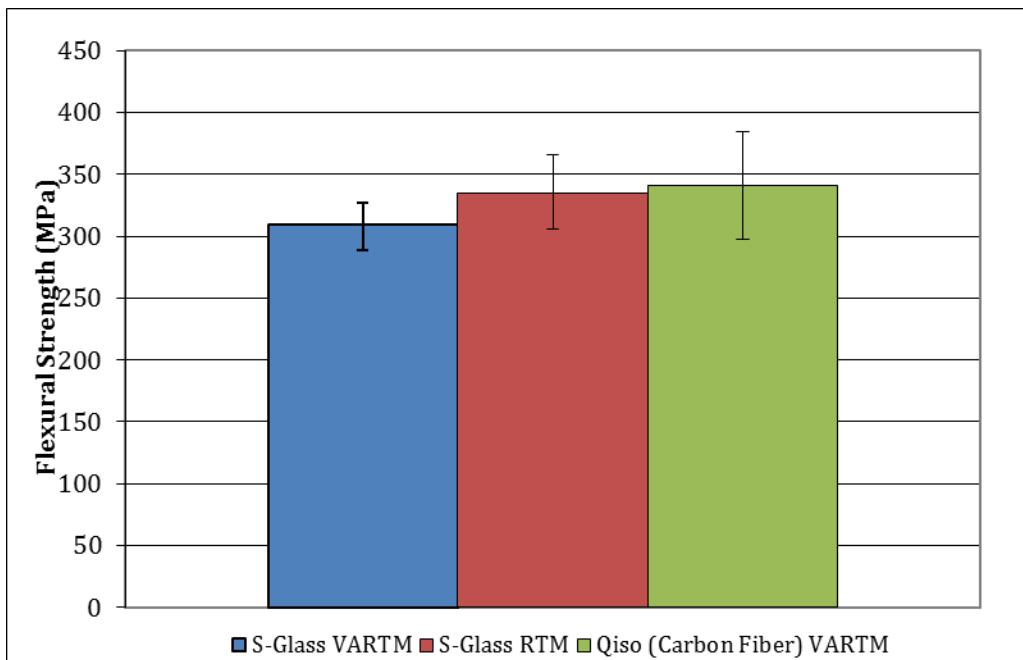


Fig. 9.2.16 Average flexural strength comparison

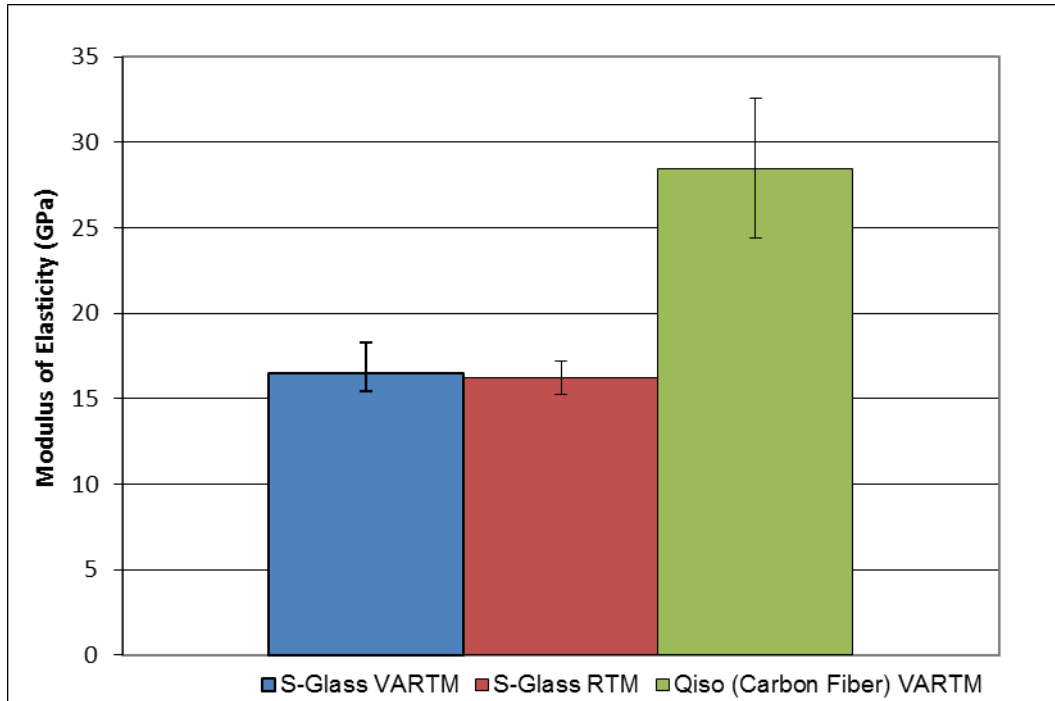


Fig. 9.2.17 Average flexural modulus comparison

Table 9.2.5 Flexural test results

Material	Qiso		RTM S-2 Glass		VARTM S-2 Glass	
	Flexural		Flexural		Flexural	
Property	Modulus (MPa)	Strength (MPa)	Modulus (GPa)	Strength (MPa)	Modulus (GPa)	Strength (MPa)
Average	28.47	341.11	16.23	334.61	16.48	309.2
STD	4.07	43.28	0.45	17.5	1.03	17.11
CV (%)	14.31	12.69	2.79	5.23	6.26	5.53

9.2.6 Summary

Upon examination of the test results, a few general trends can be observed. The Qiso material and its coupons generally appear to be the overall strongest while exhibiting most of the highest ultimate strengths and highest moduli. The RTM-produced S-Glass exhibits the next highest strengths and moduli, followed by the VARTM S-Glass. This trend seen in the S-Glass specimens is because RTM-produced panels use a much greater compaction force when infused than the VARTM panels. As pressure increases so does the fiber volume fraction, giving the RTM S-Glass more fibers to resist external forces in each coupons' area than the VARTM samples. The Qiso's carbon fiber triaxial braided nature high strengths in comparison to the S-Glass were evident throughout testing, especially

when separate shear testing methods were needed, as well as greater span-to-depth ratios during flexural testing. Blast and impact testing to investigate fiber breakage will be needed to further pursue validation for vehicle implementation.

9.2.7 Bibliography

- “Standard Test Method for Flexural Properties of Unreinforced and Reinforced Plastics and Electrical Insulating Materials by Four-Point Bending,” *ASTM Standard D6272*, 2010
- “Standard Test Method for Tensile Properties of Polymer Matrix Composite Materials,” *ASTM Standard D3039*, 2008
- “Standard Test Method for Compressive Properties of Polymer Matrix Composite Materials Using a Combined Loading Compression (CLC) Test Fixture,” *ASTM Standard D6641*, 2009
- “Standard Test Method for Shear Properties of Composite Materials by the V-Notched Beam Method,” *ASTM Standard D5379*, 2012
- “Standard Test Method for Shear Properties of Composite Materials by the V-Notched Rail Shear Method,” *ASTM Standard D7078*, 2012

9.3 Design and Manufacture of a High-Mobility Multipurpose Wheeled Vehicle (HMMWV) Component

Alfred C Loos and Adam C Klein

9.3.1 Summary

The overall objective of this project was to identify, design, and manufacture a door or component of similar complexity for a HMMWV. This report focuses on the selection, design, and manufacture of a rear bumper support strut.

9.3.2 Introduction

The main objectives of the work package were as follows:

- To identify a component of the vehicle that would be suitable for design and manufacture using composites
- To design and manufacture a component of the HMMWV using composites
- To work with other thrust areas to demonstrate Composite Vehicle Research Center (CVRC)-developed technologies

This report will provide detailed information on the approach and the work completed on this project.

9.3.3 Component Identification

Initially 2 parts of the vehicle were identified for potential use in this project: the rear bumper assembly and the tailgate. Figures 9.3.1 and 9.3.2 show the tailgate and the rear bumper assembly, respectively, after they had been removed from the vehicle.



Fig. 9.3.1 Tailgate



Fig. 9.3.2 Rear bumper assembly

Based on recommendations by the sponsor and the potential to incorporate CVRC-developed sensing technologies, we selected the rear bumper assembly as the component to focus on for the project. With the rear bumper assembly, we could incorporate advanced and multimaterial joining applications. The bumper assembly was also seen as a possible location for the incorporation of multifunctional materials.

Because of the level of complexity of the bracketry on the rear bumper assembly, we decided that the focus would be on a single strut piece. The strut piece used is shown in Fig. 9.3.3.

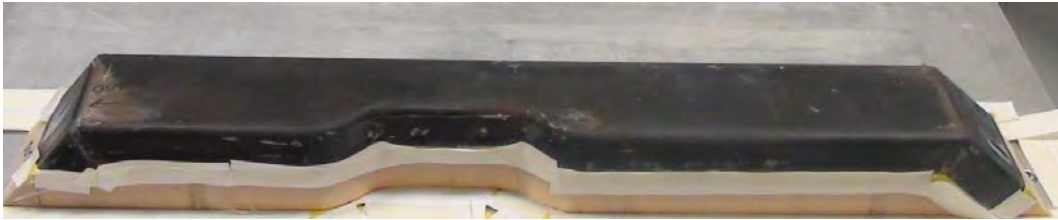


Fig. 9.3.3 Rear bumper strut

The bumper strut was removed from the rear bumper assembly and used as the mold for the fabrication of the composite bumper strut. The strut was about 26 inches long and 4 inches wide. The strut weighed 8 lb, but the composite strut was predicted to weigh significantly less.

9.3.4 Materials and Process

The mold in which the preform was draped was the original steel bumper strut that had been removed from the vehicle. A high-density closed-cell PVC foam was fitted into the channel of the steel strut. This fitting allowed for the vacuum bag to be sealed around the edges and ends of the steel mold.

The preform comprised 6 layers of an S-2 Glass fabric with an 8-harness satin weave supplied by US Composites. This weave pattern allowed for enough flexibility in the preform so that it could conform to the different curvatures of the mold. The 6 layers were stitched together using the Laystitch stitching machine. The preform was draped over the mold, and the corners were then notched to avoid wrinkling in the corners. Figure 9.3.4 shows the fabric and the cut shape of the preform.

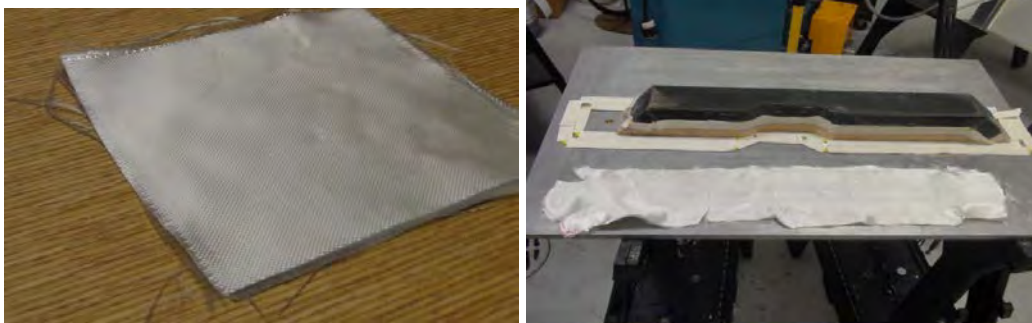


Fig. 9.3.4 Fabric and cut preform

Where the fabric was slit to conform to the inside corners in the mold, the preform tended to open up and expose the mold in these areas, creating spots that were lacking in reinforcement. To solve this problem, thin filler strips of fabric were inserted between each layer of fabric to reinforce these inside corners.

After the fabric had been draped over the mold, a peel ply, resin transfer medium, and vacuum bag, respectively, were placed on top of the preform. The vacuum bag was then sealed around the sides and ends of the mold to prevent resin flow channels from occurring.

After the vacuum bag was sealed around mold, the bag was then sealed with 2 layers of sealant tape to the tooling plate. This seal ensured that a satisfactory vacuum pressure was able to be achieved prior to the resin infusion. Figure 9.3.5 shows the draping of the preform over the steel mold while Fig. 9.3.6 shows the final layup after all of the layers have been sealed under the vacuum bag.

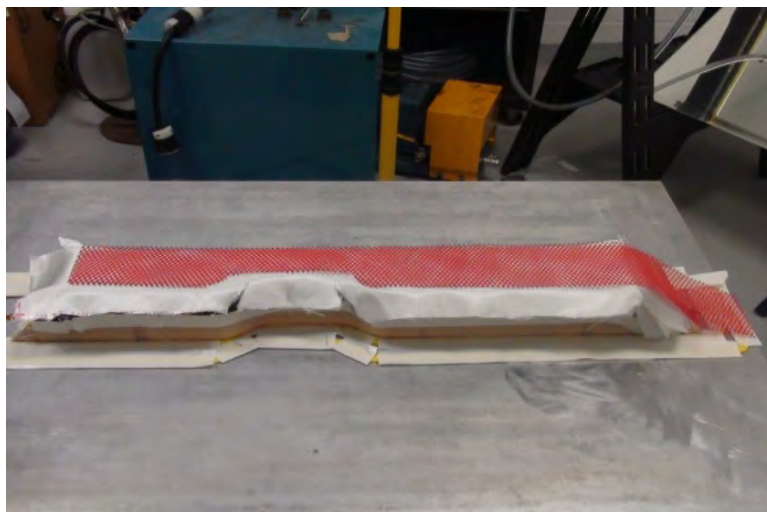


Fig. 9.3.5 Preform draping

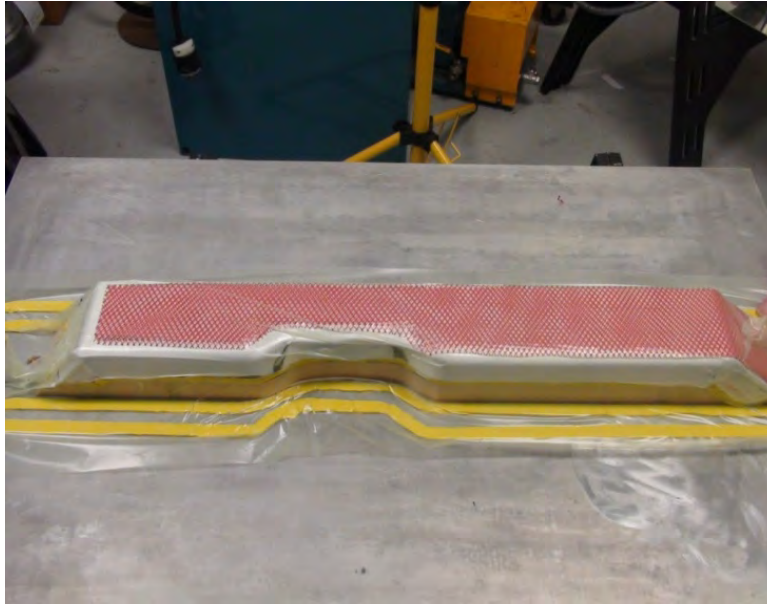


Fig. 9.3.6 Final layup stage

The vacuum-assisted resin transfer molding (VARTM) process was used for the fabrication of the composite bumper strut. In this process a fabric preform is infused with an Applied Poleramic SC-15 2-phase epoxy resin and oven cured. The curing cycle consisted of curing at a temperature of 60 °C for 2 h and then curing for an additional 4 h at 94 °C. Figure 9.3.7 shows the VARTM setup used for the infusion of the strut preform.

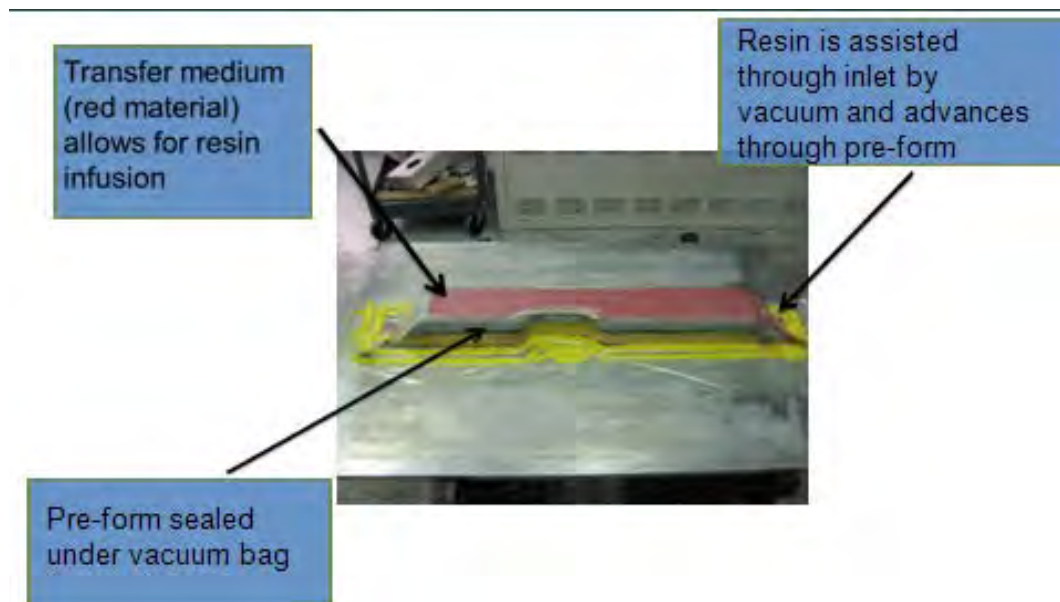


Fig. 9.3.7 VARTM setup

9.3.5 Trials

Several fabrication trials were performed, with improvements being made after each trial leading to better results.

For the first trial, the vacuum bag was sealed to the tooling plate but not around the mold or the preform. Thus, during the infusion, resin flowed around the edges of the mold and flowed between the mold and the foam core. This led to inconsistent saturation of the preform as well as the foam core becoming covered with resin. Figure 9.3.8 shows trial 1 after infusion. It can clearly be seen from the picture that flow channels developed around the mold and that the resin flowed under the mold and down the sides of the foam core.

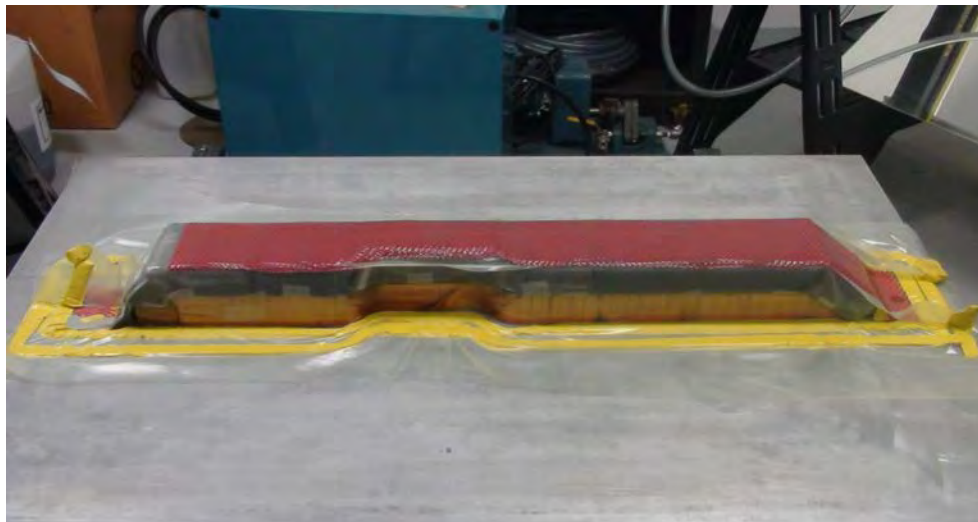


Fig. 9.3.8 Trial 1 after infusion

Based on the results from the first trial, several improvements were made for trial 2. Trial 2 was infused with oil that had a similar viscosity to that of the SC-15 epoxy resin. Also, before the infusion of trial 2, the vacuum bag was sealed around the sides and ends of the mold. This seal was done to prevent the resin from running under the steel mold and from creating flow channels around the side of the mold. The infusion was successful, and thorough saturation of the preform was achieved.

For the third trial, minor changes were made to improve the results even more. The filler strips described earlier were added to the inside corners for reinforcement. For this trial SC-15 resin was used for the infusion instead of the oil used for the infusion in trial 2. The resin was also oven cured after infusion for trial 3.

9.3.6 Results

The outcome of this project yielded several important results. An efficient manufacturing technique was developed for the fabrication of composite parts with complex shapes using the VARTM process. Also, a successful prototype of the rear bumper strut was fabricated from composites. Figure 9.3.9 shows a photograph of the completed bumper strut prototype.



Fig. 9.3.9 Composite bumper strut prototype

The results of this project also helped pinpoint the areas of composite manufacturing of complex geometries that need improvement. An improved vacuum bagging technique needs to be used to reduce wrinkles on the surface of the finished part. In Fig. 9.3.10 a wrinkle in the outer surface of the part can be seen above the recessed inside corner area of the part inside the red border.



Fig. 9.3.10 Highlighted wrinkle in part surface

Because of the difficulties that were discovered in removing the part from the steel mold, an improved release mechanism needs to be incorporated into the process. The use of tackified fabrics may also be beneficial to reduce the sliding of the various layers during the layup process and to help reduce fraying of the fabric preform.

9.4 Interlaminar Reinforcement of Glass Fiber/Epoxy Composites with Graphene Nanoplatelets

Nicholas T Kamar, Mohammad Mynul Hossain, Lawrence Drzal, and Alfred Loos

9.4.1 Summary

Incorporation of carbonaceous nanomaterials into fiber-reinforced/epoxy polymer composites (FREPCs) has been shown to improve a variety of intralaminar mechanical properties. Our research investigated the ability of graphene nanoplatelets (GnPs) to improve the interlaminar properties of glass-reinforced multilayer composites. We developed a novel method for the inclusion of GnPs into plain-weave glass fabric FREPCs processed with vacuum-assisted resin transfer molding (VARTM). Pristine GnPs are dispersed in a solvent solution of diglycidyl ether of bisphenol A epoxy resin and then uniformly coated onto the surface of glass fabrics at different concentrations prior to laminate stacking. The sizing/GnP combination adheres to the glass fabric and allows full resin infusion using a conventional VARTM processing method. Subsequently, 4-point bending flexural test results on the cured laminate produces a 29% improvement in flexural strength with the addition of only 0.25 wt% GnP compared to the pristine glass FREPCs. At the same loading, mode-I fracture toughness testing revealed a 25% improvement. Additionally, low-velocity drop weight impact testing indicated improved energy absorption capability with increasing interlaminar concentration of GnPs. Qualitatively, ultrasonic c-scans and dye penetration inspection analysis supports these results.

9.4.2 Introduction

Recently, in an effort to reduce carbon dioxide emissions, the Environmental Protection Agency (EPA) and the National Highway Traffic Safety Administration (NHTSA) have introduced strict fuel economy standards for light duty vehicles [1]. Light-weighting vehicles with high-performance fiber-reinforced epoxy polymer composites (FREPCs) will likely play a major role in continuing to meet or exceed EPA and NHTSA standards. Compared to steel, FREPCs offer very high specific strength and stiffness at a low density. However, FREPCs are brittle materials, owing to their cross-linked polymer structures and strong and stiff glass fibers that facilitate their high strength and modulus [2]. Therefore, over the last 4 decades, researchers have investigated the incorporation of micron and, more recently, nanoscale materials to improve FREPC toughness [3].

Because of their outstanding thermal, electronic, and mechanical properties, carbonaceous nanomaterials have shown considerable promise as additives to epoxy polymer composites (EPCs) [4] and FREPCs [5] in improving a variety of composite mechanical properties. These materials include carbon nanotubes (CNTs), buckminsterfullerene (C_{60}), and, more recently, GnPs [4,6]. In particular, CNTs as additives to polymer matrices have been explored extensively [7]. Their high aspect ratios and high specific strength and stiffness have been shown to improve strength, stiffness, and toughness of EPCs and FREPCs; of course, their beneficial effects are contingent on the degree of their dispersion throughout the composite matrix [8]. Chemical functionalization of CNTs can provide enhanced dispersion and improved interfacial interaction between the polymer matrix and functional nanomaterial [7].

Indeed, the beneficial incorporation of CNTs into EPC matrices has been demonstrated. However, CNTs are expensive, available at a cost of about 100 US dollars per gram [9]. Therefore, to enhance EPC properties in a cost-effective manner, researchers have investigated the incorporation GnPs, which share CNT's outstanding thermal, electronic, and mechanical properties at about 1/500th of the cost [10]. These materials are conceptually different from graphene oxide, which is produced via an oxidative process that disrupts the sp^2 basal plane hybridization, effectively reducing graphene's outstanding properties; reduced graphene oxide shares these effects [11–13]. Furthermore, GnPs share nanoclay's layered structure in which graphene sheets are held together via weak van der Waals dispersive forces. As such, GnPs can be intercalated and exfoliated throughout an EPC matrix.

Two primary methods to introduce nanoparticles into laminate composite materials made via resin transfer molding (RTM) are described in the literature. One method involves dispersing the nanoparticles into a resin system, followed by nanoenhanced resin infusion of the laminate plies. However, the high surface area and aspect ratio of the nanoparticles can result in significant increases in resin viscosity [14]. Furthermore, filtration of the nanoparticles at the resin inlet by the fiber reinforcement can prevent a homogeneous dispersion. Another method involves coating/sizing the nanoparticles directly onto the fiber surfaces [15], followed by resin infusion, which can eliminate problems created with the first technique.

Indeed, researchers have investigated the strengthening and toughening mechanisms of graphene in epoxy polymer nanocomposites [16,17]. However, to our knowledge, the current literature does not describe the addition of pristine GnPs in the interply regions of FREPCs produced via VARTM. As such, this work will investigate the dispersion of GnPs onto the surface of plain-weave glass

fabric prior to infusion with a 2-part diglycidyl ether of bisphenol A epoxy resin system. The influence of interply GnP concentration on nanocomposite flexural properties, mode-I fracture toughness, and low-velocity impact properties will be described.

9.4.3 Methods

9.4.3.1 Materials

A low-viscosity 2-part resin system—namely, Applied Polymeric SC-15 epoxy resin (SC-15A) and SC-15 amine hardener (SC-15B)—was used in both the coating and VARTM processing. The fiber reinforcement was Owens-Corning ShieldStrand S-2 Glass in plain-weave with an areal-specific weight of 818 g/m². Exfoliated graphene nanoplatelets (xGnP-5) with a mean diameter of 5 μm and a thickness of 7 nm were kindly provided by XG Sciences in Lansing, Michigan.

9.4.3.2 Coating Process

To disperse the GnPs into a solvent for subsequent coating onto glass fabric, measured quantities of GnPs were added to a solution of 30 g of SC-15A, 2.25 g of SC-15B, and 500 mL of 2-isopropanol. The mixture was then stirred for 5 min, followed by tip sonication at 35% amplitude for 1 h. After sonication, aliquots of solution were weighed and brushed onto the surface of S-2 Glass fabrics such that the final composite laminate panels had concentrations of 0.10, 0.25, 0.50, and 1.0 wt%, respectively. The coated fabrics were degassed in a fume hood for 12–15 h prior to infusion.

9.4.3.3 Composite Production

Glass fabrics with dimensions of 30.48 by 30.48 cm (for flexural and fracture toughness test specimens) and 60.96 by 30.48 cm (for impact test specimens) were infused with the SC-15 resin system using the VARTM process, where the ratio of SC-15 A:B was 100:30 by weight. A 4-ply layup was used to manufacture flexural and impact test specimens, while 8-ply layups were used to produce fracture toughness test specimens. Further, a 140-mm impervious Teflon peel-ply material, which spanned the length of the panel, was folded in half and placed between the fourth and fifth plies of the fracture toughness test specimens. The infusion system consisted of a 91.44- by 60.96-cm steel tooling plate with a single injection port and a single vacuum port. The layup consisted of a tooling plate, a small quantity of liquid mold release, coated (as described in 9.4.3.2) or pristine glass fabric, release ply material, and distribution media. The layup was vacuum

bagged under 0.2 kPa, and the infusion was completed within 2 to 4 min. The infusion system was then placed into a convection oven for cure at 60 °C for 2 h and postcure at 94 °C for 4 h.

9.4.4 Testing

9.4.4.1 Flexural Testing

Four-point bending flexural specimens were prepared and tested in accordance with ASTM D-6272, the test method for flexural properties of unreinforced and reinforced plastics by 4-point bending. Sample testing was performed on a Materials Test System (MTS) 810 in conjunction with a laser extensometer to accurately measure sample displacement. The coupons were 12.7×60 mm with an average thickness of 2.60 mm. Each coupon was carefully placed onto the support bars to ensure symmetric and level sample loading. The load span was taken as one-third of the support span, and the samples had a 16:1 span-to-depth ratio. A 20-N preload was applied at the beginning of each flexural test. A 1.215-mm/min crosshead speed, as calculated from the support span and sample thickness, was applied to each specimen. The specimens were tested until failure, and their load-displacement data were recorded for analysis.

9.4.4.2 Fracture Toughness Testing

Eight-ply panels with a folded 70-mm impervious Teflon peel-ply material insert located between the fourth and fifth middle plies were manufactured for mode-I testing. Specimens were prepared and tested on the basis of ASTM 5528, the test method for mode-I interlaminar fracture toughness of unidirectional fiber-reinforced polymer matrix composites, except that the piano hinges were rotated 180° for simpler attachment. Since the standard calls for a 50-mm insert, 20 mm of the 70-mm initial insert and panel edge were removed with a diamond-tip saw. Piano hinges with a width of at least 25.4 mm were attached with a 5-min cure Quickset epoxy to the ends of the 25.4-mm-wide and 152.4-mm-long samples. The average sample thickness was 4.85 mm. A clean razor blade was then carefully used to remove the starter crack Teflon material, and the sample was placed onto the MTS grips for testing. A constant loading rate of 5 mm/min was applied to open the samples under mode-I, and a Cannon EOS Rebel T4i was used to record the crack event. The drawing program Corel was used to calculate the length of the crack from the end of the starter crack to the initial onset of failure. Mode-I fracture toughness (G_{Ic}) values were calculated according to modified beam theory, as shown in Eq. 9.4.1.

$$G_{Ic} = \frac{3P\delta}{2ba}, \quad (9.4.1)$$

where P is the load (newtons), δ is the load point displacement (meters), b is the specimen width (meters), and a is the delamination length (meters).

9.4.4.3 Low-Velocity Impact Testing

A Drop-Weight Instron Dynatup 8250 impact machine was used for impact testing. The machine setup consists of a 12.7-mm-diameter instrumented tup mounted on a crosshead with a provision for attachment of weights. To perform an impact test, the 11.82-kg impactor is released along stiff, smooth guide columns and singularly impacts a mounted composite sample. The 12.7- × 12.7-cm samples were clamped at the base of the test fixture by 8 bolts. The energy of impact is governed by the drop height; 4 different energy levels were used for testing: 20, 40, 60, and 80 J, respectively. Load displacement curves were recorded for analysis.

9.4.4.4 Dye-Penetration Inspection

Dye penetration inspection (DPI) was performed to investigate the surface damage caused by a low-velocity impact event, which was not visible to the naked eye. Zyglo Penetrant ZL-27A fluorescent inspection dye was sprayed onto the impact surfaces and back sides of the impacted samples. After 30 min, excess penetrant was removed, and Zyglo Developer Z9-9F was added to provide contrast. Ultraviolet light was then applied to each side of the sample, and fluorescence was captured by a digital camera.

9.4.4.5 Ultrasonic C-Scanning

To evaluate the internal structure of the impacted specimens, ultrasonic C-scanning was performed using the Pulse-Eco method. An ultrasonic ULTRAPAC II system (automated immersion system), in association with UTwin™ software, was used to perform data acquisition, imaging, and analysis. The scanning rate was 5 MHz, and a 12.70-mm-diameter transducer was used. To perform ultrasonic inspection, the sample was placed in a water tank and the transducer was brought over the sample. The scan area was selected by choosing the x and y position that would result in complete scanning of the specimen. As the ultrasound propagated through the water medium, a portion is reflected back from the top surface of the sample, while the rest of the sound passes through the material. Defects present in the FREPC act as reflectors, and a defect echo is obtained. To evaluate the reflected signal amplitude changes through the back of each specimen, an electronic gate was set on the back surface echo to digitize the

signal. For each impacted specimen, scanning was carried out for both the front (impact side) and back surface facing the transducer. The digitized data were further analyzed by pseudo-coloring to get a colored map to differentiate a defective area from a “good” area.

9.4.5 Results and Discussion

9.4.5.1 Mechanical Properties

The stress-strain behavior of a single 4-point flexural test at GnP concentrations of 0 (“pristine”), 0.10, 0.25, and 0.50 wt% specimens is shown in Fig. 9.4.1. The slope of the elastic region is fairly linear until the first load drop; this point was used to calculate the maximum flexural strength per sample. The largest maximum flexural strengths were observed for samples with low loadings of GnPs—namely, 0.10 and 0.25 wt%. Once the concentration of GnPs reached 0.5 wt%, the specimen stress-strain response closely resembled that of the pristine samples. These trends were observed for all samples tested.

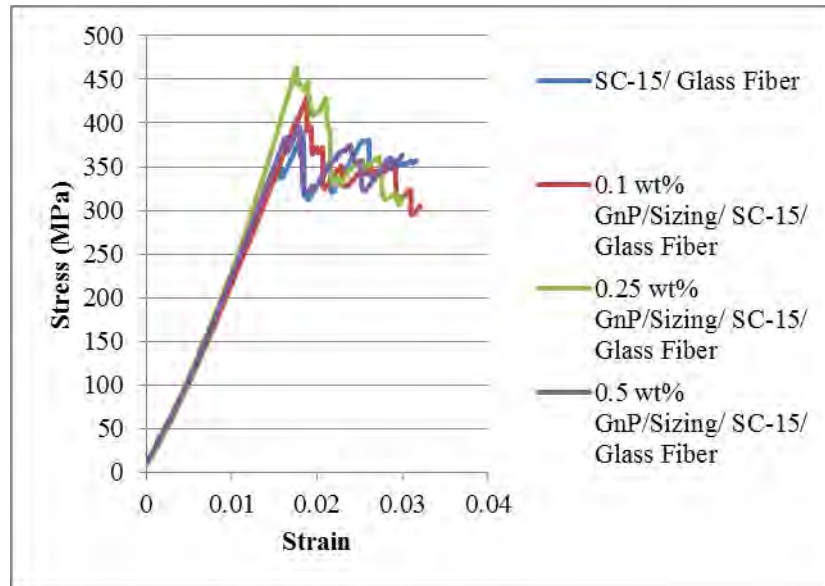


Fig. 9.4.1 Four-point flexural test results for pristine and 0.10, 0.25, and 0.50 wt% GnP samples

The average maximum flexural strength of 0, 0.10, 0.25, 0.50, and 1.0 wt% GnP specimens, along with corresponding error bars, is shown in Fig. 9.4.2. Pristine specimen flexural strength values are slightly larger than those reported in the literature for the S-2 Glass/SC-15 system: Haque et al. [18] determined an average value of 298 MPa, and we report a value of 324.78 ± 31.62 MPa. In the system described here, the GnP concentration was optimized at 0.25 wt%, resulting in a 29% increase in flexural strength compared to the pristine

specimens. At 0.50 wt% GnP, the nanocomposite flexural strength showed a less dramatic increase. At 1.0 wt% GnP, the error bars between the pristine and GnP samples overlap, and no improvement is observed. Furthermore, these enhancements in flexural strength are comparable to those reported by Haque et al., but at one-fourth wt% of nanofiller; it appears that GnPs are more efficient nano-additives than intercalated and phase-separated montmorillonite clay in the S-2 Glass/SC-15 system. Additionally, the concentration of GnP had an effect on the failure mode of the samples during flexural testing. Those samples with lower concentrations of GnPs (0.10 and 0.25 wt%) failed on the tension side, while those samples with higher concentrations of GnP (0.50 and 1.0 wt%) failed on the compression side or by delamination.

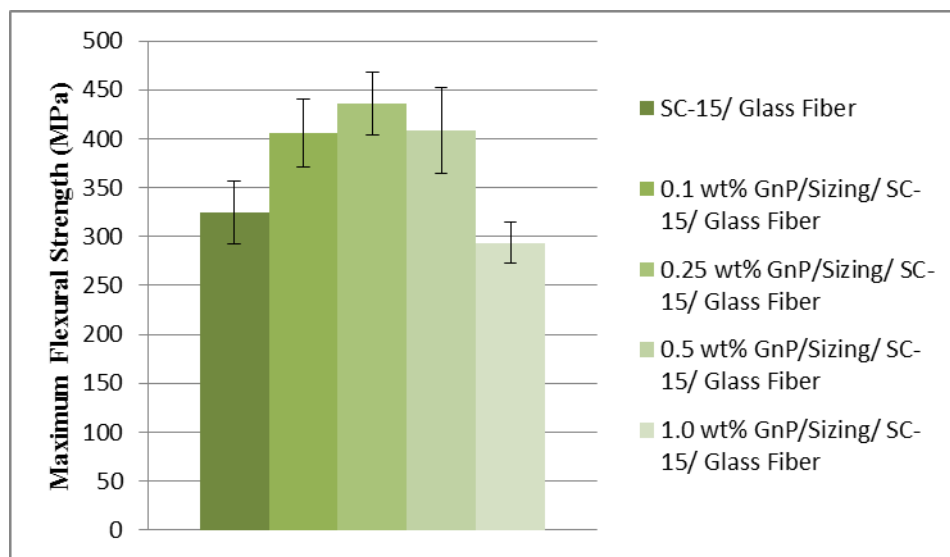


Fig. 9.4.2 Average maximum flexural strength of pristine and 0.10, 0.25, and 0.50 wt% GnP samples

Mode-I fracture toughness (G_{Ic}) testing results for pristine, 0.25 wt%, and 1.0 wt% GnP specimens, and their corresponding error bars, are shown in Fig. 9.4.3. G_{Ic} was optimized at 0.25 wt% GnP loadings, yielding a 25% improvement relative to the pristine samples. However, the 1.0 wt% GnP specimens indicated a substantial decrease in G_{Ic} values, which could be due to agglomeration of GnPs at the fiber/matrix interface. In addition to acting as stress concentrators, such aggregates can form a path for crack propagation [19].

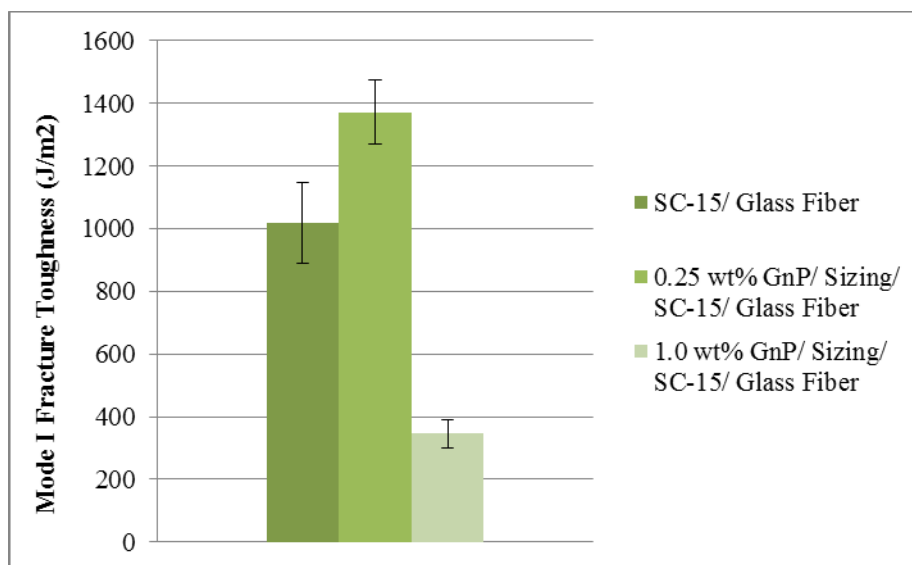


Fig. 9.4.3 Mode-I fracture toughness (G_{IC}) results of pristine, 0.25 wt%, and 1.0 wt% GnP samples

Mode-I fracture surfaces of specimens with varying concentrations of GnPs were analyzed under scanning electron microscopy (SEM). A variety of details are visible at both low and high magnifications of pristine and GnP-doped samples. For all specimens, the SEM images indicated that the propagating crack was limited to the region between the middle plies.

RTM processes, in which a fabric preform is infused with a 2-part resin system, can introduce voids which are most likely due to mechanically entrapped air [20]. Infused fabrics in plane-weave have 2 regions in which voids can form: the smaller region between the individual fibers within a tow and the larger region between individual tows where the warp and fill cross over one another; voids formed in these regions are called “tow voids” and “channel voids”, respectively [20].

Channel voids were predominately located at the warp and fill crossover regions, as determined by inspection of the fracture surfaces. One such void is shown in Fig. 9.4.4a; this void has a diameter on the order of 1 mm. Figures 9.4.4b and 9.4.4c show progressively higher magnification views of the color mapped boxed areas. The wavy surface pattern in Fig. 9.4.4c indicates a free surface. In addition to larger-scale channel voids, submicron scale voids are scattered throughout the polymer matrix. These submicron scale voids could be due to phase separation followed by cavitation of the toughening agent present in the Applied Polymeric SC-15 resin system. During cure, the epoxy resin will cross-link via a ring-opening mechanism in which partially positive carbon atoms on the epoxide rings are attacked by the nucleophilic amine groups of the hardener; this exothermic

curative process is governed by the enthalpy term in the Gibb's free energy of mixing [21]. Meanwhile, the proprietary toughening agent in SC-15 can phase-separate from the mixture [21–23]. During fracture of the cured specimen, the thermoplastic particles stretch and break. Once the fracture is complete, the particles will fall back into expanded cavities, which appear as submicron and micron-scale voids [24]. These submicron-scale voids were also present in the samples containing GnPs and look quite similar to those cavities present in the fracture surfaces of rubber-toughened epoxy systems [25].

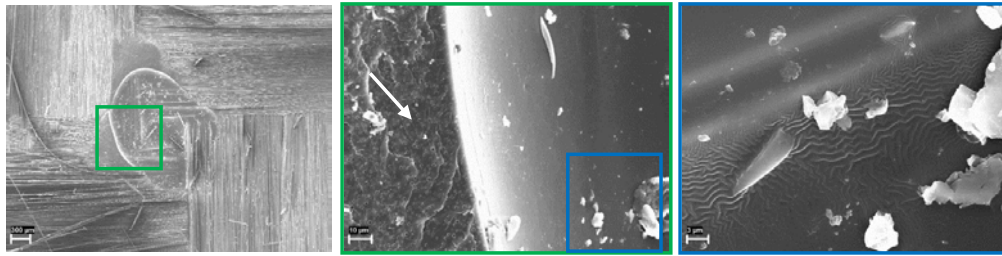


Fig. 9.4.4 SEM image of a pristine mode-I fracture surface. Image a) shows a macrovoid, and images b) and c) are progressively higher magnifications of a void edge, as indicated by the colored boxes.

Samples containing interply dispersed GnP exhibit different fracture surface morphologies at the warp and fill crossover regions. For example, Fig. 9.4.5a shows that the channel regions in the 0.25 wt% GnP specimens have a rougher edge morphology than those same regions in the pristine specimens. Figure 9.4.5b shows a closer view of the 0.25 wt% GnP mode-I fracture surface fibers. GnPs present on these surfaces appear to be aggregated to some extent. Figure 9.4.5c shows an intertow aggregate of GnP-5, which should have an average platelet diameter of 5 μm . This platelet appears to have a basal plane larger than the mean diameter.

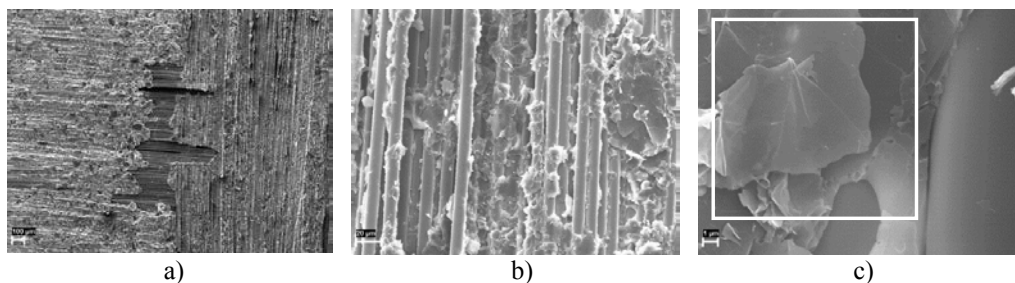


Fig. 9.4.5 Mode-I fracture surface of a 0.25 wt% GnP sample. Image a) shows a typical channel region, image b) is a closeup of the fibers on the fracture surface, and image c) shows a GnP aggregate lying between fibers, as highlighted by a white box.

Resin-rich regions of the 0.25 wt% GnP fracture surfaces are shown in Fig. 9.4.6. A GnP aggregate is highlighted in Fig. 9.4.6 by a green box. Submicron-scale voids are also present and have the characteristic shape, size, and texture of those formed by cavitation because of the presence of a phase-separated rubber toughening agent, as described previously.

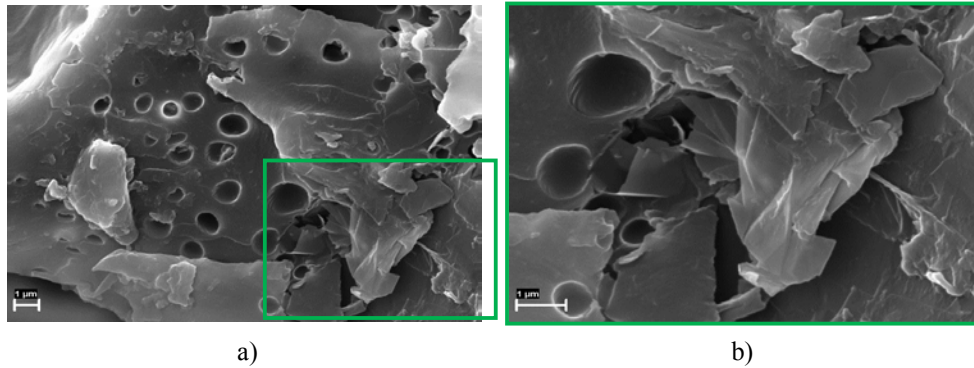


Fig. 9.4.6 Intertow region of the 0.25 wt% GnP nanocomposite: a) low and b) high magnification

9.4.5.2 Low-Velocity Drop Weight Impact Properties

The impact test results for pristine, 0.25 wt%, and 1.0 wt% GnP specimens are presented in Figs. 9.4.7–9.4.11, and the corresponding peak loads are shown in Table 9.4.1. The force-time histories of pristine, 0.25 wt%, and 1.0 wt% GnP specimens impacted at 20, 40, 60, and 80 J, respectively, are shown in Fig. 9.4.7.

Table 9.4.1 Impact results summary

Impact Energy	As Received		0.25wt% xGnPs		1wt% xGnPs	
	Peak Load (kN)	Absorbed Energy (J)	Peak Load (kN)	Absorbed Energy (J)	Peak Load (kN)	Absorbed Energy (J)
20	7.661	4.744	7.483	6.155	6.945	11.216
40	11.399	16.614	11.497	17.868	9.33	26.724
60	12.974	48.326	12.129	43.385	11.663	44.456
80	13.855	^a	14.478	^a	11.672	75.59

^a Perforation

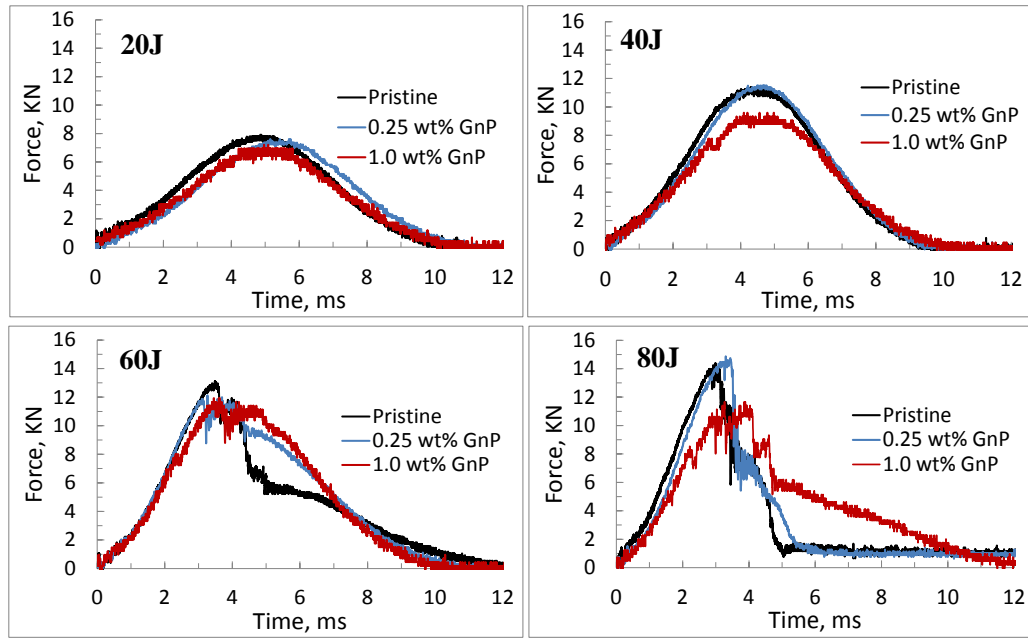


Fig. 9.4.7 Force-time response of pristine, 0.25 wt%, and 1.0 wt% GnP specimens at 20-, 40-, 60-, and 80-J impact energies, respectively

At 20 J of impact energy, the specimen responses are symmetric about the peak load for both pristine and GnP-reinforced composite laminate plates, which indicates a lack of prominent specimen damage. Peak loads for the pristine specimens are larger than those reported in the literature for the S-2 Glass/SC-15 system [26]. However, the peak load decreased with increasing GnP concentration, which could result from minor interlaminar damage and/or debonding between the polymer matrix and GnP nanoparticles. At 40-J impacts, the specimen responses exhibited a slight asymmetry about the peak load, indicating the presence of damage in the specimens. Also, at 40 J, the 1.0 wt% specimens exhibited a sharp load drop at about 7.8 kN, followed by a climb up to peak load. This load drop at 7.8 kN was also present for the 1.0 wt% samples at 60 and 80 J but was not visible in the 1.0 wt% specimens tested at 20 J. This abrupt load drop may have resulted from interfacial failure in the specimens.

At 60 and 80 J, the load-time specimen responses were substantially asymmetric about the peak load. Beyond this load point, several subsequent load drops occurred prior to the saturation level; the number of load drops was found to increase with increasing energy levels. Each load drop indicates some damage, which may be due to fiber breakage on the front and back surfaces and/or interfacial delamination. For both 60- and 80-J energy levels, the area under the load-time curves up to saturation was increased with increasing weight percent of GnPs, which implies that energy absorption performance increases with increasing addition of GnPs.

The energy-time histories of pristine, 0.25 wt%, and 1.0 wt% GnP specimens impacted at 20, 40, 60, and 80 J, respectively, are shown in Fig. 9.4.8, and the corresponding absorbed energies are noted in Table 9.4.1.

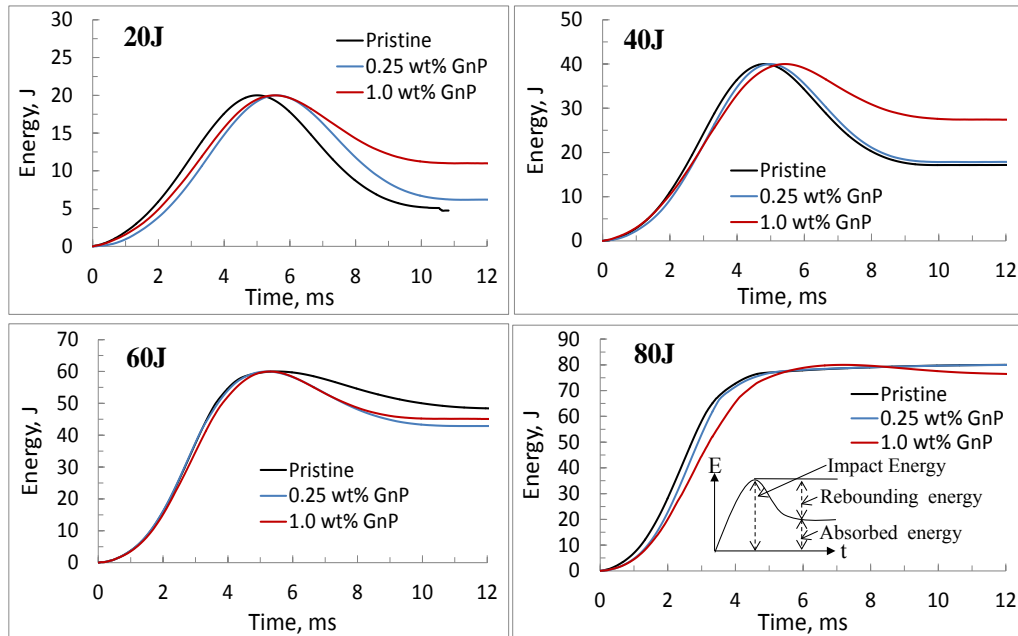


Fig. 9.4.8 Energy-time response of pristine, 0.25 wt%, and 1.0 wt% GnP specimens at 20-, 40-, 60-, and 80-J impact energies, respectively

At 20- and 40-J impact energies, energy absorption performance increased with increasing concentration of GnPs, where absorbed energy is defined as the difference between the impact and rebound energies and is shown schematically in Fig. 9.4.8. However, at 60 J, the energy absorption performance was highest for the pristine specimen; the GnP-reinforced samples exhibited the same trend as that described for 20- and 40-J impact energies. This anomaly may be the result of thickness variation between tested specimens. At 80 J, the energy absorption performance reached saturation for both pristine and 0.25 wt% GnP samples; perforation of the tested specimens by the impactor tup was observed. Contrarily, the 1.0 wt% GnP samples were able to absorb some of the impact energy, protecting the specimen from perforation.

The force-deflection histories of pristine, 0.25 wt%, and 1.0 wt% GnP specimens impacted at 20, 40, 60, and 80 J respectively, are shown in Fig. 9.4.9.

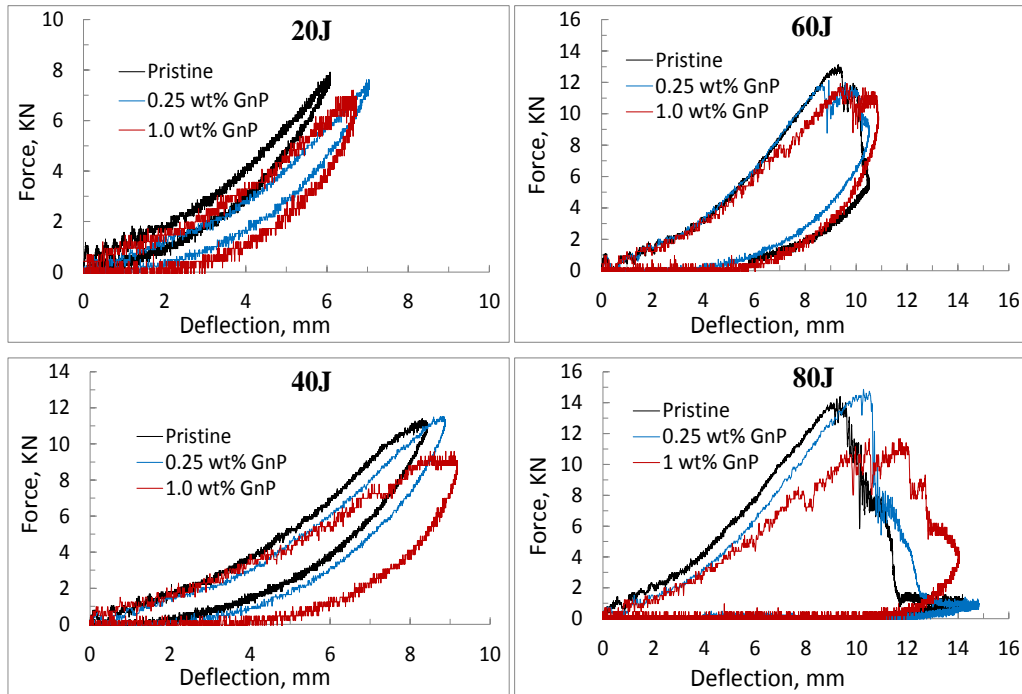


Fig. 9.4.9 Force-deflection response of pristine, 0.25 wt%, and 1.0 wt% GnP specimens at 20, 40, 60, and 80 J impact energies, respectively

At 20, 40, and 60 J of impact energy, the pristine, 0.25 wt% GnP, and 1.0 wt% GnP specimens show a closed loop. This area inside the loop is the energy absorbed during impact, and the area under the curve is the energy transferred from the tup to the plate and back [27]. As expected, these loops were observed to increase with increasing impact energy. It is evident that none of the tested specimens were perforated within 60 J of impact energy. As described previously, at 80 J the pristine and 0.25 wt% GnP specimens were completely perforated. However, at 80 J the 1.0 wt% GnP specimens show a closed loop.

Analysis of Figs. 9.4.7–9.4.9 shows that the slopes of the pristine and 0.25 wt% GnP specimens are quite similar at all of the energies tested. However, the 1.0 wt% GnP specimens have a different slope than the other concentrations tested in this study; this effect is more pronounced at higher impact energies. As such, it can be concluded that samples with 1.0 wt% interlaminar concentrations of GnP will exhibit different failure modes under low-velocity impact than the baseline or 0.25 wt% GnP specimens.

Postimpact testing specimens were examined under DPI. Figure 9.4.10 shows the DPI images of pristine, 0.25 wt%, and 1.0 wt% GnP samples tested at 20, 40, 60, and 80 J, respectively.

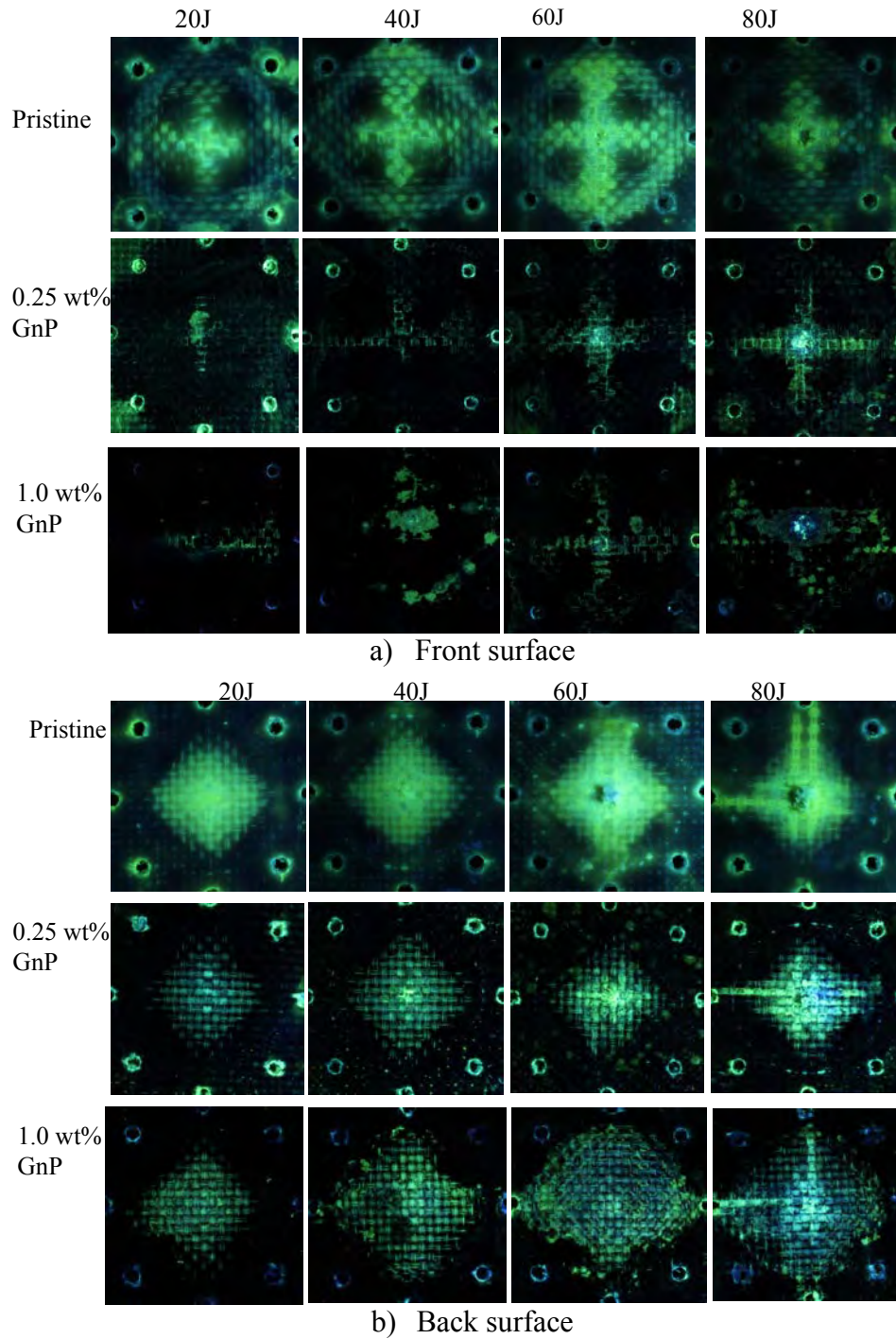


Fig. 9.4.10 Dye-penetration inspection (DPI) images of impacted a) and back b) surfaces

The DPI images of the pristine specimens indicate prominent surface damage, which could have resulted from matrix and/or fiber breakage. This damage increases with increasing impact energy levels. At each energy level, the images show a decrease in damage area with increasing GnP concentration (down a

column). At 80 J, both the pristine and 0.25 wt% GnP samples show evidence of perforation. However, at 1.0 wt% loadings, the damage appears to delocalize throughout the surface layers. The back sides of the impacted specimens were also analyzed via DPI and are shown in Fig. 9.4.10b. These images indicate that fiber breakage occurred for pristine and 0.25 wt% samples tested at 40, 60, and 80 J. For 1.0 wt% samples, fiber breakage was only observed after an 80-J impact. It was also observed that the back surfaces have a larger damage area than the front surfaces, which was due to bending of the specimens by the impactor tup.

The attenuation images from ultrasonic c-scanning of 0, 0.25, and 1.0 wt% GnP-reinforced specimens impacted at 20, 40, 60, and 80 J, respectively, are shown in Fig. 9.4.11. It was difficult to differentiate the defective and structurally sound areas using the attenuation images from the front surfaces facing the transducer. Therefore, only those images of the back surfaces are shown.

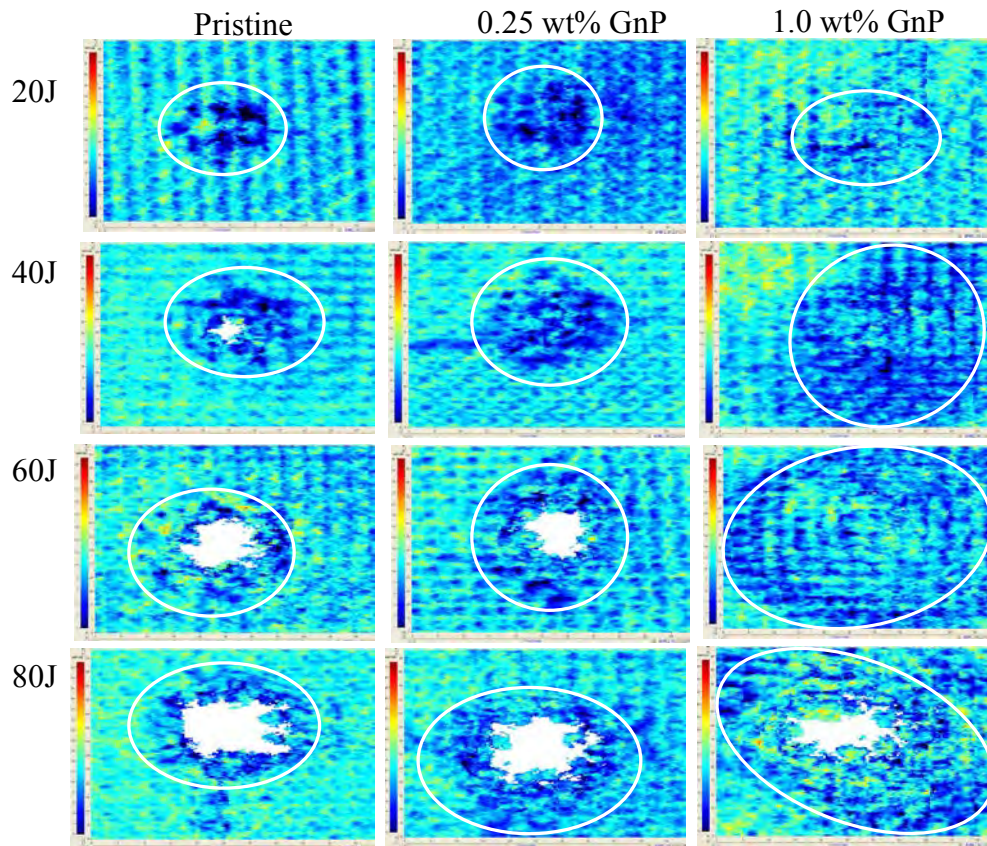


Fig. 9.4.11 C-scan images of back surfaces

The attenuation images indicate the extent of damage in the impact-tested specimens. White, closed loop-lines are drawn onto Fig. 9.4.11 to surround these areas. Within these loops, the white color indicates perforation and/or matrix and fiber breakage, while the deep blue color represents interfacial damage. Complete perforation was only observed for pristine and 0.25 wt% GnP specimens at 80 J. As such, the white regions in the other specimens represent significant surface damage.

The damage profile of the pristine specimens is highly concentrated; a similar result is observed for the 0.25 wt% GnP specimens. However, at higher concentrations the GnPs are better able to absorb and dissipate impact energy throughout the specimens, leading to increased interfacial damage on the back surfaces. These trends were not observed at or near the impact surfaces.

9.4.6 Conclusion

We have developed a novel method for dispersing GnPs into the interply regions of FREPCs produced with VARTM. The concentration of GnPs in the nanocomposite was optimized to 0.25 wt%, providing a 29% improvement in flexural strength and a 25% improvement in mode-I fracture toughness. However, at higher loadings of GnPs, flexural strength parallels that of the baseline samples, and drastic reductions in fracture toughness were observed. Fractographic investigation of the mode-I-tested specimens indicated that channel regions, where the warp and fill cross over, show a rougher fracture surface morphology by the addition of GnPs. Low-velocity drop-weight impact testing of FREPCs revealed enhanced energy absorption performance by interlaminar incorporation of GnPs. This enhancement was observed to increase with increasing concentration. Postimpact damage analysis by DPI and ultrasonic c-scanning qualitatively confirmed these results.

In conclusion, the relatively simple nanocomposite production method developed here is compatible with existing VARTM composite processing technologies and leads to significant improvements in both flexural strength and mode-I fracture toughness of FREPCs with continuous enhancement in impact damage resistance. Future work should be done to explore chemical functionalization of the nanoadditive to improve dispersion quality and interfacial interaction between the polymer matrix, fiber reinforcement, and GnPs, which may further increase both nanocomposite strength and toughness.

9.4.7 References

- [1] U. EPA, “GHG Emission Standards for Light-Duty Vehicles: Manufacturer Performance Report for the 2012 Model Year.” [Online]. Available: <http://www.epa.gov/otaq/climate/ghg-report.htm>. [Accessed: 16-May-2014].
- [2] B. Wetzel, P. Rosso, F. Hauptert, and K. Friedrich, “Epoxy nanocomposites – fracture and toughening mechanisms,” *Eng. Fract. Mech.*, vol. 73, no. 16, pp. 2375–2398, Nov. 2006.
- [3] A. F. Yee and R. A. Pearson, “Toughening mechanisms in elastomer-modified epoxies,” *J. Mater. Sci.*, vol. 21, no. 7, pp. 2462–2474, Jul. 1986.
- [4] S. Chatterjee, F. Nafezarefi, N. H. Tai, L. Schlagenhauf, F. A. Nüesch, and B. T. T. Chu, “Size and synergy effects of nanofiller hybrids including graphene nanoplatelets and carbon nanotubes in mechanical properties of epoxy composites,” *Carbon*, vol. 50, no. 15, pp. 5380–5386, Dec. 2012.
- [5] F. Yavari, M. A. Rafiee, J. Rafiee, Z.-Z. Yu, and N. Koratkar, “Dramatic Increase in Fatigue Life in Hierarchical Graphene Composites,” *ACS Appl. Mater. Interfaces*, vol. 2, no. 10, pp. 2738–2743, Oct. 2010.
- [6] T. Ogasawara, Y. Ishida, and T. Kasai, “Mechanical properties of carbon fiber/fullerene-dispersed epoxy composites,” *Compos. Sci. Technol.*, vol. 69, no. 11–12, pp. 2002–2007, Sep. 2009.
- [7] P.-C. Ma, N. A. Siddiqui, G. Marom, and J.-K. Kim, “Dispersion and functionalization of carbon nanotubes for polymer-based nanocomposites: A review,” *Compos. Part Appl. Sci. Manuf.*, vol. 41, no. 10, pp. 1345–1367, Oct. 2010.
- [8] F. Hussain, M. Hojjati, M. Okamoto, and R. E. Gorga, “Review article: Polymer-matrix Nanocomposites, Processing, Manufacturing, and Application: An Overview,” *J. Compos. Mater.*, vol. 40, no. 17, pp. 1511–1575, Sep. 2006.
- [9] “Materials Science Products,” *Sigma-Aldrich*. [Online]. Available: <http://www.sigmaaldrich.com/materials-science/material-science-products.html?TablePage=16376687>. [Accessed: 09-Jun-2014].
- [10] J. R. Potts, D. R. Dreyer, C. W. Bielawski, and R. S. Ruoff, “Graphene-based polymer nanocomposites,” *Polymer*, vol. 52, no. 1, pp. 5–25, Jan. 2011.

- [11] Y. Hernandez, V. Nicolosi, M. Lotya, F. M. Blighe, Z. Sun, S. De, I. T. McGovern, B. Holland, M. Byrne, Y. K. Gun'Ko, J. J. Boland, P. Niraj, G. Duesberg, S. Krishnamurthy, R. Goodhue, J. Hutchison, V. Scardaci, A. C. Ferrari, and J. N. Coleman, "High-yield production of graphene by liquid-phase exfoliation of graphite," *Nat. Nanotechnol.*, vol. 3, no. 9, pp. 563–568, Sep. 2008.
- [12] L. Liu, J. Zhang, J. Zhao, and F. Liu, "Mechanical properties of graphene oxides," *Nanoscale*, vol. 4, no. 19, p. 5910, 2012.
- [13] C. K. Chua and M. Pumera, "Covalent chemistry on graphene," *Chem. Soc. Rev.*, vol. 42, no. 8, pp. 3222–3233, Mar. 2013.
- [14] Z. Fan, K.-T. Hsiao, and S. G. Advani, "Experimental investigation of dispersion during flow of multi-walled carbon nanotube/polymer suspension in fibrous porous media," *Carbon*, vol. 42, no. 4, pp. 871–876, 2004.
- [15] S. Movva, G. Zhou, D. Guerra, and L. J. Lee, "Effect of Carbon Nanofibers on Mold Filling in a Vacuum Assisted Resin Transfer Molding System," *J. Compos. Mater.*, vol. 43, no. 6, pp. 611–620, Mar. 2009.
- [16] T. Kuilla, S. Bhadra, D. Yao, N. H. Kim, S. Bose, and J. H. Lee, "Recent advances in graphene based polymer composites," *Prog. Polym. Sci.*, vol. 35, no. 11, pp. 1350–1375, Nov. 2010.
- [17] S. Chandrasekaran, N. Sato, F. Tölle, R. Mülhaupt, B. Fiedler, and K. Schulte, "Fracture toughness and failure mechanism of graphene based epoxy composites," *Compos. Sci. Technol.*, vol. 97, pp. 90–99, Jun. 2014.
- [18] A. Haque, M. Shamsuzzoha, F. Hussain, and D. Dean, "S2-Glass/Epoxy Polymer Nanocomposites: Manufacturing, Structures, Thermal and Mechanical Properties," *J. Compos. Mater.*, vol. 37, no. 20, pp. 1821–1837, Oct. 2003.
- [19] A. F. Avila, M. I. Soares, and A. Silva Neto, "A study on nanostructured laminated plates behavior under low-velocity impact loadings," *Int. J. Impact Eng.*, vol. 34, no. 1, pp. 28–41, Jan. 2007.
- [20] C. H. Park and L. Woo, "Modeling void formation and unsaturated flow in liquid composite molding processes: a survey and review," *J. Reinf. Plast. Compos.*, vol. 30, no. 11, pp. 957–977, Jun. 2011.
- [21] C. B. Bucknall and I. K. Partridge, "Phase separation in epoxy resins containing polyethersulphone," *Polymer*, vol. 24, no. 5, pp. 639–644, May 1983.

- [22] J. L. Hedrick, I. Yilgör, G. L. Wilkes, and J. E. McGrath, "Chemical modification of matrix Resin networks with engineering thermoplastics," *Polym. Bull.*, vol. 13, no. 3, pp. 201–208, Mar. 1985.
- [23] J. H. Hodgkin, G. P. Simon, and R. J. Varley, "Thermoplastic toughening of epoxy resins: a critical review," *Polym. Adv. Technol.*, vol. 9, no. 1, pp. 3–10, Jan. 1998.
- [24] W. D. Bascom, J. L. Bitner, R. J. Moulton, and A. R. Siebert, "The interlaminar fracture of organic-matrix, woven reinforcement composites," *Composites*, vol. 11, no. 1, pp. 9–18, Jan. 1980.
- [25] Y. L. Liang and R. A. Pearson, "The toughening mechanism in hybrid epoxy-silica-rubber nanocomposites (HESRNs)," *Polymer*, vol. 51, no. 21, pp. 4880–4890, Oct. 2010.
- [26] M. V. Hosur, M. R. Karim, and S. Jeelani, "Experimental investigations on the response of stitched/unstitched woven S2-glass/SC15 epoxy composites under single and repeated low velocity impact loading," *Compos. Struct.*, vol. 61, no. 1–2, pp. 89–102, Jul. 2003.
- [27] G. Belingardi and R. Vadori, "Low velocity impact tests of laminate glass-fiber-epoxy matrix

1 DEFENSE TECHNICAL
(PDF) INFORMATION CTR
DTIC OCA

2 DIRECTOR
(PDF) US ARMY RESEARCH LAB
RDRL CIO LL
IMAL HRA MAIL & RECORDS
MGMT

1 GOVT PRINTG OFC
(PDF) A MALHOTRA

1 DIR USARL
(PDF) RDRL WMM A
W SPURGEON

INTENTIONALLY LEFT BLANK.